Award Number: W81XWH-12-M-9532

TITLE: Understanding and Modeling Aggressive ER+ Luminal Adenocarcinoma: Toward Effective Therapeutics

PRINCIPAL INVESTIGATOR:
Bissell, Mina J.

CONTRACTING ORGANIZATION:
Lawrence Berkeley National Laboratory/University of California

Berkeley, CA 94720

REPORT DATE:
December 2018

TYPE OF REPORT:
Final Report

PREPARED FOR: U.S. Army Medical Research and Materiel Command
Fort Detrick, Maryland 21702-5012

REPORT DOCUMENTATION PAGE

Form Approved
OMB No. 0704-0188

1. REPORT DATE	**2. REPORT TYPE**	**3. DATES COVERED**
December 2018	Final	**01 SEP 2013- 31 AUG 2018**

4. TITLE AND SUBTITLE
Understanding and Modeling Aggressive ER+ Luminal Adenocarcinoma: Toward Effective Therapeutics

5a. CONTRACT NUMBER

5b. GRANT NUMBER
W81XWH-12-M-9532

5d. PROJECT NUMBER

5e. TASK NUMBER

5f. WORK UNIT NUMBER

6. AUTHOR(S)

Mina J. Bissell

E-Mail: mjbissell@lbl.gov

7. PERFORMING ORGANIZATION NAME(S) AND ADDRESS(ES)
Lawrence Berkeley National Laboratory
1Cyclotron Rd
Berkeley CA 94702

8. PERFORMING ORGANIZATION REPORT NUMBER

9. SPONSORING / MONITORING AGENCY NAME(S) AND ADDRESS(ES)

U.S. Army Medical Research and Materiel Command
Fort Detrick, Maryland 21702-5012

10. SPONSOR/MONITOR'S ACRONYM(S)

11. SPONSOR/MONITOR'S REPORT NUMBER(S)

12. DISTRIBUTION / AVAILABILITY STATEMENT

Approved for Public Release; Distribution Unlimited

13. SUPPLEMENTARY NOTES

14. ABSTRACT

Our research was designed to further the development of breast cancer therapeutics by generating new, clinically-relevant models of luminal breast cancer. Our goal was to determine the characteristics of tumorigenicity among the many cell subpopulation of breast tumors and to determine how the role of a particular mucin (MM) correlated with aggressive breast cancer cell behavior. In the course of our research, we discovered a novel connection between p53, laminins and nitric oxide, which steered our research in an unexpected and productive course. Progress during this award includes the ability to isolate 10 different highly purified cell subtypes from fresh non-malignant breast tissue. RNA sequencing from these cell types provided a rich data set for us to analyze. We advanced our ability to perform high resolution imaging of primary tumors to develop a FACS strategy to isolate subpopulations from tumor samples. Our unexpected findings of p53, laminins and nitric oxide signaling allowed us better understand signaling mechanisms that drive breast cell behavior in an aggressive manner. The significance of our findings allowed us to contribute strongly to the understanding of breast cancer progression and opened up avenues for new and effective treatments for breast cancer.

15. SUBJECT TERMS

16. SECURITY CLASSIFICATION OF:			**17. LIMITATION OF ABSTRACT**	**18. NUMBER OF PAGES**	**19a. NAME OF RESPONSIBLE PERSON**
a. REPORT	**b. ABSTRACT**	**c. THIS PAGE**			USAMRMC
Unclassified	Unclassified	Unclassified	Unclassified		**19b. TELEPHONE NUMBER** *(include area code)*

Table of Contents

TITLE: Understanding and Modeling Aggressive ER+ Luminal Adenocarcinoma: Toward Effective Therapeutics

1. INTRODUCTION:

Our laboratory has a long track record of developing and utilizing physiologically relevant three-dimensional cell culture models and rodent models for the study of breast cancer progression and mammary gland development. We relied on this expertise to make progress toward the goals of this five-year project. Our research project, which was completed August of this year (2018), was designed to identify new effective therapeutics that can be transferred to the clinic for breast cancer treatment, and to identify prognostic markers. One of the major goals of this research funded by the DoD BCRP focused on the need to develop tractable, predictive models of ER+ luminal adenocarcinoma. The parent Innovator Award supported our development of the first robust model of ER+ luminal adenocarcinoma suitable for development and testing of novel therapeutics for this disease. This research was published in Breast Cancer Research and Treatment (Hines et al, BCRT, 2016). Our experience and the tools developed under the original Innovator Award formed the basis for these original specific aims of this Innovator Expansion award, which are:

Specific Aim1: Identify microenvironmental conditions affecting specific tumor phenotypes. The therapeutic significance of this work is that identification of those factors that promote a more aggressive phenotype enables development of therapeutic interventions or inhibitors that ideally could affect cancer prevention, regression, or even reversion of tumors to normal tissue phenotype.

Specific Aim 2: To determine how many distinct non-stem-cell subpopulations of breast tumors have tumorigenic potential? This question derives from our publication (Kim, PNAS, 2012) in which we reported that at least 3 distinct non-stem-cell breast tumor subpopulations, including fully differentiated cell types, are tumorigenic; so now we ask how extensive is this tumorigenic property? The answer would clearly inform therapeutic strategies for breast cancer as it would identify which elements of this heterogeneous disease must be treated to effect cures.

Specific Aim 3: To determine whether the glycan/carbohydrate epitope of the M18 antibody, which our data published in Kim PNAS 2012 indicated was required for breast cancer invasion and metastasis, whether this specific epitope was truly a critical factor required for invasiveness.

In the course of our research we discovered an unexpected signaling circuitry involving specific micro RNAs, p53, nitric oxide (NO) and laminin signaling. At our last progress report, we noted the difficulties in our reagents needed to complete Specific Aim 3 and we contacted the scientific program officer to make modifications to our original specific aims in order to further investigate the role of this signaling mechanism that controls breast cancer cell aggressiveness. The revised Specific Aim 3 is:

Revised Specific Aim 3: to identify miRNA gene targets for phenotypic reversion of breast tumor cells and verify a role of p53, laminins, and nitric oxide in balancing the reciprocal signaling circuitry between mammary cells and their microenvironment. The changes to our specific aim 3, allowed us to complete this exciting work, which was published earlier this year in elife (Furuta, et al., elife 2018).

Over the five years of this funding, we have made significant progress on all of our aims, as demonstrated by the completion of several peer-reviewed publications and one manuscript currently in revision.

2. KEYWORDS:
Breast cancer models, Luminal adenocarcinoma, Estrogen Receptor, three dimensional (3D) cultures, primary human breast cells, xenograft models, tumorigenicity, RNAseq, glycans, lectins

3.ACCOMPLISHMENTS:

Summary of accomplishments:

- Over the five-year span of this project, significant progress was made on all three original Aims as well as progress towards Aim 3 modifications made at last year's report, with permission from our Program Director.
- Deliverables include a multitude of presentations at scientific meetings and several publications over the lifetime of this funding.
- Pertinent to the training mission of the CDMRP:
    - we reported that Dr. Curt Hines, whose mentoring and training by Dr. Mina Bissell was germane to this award, earned a position on the faculty of the University of New Mexico, which he assumed on July 1, 2016.
    - With the completion of the training of Dr. Hines, Dr. Bissell has assumed mentorship of Dr. Seema Jamil. Dr. Jamil's research focused on Aim2 of this award, which strives to identify the various heterogeneous subpopulations of breast tumors, and, importantly the tumorigenic potential of each. Dr. Jamil, has completed her training.
    - Additionally, during this award, Rosalyn Sayaman completed her Ph.D. and is currently continuing her training as a post-doctoral fellow at the City of Hope, Duarte, CA
- Progress on each Specific Aim is summarized below.
- Our results towards the Aims were disseminated to the scientific community through a number of lectures given by Dr. Bissell and in peer reviewed journals (selected published articles are appended for detailed information of the science).

Specific Aim 1: To create clinically relevant models of luminal breast cancer from normal primary human cells. Our goal here is to create models in which the roles of the different components of the tumor microenvironment can be independently manipulated to learn the tumor promoting or suppressive effects of each, as well as effect of each on response to estrogen ablation therapy.

Progress:

- In years 1&2 we reported development of a FACS-based strategy to isolate 12 distinct, highly pure cell subpopulations from fresh non-malignant human breast tissues, successful phenotypic stabilization in culture 11 of these populations (red blood cells being the 12th subpopulation and thus non-culturable), and derivation of detailed and highly replicable

RNA seq datasets from each freshly isolated (uncultured) subpopulation. The RNA seq database so generated is incomparable providing a rich resource of data for future work.

- To facilitate generation of new models of luminal adenocarcinoma from the freshly isolated luminal subpopulations of the breast, we published our protocol for overcoming the inherent transduction bias of human breast epithelia and also reported our development of lentiviral vectors encoding genes capable of overcoming senescence barriers and inducing cancerous progression (Hines, et al., Nat Comm, 2015, appended)

- Over the last two years of our work we, we have reproducibly isolated RNA from multiple samples of non-malignant human breast tissue. From this we obtained detailed and extensive RNA sequence database of the 12 subpopulations. This is a very large data set to be mined. We have analyzed these data with a focus on identifying receptor and ligand pairs to predict specific "inter-type" cellular communication patterns important to generate and/or maintain tissue phenotype. These data are the center of a publication in preparation.

- In the last year of this funding, we finalized data with our collaborator Kornelia Polyak, at Dana-Farbor Cancer Institute, Boston, Massachusetts. This work resulted in a manuscript, which is currently in revision. In this work, we investigated regulators of normal myoepithelial cell differentiation and perturbations of these regulators in *BRCA1* and *BRCA2* mutation carriers and in DCIS by analyzing gene expression and chromatin profiles. We identified an interconnected auto-regulatory transcriptional network orchestrated by p63 and TCF7, and defined the enhancer landscape and genomic targets of these transcription factors by ChIP-seq. While the majority of myoepithelial cells co-express p63 and TCF7 in normal breast of control women, the frequency of these cells is significantly lower in *BRCA1* mutation carriers and in DCIS. Downregulation of p63 in MCF10DCIS cells leads to loss of myoepithelial cells and invasive tumors, whereas overexpression of TCF7 enhances tumor growth. Our findings suggest that loss of normal myoepithelial cell function facilitates *in situ* to invasive carcinoma transition and it may also enhance tumor initiation and progression in *BRCA* mutation carriers.

Specific Aim 2: To define the cell subpopulations of luminal/ER+ breast tumors, and their phenotypic interdependence.

The **importance or significance** of this Aim is toward defining which subpopulations of tumors must be eradicated to effect cures. Our research shows that eradication of the postulated breast cancer stem cells would *not* be sufficient to effect a cure. Our Aim is to learn how "widespread" or extensive is the tumorigenic phenotype?

Our publication, Kim et al PNAS 2012, described the tumorigenicity of two distinct, hierarchically related subpopulations (CD271+ and MM+) present in all subtypes of breast cancer. The tumorigenic potential of the MM+, i.e. differentiated luminal breast cancer cells, was particularly surprising. Additionally, the bulk of the tumor cells after removing MM+ and CD271+ cells was also tumorigenic, raising the question of how many additional tumorigenic subpopulations of breast tumors could be identified. We also hold out the possibility that a given subpopulation may not be tumorigenic on its own, but rather require the presence or interaction with another

subpopulation in order to reveal its tumorigenic potential (as has been shown for subclones of lung cancers. Such interdependence is presumably related to the observed intratumoral heterogeneity of most tumors.). Additionally, the role of the tumor microenvironment is an important driver of cellular behavior, but as a whole, the mechanisms underlying how the microenvironment influences cellular behavior is poorly understood.

Progress:

- In years 1&2 of this award we obtained very precious but small (core biopsies) amounts of ER+ luminal breast tumors and reported our FACS analyses of these tumor samples. However, given the very small cell numbers, further research with the isolated subpopulations was not possible. Therefore, we returned to use of the cell line MCF-7, as we had in Kim PNAS 2012, using the M18 antibody used to isolate the MM+ subpopulation, the anti-CD271 to isolate its cognate subpopulation, thus leaving the (-/-) cells available for further separation into sub-sub-populations to test the extensiveness of the tumorigenic phenotype.

- Dr. Seema Jamil, who obtained her PhD at Karolinska Institute, joined Dr. Bissell's group in 2016 focused on this aim. During her training in the laboratory her progress was somewhat slowed by challenges in instruments and reagents. The M18 antibody critical to the project had degraded, and the FACS facility in our building failed repeatedly. (The latter is an ongoing problem, as support for the FACS facility is very limited and our FACS experts left the division.). However, Dr. Jamil did make progress and been successfully generated a renewed supply of the M18 antibody (which is an IgM and not commercially available). Dr. Jamil also traveled to Denmark to our collaborator's laboratory to verify that her reagents are now working properly.

- Dr. Jamil's over-arching project entailed characterizing tumorigenic potential of the bulk of tumor that lacks both luminal-like phenotype and basal-like activity (-/-). Her approach was to start with separating populations positive for CD271 and M18, representing basal-like and luminal-like cells respectively i.e., the differentiated cell populations from the undifferentiated (-/-) population. She made progress with her work and plans to collate her results for publication.

- Within the last two years, together with our collaborator, Marina Simian at the University of Buenos Aires, Buenos Aires Argentina, we uncovered and interesting mechanism of microenvironment regulation of the estrogen receptor in breast tissue. Understanding what activates ERα is critical for cancer treatment in particular and cell biology in general. Using biochemical approaches and super-resolution microscopy, we found that estrogen drives membrane ERα into endosomes in breast cancer cells and that its fate is determined by the presence of fibronectin (FN) in the extracellular matrix; it is trafficked to lysosomes in the absence of FN and avoids the lysosomal compartment in its presence. In this context, FN prolongs ERα half-life and strengthens its transcriptional activity. We found also that ERα is associated with β1-integrin at the membrane, and this integrin follows the same endocytosis and subcellular trafficking pathway triggered by estrogen. Moreover, ERα+ vesicles are present within human breast tissues, and colocalization with β1-integrin is

detected primarily in tumors. Our work unravels a key, clinically relevant mechanism of microenvironmental regulation of ERα signaling. This work was published in the Journal of Cell Biology (Sampayo, et. Al., 2018, appended).

Specific Aim 3:
Test the hypothesis that the glycan recognized by the M18 antibody, MM, is required for the aggressive behavior of MM+ luminal breast cancer cells.

As discussed above, there have been problems with reagents associated with characterizing the role of a particular glycan MM in driving the aggressive, invasive behavior of breast cancer cells. In particular, the M18 antibody was in poor condition and new stocks needed to be generated. As it is an IgM antibody, generating and purifying this protein proved to be difficult. However, our research uncovered another glycan-lectin interaction that we were able to demonstrate controls invasiveness. We recently published this research in PNAS (Bhat, et al PNAS, 2016, appended). The significance lies in the fact that our findings potentiate development of a new class of therapeutics targeting the pool of extracellular Galectin-1, thus preventing nuclear translocation of Galectin-1, which in turn would suppress the invasive potential of malignant breast cells.

Due to the difficulties with reagents, we requested to revise this aim last year and with permission from our Program Manager, during last year's (2017) progress report, we revised our Aim 3.

Progress:

- Since the writing of the original aims, we found through the course of our research that other glycans are involved in breast cancer cell behavior. Together with our collaborator, Dr. Carolyn Bertozzi, (who was at Lawrence Berkeley Laboratory at the time and now at Stanford University), we investigated how glycans in the tumor extracellular microenvironment (ECM) control and communicate with the nucleus of each transformed cell to cause that cell to become invasive and hence metastatic. As we reported in 2016, and published in Bhat et al. PNAS 2016 (appended), we pursued the role of a small glycan-binding protein lectin, Galectin-1, in culture and in vivo in mouse tissues, and ex vivo human samples. We found that increased Galectin-1 nuclear levels potentiate the cell to become invasive, both during normal development and in cancer progression. Nuclear galectin-1 is regulated by the relative levels of α2,6–sialic acids and *N*-acetyllactosamine on extracellular glycans. Reductions in these carbohydrates in the ECM release Galectin-1, allowing it to translocate to the nucleus of the cell, thus releasing the invasive potential of the cell. Thus, by this mechanism the ECM controls the invasive potential of the nearby cell. By focusing our resources onto understanding the role of Galectin-1 in invasive potential, we were able to complete and publish this work rather efficiently. We describe this research in the appended publication, Bhat et al. PNAS 2016.

- Revised Aim 3: Identify miRNA gene targets for phenotypic reversion of breast tumor cells and verify a role of p53, laminins (LN) and nitric oxide (NO) in balancing the reciprocal signaling circuitry between mammary cells and their microenvironment.

  To complete this work, we proposed to accomplish the following, which were able to

complete and we published this work in Furuta, et al., elife, 2018 (appended for detailed science).

- Using our human breast tumor progression series (HMT-3522) and other established cell lines, identify potential common miRNAs (microRNAs) that target the genes from our published list of 60 genes (Fournier et al., 2006) that are modulated during phenotypic reversion of tumor cells.
- Define the role of p53 in the reciprocal signaling circuitry of mammary acinar formation using the HMT-3522 progression series and other human mammary cell lines.
- Verify a role of NO in the signaling between p53 and laminins using the HMT-3522 progression series and other human mammary cell lines (Furuta, et al., elife, 2018 and Ricca, et al., elife 2018)

Literature Cited:

Bhat R, Belardi B, Mori H, Kuo P, Tam A, Hines WC, Le QT, Bertozzi CR and **Bissell MJ** (2016). Nuclear repartitioning of galectin-1 by an extracellular glycan switch regulates mammary morphogenesis. Proc Natl Acad Sci U S A. 2016 Aug; 113(33): E4820-E4827. doi: 10.1073/pnas.1609135113 (Cover Feature)

Fournier MV, Martin KJ, Kenny PA, Xhaja K, Bosch I, Yaswen P and **Bissell MJ** (2006). Gene expression signature in organized and growth–arrested mammary acini predicts good outcome in breast cancer. *Cancer Res.* 2006 Jul 15; 66(14):7095–102.

Furuta S, Ren G, Mao J-H and **Bissell MJ** (2018). Laminin signals initiate the reciprocal loop that informs breast-specific gene expression and homeostasis by activating NO, p53 and microRNAs. eLife. 2018 Mar; 7: e26148. doi: 10.7554/eLife.26148

Hines WC, Yaswen P and **Bissell MJ** (2015). Modelling breast cancer requires identification and correction of a critical cell lineage-dependent transduction bias. *Nat Commun.* 2015 Apr; 6: 6927. doi:10.1038/ncomms7927

Hines WC, Kuhn I, Thi K, Chu B, Stanford-Moore G, Sampayo R, Garbe JC, Stampfer M, Borowsky AD and **Bissell MJ** (2016). 184AA3: a xenograft model of ER^+ breast adenocarcinoma. *Breast Cancer Res Treat.* 2016 Jan; 155(1): 37-52.

Kim J, Villadsen R, Sørlie T, Fogh L, Grønlund SZ, Fridriksdottir AJ, Kuhn I, Rank F, Wielenga VT, Solvang H, Edwards PAW, Børresen-Dale A-L, Rønnov-Jessen L, **Bissell MJ*** and Petersen OW* (2012). Tumor initiating but differentiated luminal-like breast cancer cells are highly invasive in the absence of basal-like activity. *Proc Natl Acad Sci U S A*. 2012 Apr; 109(16): 6124-6129. (*Senior authors contributed equally.)

Ricca BL, Venugopalan G, Furuta S, Tanner K, Orellana WA, Reber CD, Brownfield DG, **Bissell MJ** and Fletcher DA (2018). Transient external force induces phenotypic reversion of malignant epithelial structures via nitric oxide signaling. *eLife.* 2018 Mar; 7: e26161. doi: 10.7554/eLife.26161

Sampayo RG, Toscani AM, Rubashkin MG, Thi K, Masullo LA, Violi IL, Lakins JN, Càceres A, Hines WC, Leskow FC, Stefani FD, Chialvo DR, **Bissell MJ,** Weaver VM and Simian M (2018). Fibronectin rescues estrogen receptor alpha from lysosomal degradation in breast cancer cells. J Cell Biol. 2018 Jul; 217(7): doi:10.1083/jcb.201703037

4. **IMPACT**

Mentoring:
Of significant impact is the training of scientists with strong potential to contribute to the discovery and testing of effective therapeutics for breast cancer. For example, Dr. Curt Hines, who trained with Dr. Bissell and was central to much of the research performed under this funding is now a faculty member at the University of New Mexico; Rosalyn Sayaman, PhD completed her graduate work and is a Post-doctoral Fellow at the City of Hope in Duarte, California; Dr. Seema Jamil just completed her last two years of postdoctoral training with Dr. Bissell; there are several other postdocs and graduate students within the Bissell group that have completed their training during the course of this funding. Additionally, the Bissell group hosts several student assistants and affiliates from the University of California, Berkeley. They gravitate to the Bissell laboratory to gain practical experience in breast cancer progression in order to support their career path during their undergraduate education.

International student enthusiasm to engage in breast cancer research for the cure:
Dr. Bissell is often requested to present at meetings, both national and international (a glance at the list of keynote and plenary talks Dr. Bissell has given this year will give an idea of how frequently she presents and to what a wide audience). During the course of these travel engagements, Dr. Bissell always makes certain she has time to meet with students and postdoctoral fellows. The students are very appreciative of the time and energy she puts in to discussing their research and career opportunities with them. They often write to thank her for her enthusiasm for breast cancer research.

5. **CHANGES/ PROBLEMS:**

As noted in progress towards Aim 2 and 3 above, there were difficulties with the antibody reagent M18. This resulted in redirection of our research. As noted, during the course of the research, we discovered the role of different glycans and lectins on the aggressive and invasive behavior of breast cancer cells. Although our efforts were particularly hampered with respect to Aim 3, we found discovered other microenvironmental components (laminins and nitric oxide) which modulate breast cell behavior through a signaling mechanism involving p53, nictric oxide, laminins and specific micro-RNA's. With the assistance or our scientific program officer, we revised Aim 3 in order to complete work that was published in elife (Furuta, et al., elife 2018)

6. **PRODCUTS:**

1) **Dr. Mina Bissell has given a larger number of lecture and seminars over the course of this funding (2013-2018). The following is a list of highlighted lectures**

HONORARY/NAMED LECTURES (Since 2013, total 17):
Aharon Katzir-Katchalski Lecture (2013, Weizmann Institute of Science, Rehovot, Israel)
Charles Gowdey Distinguished Lecture (2013, The University of Western Ontario, Canada)
Distinguished Lectureship (2014, McGowan Institute for Regenerative Medicine Annual Mtg, MA)
Joseph L. Melnick Lecture (2014, Baylor College of Medicine Graduate Student Symposium, TX)

Reilly Lectures (3) (2015, University of Notre Dame, IN)
Bagrit Lecture (2015, Imperial College, UK)
Bennett Family Lecture (2016, BC Cancer Research Centre, Canada)
Bolie Lecture (2016, University of Colorado Denver, CO)
Fanger Lecture (2016, Brown University and Rhode Island Hospital, RI)
Kewaunee Lecture (2016, Duke University, NC)
E.B. Wilson Lecture (2016, ASCB Annual Mtg, CA)
Marc J. Mass Memorial Distinguished Lecture (2017, UNC Chapel Hill, NC)
Sheldon Weinbaum Distinguished Lecture (2017, Rensselaer Polytechnic Institute, NY)
Joseph A. Madri Inaugural Lecture (2017, Yale School of Medicine, CT)
Mildred-Scheel Lectureships (2) (2017, University of Essen and University of Cologne, Germany)
George Klein Lecture (2018, Karolinska Institutet, Sweden)
Chappel Memorial Lecture (2018, Ontario Veterinary College (OVC) and University of Guelph, Canada)

KEYNOTE LECTURES (Since 2013, total 49):
Max Planck Institute (MPI) for Molecular Genetics (2013, Berlin, Germany)
Cancer Research Center of Lyon (CRCL) International Symposium (2013, Lyon, France)
International AEK Cancer Congress (2013, Heidelberg, Germany)
Centre for Cancer Biomarkers (CCBIO) Annual Symposium (2013, Bergen, Norway)
International Society for Stem Cell Research (ISSCR) Annual Mtg (2013, Boston, MA)
NDPK/Nm23 Congress (2013, Boston, MA)
Carnegie Mellon University Biomechanics Day (2013, Pittsburgh, PA)
International Breast Cancer Nutrition (IBCN) Conference (2013, Saumur, France)
International Conference on Tumor Progression and Therapeutic Resistance (TPTR) (2014, Boston, MA)
Materials Research Society (MRS) Spring Mtg (2014, SF, CA)
Annual World Pharma Congress (2014, Boston, MA)
Congress of the Brazilian Society for Cell Biology (2014, Rio de Janeiro, Brazil)
International Heinrich F.C. Behr Symposium on Stem Cells and Cancer (2014, Heidelberg, Germany)
European Association for Cancer Research (EACR) Mtg on Microenvironment (2014, Berlin, Germany)
The Wistar Institute, Cancer Research and Vaccine Development (2014, Philadelphia, PA)
Rosalind Franklin Society Annual Board Mtg (2014, Washington, D.C.)
Dr. Susan Love Research Foundation's Annual Intl Symp on the Breast (2015, Santa Monica, CA)
Inaugural Fellows' Lecture, Salk Institute for Biological Studies (2015, San Diego, CA)
IPATIMUP University of Porto, "MJ Bissell Award and Symposium" (2015, Porto, Portugal)
Wound Healing Society Annual Meeting (2015, San Antonio, TX)
Cold Spring Harbor Laboratory, "The Biology of Cancer Meeting" (2015, Cold Spring Harbor, NY)
Karolinska Institute, "The Future of Tumor Biology Symposium" (2015, Stockholm, Sweden)
Gordon Research Conference (GRC) on "Science of Adhesive" (2015, Mt. Hadley, MA)
Nanjing High Tech Zone, Scientific Seminar Collaboration (2015, Nanjing, China)
The Stem Cell Niche and Cancer Microenvironment Symp, Cedars-Sinai Medical Center (2015, LA, CA)

Indian Institute of Science Education & Research Pune (2016, Pune, India)
UBC Life Sciences Institute Graduate Student Association Research Day (2016, Vancouver, Canada)
Lecture Series, Fred Hutchinson Cancer Research Center (2016, Seattle, WA)
Second Symposium of "Personalized Cancer Care" (2016, Oslo, Norway)
Cancer Discoveries: Molecules to Man, Gairdner Symposium (2016, Edmonton, Canada)
Annual Postdoctoral Science Symposium, MD Anderson Cancer Center (2016, Houston, TX)
UC San Diego Biomedical Science Retreat (2016, Palm Springs, CA)
Cancer Stem Cell Conf, National Ctr for Regenerative Med (NCRM) and Case Comp Cancer Ctr (CCCC) (2016, Cleveland, OH)
Symposium of the Collaborative Research Center 969 (2016, Konstanz, Germany)
CRBM: 50th Anniversary Symposium (2016, Montpellier, France)
EORTC NCI AACR Symposium (2016, Munich, Germany)
PhD Day 2017, Aarhus University (2017, Aarhus, Denmark)
Annual Multidisciplinary Symposium on Breast Disease, University of Florida (2017, Amelia Island, FL)
Oncology Association of Naturopathic Physicians Annual Conference (2017, Phoenix, AZ)
Dr. Susan Love Research Foundation's Annual Intl Symp on the Breast: Exploring the Human Breast: Employing New Technologies (2017, Santa Monica, CA)
International p53 Isoform Conference (2017, Bergen, Germany)
Women's Cancer, International Center for Scientific Debate, CosmoCaixa Barcelona (2017, Barcelona, Spain)
Symp on Exploring Systems Medicine: The 3 Rs of Tissue Repair: Replace, Restore and Rejuvenate, Berlin Institute of Health (2018, Berlin, Germany)
Northwestern University Feinberg School of Medicine, Research Day (2018, Chicago, IL)
Annual National Heart, Lung and Blood Institute (NHLBI), NIH, Research Day (2018, Bethesda, MD)
Symp on Biologic Scaffolds for Regenerative Med, U of Pittsburgh's McGowan Inst for Regenerative Med (2018, Napa, CA)
International Society for Extracellular Vesicles (ISEV) Annual Meeting (2018, Barcelona, Spain)
AACR Special Conference on Cancer Dormancy and Residual Disease (2018, Montreal, Canada)
Gordon Research Conf (GRC) on "Signaling Transduction from Engineered Extracellular Matrices" (2018, Andover, NH)
IPATIMUP University of Porto, "MJ Bissell Award and Symposium" (2018, Porto, Portugal)
17th Annual Pathology Research Symposium, Medical School Molecular & Cellular Pathology, University of Michigan (2018, Ann Arbor, MI)

PLENARY/DISTINGUISHED LECTURES (Since 2013, total 35):

*American Association for Cancer Research (2013, also Session Chair, X)
National Biotechnology Conference (2013, San Diego, CA)
NanoEngineering for Medicine and Biology/NEMB 2014 (2014, San Francisco, CA)
Lorne Cancer Conference (2014, Lorne, Australia)
International Women's Day Lecture, Brookhaven National Laboratory (2014, Upton, NY)
*Meeting of the Hinterzarten Circle on Cancer Research of the DFG (2014, Cadenabbia, Italy)
Cell-to-Cell Communications in Cancer Symposium-Memorial Sloan Kettering (2014, New York, NY)

Breast Cancer Research Foundation Annual Meeting (2014, New York, NY)
Stanford Cancer Institute Symposium, Heterogeneity: Implications for Targeted Therapy (2014, Stanford, CA)
Fritz Bender Foundation International Symposium (2014, Bangkok, Thailand)
Intl Symp on "Cancer Research and Clinical Care: The Next 100 Years" (2014, Rotterdam, The Netherlands)
Symp of C.R. Brubacher Found, "Breakthroughs in Cancer Research and Therapy" (2015, Zurich, Switzerland)
*Fermilab Public Lecture Series (2015, Batavia, IL)
UCLA Clinical and Translational Science Institute Series (2015, Los Angeles, CA)
University of Tokyo, Akasaka Campus (2015, Tokyo, Japan)
Nanjing Medical University (2015, Nanjing, China)
European Academy of Dermatology and Venereology Congress (2015, Copenhagen, Denmark)
Symposium on Cancer Research, "Emerging Concepts in Host Response to Cancer" (2015, Houston, TX)
Landspitali-University Hospital (2015, Reykjavík, Iceland)
Breast Oncology Scientific Retreat, UCSF (2016, San Francisco, CA)
Annual Molecular Medicine TriConference (2016, San Francisco, CA)
Envision Corporation, The National Youth Leadership Forum: UC Berkeley (2016, CA)
Joint Society for Developmental Biology Annual Mtg/Intl Society of Differentiation Conf (2016, Boston, MA)
EMBO/EMBL Symp on Organoids: Modelling organ development and disease in 3D culture (2016, Heidelberg, Germany)
Special Guest Seminar, Max Planck Institute of Immunobiology and Epigenetics (2016, Freiberg, Germany)
*AACR Annual Meeting, Lifetime Achievement Award Meet-the-Expert Speaker (2017, Washington, D.C.)
Icahn School of Medicine at Mount Sinai, Department of Oncological Sciences (2017, New York, NY)
Immuno Concept Talk: Tumor Microenvironment, University of Bordeaux (2017, Bordeaux, France)
Cancer Research Centre of Lyon (CRCL) International Symposium (2017, Lyon, France)
Revised Theory of Cancer, Konrad Lorenz Inst (KLI) (2017, also Organizer, Klosterneuburg (Vienna), Austria)
Cancer Genomics Consortium: New Horizons in Cancer Research, KIT Royal Tropical Inst (2017, Amsterdam, The Netherlands)
Models of Cancer to Advance Patient Therapy, UCSF Helen Diller Family Comp Cancer Ctr (2018, SF, CA)
Feinstein Academy of Scholars Symp, Feinstein Institute for Med Research-Northwell Health (2018, NY, NY)
BioFrontiers Scientific Symp and Workshop, BioFrontiers Inst and U Colorado-Boulder (2018, Boulder, CO)

ADDITIONAL LECTURES (Since 2013, total 17):
Arizona State University (2013)
Indiana University (2013, Indianapolis, IN)

Cleveland Clinic/Case Western Reserve University (2013, Cleveland, OH)
University of California Berkeley (2013, Berkeley, CA)
Cleary University (2013, Howell, MI)
University of Southern California (2013, LA, CA)
Arizona State University (2014)
University of New Mexico (2014, Albuquerque, NM)
University of Sao Paulo (2014, Sao Paulo, Brazil)
Children's Hospital Oakland Research Institute (2014, Oakland, CA)
Stanford University (2014, Stanford, CA)
Women's Environmental Mutagenesis & Genomics Society Meeting (2015, New Orleans, LA)
Commemorative Symposium for 31st International Prize for Biology (2015, Kyoto, Japan)
Guest Seminar, Technical University of Munich (2016, Munich, Germany)
Scientific Symposium to Celebrate Susan Lindquist (2017, Boston, MA)
Novartis Institutes for Biomedical Research Lecture Series, Novartis (2017, Cambridge, MA)
Honorary Faculty-Opponent for Ph.D. Defense, Karolinska Institutet (2017, Stockholm, Sweden)
Induction to European Molecular Biology Organization (EMBO) Members' Meeting (2018, Heidelberg, Germany)

2) <u>This funding supported or partially supported the work published in the following peer reviewed primary articles and reviews</u>

1. Hines WC, Yaswen P and **Bissell MJ** (2015). Modelling breast cancer requires identification and correction of a critical cell lineage-dependent transduction bias. Nat Commun. 2015 Apr; 6: 6927. doi:10.1038/ncomms7927
2. Lee SE, Chen Q, Bhat R, Petkiewicz S, Smith JM, Ferry VE, Correia AL, Alivisatos AP and **Bissell MJ** (2015). Reversible aptamer-Au plasmon rulers for secreted single molecules. Nano Lett. 2015 Jun; 15(7): 4564-4570. doi: 10.1021/acs.nanolett.5b01161
3. Hines WC, Kuhn I, Thi K, Chu B, Stanford-Moore G, Sampayo R, Garbe JC, Stampfer M, Borowsky AD and **Bissell MJ** (2016). 184AA3: a xenograft model of ER+ breast adenocarcinoma. Breast Cancer Res Treat. 2016 Jan; 155(1): 37-52. doi.org/10.1007/s10549-015-3649-z
4. Bhat R, Belardi B, Mori H, Kuo P, Tam A, Hines WC, Le QT, Bertozzi CR and **Bissell MJ** (2016). Nuclear repartitioning of galectin-1 by an extracellular glycan switch regulates mammary morphogenesis. Proc Natl Acad Sci U S A. 2016 Aug; 113(33): E4820-E4827. doi: 10.1073/pnas.1609135113 (Cover Feature)
5. Simian M and **Bissell MJ** (2016). Organoids: A historical perspective of thinking in three dimensions. J Cell Biol. 2016 Dec; 216(1): 31-40. doi: 10.1083/jcb.201610056
6. Jorgens DM, Inman JL, Wojcik M, Robertson C, Palsdottir H, Tsai WT, Huang H, Bruni-Cardoso A, López CS, **Bissell MJ,** Xu K and Auer M (2017). Deep nuclear invaginations linked to cytoskeletal filaments – integrated bioimaging of epithelial cells in 3D culture. J Cell Sci. 2017 Jan; 130(1): 177-189. doi: 10.1242/jcs.190967 (Cover Feature)
7. **Bissell MJ** (2017). Goodbye flat biology – time for the 3rd and the 4th dimensions. *J Cell Sci.* 2017 Jan; 130(1): 3-5.
8. Fiore APZP, Spencer VA, Mori H, Carvalho HF, **Bissell MJ** and Bruni-Cardoso A (2017). Laminin-111 and the level of nuclear actin regulate epithelial quiescence via XPO6: A

pathway defective in malignant cells. Cell Rep. 2017 Jun; 19(10): 2102-2115. doi.org/10.1016/j.celrep.2017.05.050
9. Furuta S, Ren G, Mao J-H and **Bissell MJ** (2018). Laminin signals initiate the reciprocal loop that informs breast-specific gene expression and homeostasis by activating NO, p53 and microRNAs. eLife. 2018 Mar; 7: e26148. doi: 10.7554/eLife.26148
10. Sampayo RG, Toscani AM, Rubashkin MG, Thi K, Masullo LA, Violi IL, Lakins JN, Càceres A, Hines WC, Leskow FC, Stefani FD, Chialvo DR, **Bissell MJ,** Weaver VM and Simian M (2018). Fibronectin rescues estrogen receptor alpha from lysosomal degradation in breast cancer cells. J Cell Biol. 2018 Jul; 217(7): doi:10.1083/jcb.201703037
11. Lee S-Y and **Bissell MJ** (2018). A functionally robust phenotypic screen that identifies drug resistance-associated genes using 3D cell culture. Bio-Protocol.
12. Ding L, Su Y, Qiu X, Harper N, Fassl A, Hinohara K, Huh SJ, Bloushtain-Qimron N, Jovanovic B, Ekram M, Choudhury S, Zi X, Sicinski P, Long H, Garber J, , Hines W, Merino V, Ethington G, Panos L, Grant M, Herlihy W, Au A, Rosson G, Argani P, Richardson A, Allred C, Babski K, Kim EMH, McDonnell III C, Wagner J, Rowberry R, Bobolis K, Kleer C, Hwang ES, Blum J, Fan R, Sukumar S, Park SY, **Bissell MJ** ,Jun Yao and Polyak K (2018). Myoepithelial cell perturbations in BRCA mutation carriers play essential roles in ductal carcinoma in situ (DCIS). Nat Comm. [submitted, in revision]

7. **PARTICIPANTS & OTHER COLLABORATING ORGANIZATIONS**

Name	**Project Role**	**Percent Effort over 5 years**	**Institution**
Davina Abram-Blakely	Administrative Support	8%	LBNL
Jamie Inman-Acosta	Sr. Research Assoc	37%	LBNL
Alexieva-Botcheva, Krassimira	Post-doc Fellow	4%	LBNL
Bahram Baharmi	Project Scientist	3%	LBNL
Ramray Bhat	Post-doc Fellow	9%	LBNL
Mina Bissell	Principal Investigator	19%	LBNL
Alexander Davies	Post-doc Fellow	4%	LBNL
Saori Furuta	Post-doc Fellow/Proj Scientist	17%	LBNL
Curtis Hines	Proj Scientist	23%	LBNL
Candace Hunter	Administrative Support	4%	LBNL
Irene Kuhn	Research Scientist/Lab Manager	13%	LBNL
Sara Lee	Administrative Support	22%	LBNL
Sun-Young Lee	Sr. Research Assoc/Project Scientist	24%	LBNL
Alvin Lo	Research Assoc	2%	LBNL
Jessica Marinez-Esquivel	Administrative Support	1%	LBNL
Joni Mott	Research Scientist/Lab Manager	19%	LBNL
Cynthia Richardson	Technician	3%	LBNL
Claire Robertson	Post-doc Fellow	3%	LBNL
Vishal Samboju	Student Assist	2%	LBNL

Name	Project Role	Percent Effort over 5 years	Institution
Rosalyn Sayaman	Graduate Student	23%	LBNL
Richard Schwarz	Research Scientist	5%	LBNL
Andrew Tam	Administrative Support	2%	LBNL
Chin Thi	Research Assoc	31%	LBNL
Keith Vann	Research Assoc	3%	LBNL
Elizabeth Yu	Administrative Support	3%	LBNL

8. SPECIAL REPORTING REQUIREMENTS: None known.

9 APPENDICES:

Hines WC, Yaswen P and **Bissell MJ** (2015). Modelling breast cancer requires identification and correction of a critical cell lineage-dependent transduction bias. Nat Commun. 2015 Apr; 6: 6927. doi:10.1038/ncomms7927

Hines WC, Kuhn I, Thi K, Chu B, Stanford-Moore G, Sampayo R, Garbe JC, Stampfer M, Borowsky AD and **Bissell MJ** (2016). 184AA3: a xenograft model of ER+ breast adenocarcinoma. Breast Cancer Res Treat. 2016 Jan; 155(1): 37-52. doi.org/10.1007/s10549-015-3649-z

Bhat R, Belardi B, Mori H, Kuo P, Tam A, Hines WC, Le QT, Bertozzi CR and **Bissell MJ** (2016). Nuclear repartitioning of galectin-1 by an extracellular glycan switch regulates mammary morphogenesis. Proc Natl Acad Sci U S A. 2016 Aug; 113(33): E4820-E4827. doi: 10.1073/pnas.1609135113 (Cover Feature)

Furuta S, Ren G, Mao J-H and **Bissell MJ** (2018). Laminin signals initiate the reciprocal loop that informs breast-specific gene expression and homeostasis by activating NO, p53 and microRNAs. eLife. 2018 Mar; 7: e26148. doi: 10.7554/eLife.26148

Sampayo RG, Toscani AM, Rubashkin MG, Thi K, Masullo LA, Violi IL, Lakins JN, Càceres A, Hines WC, Leskow FC, Stefani FD, Chialvo DR, **Bissell MJ,** Weaver VM and Simian M (2018). Fibronectin rescues estrogen receptor alpha from lysosomal degradation in breast cancer cells. J Cell Biol. 2018 Jul; 217(7): doi:10.1083/jcb.201703037

nature COMMUNICATIONS

ARTICLE

Received 12 Feb 2015 | Accepted 13 Mar 2015 | Published 21 Apr 2015

DOI: 10.1038/ncomms7927 OPEN

Modelling breast cancer requires identification and correction of a critical cell lineage-dependent transduction bias

William C. Hines[1], Paul Yaswen[1] & Mina J. Bissell[1]

Clinically relevant human culture models are essential for developing effective therapies and exploring the biology and etiology of human cancers. Current breast tumour models, such as those from oncogenically transformed primary breast cells, produce predominantly basal-like properties, whereas the more common phenotype expressed by the vast majority of breast tumours are luminal. Reasons for this puzzling, yet important phenomenon, are not understood. We show here that luminal epithelial cells are significantly more resistant to viral transduction than their myoepithelial counterparts. We suggest that this is a significant barrier to generating luminal cell lines and experimental tumours *in vivo* and to accurate interpretation of results. We show that the resistance is due to lower affinity of luminal cells for virus attachment, which can be overcome by pretreating cells—or virus—with neuraminidase. We present an analytical method for quantifying transductional differences between cell types and an optimized protocol for transducing unsorted primary human breast cells in context.

[1] Life Sciences Division, Lawrence Berkeley National Laboratory, Mailstop 977R225A, 1 Cyclotron Road, Berkeley, California 94720, USA. Correspondence and requests for materials should be addressed to M.J.B. (email: mjbissell@lbl.gov) or to W.C.H. (email: chines@lbl.gov).

The breast is an intricate structural composition of epithelial and endothelial cells, adipocytes, fibroblasts and other immune and bone marrow derived cells, among others. Breast cancers arise from the epithelial compartment, which consists of both luminal epithelial and myoepithelial cells (LEPs and MEPs)[1]. Interactions between these cells along with other cells and extracellular molecules in the tissue microenvironment substantially influence cell physiology and tumour development, ultimately leading to tumours with distinct pathologies (reviewed in refs 2–4). Although breast cancers are complex heterogeneous entities, they fall into several molecularly defined 'intrinsic subtypes'[5,6]. Most prevalent are the luminal tumours; they constitute 75–80% of breast cancer cases[7] and characteristically express receptors for oestrogen and progesterone hormones. Whereas most of these respond well to treatment, about 30% either are—or progress to—forms that are more aggressive[8]. Learning what distinguishes this population from the rest is critical to our understanding of how to treat breast cancer patients effectively.

The answer to this question has nevertheless been hampered by the dearth of representative models of luminal cancer, including those produced by genetically engineered mice and xenografts[9–11]. This includes also tumours formed from existing luminal cell lines, which fail to produce key histological features of luminal breast cancers[12]. Accurate models of luminal cells and cancers are thereby needed to explore the fundamental processes specific to this cell subtype to gain a more thorough understanding of breast cancer.

Current methods for generating such models are to isolate cancer cells directly from tumours/metastases or to transform normal cells by viral transduction (for review, see refs 10,13). Culturing luminal tumour cells from clinical samples has proven to be particularly challenging because of the difficulties adapting these cells to growth conditions and either selection of—or conversion to—basal phenotypes in culture[12]. The second option of transducing cells derived from normal tissues[14] is well suited for studying early events in malignant transformation. Yet when the primary epithelial cells from breast reduction tissues, which contain both LEPs and MEPs, are treated with transforming viruses to produce xenografts, the outcome overwhelmingly favours the formation of squamous or basal-like tumours[15–19]; the reasons for this discrepancy are not known.

These findings are surprising because the data in the literature appear to be based on the assumption that epithelial cells in the breast (or other organs) will have a similar potential of being transduced. We show here that this assumption is unwarranted. When primary breast cultures are inoculated with lentivirus, the resulting transductions are heavily biased in favour of MEPs. Here, we provide a mechanism as to why this is so and describe a generalizable analytical method for comparing the lentiviral transduction efficiencies of heterogeneous cell populations. Most importantly, we provide a simple method to overcome this disparity and efficiently transduce luminal epithelial cells.

Results

Transduction of primary cells exposes a bias. Primary breast cultures established from reduction mammoplasty tissues contain diverse populations of cells with distinct morphologies (Fig. 1a). Continuous passaging of these cells leads to a dramatic phenotypic drift through competitive selection of cells exhibiting or acquiring a basal phenotype[10,13,20–22]. We therefore used only primary or first-passage cells to maintain the cellular heterogeneity of the tissue, and transduced these cultures with different fluorescent protein-encoding lentiviral vectors. The finding of a sharp delineation between transduced and untransduced cells (Fig. 1b) led us to hypothesize that viral susceptibility may be lineage dependent. This was indeed the case: staining virus-treated cultures for LEP- and MEP-specific markers (keratin 19 and 14) indicated that whereas the majority of MEPs expressed green fluorescent protein (GFP), very few LEPs were transduced (Fig. 1c). These findings were independent of the promoter–reporter combinations used (Fig. 1d), and the bias was present in both primary and secondary cultures and with all lentiviral constructs tested (Fig. 1a–d and Supplementary Table 1).

To quantify the transduction efficiencies, we used multi-parameter flow cytometry and antibodies specific for markers of LEPs (Muc1, c-Kit) and MEPs (CD10, CD49f, Thy1; Fig. 1e). In each case, viral resistance tracked with markers of the luminal phenotype, confirming the immunofluorescence data. Selection of the transduced cells led to a dramatic shift in the relative proportions of LEPs and MEPs present, as demonstrated by the analysis of GFP expression in the Thy1- and Muc1-expressing cells (Fig. 1f). We observed this bias when cultures were inoculated either as unsorted-heterogeneous or fluorescence-activated cell sorting (FACS)-purified populations, on two-dimensional substratum or in suspension; it persisted in both primary and secondary cultures at all lentiviral doses, even at high multiplicities of infection of 680 transductional units per cell (Fig. 1g, Supplementary Fig. 1 and Supplementary Table 1). The bias also did not correspond to quiescence of the LEP subpopulation or to differences in growth rate as assayed by staining of Ki-67 and incorporation of EdU (5-ethynl-2′-deoxyuridine; Fig. 1d, Supplementary Fig. 2). Moreover, a broad mechanism of resistance was indicated by the fact that lentiviruses pseudotyped with a set of envelope glycoproteins from other viral species did not increase LEP transduction efficiency (Supplementary Fig. 3). These findings provided further evidence supporting our initial observations linking viral resistance to the luminal cell lineage.

The above results indicated that transductional sensitivities are intrinsic properties that may be preserved in MEP- and LEP-immortalized cell lines. We thus sought a cell model that would facilitate identifying why the luminal cells were more resistant. There are just a few well-characterized non-malignant breast cell lines, such as MCF10A[23] and HMT3522-S1 (ref. 24), but both

Figure 1 | Lentiviral transduction of primary breast cells strongly favours myoepithelial cells. (**a**) Primary cell outgrowth, derived from a reduction mammoplasty tissue (RMT) from a 24-year-old woman, cultured in MCDB170 medium, and inoculated with pLenti6/CMV-H2B-GFP lentivirus (1 μg ml^{-1} polybrene). (**b**) Overlay of H2b-GFP signal. (**c**) Overlay of keratin 19 (blue) and keratin 14 (red) immunofluorescence with TO-PRO-3 nuclear counterstain (white). (**d**, left) Primary breast cells (passage 1), derived from RMT from a 34-year-old woman, transduced with pLenti6/CMV-ZsGreen lentivirus (+6 μg ml^{-1} polybrene) and immunostained as in **c**. (**d**, right) Digital removal of red keratin 14 signal; arrowheads mark 3 of the 12 k19^{+} mitotic cells (**e**) Flow cytometric characterization of primary cells, derived from RMT from a 26-year-old woman (sample N135), cultured in M87 medium and inoculated with pLenti6/CMV-H2B-GFP lentivirus. GFP in transduced cells is compared with the cell expression of lineage markers associated with luminal (Muc1, c-Kit) and basal (CD10, CD49f, Thy1) cell types. (**f**) Quantification of flow cytometry data shown in **e**. (**g**) Transduction efficiencies of first passage of N135 cells (mixed culture) inoculated with twofold serial dilutions of 1,500 × concentrated CMV-H2B-GFP lentivirus. The fraction of GFP+ cells in the MEPs and LEPs was determined by multi-parameter flow cytometry using Muc1 and Thy1 specific antibodies. The transductional bias has been observed in every (over two dozens) primary culture tested to date. (**a**–**d**) Scale bars, 100 μm.

have a predominantly basal phenotype[25,26]. Hence, we turned to cancer-derived cell lines classified as being 'luminal' based on their gene expression patterns[25]. We randomly selected and measured the transduction efficiencies of four of these cell lines, along with six other basal cell lines classified as being either 'Basal A' or 'Basal B'[25]. A wide range of transduction efficiencies

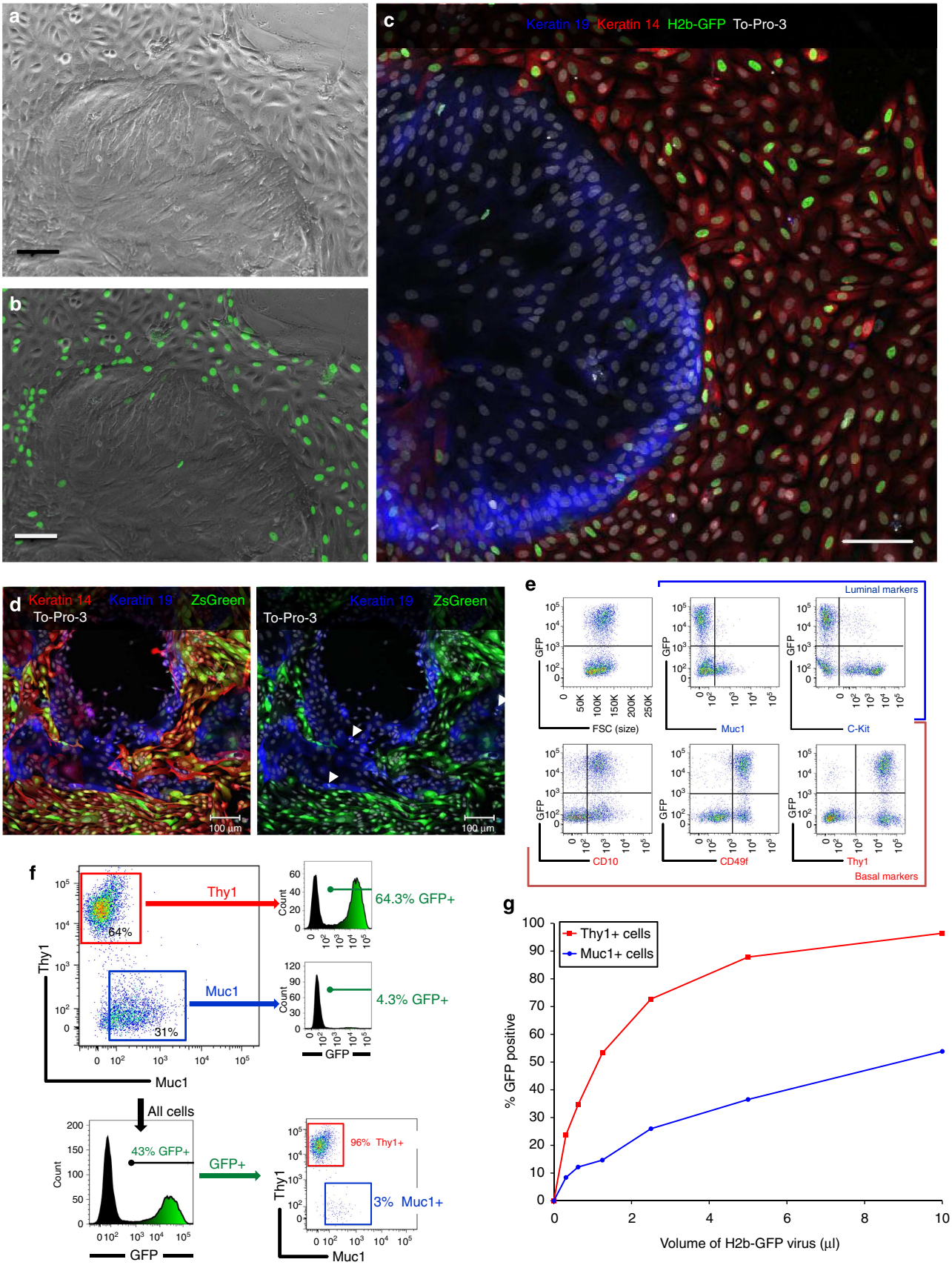

were found—from 14 to 99% cells transduced (Fig. 2a). When grouped according to class, these cell lines also formed a noticeable trend that reflected the bias observed in primary cells. Whereas the three 'Basal B' cells were all readily transduced (94, 97, 98% ZsGreen$^+$), the 'Luminal' cell lines were significantly more resistant (14, 38, 51, 64.7% ZsGreen$^+$) and the 'Basal A' cells were divergent (36, 49, 99%, Fig. 2a). To model the transductional bias observed in primary cells, we chose the most resistant luminal cell line (MCF-7) and Basal A and Basal B cell lines with high (MDA-MB-468) and intermediate (MDA-MB-231) levels of susceptibility (Fig. 2b) for further characterization.

Cell types are transduced similarly despite bias. To distinguish between stochastic and intrinsic transduction models, we inoculated MCF-7 cells with lentivirus and isolated the GFP-negative (resistant) population by FACS. We then reinoculated these cells using conditions identical to that of the previous infection, and compared the resulting transduction efficiencies of this 'resistant' population with that of the parental cell line (Fig. 2c). The pattern repeated itself, as selection of the GFP-negative population provided no heritable enrichment in resistance. The nearly identical transduction efficiencies of the two populations indicated there was no intrinsically ultra-resistant or sensitive subpopulation coexisting in MCF-7 cultures. Instead, this result supported a stochastic model wherein most or all cells in the culture are equally susceptible to viral transduction, although this level of susceptibility differs among cell lines.

On the basis of this finding, we hypothesized that the processes governing cell transduction of the different cell types were similar, despite their large quantitative differences. To examine this possibility, we devised a new approach to calculate and express viral titre that reliably reflects not only the contributions of cell type, but also specific conditions to infectivity (for example, type of medium, presence of fetal bovine serum (FBS), polybrene and so on that will be used in the experiment). We coined a new term, the effective cell-transducing volume (ECTV), which we defined as the volume of a viral stock that is equivalent to a single 100% effective transduction unit when applied to a given cell population under specific experimental conditions. An advantage of using ECTV over particle-based methods is that it will more accurately predict the volume of viral stock needed to achieve a given level of transduction by taking into account the probability of cells having multiple viral integrants. The use of ECTVs circumvents the need to convert volumes of virus to a measure of viral particles, such as colony-forming units or infectious-forming units, distinguishing it from other biological methods of titration. Most importantly, however, it provided us a single metric for comparing the influences of cell type and experimental conditions to viral infectivity between cell lines, and was especially important for comparing differences among the coexisting primary cell populations. The definition, derivation and other benefits of using ECTV are explained more fully in Supplementary Notes 1 and 2.

We used this new approach to investigate the manner by which the three representative cell lines become transduced by inoculating them with serial dilutions of virus and then calculated the ECTVs for each (Fig. 3a,b). Using these values, we compared the fraction of transduced cells with the 'effective dose' (ECTVs per cell) at each dilution, which in turn permitted a direct comparison with the theoretical values predicted by the Poisson distribution (Fig. 3c). Remarkably, we found that data from each of three cell lines fit well to the predicted values, demonstrating that the cell lines were being transduced in a similar qualitative manner (Fig. 3c), despite their quantitative differences (Fig. 3a,b).

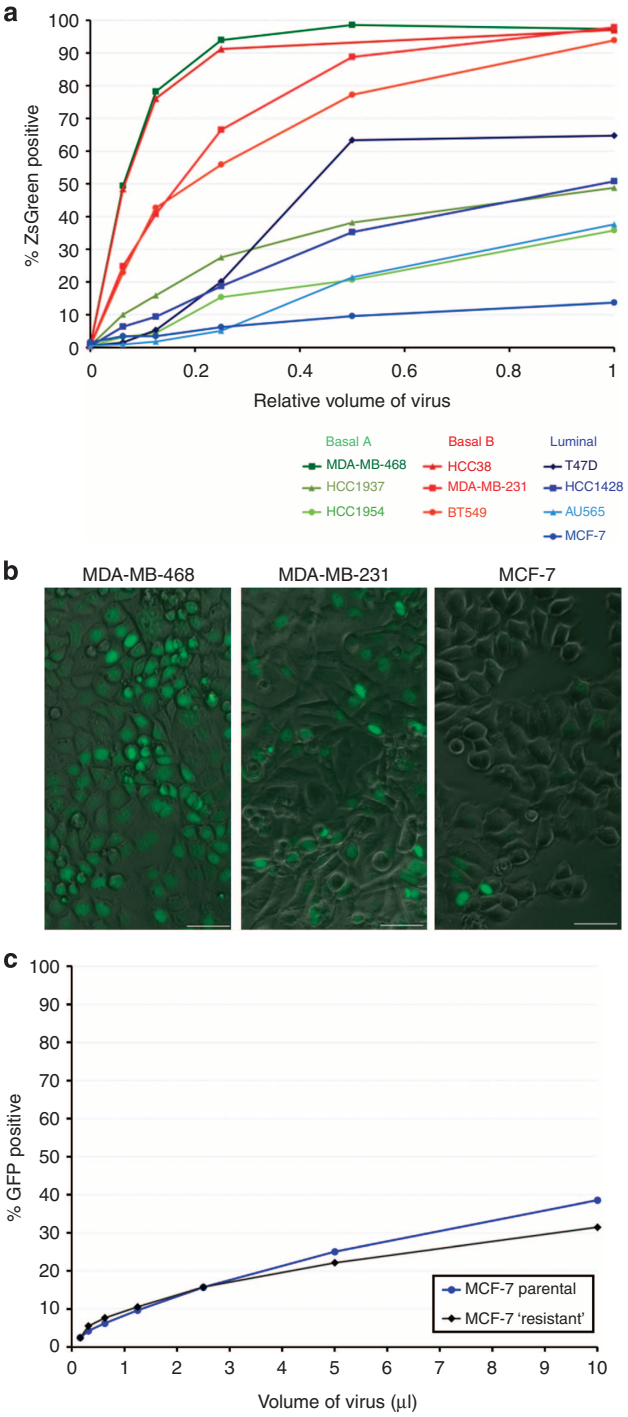

Figure 2 | Cancer-derived cell lines also exhibit a lineage-related transductional bias. (**a**) Transductional efficiencies exhibited by 10 breast cancer cell lines, grouped by their mRNA expression profiles. Cell lines were inoculated in parallel with the identical twofold serial dilution series of pLenti6/CMV-ZsGreen lentivirus (inoculated in DMEM/10% FBS, 6 µg ml^{-1} polybrene) and analysed by FACS. (**b**) Fluorescent and phase-contrast image overlays of three representative cell lines, MDA-MB-468, MDA-MB-231 and MCF-7, inoculated with pLenti6/CMV-H2B-GFP lentivirus. (**c**) Flow cytometry analysis of MCF-7 cells inoculated with a twofold dilution series of pLenti6/CMV-H2B-GFP lentivirus ('Parental,' blue trace). Virally resistant cells (GFP negative) were sorted by FACS from the culture inoculated with the highest dose of virus. These sorted 'resistant' cells (black trace) were reinoculated with virus and analysed under conditions identical to the previous infection.

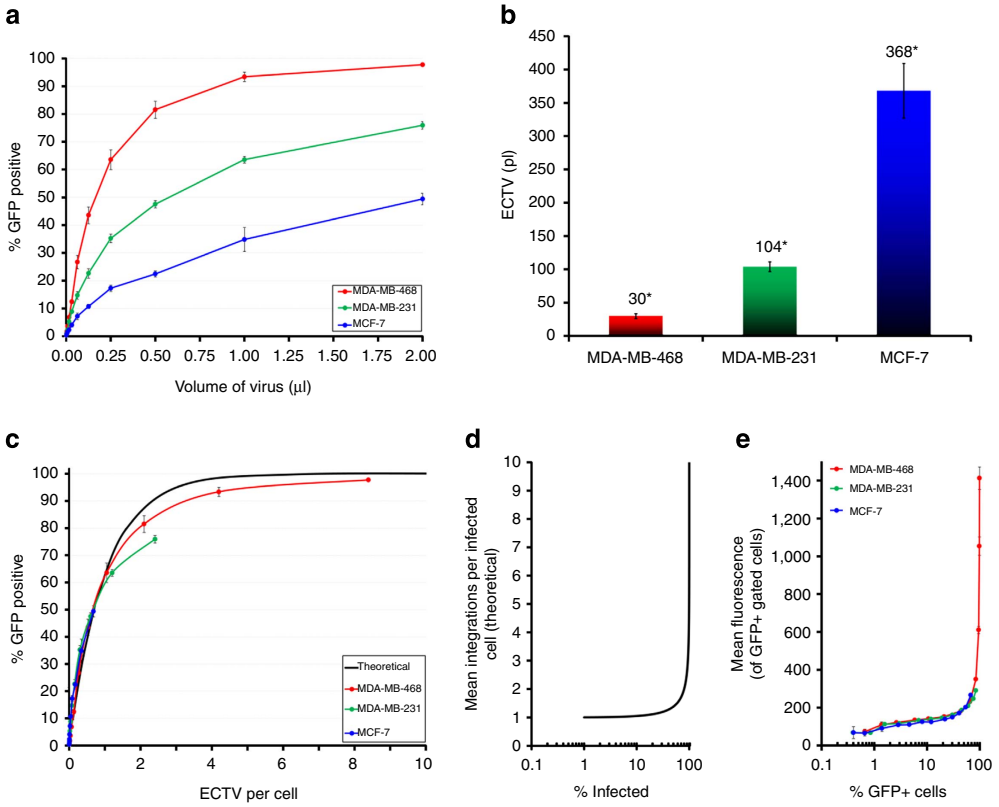

Figure 3 | ECTVs provide insight into viral transductions. (**a**) Transduction efficiencies (±s.d.) of MDA-MB-468, MDA-MB-231 and MCF-7 cell lines inoculated with twofold serial dilutions of pLenti6/CMV-H2B-GFP lentivirus in DMEM/10% FBS. (**b**) Calculated mean ECTVs (±s.d.) for cell lines and conditions shown in **a**, reported as picoliters (pl) of viral stock; *indicates P value <0.01 (t-test for all three possible comparisons). (**c**) Fraction of transduced cells plotted with respect to the effective viral dose (ECTVs per cell); black trace indicates the theoretical fraction of transduced cells predicted by the Poisson distribution. (**d**) Poisson-predicted relationship between average number of viral integrations (per cell) that will occur at a given transductional level (% infected). (**e**) GFP levels (mean ± s.d.) in transduced cells (GFP^+ gated) compared with the fraction of all cells transduced (% GFP^+) at each viral dose. Cells were inoculated with pLenti6/CMV-H2B-GFP lentivirus in DMEM/1% FBS.

These ECTVs highlight the fundamental differences in susceptibility of each cell line to lentiviral transduction; for example, under these specific conditions, MCF-7 cells must be inoculated with over 12-fold (368/30) more virus than MDA-MB-468 cells to achieve an equivalent transduction efficiency (Fig.3b). Strikingly, the MEP and LEP subpopulations in primary mixed cultures followed the same pattern of transduction, and calculation of the ECTVs (from data presented in Fig. 1g) revealed a similar bias: 257 and 33 pl for the respective LEP and MEP subpopulations (7.8-fold difference, Supplementary Fig. 4).

When applied to the problem of viral transductions, the Poisson distribution predicts that the number of viral integrations a cell will acquire will sharply rise as the fraction of cells transduced approaches 100% (Fig. 3d, Supplementary Fig. 5). Using quantitative PCR (qPCR) to measure viral integrations in transduced (GFP^+ sorted) MDA-MB-468 cells, we found this was indeed the case (Supplementary Fig. 6a–e). The association was reflected also in the per-cell GFP fluorescence measured by flow cytometry, which we found useful as a proxy for per-cell integrations (Supplementary Fig. 6d). Moreover, the pattern was the same for each of the three cell lines (Fig. 3e), supporting the notion that the processes governing cell transduction were similar among cell types, and that the subpopulations with increased viral susceptibility did not exist in these cultures. Nevertheless, the inherent differences in susceptibility among the different cell lines remained. Thus, to overcome the luminal cell resistance, we needed to identify the basis of these transductional differences.

Neuraminidase enhances lentiviral transduction. After considering each step of viral infection and transduction, we found a critical step to be the interaction between the virus particles and cells. This was determined by constructing GFP-tagged lentiviral particles (using a GFP–VSV-G fusion construct) and incubating these fluorescent viruses in suspension with the three representative cell lines. Cellular affinity for the virus was then evaluated by confocal microscopy and flow cytometry. We found stark differences in the amount of virus bound to MCF-7 cells in comparison with the two basal cell lines (Fig. 4a). Quantification by flow cytometry showed that the affinity of the cell lines (Fig. 4a) and primary cells (Fig. 4b) to lentivirus mirrored their relative transduction efficiencies, that is, 468 > 231»MCF-7 and MEP»LEP (Figs 1g and 3a).

To understand the resistance of viral binding to the different cell types, we looked for a physiological explanation: there are several components in breast milk with demonstrable protective effects against a range of bacterial and viral pathogens, including Muc1 (sialomucin) and several other mucins that are expressed exclusively by luminal epithelial cells[27]. We thus hypothesized that a probable barrier to infection was attributed to cell surface glycans that are differentially expressed between cell types. We screened several glycan-modifying enzymes: α-L-Fucosidase, β-(1→3,4,6)-Galactosidase, Neuraminidase and Hyaluronidase, for their ability to alter primary cell transduction, and found both hyaluronidase and neuraminidase improved transduction efficiencies. We therefore further optimized the conditions and

tested the effects of neuraminidase and hyaluronidase on cell lines and primary cells.

Pretreatment of the representative cell lines with neuraminidase before lentiviral infection improved transduction of each, having the most significant impact on MCF-7 cells (3.05-fold improvement versus 1.65 and 1.11 for MDA-MB-468 and MDA-MB-231, Fig. 4c,d, with no visible signs of toxicity or alterations in cell morphology). Similarly, pretreating primary cultures with

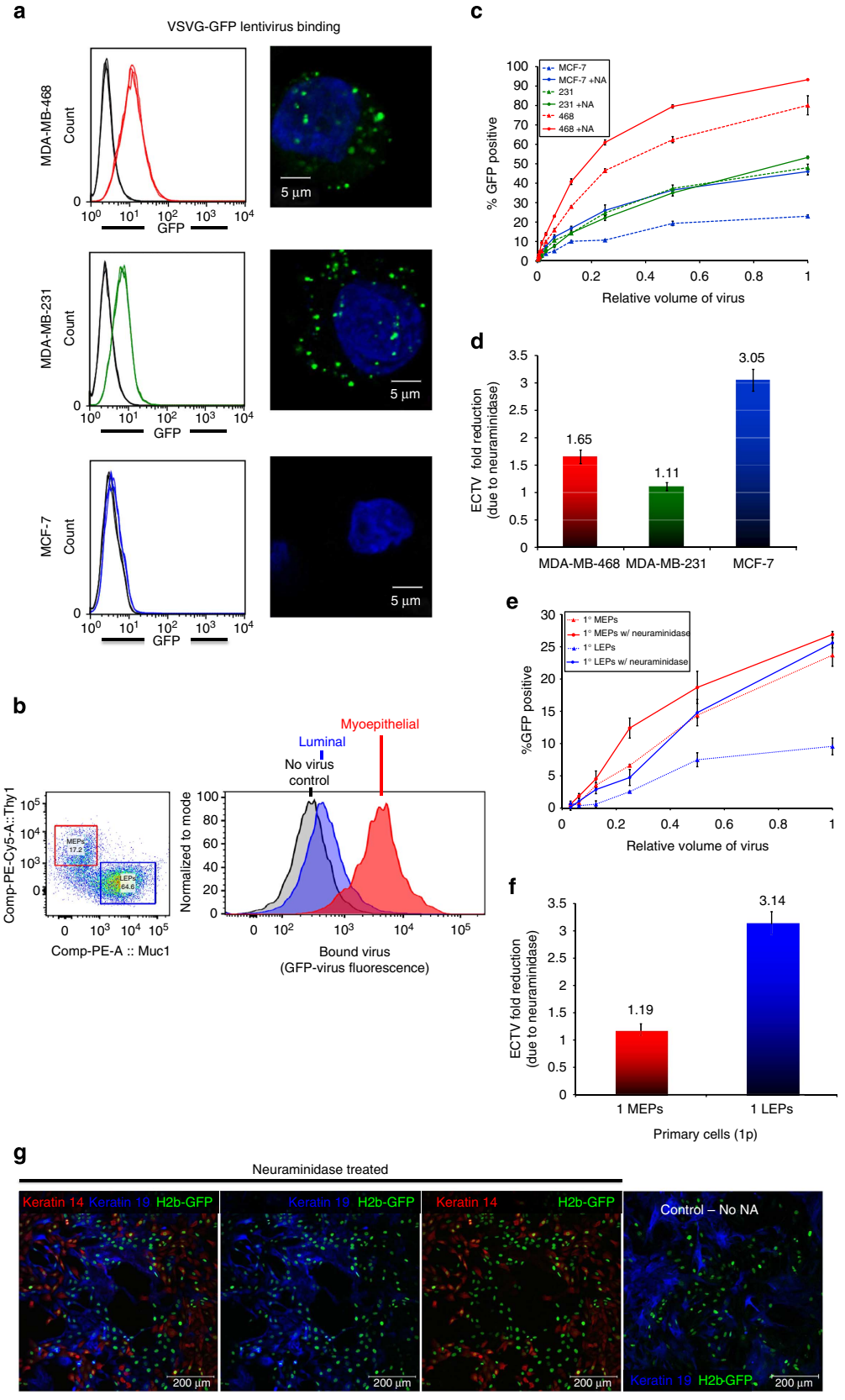

the enzyme indeed improved the transduction efficiencies of LEPs and MEPs (Fig. 4e,f), the degree of which was remarkably similar to that observed for MCF-7 and MDA-MB-231 cell lines (compare Fig. 4f–d). Thus, with neuraminidase cell pretreatment, the respective transduction of the LEPs and MEPs was 25.6% and 26.9% at the highest viral dose, effectively equalizing transductions of these two primary cell populations (Fig. 4e).

After determining that we could dramatically alter the ratio of transduced cell types by pretreating the cells with neuraminidase, we wondered if pretreating virus with the enzyme would have a similar effect, or any at all, on the amount and types of cells transduced. Remarkably, it did. Virus treated with different concentrations of neuraminidase (20, 200 and 2,000 mU ml^{-1}) incubated at two different temperatures (22° or 37 °C) improved the overall transduction of cells, as well as the ratio of LEPs to MEPs transduced, at all doses and temperatures tested (Supplementary Fig. 7). Virus incubated with 200 mU ml^{-1} neuraminidase at 37 °C, for example, improved the overall transduction efficiency from 2.57 to 18.23%, while reducing the transduced MEP:LEP ratio from 5.19 to 1.85. In viral-binding experiments, untreated virus again demonstrated a notably low affinity to LEPs, whereas virus treated with neuraminidase had a noticeably improved affinity to both primary cell types (Supplementary Fig. 8). This simple treatment of virus thus had a dramatic effect by improving the overall effective viral titre while correcting for the biased transduction between primary cell subpopulations. We found it to be easily performed after virus preparation, which circumvented the need of more lengthy cellular treatments and any unintended consequences that may have. Because of the lower volumes involved, it required also much less enzyme, reducing costs while providing similar results.

To characterize the practical application and reproducibility of our method, we tested on different primary cultures the individual and combined effects of two enzymatic pretreatments: (a) treating cells with hyaluronidase and (b) treating virus with neuraminidase. Over the course of several months, using multiple batches of virus (required for the many treatments and replicates) and independent primary cultures derived from tissues of six different subjects, we explored the individual and combined effects of these optimized treatments and found a strikingly reproducible pattern they had on narrowing (and widening) the divide between transduced MEPs and LEPs (Supplementary Fig. 9). As revealed by the transduced MEP:LEP ratios, untreated controls, consistent with our prior findings, always exhibited a bias in favour of MEPS. The degree of the bias expectedly varied among the different primary cultures, but was internally reproducible among replicate experiments, ranging from as low as 1.6-fold to as high as 4.8-fold under these conditions, and extending as high as 13.2-fold in hyaluronidase-treated cells. Although treating the cells with hyaluronidase on average led to a 63% higher fraction of cells transduced (1.63 ± 0.59-fold), the impact on the cell types was uneven, often improving transduction of the MEPs more than the LEPs, producing an even larger bias in six out of seven experiments. Neuraminidase, however, when used to pretreat the virus before infection, reduced the bias every time (seven out of seven), by an average of 42% (0.58 ± 0.15-fold difference in MEP:LEP). Whereas combining the two treatments (that is, cells with hyaluronidase and virus with neuraminidase) led to higher transduction efficiencies in five out of seven experiments, it resulted in slightly higher MEP:LEP ratios compared with infections using treated virus alone (2.51 ± 0.68 versus 1.67 ± 0.60, Supplementary Fig. 9). Therefore, we find the best method to reduce the bias between MEPs and LEPs is to use neuraminidase-treated virus.

Creation of extended lifespan luminal cells and cell lines. Knowledge of the transductional bias and the ability to efficiently transduce primary luminal cells has enabled us to create extended lifespan cultures of LEPs that have retained their luminal phenotype for over four months in culture (20 passages, Supplementary Fig. 10). To generate these cell lines, we constructed a lentivirus encoding the SV40 early region (SV40er) and, using neuraminidase treatment, transduced primary cultures with either SV40er or H2b-GFP (control) lentiviruses, then sorted the transduced cells into LEP (Muc1$^+$) and MEP (Thy1$^+$) fractions. MEP cultures transduced with either SV40er or H2b-GFP grew continuously for more than 20 passages and maintained a basal phenotype (measured by K14, Thy1 and p63 staining). Whereas LEP control cells (H2b-GFP and uninfected) became senescent after the fourth passage, LEPs transduced with SV40er did not lag in their growth, and have maintained their luminal phenotype, measured by K18 and Muc1, for more than 20 passages (Supplementary Fig. 10). These results clarify that it is transduction efficiency rather than any selective or 'differentiation-inducing property' of the SV40 early region that determines the subclasses of extended lifespan cultures obtained.

Discussion

Cell lines created through carcinogen or oncogene exposure of cultured breast cells are essentially phenotypically 'basal.' The reasons for this proclivity have been puzzling, but this predisposition nonetheless has resulted in a dearth of representative models of luminal breast cancer and uncertainty regarding the relevance of existing oncogenic models to the processes that induce clinical breast cancers. Here, we set out to determine the biology behind this consequential discrepancy, and to find measures that would rectify this imbalance.

Analysis of primary tissues transduced with lentiviruses led us to the discovery that regardless of the specific composition of the

Figure 4 | Neuraminidase enhances lentiviral transduction. (**a**, left column) Viral-binding assay: flow cytometry histograms of MDA-MB-468, MDA-MB-231 and MCF-7 cells incubated with (VSV-G-GFP) fluorescent lentiviral particles (red, green and blue traces, respectively) compared with negative controls (no virus, black traces). (**a**, right column) Confocal images of lentivirus (Green) bound to cells counterstained with DAPI (blue). (**b**) Viral binding to primary cells derived from RMT of a 32-year-old woman. (**b**, left) After incubating the cells with fluorescent lentiviral particles, the cells were stained with Muc1 and Thy1 antibodies, and analysed by flow cytometry to determine cell lineage. (**b**, right) Histograms indicating the amount of virus bound (GFP fluorescence) to luminal (LEPs, blue) and myoepithelial cells (MEPs, red). (**c**) Transduction efficiencies of the three representative cell lines, MDA-MB-468, MDA-MB-231 and MCF-7 cells (inoculated with or without 100 mU ml^{-1} neuraminidase pre-incubation) measured by flow cytometry. (**d**) ECTV reduction resulting in fold improvement of effective viral titre after neuraminidase pretreatment. (**e**) Transduction efficiencies of primary cells derived from RMT of a 31-year-old woman, inoculated with serial dilutions of pLenti6/CMV-H2B-GFP lentivirus, with—or without—neuraminidase pretreatment. Cell lineage was determined by co-staining for Thy1 (red, MEPs) and Muc1 (green, LEPs). (**f**) ECTV reduction resulting in fold improvement of effective viral titre after neuraminidase pretreatment of primary cells follow the same trend as the cell lines (**c**). (**g**) Photographs of first-passage primary cells, derived from RMT of a 20-year-old woman inoculated with pLenti6/CMV-H2B-GFP lentivirus, with—or without—neuraminidase preincubation, and stained as in Fig. 1a–d. Digital removal of keratin 14 and keratin 19 in panels 2–4 allow for better comparison to GFP signal in transduced cells.

vector or the encoded genes, there is a substantial transductional bias in heterogeneous populations of breast cells. The finding and characterization of this bias is the single-most important aspect of the work presented here; however, nearly equally important is the identification of techniques that effectively correct this bias. We describe also a method of measurement (that is, ECTV) that can be easily and productively used to more accurately predict the volume of viral stock needed to achieve a given level of transduction. This method provides a single metric for considering viral infections and comparing obstacles that influence viral infectivity of luminal and myoepithelial cells (LEPs and MEPs) of the human breast, but which can be applied also to other tissues and cancers.

Directed oncogenic transformation of primary cells requires viral vectors for delivery of the required genes[28]. An attractive feature of lentiviral vectors is their rare ability to transduce quiescent cells, thereby avoiding yet another well-characterized selection bias, something that oncoretroviruses, such as MLV, cannot do. Consequently, lentiviruses have become the vector of choice in the field, particularly when targeting stem cells or other quiescent cell types[29,30]. We discovered that breast LEPs are significantly more resistant to lentiviral (or other viral) transduction than their MEP counterparts (Fig. 1). This bias was present in normal primary cells and established cell lines, and was independent of cell passage, growth rate, media, presence of polybrene, infection in suspension or specific characteristics of the viral constructs, such as the promoter, gene product or viral pseudotype (Fig. 1; Supplementary Figs 1 and 3)

We discovered that despite the substantial resistance of LEPs to lentivirus, resistance to infection is not absolute; rather the probability of LEPs becoming transduced is much lower than MEPs. This could either be because the susceptibility is intrinsic, such that there are fewer cells in the luminal compartment that are able to be transduced. Or each of the luminal cells has the same potential of being transduced, but inherent differences between luminal and basal cells exist and produce the observed transductional bias. Our data support the latter.

We found the absolute number of LEPs capable of being transduced is not fixed; using higher doses of concentrated virus in serial dilution experiments led to higher transduction efficiencies (Fig. 1g). However, regardless of the viral dose, the bias between LEPs and MEPs always remained. We show also that uninfected, 'resistant' cells from one round of lentiviral exposure were no more resistant to subsequent exposure than the unenriched parental population from which they were derived (Fig. 2c). Most important, however, is our demonstration that the data from both luminal and basal cells—whether primary or cell lines—fit to a Poisson model of infection, demonstrating that these cells are transduced in a similar qualitative manner, despite their large quantitative differences.

The need to compare transductions of different cells simultaneously to levels predicted by the Poisson distribution led to the development of a new means to calculate viral titre, which we coined the ECTV. This is defined as the volume of virus equivalent to a single theoretical 'transduction unit' and is dependent on the specific cell type and experimental conditions used, which emphasizes the importance of each to viral transduction. ECTV calculation incorporates predictions of the Poisson distribution and thus more reliably predicts the amount of viral stock needed to achieve a given level of transduction (Supplementary Notes 1 and 2; Fig. 3). Direct quantitative comparisons of ECTV for different cell lines led us to search for the probabilistic basis of the transductional bias as we considered each step of the viral infection process.

This turning point in our study clarified a distinction between the two major cell types in the breast, and pointed to a possible mechanism by which LEPs and MEPs could differ in resistance. We traced the source of the variability to the cell surface and showed luminal cells to be relatively deficient in their ability to bind lentivirus (Fig. 4a). This led us to consider the glycans, sugar moieties that coat the cells and play key roles in the infection process of many different viral species. Ultimately, we found that neuraminidase treatment of the cells significantly improved lentiviral transduction, more so for LEPs than MEPs, thus effectively balancing transduction of these two populations. Arcasoy *et al.*[31] showed more than a decade ago that the inhibition of adenoviral infection of MDCK cells by Muc1 and other sialoglycoconjugates could be improved by pretreating the cells with neuraminidase before infection. Whether the mechanism of this effect is the same between adenovirus and lentivirus, or even MDCK canine cells and primary human breast cells, remains a mystery. However, we find that to obtain a balancing effect in primary breast cells, treatment of the cells is not necessarily required: treating virus alone significantly improves the ratio of LEPs to MEPs transduced. Notably, hyaluronidase treatment of cells also improved transductions, but often led to an even greater bias between cell types.

Some researchers use hyaluronidase along with collagenase when digesting tissues; these conditions may thus cause an even higher transductional bias than what we report using tissues digested with collagenase alone. It is our experience that even slight differences in digest protocols can have dramatic and misleading consequences[32]. Knowledge of the transductional imbalance, along with the ability to overcome it, will likely provide for a higher level of reproducibility.

There are profound implications for the ability to balance lentiviral transductions, and we highlight some in the context of developing culture models of cancer: The first is that developing luminal cell lines and models of luminal cancer have been woefully difficult and yet crucial for understanding three-fourth of all breast cancers. We believe the bias described here has been a significant barrier to developing such models. Current models of transformation rely on multiple viral transductions, such that the bias, which is already quite large for a single vector, expands by compounding the probabilities with each vector added. One example of this is the work of Kuperwasser and co-workers[18], who employed an immunomagnetic enrichment strategy before viral transduction with oncogene combinations. Consistent with our findings, these authors noted that the transformation of unsorted populations resulted in tumours with primarily basal features, whereas oncogenic transduction of luminal marker-enriched cell population resulted in tumours with partial luminal characteristics. The reason behind the observation was not explored. We have now, after controlling for this bias, succeeded in passaging SV40er transduced luminal cells for more than 20 passages where they retain their luminal characteristics, effectively creating missing models of luminal breast cancers, but most importantly clearing a path for future developments. Relative contributions of starting cell subtypes and oncogene combinations, as well as microenvironmental factors, to the range of individual features expressed by resulting tumours are important topics for future research that will be enabled by more uniform viral transduction efficiencies made possible by the techniques presented herein. We submit that these concepts and procedures open an opportunity to study not only breast tumour heterogeneity, but would be applicable also to a range of other organs and tumours.

Methods

Breast tissues and primary cultures. Breast tissues from reduction mammoplasties were obtained from the Cooperative Human Tissue Network, a programme

funded by the National Cancer Institute. All specimens were collected with patient consent and were reported negative for proliferative breast disease by board-certified pathologists. Use of these anonymous samples was granted exemption status by the University of California at Berkeley Institutional Review Board according to the Code of Federal Regulations 45 CFR 46.101. On receipt, the tissues were minced and treated with 0.1% collagenase I (Gibco/Invitrogen) for 12–18 h in Dulbecco's Modified Eagle Medium containing 100 U ml^{-1} penicillin, 100 µg ml^{-1} streptomycin and 100 µg ml^{-1} Normocin (Invivogen, San Diego, CA) with gentle agitation[32]. The resulting divested tissue fragments (organoids) were collected by centrifugation (100g × 2 min) and either archived in liquid nitrogen (90% FBS + 10% dimethylsulphoxide) or immediately placed into culture using serum-free MCDB170 (Lonza)[33] or M87 (M87 + CT + X) minimal serum (0.25% FBS) medium[34], as indicated in the figure legends.

Cell lines. MDA-MB-231, HCC38, BT549, T47D, HCC1428, AU565, MCF-7, MDA-MB-468, HCC1937 and HCC1954 breast cancer-derived cell lines were obtained directly from the American Type Culture Collection (ATCC). Media and culture conditions are provided in Supplementary Table 2; any deviations from these conditions are noted within figure legends. ATCC designation and passage number are provided in the Supplementary Methods (Supplementary Table 2).

Reagents and antibodies. Anti-CD49f, c-Kit and EpCam antibodies were obtained from BioLegend (San Diego, CA); Anti-CD10, Muc1 and Thy1 antibodies were obtained from BD Biosciences (San Jose, CA); and anti-keratin 14 and keratin 19 antibodies were purchased from Neomarkers/ThermoScientific (Fremont, CA). Detailed information on the clones and conjugates are provided in Supplementary Table 3. Muc1 antibody was custom labelled using the PacificBlue Antibody Labeling Kit (Invitrogen, Carlsbad, CA). Polybrene/hexadimethrine bromide (H9268), α-L-Fucosidase from bovine kidney (F5884), β-(1→3,4,6)-Galactosidase (G1288), Hyaluronidase (H3506) and neuraminidase (type III) from *Vibrio cholera* (N7885) were purchased from Sigma-Aldrich (St Louis, MO).

Lentiviral constructs. Lentiviruses used in this study (pLenti6, Invitrogen) are derived from a third-generation human immunodeficiency virus -1-based self-inactivating lentiviral vector[35]. Lentiviral transfer vectors were constructed using the modular MultiSite Gateway cloning technology (Invitrogen) to generate pLenti6/UbC-EGFP, pLenti6/CMV-ZsGreen, pLenti6/CMV-H2B-GFP, pLenti6/UbC-mCherry and pLenti/CMV-SV40er. Detailed cloning information is provided in the Supplementary Materials.

Lentivirus production and titration. To prepare VSV-G-pseudotyped lentivirus particles, twenty 150-mm culture dishes, containing 80–85% confluent HEK293FT cells, were calcium phosphate transfected with an equimolar mix of plasmids (57.5 µg per dish), containing the desired pLenti6 transfer vector and three lentiviral packaging plasmids: pLP1 (gag/pol), pLP2 (Rev) and pLP/VSV-G (VSV-G, Invitrogen). Supernatant was collected at 48 and 72 h post transfection and filtered through a 0.4-µm Nalgene filtration unit. Lentivirus particles in this 600 ml of filtrate were concentrated by sequential rounds of ultracentrifugation (100,000g for 90 min) through a 20% sucrose/PBS cushion. The final pellet was dissolved in 400 µl of Hank's balanced salt solution and vortexed in a foam microtube holder for 30 min at room temperature. The 1,500 × concentrated virus was cleared of sediment by centrifuging at 13,000g for 5 min. If performed, a fraction of the lentivirus preparation was treated with neuraminidase at this stage, the specific details of which are provided in the figure legends. Controls, that is, untreated virus, were incubated in parallel under identical conditions. Virus was stored at − 80 °C in either 10 or 20 µl aliquots before titration/use. Physical titre was determined by p24 enzyme-linked immunosorbent assay[36] using plates and standards from the National Cancer Institute AIDS and Cancer Virus Program (Frederick, MD). Vector yield of VSV-G-pseudotyped lentivirus ranged between 2.0×10^5 and 3.1×10^5 ng of p24 per ml of concentrated virus stock, an average of 2.72×10^{10} TU ml^{-1}. Biological activity of the virus was determined by inoculating the three cell lines (MCF-7, MDA-MB-231 and MDA-MB-468) with 2 × dilution series of lentivirus, and measuring the fraction of fluorescent cells by flow cytometry 3 days after inoculation. Calculation of ECTVs is described in the body of the manuscript and detailed in Supplementary Note 1. Alternate lentiviral pseudotypes were prepared by substituting the VSV-G-encoding plasmid with those encoding glycoproteins derived from either Rabies (Addgene 15785), Mokola (Addgene 15811), LCMV (Addgene plasmids 15793 and 15796), MMLV (Addgene 15799)[37]; Ebola (pEZGP and EboZ delta O), a gift of Dr David Sanders[38]; or Baculovirus (gp64/PCDNA3.1), generously provided by Dr Joshua Zimmerberg[39]. GFP-labelled virions used in the binding assay (Ubc-mCherry (GFP–VSV-G)) were similarly produced by replacing the VSV-G-encoding plasmid for GFP–VSV-G (Addgene 11912)[40].

Cell inoculation/infection. Primary cells (typically grown for 5–7 days) in 24-well dishes, were inoculated overnight in 250 µl medium containing desired amount of virus, typically 1–10 µl of a 1,500 × concentrated stock. Cells pretreated with neuraminidase received a 4-h incubation at 4 °C with 200 mU ml^{-1} neuraminidase diluted in growth medium (M87) and were thoroughly rinsed before adding virus-containing medium. All infections were performed at 37 °C overnight (at least 15 h). The following morning, the virus-containing medium was removed and refreshed with 500 µl growth medium and the cells were cultured for an additional three days to allow for GFP expression before analysis by microscopy or flow cytometry. Serial dilution experiments were similarly performed using either a 24-well or a 96-well format. For 24-well dishes, 50,000 cells were seeded into each well, allowed to attach overnight and incubated in 250 µl medium containing 2 × dilutions of lentivirus. For 96-well format, 8,000 cells were seeded and infected in 50 µl volume. Specific details to each experiment are contained in the figure legends. Polybrene did not improve the transductional bias and we do not recommended using it with primary cells because it alone induced dramatic morphological changes in the cells at concentrations as low as 5 µg ml^{-1} (Supplementary Fig. 11).

Immunofluorescence. Immunofluorescence was performed on monolayer cell cultures fixed with 4% paraformaldehyde for 5 min at 23 °C, and then treated with 4% formaldehyde/0.1% saponin (BD Cytofix/Cytoperm kit) for 15 min at 4 °C. The cells were subsequently incubated for 20 min. in wash buffer (0.1% saponin/1% FBS in PBS), and incubated with keratin 14 (rabbit polyclonal, Thermo/labvision) and keratin 19 (mouse clone A53-B/A2.26, Neomarkers) antibodies diluted 1:200 (1 µg ml^{-1}) in wash buffer for 1 h at 37 °C. Following the primary antibody incubation, the cells were washed and incubated with anti-mouse and anti-rabbit secondary antibodies, respectively, conjugated with Alexafluor 405 and Alexfluor 594 (Invitrogen), diluted 1:400. Nuclei were stained by incubating cells in 1 µM To-Pro-3 iodide (Invitrogen). Four-colour images were captured using a Zeiss LSM710 confocal microscope and processed using Zen Software (Zeiss, version 2009).

Virus-binding assay. Lentivirus binding analysis was performed as previously described[41]. In brief, MDA-MB-468, MDA-MB-231 and MCF-7 cells were dissociated with trypsin, rinsed in PBS/2% FBS and filtered through a 40-µm cell strainer. Primary cells were dissociated similarly, but were first treated with non-enzymatic dissociation solution (Sigma# C1419) to reduce the amount of trypsin required, which was inactivated by 0.1% w/v soybean trypsin inhibitor (Sigma# T9128). To 1×10^5 cells, 10 µl of a 1,500 × concentrated lentivirus UbC-mCherry(GFP–VSV-G) or 10 µl PBS (negative control) was added, and the cells were incubated at 4 °C in the dark, with gentle rocking for 2 h. Afterwards, the cells were washed once with PBS and analysed by flow cytometry (BD FACS Calibur). Remaining cells were fixed in 2% paraformaldehyde, counterstained with DAPI (4′,6-diamidino-2-phenylindole), mounted to slides with Fluormount-G (Southern Biotech; Birmingham, AL) and imaged using a Zeiss LSM710 confocal microscope.

qPCR viral integration assay. To measure lentiviral integrations in the host cell genome, we transduced MDA-MB-468 cells (grown in DMEM/10% FBS) with twelve 2 × serial dilutions of CMV-H2b-GFP virus, diluted in M87 medium. After overnight incublation, the medium was refreshed with regular growth medium, DMEM/10% FBS. At 3 days post innoculation, the cells were photographed, dissociated and the GFP$^+$ fractions were measured and FACS sorted into either 6, 24, 48 or 96-well dishes (dependent on transduction efficiency per cell yield). After expansion in culture for 1 week, DNA was isolated (DNEasy columns, Qiagen) from cultures derived from dilutions 1–9 (which had accumulated enough cells at that time). Viral integrations in genomic DNA were measured by qPCR using primers specific to the lentiviral GAG sequence (For: 5′-AGG GAG CTA GAA CGA TTC GCA GTT-3′, Rev: 5′-TCT GAT CCT GTC TGA AGG GAT GGT-3′), Lentiviral gene dose was normalized to the single copy gene, albumin[42], (FOR: 5′-TGT AGA GAA GTG CTG CAA GGC TGA-3′, REV:5′-TGT CCC ACA TGT ACA AAG CCT CCT-3′). PCR reactions (45 cycles: 95 °C × 15 s, 60 °C × 60 s) were performed in quadruplicate and quantified using the ddCT method; error was propagated using the square root of the sum of squares method and values are expressed as a percentage of albumin.

Flow cytometry and FACS. Lentiviral transductions of primary cells were analysed by multi-parameter flow cytometry at 72–96 h post inoculation by first dissociating the cells to single-cell suspensions with trypsin, and filtering them through 40-µm nylon mesh cell strainers (BD Biosciences). Cells were rinsed twice with PBS/2% FBS and incubated with conjugated antibodies for 30 min at 4 °C. Flow cytometry data (typically 20,000 gated events per sample) were collected. Cells were sorted using a BD FACS Vantage cytometer (FACSDIVA software, version 5.0.3). Doublets were excluded by forward scatter (height) vs. side scatter (width) gating. Compensation was determined using compensation beads custom-labelled with each fluorophor (APC anti-mouse bead kit (Molecular Probes/Invitrogen). Negative controls consisted of unlabelled beads and cells incubated with isotype control antibodies conjugated to PE, APC, PE/Cy5, FITC (BD Biosciences); PE/Cy7, APC/Cy7 (Biolegend); and Pacific Blue (Invitrogen). Serial dilution experiments were collected on a BD FACS Calibur with robotic high throughput sampler (HTS) attachment (5,000 events per sample) in a 96-well format. All FACS data were analysed using Flowjo software (version 7.6.3, Tree Star Inc.).

Statistical analysis. Statistical analysis was performed using JMP 7 statistical software (SAS Institute). Error for the quotient 'fold difference in ECTV,' was calculated using standard deviations (s.d.) of triplicate parallel infections to determine per cent relative error and propagated using the square root of the sum of squares method. In all other cases, error bars indicate the s.d. of multiple biological replicates.

References

1. Hoda, S. A., Brogi, E., Koerner, F. & Rosen, P. P. *Rosen's Breast Pathology* (Lippincott Williams & Wilkins, 2014).
2. Tarin, D. Clinical and biological implications of the tumor microenvironment. *Cancer Microenviron.* **5,** 95–112 (2012).
3. Bissell, M. J. & Radisky, D. Putting tumours in context. *Nat. Rev. Cancer* **1,** 46–54 (2001).
4. Bissell, M. J. & Hines, W. C. Why don't we get more cancer? A proposed role of the microenvironment in restraining cancer progression. *Nat. Med.* **17,** 320–329 (2011).
5. Perou, C. M. *et al.* Molecular portraits of human breast tumours. *Nature* **406,** 747–752 (2000).
6. Cancer Genome Atlas Network. Comprehensive molecular portraits of human breast tumours. *Nature* **490,** 61–70 (2012).
7. O'Brien, K. M. *et al.* Intrinsic breast tumor subtypes, race, and long-term survival in the Carolina Breast Cancer Study. *Clin. Cancer Res.* **16,** 6100–6110 (2010).
8. Massarweh, S. & Schiff, R. Unraveling the mechanisms of endocrine resistance in breast cancer: new therapeutic opportunities. *Clin. Cancer Res.* **13,** 1950–1954 (2007).
9. Vargo-Gogola, T. & Rosen, J. M. Modelling breast cancer: one size does not fit all. *Nat. Rev. Cancer* **7,** 659–672 (2007).
10. Petersen, O. W. & Polyak, K. Stem cells in the human breast. *Cold Spring Harb. Perspect. Biol.* **2,** a003160 (2010).
11. Borowsky, A. D. Choosing a mouse model: experimental biology in context--the utility and limitations of mouse models of breast cancer. *Cold Spring Harb. Perspect. Biol.* **3,** a009670 (2011).
12. Holliday, D. L. & Speirs, V. Choosing the right cell line for breast cancer research. *Breast Cancer Res.* **13,** 215 (2011).
13. Dimri, G., Band, H. & Band, V. Mammary epithelial cell transformation: insights from cell culture and mouse models. *Breast Cancer Res.* **7,** 171–179 (2005).
14. Bartek, J. *et al.* Efficient immortalization of luminal epithelial cells from human mammary gland by introduction of simian virus 40 large tumor antigen with a recombinant retrovirus. *Proc. Natl Acad. Sci. USA* **88,** 3520–3524 (1991).
15. Elenbaas, B. *et al.* Human breast cancer cells generated by oncogenic transformation of primary mammary epithelial cells. *Genes Dev.* **15,** 50–65 (2001).
16. Ince, T. A. *et al.* Transformation of different human breast epithelial cell types leads to distinct tumor phenotypes. *Cancer Cell* **12,** 160–170 (2007).
17. Wu, M. *et al.* Dissecting genetic requirements of human breast tumorigenesis in a tissue transgenic model of human breast cancer in mice. *Proc. Natl Acad. Sci. USA* **106,** 7022–7027 (2009).
18. Keller, P. J. *et al.* Defining the cellular precursors to human breast cancer. *Proc. Natl Acad. Sci. USA* **109,** 2772–2777 (2012).
19. Zhao, J. J. *et al.* Human mammary epithelial cell transformation through the activation of phosphatidylinositol 3-kinase. *Cancer Cell* **3,** 483–495 (2003).
20. Taylor-Papadimitriou, J. *et al.* Keratin expression in human mammary epithelial cells cultured from normal and malignant tissue: relation to in vivo phenotypes and influence of medium. *J. Cell Sci.* **94,** 403–413 (1989).
21. Ethier, S. P., Mahacek, M. L., Gullick, W. J., Frank, T. S. & Weber, B. L. Differential isolation of normal luminal mammary epithelial cells and breast cancer cells from primary and metastatic sites using selective media. *Cancer Res.* **53,** 627–635 (1993).
22. Pechoux, C., Gudjonsson, T., Ronnov-Jessen, L., Bissell, M. J. & Petersen, O. W. Human mammary luminal epithelial cells contain progenitors to myoepithelial cells. *Dev. Biol.* **206,** 88–99 (1999).
23. Soule, H. D. *et al.* Isolation and characterization of a spontaneously immortalized human breast epithelial cell line, MCF-10. *Cancer Res.* **50,** 6075–6086 (1990).
24. Briand, P., Petersen, O. W. & Van Deurs, B. A new diploid nontumorigenic human breast epithelial cell line isolated and propagated in chemically defined medium. *In Vitro Cell. Dev. Biol.* **23,** 181–188 (1987).
25. Neve, R. M. *et al.* A collection of breast cancer cell lines for the study of functionally distinct cancer subtypes. *Cancer Cell* **10,** 515–527 (2006).
26. Kenny, P. A. *et al.* The morphologies of breast cancer cell lines in three-dimensional assays correlate with their profiles of gene expression. *Mol. Oncol.* **1,** 84–96 (2007).
27. Schroten, H. *et al.* Inhibition of adhesion of S-fimbriated Escherichia coli to buccal epithelial cells by human milk fat globule membrane components: a novel aspect of the protective function of mucins in the nonimmunoglobulin fraction. *Infect. Immun.* **60,** 2893–2899 (1992).
28. Hahn, W. C. *et al.* Creation of human tumour cells with defined genetic elements. *Nature* **400,** 464–468 (1999).
29. Akkina, R. K. *et al.* High-efficiency gene transfer into CD34+ cells with a human immunodeficiency virus type 1-based retroviral vector pseudotyped with vesicular stomatitis virus envelope glycoprotein G. *J. Virol.* **70,** 2581–2585 (1996).
30. Welm, B. E., Dijkgraaf, G. J., Bledau, A. S., Welm, A. L. & Werb, Z. Lentiviral transduction of mammary stem cells for analysis of gene function during development and cancer. *Cell Stem Cell* **2,** 90–102 (2008).
31. Arcasoy, S. M. *et al.* MUC1 and other sialoglycoconjugates inhibit adenovirus-mediated gene transfer to epithelial cells. *Am. J. Respir. Cell Mol. Biol.* **17,** 422–435 (1997).
32. Hines, W. C., Su, Y., Kuhn, I., Polyak, K. & Bissell, M. J. Sorting out the FACS: a devil in the details. *Cell Rep.* **6,** 779–781 (2014).
33. Hammond, S. L., Ham, R. G. & Stampfer, M. R. Serum-free growth of human mammary epithelial cells: rapid clonal growth in defined medium and extended serial passage with pituitary extract. *Proc. Natl Acad. Sci. USA* **81,** 5435–5439 (1984).
34. Garbe, J. C. *et al.* Molecular distinctions between stasis and telomere attrition senescence barriers shown by long-term culture of normal human mammary epithelial cells. *Cancer Res.* **69,** 7557–7568 (2009).
35. Zufferey, R. *et al.* Self-inactivating lentivirus vector for safe and efficient *in vivo* gene delivery. *J. Virol.* **72,** 9873–9880 (1998).
36. Barde, I., Salmon, P. & Trono, D. Production and titration of lentiviral vectors. *Curr. Protoc. Neurosci.* **Chapter 4,** Unit 4 21 (2010).
37. Sena-Esteves, M., Tebbets, J. C., Steffens, S., Crombleholme, T. & Flake, A. W. Optimized large-scale production of high titer lentivirus vector pseudotypes. *J. Virol. Methods* **122,** 131–139 (2004).
38. Jeffers, S. A., Sanders, D. A. & Sanchez, A. Covalent modifications of the ebola virus glycoprotein. *J. Virol.* **76,** 12463–12472 (2002).
39. Kumar, M., Bradow, B. P. & Zimmerberg, J. Large-scale production of pseudotyped lentiviral vectors using baculovirus GP64. *Hum. Gene. Ther.* **14,** 67–77 (2003).
40. Presley, J. F. *et al.* ER-to-Golgi transport visualized in living cells. *Nature* **389,** 81–85 (1997).
41. Coil, D. A. & Miller, A. D. Phosphatidylserine is not the cell surface receptor for vesicular stomatitis virus. *J. Virol.* **78,** 10920–10926 (2004).
42. Bieche, I., Franc, B., Vidaud, D., Vidaud, M. & Lidereau, R. Analyses of MYC, ERBB2, and CCND1 genes in benign and malignant thyroid follicular cell tumors by real-time polymerase chain reaction. *Thyroid* **11 147–152 (2001).**

Acknowledgements

We thank Irene Kuhn, Alex Bazarov and Ritu Mukhopadhyay (Lawrence Berkeley National Laboratory), Sandy Borowsky (U.C. Davis) and Curtis Hines (Sandia National Laboratory, retired) for thoughtful scientific discussions and critical review of the manuscript. We thank Kate Thi, Gaelen Stanford-Moore, Maria Rojec, Melody Ju and Xuefei Tian for their technical assistance and Jim Garbe for providing M87 cell medium. We express special gratitude to Michelle Scott of the LBNL flow cytometry and microscopy facility for her expert technical advice and assistance. Grant support: Komen Foundation PDF0707408 (W.C.H.), U01 ES019458/ES/NIEHS NIH HHS/United States (P.Y.), an Innovator award to M.J.B. from the U.S. Department of Defense (W81XWH0810736 and W81XWH12M9532) and in part by National Cancer Institute awards (R37CA064786, R01CA140663, U54CA112970, U01CA143233 and U54CA143836—Bay Area Physical Sciences–Oncology Center, University of California, Berkeley, California) and by grants from the U.S. Department of Energy, Office of Biological and Environmental Research and Low Dose Scientific Focus Area (contract no. DE-AC02-05CH1123) and the Breast Cancer Research Foundation. The funders had no role in the study design, data collection and analysis, decision to publish or preparation of the manuscript.

Author contributions

W.C.H. and M.J.B. were responsible for the study conception and design, methodology development and analysis and interpretation of data; W.C.H., P.Y. and M.J.B. were responsible for the acquisition of data (provided reagents, acquired patient samples, provided facilities); W.C.H., P.Y. and M.J.B. were responsible for writing, review and revision of the manuscript.

Additional information

Supplementary Information accompanies this paper at http://www.nature.com/naturecommunications

Competing financial interests: The authors declare no competing financial interests.

Reprints and permission information is available online at http://npg.nature.com/reprintsandpermissions/

How to cite this article: Hines, W. C. *et al.* Modelling breast cancer requires identification and correction of a critical cell lineage-dependent transduction bias. *Nat. Commun.* 6:6927 doi: 10.1038/ncomms7927 (2015).

HHS Public Access

Author manuscript

Breast Cancer Res Treat. Author manuscript; available in PMC 2017 January 01.

Published in final edited form as:

Breast Cancer Res Treat. 2016 January ; 155(1): 37–52. doi:10.1007/s10549-015-3649-z.

184AA3: A Xenograft Model of ER+ Breast Adenocarcinoma

William C. Hines[*,†,‡], **Irene Kuhn**[*,‡], **Kate Thi**[*], **Berbie Chu**[*], **Gaelen Stanford-Moore**[*], **Rocío Sampayo**[§], **James C. Garbe**[*], **Martha Stampfer**[*], **Alexander D. Borowsky**[‖], and **Mina Bissell**[*,†]

[*]Life Sciences Division, Lawrence Berkeley National Laboratory; Mailstop 977R225A, 1 Cyclotron Road; Berkeley, CA 94720, USA

[§]Área Investigación, Instituto de Oncología Angel H. Roffo-UBA, Buenos Aires, Argentina

[‖]Department of Pathology and Laboratory Medicine and Center for Comparative Medicine, University of California, Davis

Abstract

Purpose—Despite the prevalence and significant morbidity resulting from estrogen receptor positive (ER^+) breast adenocarcinomas, there are only a few models of this cancer subtype available for drug development, and arguably none for studying etiology. Those models that do exist have questionable clinical relevance.

Methods—Given our goal of developing luminal models, we focused on six cell lines derived by minimal mutagenesis from normal human breast cells, and asked if any could generate clinically relevant xenografts, which we then extensively characterized.

Results—Xenografts of one cell line, 184AA3, consistently formed ER+ adenocarcinomas that had a high proliferative rate and other features consistent with “luminal B” intrinsic subtype. Squamous and spindle cell/mesenchymal differentiation was absent, in stark contrast to other cell lines that we examined or others have reported. We explored intratumoral heterogeneity produced by 184AA3 by immunophenotyping xenograft tumors and cultured cells, and characterized marker expression by immunofluorescence and flow cytometry. A $CD44^{High}$ subpopulation was discovered, yet their tumor forming ability was far less than $CD44^{Low}$ cells. Single cell cloning revealed the phenotypic plasticity of 184AA3, consistent with the intratumoral heterogeneity observed in xenografts. Characterization of ER expression in cultures revealed ER protein and signaling is intact, yet when estrogen was depleted in culture, and *in vivo*, it did not impact cell or tumor growth, analogous to therapeutically resistant ER+ cancers.

Conclusions—This model is appropriate for studies of the etiology of ovarian hormone independent adenocarcinomas, for identification of therapeutic targets, predictive testing and drug development.

[†]To whom correspondence should be addressed: MJBissell@LBL.GOV or CHines@LBL.GOV.
[‡]These authors contributed equally to this work

Conflicts of interest: The authors declare that they have no conflict of interest.

Animal Welfare: All procedures performed in studies involving animals were in accordance with the ethical standards of the Lawrence Berkeley National Laboratory, at which all such studies were conducted.

Keywords

Luminal breast cancer models; xenograft; intratumoral heterogeneity; microenvironment

Introduction

A pressing goal for cancer researchers is recognizing different clinical forms and subtypes of tumors, and understanding how and why each type manifests. Defining the cellular origins and steps to malignant progression are critical to improved and personalized cancer-prevention and treatment strategies. Model systems with known origins, that faithfully recapitulate specific clinical cancer phenotypes and behaviors allow us to explore intricate tumor biology and dynamic relationships between tumor cells and their microenvironments; and most importantly, to investigate how these interactions influence clinical pathology and therapeutic response. No model is perfect, but some are more useful than others[1].

Our ability to explore biology of 'luminal-type' breast adenocarcinoma is limited unfortunately, due to the relatively few models available [2,3]. A notable deficiency, given the luminal subtype is by far the most prevalent form of breast cancer in the clinic. Over 70% of newly diagnosed breast malignancies are assigned to this class each year by positive staining for estrogen and progesterone receptors (ER/PR) or gene expression profiling[4,5]. Most women with these ER^+ tumors respond well to hormone-targeted therapies, such as selective estrogen-receptor response modulators, aromatase inhibitors, luteinizing hormone-releasing hormone agents, ER down regulators, or prophylactic ovary removal. Nevertheless, roughly 30% of patients have luminal tumors that don't respond to treatment that leads to poorer outcomes[6]. Despite a better prognosis, the higher prevalence means that more women die each year from ER positive luminal breast cancers than all other subtypes combined[7]. This underscores how much we have to learn, and the lack of appropriate models is a fundamental obstacle.

Current models, such as established cell lines, are convenient tools for research and have taught us a great deal, but they do have drawbacks[8] –and none have generated the luminal adenocarcinomas of interest *in vivo* when xenografted into immunodeficient mice[9]. Grafting primary tumors directly into mice has been more successful in this regard, particularly in reproducing some features of the parent tumor. For reasons unknown however, the graft success-rate of ER^+ luminal subtype tumors continues to be far lower than that for the basal subtypes[9]. As a result, there is even a paucity of patient-derived xenograft (PDX) models of luminal breast cancer[10,11].

To fill this model gap, we looked to several cell models of breast cancer progression. Isogenic progression-series of cell lines are potent tools—especially for etiological studies—as they include both the non-malignant precursor cell line and fully malignant derivatives to which comparisons can be drawn, with intermediate and parallel lines sometimes also available for study. These collections of cell lines allow exploration of early transformative events, adding insight into tumorigenic initiation, something PDX and other end-stage models, by their nature, cannot provide. For example, two human breast cancer progression series, HMT-3522-LBNL[12,13] and MCF10A[14], have been central to discovering the

dominant role of microenvironmental factors in regulating cell phenotype and have revealed novel targets for breast cancer therapeutics[14,15]. Yet, neither is an ideal model of luminal breast cancer, as malignant lines from these series produce xenografts with squamous/basal-like histology, and not the ER^+ adenocarcinomas seen most often in the clinic[13,16]. To solve this dilemma, we turned to another isogenic progression series, the 184 collection, to determine if any derivative lines in this series could form tumors with a luminal phenotype.

The 184 progression series[17,18] began with a culture of normal finite-lifespan cells and, following exposure to oncogenic agents, includes cell lines with either finite, extended, or immortal lifespans. Some immortal cell lines in the series display a transformed phenotype in culture, and recent genome sequencing in BaP-treated lines has revealed mutation patterns similar to clinical specimens[19]. Yet, we were uncertain of the tumor phenotypes that would emerge from most of the 184 derivatives, or whether they would form tumors at all.

To determine tumorigenicity of 184-derived cells, we orthotopically xenografted each cell line possessing anchorage independent growth into NOD *scid* gamma mice (NSG; NOD.Cg-$Prkdc^{scid}$ $Il2rg^{tm1Wjl}$/SzJ) and monitored for tumor growth. Whereas most xenografts resulted in either squamous carcinomas or no tumors at all, one—184AA3—produced adenocarcinomas closely resembling clinical breast tumors. 184AA3 xenografts were invasive and expressed several key luminal markers—including estrogen receptor—yet were insensitive to hormone ablation via ovary removal. Here, we present and describe this novel model of ER^+ luminal breast cancer.

Results

184AA3 xenografts produce ER^+ adenocarcinomas

The primary founding culture of the 184 cell progression series was established from a reduction mammoplasty in 1980[17]. Many different sub-lines have since been produced, and several have acquired phenotypes associated with malignancy, such as anchorage-independent growth (AIG) when embedded in methylcellulose[18]. To determine *in vivo* tumorigenicity of these AIG^+ lines; i.e., 184ZNMY3-N, 184B5ME, 184FMY2, 184AaGS1, 184AA2, and 184AA3; we xenografted each bilaterally into cleared #4 inguinal mammary fat pads of NSG immunodeficient mice. Injections included also primary-derived fibroblasts, 50% of which were treated with 0.3Gy X-ray radiation. Over the course of 15 months, four of six cell lines were found to produce tumors, these were: 184AaGS1(1/6 mice), 184ZNMY3-N (7/7 mice), 184AA2 (5/7 mice), and 184AA3 (5/5 mice). 184AaGS1, 184ZNMY3-N and 184AA2 produced similar histologies –all predominantly squamous, occasionally containing areas with calcifications and metaplasia (Fig. 1a). 184AA3-derived tumors however, were remarkable in that they formed adenocarcinomas phenotypically identical to human invasive ductal carcinomas. These would be scored as high combined histologic grade cancers with minimal tubule formation, large nuclei, and high proliferative rate (Fig. 1b). Xenografts exhibited large areas of variable ERα positivity—ranging from barely detectable to very intense—and a generally weak level of PR expression (Fig. S1a). Immunostaining highlighted clustered islands of tumor cells surrounded by streams of reactive stromal mesenchymal cells, similar to many human cancers; and in some cases, areas where tumor cells had invaded adipose and underlying muscle. In addition to ERα,

cells exhibited strong expression of keratin19, keratin 5, and E-cadherin (indicative of ductal and not lobular differentiation); and to a lesser extent keratin 8/18 and keratin 6. Muc1 and Her2 were expressed also, as was p63 (Fig. S2a-c). Expression of ERα and a high proportion of $Ki67^{+}$ cells indicates184AA3 xenografts likely reflect the Luminal B breast cancer subtype (fig. S1d).

To test reproducibility of 184AA3 xenograft formation, we transplanted cells into a second set of mice under identical conditions and followed the mice over the course of 1 year. Tumors formed in 6 of 8 mice (8/16 glands), and exhibited the same histology and growth rates as in the prior experiment (Fig. 2). Most tumors were first noticed 80-100 days after transplantation, however one became palpable 2 months later, on day +158. To prevent central tumor necrosis, we sacrificed mice when a tumor on either side of the mouse reached a size of ∼ 5mm diameter. Histological examination of contralateral glands (that had no palpable tumor) in several instances revealed a small cluster of 184AA3 cells present at the injection site. Had mice not been sacrificed in these cases, its possible tumors may have eventually formed. For this reason, the actual success rate (per gland) of xenograft formation may be somewhat higher than that reported here. Histological examination again revealed adenocarcinomas (Fig. 2), and we observed ERα staining in each of the formed tumors, present at some level in all cases. Expression was again markedly heterogeneous and not always confined to the nucleus (Fig. 2, Fig. S2a). To show tumors were 184AA3-derived—and did not arise from host cells—we substituted GFP-tagged 184AA3 cells into the xenograft assay and subsequently observed GFP in the tumor epithelium of formed xenografts (Fig. S2b). Notably, stroma was GFP-negative, ruling out 184AA3 as its origin, such as through an epithelial to mesenchymal transition. These findings show 184AA3 cells reliably produce ER^{+} adenocarcinomas in this model system.

All xenografts to this point were made by co-injecting into mice both 184AA3 cells and isogenic 184 fibroblasts. The dependence on fibroblasts—or this particular strain of fibroblasts—for tumor formation was important for us to ascertain. We discovered this strain of fibroblasts was not a critical factor, as it could be replaced with a newly isolated line of FACS-sorted fibroblasts transduced with hTERT, WCH-N141-TERT, which produced tumors in 8 of 8 glands with essentially identical histology to those made with 184 fibroblasts. We discovered however, an absolute dependence on irradiated fibroblasts for xenograft formation. When fibroblasts were withheld, or were not irradiated, tumors did not form (0/8 glands in each case); but parallel grafts, with the 50% mixture of irradiated fibroblasts, formed tumors (13/14 glands) as they had in every prior experiment. These findings identify fibroblasts as an essential component of this model, and provide further evidence supporting a fundamental role of stroma in forming and shaping tumors.

Cellular Heterogeneity and $CD44^{Low}$ tumor initiating cells

Intratumoral heterogeneity in breast cancer is common and may be essential for virulent cancers to develop [20-22]. 184AA3 xenografts varied in their expression of ERα, and other markers, suggesting that they may be an advantageous model for exploring mechanisms of intratumoral heterogeneity (Fig. 1, Fig.S1). We explored origins of this heterogeneity by immunostaining both 2D and 3D cultures of 184-series cells using the lineage markers

keratin 18 (K18) and keratin 14 (K14). Staining revealed a predominant basal phenotype for the normal early-passage (pre-stasis) 184 culture and post-stasis 184Aa strains, which became more heterogeneous in 184AA2, and more luminal in 184AA3 (Fig. 3a).

To quantify marker expression, we stained 184AA3 cultures with a panel of antibodies and used flow cytometry to measure binding. For comparison, we stained also uncultured luminal and myoepithelial cells isolated directly from normal breast tissue. This juxtaposition revealed in 184AA3 an irregular staining pattern which is consistent with their malignant state, and reflected also the patterns observed in xenografts. 184AA3 cells expressed high levels of Muc1, CD24, EpCAM and E-cadherin; and lower levels of Thy 1 and CD44 –all reflecting a luminal-like phenotype (Fig. 3b). On the other hand, 184AA3 expressed CD10, which is observed normally in myoepithelial cells and, to a lesser extent, in fibroblasts. Microscopic examination of 184AA3 cultures immunostained with these antibodies and more, confirmed these results (Fig. 3c). 184AA3 cells expressed ERα, PR, Muc1, CD24, E-Cadherin, keratin 18, CD49f and CD44, all proteins found to some extent within normal luminal cells. 184AA3 cells lacked Thy1, which is consistent also with a luminal phenotype. However, keratin 19 (K19) was not expressed, whereas both p63 and K14 were, a pattern associated with normal myoepithelial cells, although the latter two were expressed heterogeneously. Expression of K19 and K14 was notably different in culture compared to that in xenografts (Fig. 3c vs. Fig. S1b,c). Absent in cultured cells, K19 was expressed abundantly in tumors; and conversely, K14 was present in culture but generally lost in xenografts. This indicates a shift to a more luminal-like phenotype *in vivo*. There were also other notable differences, such as with PR and ER. PR, expressed strongly in nuclei of cultured cells, was generally weak and diffuse in the tumors. In contrast, ER expression became much more pronounced and nuclear-localized *in vivo*. Whether altered expression observed in tumors is reflective of *in vivo* regulation or that of clonal selection is a mystery.

We explored the phenotypic plasticity of 184AA3 cells by testing whether single cells could reproduce the K14/K18 heterogeneity observed in cultures and xenografts. Indeed they could. When we FACS sorted single 184AA3 cells into individual wells with fibroblast feeder layers, 7/96 cells produced a colony after 14 days in culture. Each colony exhibited mixed staining for K14 and K18, indicating expression is conditional and that this heterogeneity could arise *in vivo* from clonal selection, as reported for tumor initiating cells (Fig. S3a).

Prior reports have demonstrated breast tumor initiating cells reside in tumor cell subpopulations expressing disproportionately high levels of CD44[23-25]. The $CD44^{High}$/$CD24^{Low}$ phenotype has since become a widely reported marker of breast cancer stem cells (CSCs) or cells with more aggressive properties [26,24]. When we analyzed CD44 expression by flow cytometry, we discovered a small subpopulation of 184AA3 cells expressing CD44 at distinctly higher levels than the bulk of the culture. Inconspicuous in one dimensional FACS histogram plots, such as that provided in Fig 3b, this $CD44^{High}$ subpopulation was readily and repeatedly observed when we compared CD44 to other parameters, such as size (Forward scatter, FSC, Fig. 4a, FigS3b). When we sorted and cultured the $CD44^{high}$ and $CD44^{low}$ populations, they indeed exhibited distinct

morphologies (Fig. 4a). 184AA3-CD44^{Low} cells grew in large colonies with smooth borders, whereas the CD44^{high} cells grew at roughly the same rate, but were more migratory and most often found as single cells or in small clusters (Fig.4a). This phenotype held as we expanded the culture in order to generate enough cells for xenografting into mice. Immediately prior to implantation, we re-examined CD44 expression levels in these two cultures and found their respective CD44 phenotypes had remained largely unchanged, even after 49 days in culture (Fig. 4a). These cells, along with the parental culture, were xenografted, and mice monitored for 5 months. Over the course of two independent experiments, we found both the 184AA3 parental line and CD44^{Low} strain produced relatively the same proportion of tumors, respectively, 9/16 (56%) and 5/12(42%) tumors formed per gland injected (Fig. 4b). Surprisingly, the CD44^{High} strain, which we had presumed to contain the CSC population, produced only a single tumor out of 10 injected glands. Its histology was similar to the others –all being ER^{+} adenocarcinomas (Fig. 4b). Tumor-initiating cells in 184AA3 appear thus, not in the CD44^{High} subpopulation as anticipated, but in the remaining bulk of the population; cells that on average have less CD44 than normal myoepithelial cells (Figs. 4b, 3b).

184AA3's estrogen receptor is functional, but not essential for growth—To ascertain the levels and functionality of ERα in 184AA3, we subjected the cells to a battery of tests, the first of which was to quantify levels of ERα message. Using qRT-PCR, we measured mRNA levels in cultures of 184AA3 and compared them to those expressed by MCF-7 and the basal cell line, MDA-MB-231, as well as freshly isolated FACS-sorted primary human breast luminal cells. ERα was expressed in all, although at vastly disparate levels (Fig. 5). Not surprisingly, mRNA levels were highest in MCF-7 and barely detectable —but present—in MDA-MB-231 cells. In 184AA3, ERα was 16-fold less than that in MCF-7, but notably matched levels found in normal luminal cells from tissue (Fig. 5a). Western blot analysis revealed protein and mRNA levels corresponded. ERα was by far expressed the most in MCF-7 cells, and after increasing the contrast of the western blot image, we detected ERα in 184AA3 cells as well (Fig. 5b). Less clear was a faint signal produced by MDA-MB-231. The band on the blot is just above detection threshold (measured digitally), but low expression is consistent with qRT-PCR mRNA levels (Figs. 5a,b). With knowledge of ERα mRNA and protein levels in 184AA3, we asked whether estrogen signaling was intact.

As a steroid hormone receptor, ER is targeted—upon ligand binding—to specific DNA binding sites where it subsequently influences transcriptional activity. To determine if estrogen stimulation would induce transcriptional changes in 184AA3, we exposed cells to estradiol and monitored levels of several estrogen-regulated genes, again using MCF-7 and MDA-MB-231 as controls. Each cell line was placed into estrogen-free medium for 48 hours, then stimulated with 1μM 17-β estradiol. Three hours later, and then again at six hours post-stimulation, we collected RNA and measured expression of nine estrogen-regulated genes by qRT-PCR (Fig. 5c). As expected, the three cell lines expressed disparate levels of each gene, so results are displayed on separate graphs. We found each cell line responded to estrogen stimulation, although not always equally, nor with the same directional trend (Fig. S4). For example, when exposed to estrogen, both 184AA3 and

MCF-7 increased expression of PDZK1 and repressed ERα mRNA, whereas MDA-MB-231 cells did exactly the opposite (Fig. 5c). However, MCF-7 and 184AA3 did not always respond in kind. For example, MCF-7 increased B4GALT1 when stimulated, whereas 184AA3 held levels constant. These and other differences in how each of the three cell lines respond to estrogen are interesting and likely reflect other cell-specific forms of gene regulation or ER variants with different functions (Fig. S4, Fig.5b). These results nevertheless show 184AA3 cells can sense and respond to estrogen stimulation, indicating ER is undoubtedly functional in these cells.

Indeed, when we immunostained 184AA3 cells for ER moments after estradiol exposure, we noticed the bulk of the receptor had translocated to the nucleus (Fig. 6b), providing further evidence that signaling is intact. This effect was even clearer in 184AA3XT, a 'biofiltered' 184AA3 derivative strain cultured from an 184AA3 xenograft that abundantly expressed ER (Him25.5R, Fig. S5). 184AA3XT were found to be less migratory and invasive in culture (Fig. S6 a,b), but surprisingly, and despite having similar growth rates to 184AA3 parental line in culture, formed tumors about three-times as fast (compare Figs. S6c & Fig. 2a). It is common for tumor or xenograft-derived strains such as 184AA3XT to be more efficient and quicker to form tumors than the parental strain, and these qualities may improve their practical utility in larger and more costly *in vivo* experiments.

Knowing ER is present and functional in 184AA3 cells, we sought to determine whether 184AA3 depended on estrogen for growth. MCF-7 cells, for example, are notoriously estrogen-dependent, and we were curious if 184AA3 and 184AA3XT cultures would display the same sensitivity. We cultured 184AA3 and 184AA3XT for six weeks, with or without estrogen, and compared their growth to both MCF-7 and MDA-MB-231 cell lines. The results were unexpected, but clear. Whereas MCF-7 cells stopped growing immediately in estrogen-free medium, 184AA3 and 184AA3XT were unaffected by estradiol depletion and unabashedly kept dividing (Fig. 6a), indicating estrogen signaling and growth are not linked within these cells.

To mimic anti-hormonal therapy and study effects of estrogen depletion *in vivo*, we tested the consequences ovary removal had on 184AA3 tumor growth. Mice were xenografted with 184AA3, and in order to study effects on growth rather than on tumor initiation, we allowed tumors to develop until they reached 3mm in diameter prior to treatment. At that point, a fine needle biopsy of the tumor was taken and mice were alternated into one of two experimental arms; i.e., they either had their ovaries removed or received a control sham surgery. The mice were monitored afterward, and when tumors ultimately reached 8mm diameter, the mice were sacrificed and tumors removed. The uterus was removed also, and each uterine lining was examined to determine the ovarian hormone status of each animal. Similar to what we saw in culture, estrogen depletion had no effect on tumor growth. 184AA3 tumors grew at a rate independent of ovarian hormones, with no statistical difference between ovariectomized mice and controls ($p=0.17$, Fig. 6b). In fact, the median time it took to reach the endpoint trended less in ovariectomized mice than controls (22 vs. 33 days, Fig. 6b). There were no noticeable differences in histology either. However, to rule out possible transient effects, we performed another set of xenografts and ovariectomies using the same experimental design, except animals were euthanized and tumors collected at

fixed times after ovariectomy; i.e, 0.5, 1, 2, 3, 4, 5, 6, 7, and 8 weeks later. A total of 43 biopsy-tumor pairs were collected and each was analyzed for prevalence, intensity and cellular localization of ER and Ki67. We observed no ovariectomy- or sham-dependent differences at any of the time points (Fig. 6c). These results indicate 184AA3 cells have indeed somehow uncoupled ER signaling from growth, as evidenced in culture and analogous to clinical tumors that are refractory to anti-hormonal therapies.

Discussion

Tractable models for researching the causes and cures of the most prevalent form of breast cancer are wanting. The histologies of current xenograft models seldom reflect what we see in the clinic, throwing into question whether such models can be predictive. Here, we describe a cell line, 184AA3, which reliably and reproducibly forms adenocarcinomas when xenografted as described here. Tumors produced by 184AA3 likely reflect the luminal B subtype as assessed by their aggressiveness and expression of luminal markers, which includes ER. Yet, much like the 30% of clinical luminal tumors that prove fatal, another distinguishing characteristic of AA3-derived tumors is that they also do not respond to hormonal ablation.

Estrogen receptor expression is rarely observed in cultured human breast cells [27], notably lacking in primary cultures derived from normal reduction mammoplasty tissues. Only a few established cancer-derived cell lines express ER, the most well-known being MCF-7, which is quite aberrant as it has amplified the gene 20+ times over and produces over-abundant levels of the protein. Our finding of ER+ in cultures of 184AA3 (Fig. 3c) and in xenografts (Figs. 1&2; Figs. S1&2), establishes this model as a potentially valuable tool for study of ER function and regulation using a non-amplified ER gene. The tissue architecture, including invasive aspects, stromal involvement, and hormone-deprivation resistance of 184AA3 tumors will likely prove useful for identification, testing and development of therapeutics targeting aggressive luminal breast cancers.

Adding to the utility of this system, 184AA3 is part of a progression series. 184AA3 was derived from the 184Aa strain, itself a derivative of cells cultured from reduction mammoplasty tissue. Precursor cultures, and even sister lines, that are part of the 184 progression series, are available for study, giving the 184AA3 model added potential as a system for research into the etiology of refractory luminal adenocarcinomas. For instance, recent publications call into question whether mammary tumors are derived from luminal epithelial cells. The 184Aa cells from which 184AA3 was derived are K14(+)/K18/K19 (-)– a surprisingly basal phenotype for the progenitors of a line that generates ER+ luminal adenocarcinomas. Indeed we and others have observed generation of ER+ tumors (though not adenocarcinomas) from transformed primary human myoepithelial cells, raising the possibility that tumorigenicity may involve lineage de-differentiation, then re-differentiation in humans as has been reported for PIK3CAmutant tumors in mice [28,29].

Moving beyond the cytokeratins, the intratumoral heterogeneity of this model is notable. Judah Folkman once noted that heterogeneity is almost a universal feature for tumors to succeed[30], and a growing body of literature attests to its role in tumor survival, growth,

and therapeutic resistance[21,31]. It is likely that the phenotypic plasticity of 184AA3 cells contributes to the mechanism that generates the intratumoral heterogeneity observed in 184AA3 xenografts, as outgrowths of single cell clones of 184AA3 are also phenotypically heterogeneous (note that we cannot distinguish intrinsic potential of the cell line from potential that is dependent on fibroblastic factors as 7 of the 8 single cell clones of 184AA3 were grown on fibroblast feeder layers). Dissecting the origins of heterogeneity and the factors regulating it, be it clonal diversification or microenvironmental factors, are important avenues for future research that can be addressed using this system.

Further, it is clear that etiology and tumor phenotype do not rely on the epithelial cell alone. That tumorigenicity is a group activity is evidenced here by the xenografting requirement for irradiated fibroblasts. This observation reinforces prior work in dissecting the role of stroma in promoting tumorigenicity[32], which has been extensively elaborated upon, including a recent report identifying factors required for tumorigenicity that are elicited from the stroma by transformed epithelial cells, clarifying a mechanism of malignant cooperation [33].

Returning to the question of which cells are tumor-initiating, we note that the CD44+ subpopulation of 184AA3 was essentially non-tumorigenic, while the bulk of the cells efficiently generated tumors. This contradicts the early work of Al Hajj and colleagues [23] (2003), and reinforces that tumor initiation can arise from populations not previously identified as stem-like [34].

Our discovery of the conditions under which 184AA3 cells generate clinically-relevant luminal tumors is an important step towards defining and overcoming the remaining obstacles that have until now prevented development of models of luminal breast cancer. The fact that this progression model culminates in xenografts that are ovarian-hormone and estradiol independent, proliferative, and invasive suggests its use to learn which factors of the model promote these aggressive phenotypes, and thus which aspects may be changed to instead generate more benign phenotypes. Such observations can form the bases of novel clinical therapeutics.

Methods

Mice

NOD *scid* gamma mice (‘NSG’, NOD.Cg-Prkdc^{scid} Il2rg^{tm1Wjl}/SzJ) were obtained from Jackson Labs (stock#005557). Animal use protocols were obtained and procedures followed in strict accordance with guidelines established by the Lawrence Berkeley National Laboratory Animal Welfare and Research Committee (AWRC).

Breast tissues

Breast tissues from reduction mammoplasties and tumors were acquired from the Cooperative Human Tissue Network (CHTN), a program funded by the National Cancer Institute. All specimens were collected with patient consent; reduction mammoplasties were reported negative for proliferative breast disease by board-certified pathologists. Use of anonymous samples was granted exemption status by the University of California at

Berkeley Institutional Review Board, in accordance with the Code of Federal Regulations 45 CFR 46.101.

Cell lines

The primary culture and derivation of strains and cell lines in the 184 progression series have been described previously [17,35,18,36]. For this study, we have cultured normal finite pre-stasis 184 HMEC, the post-stasis 184Aa strain resulting from benzo(a)pyrene exposure of primary 184, and immortally transformed cell lines derived from184 that had been shown capable of growing in anchorage independent conditions, namely: 184ZNMY3-N, 184B5ME, 184FMY2, 184AaGS1, 184AA2, and 184AA3. 184 primary-derived fibroblasts were established as described[37]. WCH-N141-TERT fibroblasts were FACS sorted from reduction mammoplasty tissue and transduced with pLXSN-hTERT[G418], a kind gift from Judith Campisi. Fibroblasts and all HMEC were routinely cultured in M87A medium [38], unless otherwise noted in figure legends. MDA-MB-231 and MCF-7 were obtained directly from the American Type Culture Collection (ATCC). 3D cultures were established by seeding cells into 100% Growth factor depleted Matrigel (Invitrogen).

Antibodies

Supplemental Table 1 provides all necessary information regarding antibodies used in this study, including clone information, marker conjugation, supplier, and references to figures where they were used.

Xenograft transplantation

Xenograft protocol was generally as reported by Lim and colleagues[39], with the exception that the epithelial cells were pre-clustered on low attachment plates and other minor exceptions; details as follows. NSG mice (described above) were housed for stabilization and observation for 3 days prior to transplantation surgeries. The day before transplantation surgery, subconfluent passage 50 cultures of epithelial cells were dissociated with 0.05% trypsin and aggregated on low attachment polyhema-coated plates in M87A medium containing 5% growth factor reduced Matrigel™ (Invitrogen). Fibroblasts, either 184-Fb or N141-hTERT primary tissue derived fibroblasts, were plated onto two sets of plates. On the day of surgery, half of the fibroblast cultures were exposed to 0.3Gy X-ray radiation, then all the fibroblast cultures were harvested and combined to yield a tube of 50% 0.3 Gy irradiated fibroblasts. One sterile Eppendorf tube was then prepared as follows for each of the mammary glands to be transplanted; each tube contained a mixture of 2.5e5 irradiated and 2.5e5 non-irradiated fibroblasts. 2.5e5 pre-clustered 184AA3 cells were then added to each tube, and the mixture adjusted to 50% Matrigel™ and 20μl final volume containing 1μl surgical tracking dye. Both #4 inguinal fat pads of 3-week old NSG mice were cleared of their epithelial rudiments, and the cell mixture injected into the cleared pad. All animal procedures were performed in compliance with animal safety and pain prevention guidelines.

Ovariectomy protocol

For the ovariectomy experiments, xenografts were performed as described immediately above. When the first tumor in a mouse reached 3 mm diameter, a biopsy was taken using a 16 gauge biopsy needle, and the mouse was either ovariectomized or given a sham surgery. The animals were euthanized at the time points post biopsy as stated in the text, and the tumors and reproductive tracts were resected. Reproductive tracts were microscopically evaluated to determine whether the animal had effectively been ovariectomized. Portions of each tumor were flash-frozen in cell freezing medium, while both the remainder of the tumor and each of the biopsy samples were fixed, paraffin embedded and further processed at the UC Davis Mouse Pathology Laboratory for histological and immunohistochemical (IHC) analyses. Sections of each tumor and each biopsy were immunostained with antibodies to ERa and Ki67. A modified version of the Imagescope "IHC Nuclear" algorithm[36] was used to quantify intensity of immunostain signal in each epithelial cell nucleus in representative sections of each sample. Results of these analyses were then compared for each tumor and associated biopsy pair to determine whether ovariectomy-dependent changes were detectable in the 184AA3 tumors.

Flow Cytometry and Fluorescence-Activated Cell Sorting (FACS)

Analysis and cell sorting was performed using a BD FACS Vantage cytometer (FACSDIVA software, version 5.0.3). Prior to staining, we dissociated the cells, rinsed and re-suspended them in PBS/1% bovine serum albumin (Sigma # A8412). Following their filtration through 40μm nylon mesh strainers (BD Biosciences), the cells were placed into several tubes and combinations of the following antibodies were added: Muc1-FITC, Thy1-PE-Cy5, E-cadherin-Alexafluor 488, CD10-Brilliant Violet 421, CD24-PE, Cd44-PE, EpCAM-Alexafluor488, and CD49f- Brilliant Violet 421; amounts of each determined by empirical titration. Viable cells were selected by using either DAPI or To-Pro-3 dye exclusion, and we used forward scatter (height) vs. side scatter (width) gating to exclude cell doublets. Compensation was calculated using beads custom-labeled with each fluorophor (APC anti-mouse bead kit (Molecular Probes/Invitrogen). Negative controls consisted of unlabeled beads and cells incubated with conjugated isotype control antibodies. Primary cells from tissue-derived organoids served as positive controls and as a comparator sample, prepared as previously described[40]. Supplementary Figure 7 illustrates gates and full backgating used to sort the 184AA3-CD44^{High} and 184AA3-CD44^{Low} subpopulations. Cells were sorted twice—using conservative sorting masks—to ensure purity. For single cell cloning experiments, single viable 184AA3 cells were FACS sorted directly into a 96-well dish containing a subconfluent monolayer of 30Gy X-ray irradiated primary-derived fibroblasts, WCH-N141 TERT ZsGreen^{high}. Visual inspection of wells from a parallel sort, where a feeder layer was not used, allowed us to confirm both the targeting of the sort stream and seeding of single cells.

Migration and Invasion

To measure transwell migration, we suspended 10^5 cells into 200μl of their respective media: M87A for 184AA3 and 184AA3xt, H14 for S1 cells, DMEM (4.5g/L glucose) for MDA-MB-231 and MCF7. Suspensions were placed into the top chamber of tissue-culture

treated transwells containing a polyethylene terephthalate (PET) membrane with 8.0μm pore size (Corning, #353097). In the bottom chamber, we placed 300 μl of medium supplemented with 10% fetal bovine serum (FBS). The non-malignant human breast cell line, HMT3522-LBNL-S1 and malignant MDA-MB-231 cell lines served respectfully as non-invasive and invasive reference controls. Cells were incubated at 37°C for 24, 48, and 72 hours. At the end of each timepoint, we fixed the cells and stained them with 0.5% Toluidine Blue in 2% w/v Na_2CO_3. The top chamber was wiped with a cotton swab and we examined the underside of the transwell and counted cells that had migrated through the pores. To quantify, we counted the cells by hand (if only a few hundred cells had migrated) or extrapolated from images taken in each of four quadrants. Invasion was similarly measured, except a matrigel coating was applied and allowed to set prior to seeding cells(20 μl of 6% matrigel per chamber, incubated 1hr at 37°C).

qRT-PCR

RNAs from cell lines and sorted cells were isolated using silica-based spin-column extraction kits according to the manufacturer's protocol (RNeasy mini kit, Qiagen). All RNA samples were DNase I treated (DNA *free*, Ambion) to remove traces of genomic DNA. Complimentary DNA (cDNA) was synthesized by random-hexamer primed reverse transcription using Thermoscript™ reverse transcription kit (Invitrogen) and the manufacturer's standard protocol. Water was substituted for enzyme to provide negative controls. Transcript levels were measured by quantitative real-time PCR (qRT-PCR) using the Lightcycler® 480 system (Roche), Sybr Green chemistry (Roche #04707516001) and primers provided in Supplemental Table 2. Primer sets were designed to span intron/exon borders to prevent amplification from genomic DNA (except E2IG4, which has only 2 exons). ERα primers amplify mRNA sequence encoding amino acids 387-418 of the protein, an area common to all known functional splice variants. Substitution of PCR-grade water for cDNA template served as an additional negative control. Transcripts were amplified in parallel, along with a stably expressed reference gene, TBP, in triplicate reactions using equal amounts of 5x diluted cDNA (1ul per reaction). Relative levels of transcripts were calculated using the delta Ct method and normalized to those of the TBP reference transcript using the formula: $\%TBP = 2 - (Ct_{GENE} - Ct_{TBP}) \times 100\%$.

Estrogen response assays

To explore estrogen signaling in 184AA3 cells and determine if the cells could sense and respond to estrogen, we stimulated the cells with estradiol and monitored transcript levels of known estrogen-sensitive genes. For 48 hours, 184AA3 cells and the reference cell lines, MCF-7 and MDA-MB-231, were cultured in estrogen-free medium. After this time, the medium was refreshed with that containing 1uM 17-β estradiol. RNA was collected at 0-hour (untreated) and at 3 and 6 hours post-estradiol exposure. Transcripts were measured by qRT-PCR, as described above. Primers of the estrogen-sensitive genes are provided in Supplementary Table 2. We validated the assay by comparing results of MCF-7 to those published previously [41]. Nuclear translocation of ER was measured by observing the localization of ER in estradiol stimulated and unstimulated cells. We seeded fifty thousand cells (AA3 and 184AA3XT, in parallel) onto fibronectin coated (2μg/cm^2) glass coverslips and cultured them overnight to allow for attachment. After this time, cells were thoroughly

washed in PBS and placed into estrogen free medium for 24 hours (phenol red-free DMEM/F12 plus 1% charcoal-stripped FBS). The cells were then stimulated for 15 minutes in medium containing 10nM 17-β estradiol. Cells were fixed in 4% PFA, immunostained for ERα, and compared to unstimulated controls. Images were captured on an Olympus FV-1000 confocal microscope.

Immunoblots

ERα protein expression was measured in 184AA3, MDA-MB-231 and MCF-7 cells (Fig. 5b). Cells were lysed in in 4% SDS/PBS containing proteinase inhibitor cocktail set I and phosphatase inhibitor cocktail set I [Calbiochem]. After 10 second sonication and centrifugation, the protein concentration in the supernatant was measured using the BioRad DC™ Protein assay. Proteins were separated by SDSPAGE (40μg/lane) on 4-20% Tris-Glycine Gels and transferred to nitrocellulose membranes. A protein standard was included (Precision Plus Protein™ Kaleidoscope standard, BioRad #161-0375). Blots were probed with antibodies specific to ER and alpha tubulin (Supplemental Table 1). After washing and probing with HRP-conjugated secondary antibodies, blots were developed using SuperSignal West Femto chemiluminescence reagent (Pierce Biotechnology) and imaged with a FluorChem HD2 imager (Cell Biosciences/ProteinSimple). To permit accurate comparison to the protein standards, we used Photoshop (Adobe Systems) to merge the chemiluminescent image to the color image of the standards. Contrast adjustment of the captured 16-bit image was also needed, and was applied uniformly.

Immunofluorescence

Immunofluorescence was performed on monolayer cell cultures, smears of 3-dimensional cultures, and frozen tumor sections. Specimens were fixed in 4% paraformaldehyde (5 minutes, 23°C), followed by a 10 minute treatment with 4% formaldehyde+0.5% saponin, then washed in staining buffer (0.5% w/v saponin, 10% v/v goat serum in PBS). After overnight incubation with primary antibodies (diluted in staining buffer), the specimens were rinsed thoroughly and treated with anti-mouse and anti-rabbit secondary antibodies, respectively conjugated with Alexafluor 488 and Alexfluor 594 (Invitrogen), diluted 1:400 (1 hour, 37°C). Nuclei were stained using 0.3 μM DAPI (Molecular Bioprobes) and mounted with Fluormount G mounting medium (Southern Biotech). We captured and processed images using an AxioImager fluorescent microscope and Axiovision (Zeiss) and/or Photoshop (Adobe) software. If contrast adjustments were needed, they were applied uniformly. Primary antibodies are provided in Supplementary Table 1.

Immunohistochemistry

Processing of xenograft specimens, including paraffin embedding, sectioning, and all staining, was performed by the Mutant Mouse Pathology Laboratory at the Center for Comparative Medicine at the University of California, Davis. Four micrometer thick paraffin sections were stained with Mayer's hemotoxylin and eosin or immunostained as described previously,[42] with some antibody-dependent and empirical based modifications; e.g., lot-based differences in antibody dilutions. Antigen retrieval was performed at 125°C in pH 6.0 citrate buffer, using a Decloaking Chamber (Biocare Medical, Concord, CA) pressurized to 15psi. The total incubation time was 45 min. Antibodies used for

immunohistochemistry are provided in Supplementary Supplementary Table 1. Specimens were incubated with primary antibodies overnight at room temperature in a humidified chamber. Slides were scanned at 20× magnification using an Aperio® XT slide scanner (Leica Biosystems), imported into the Aperio Spectrum database, and visualized with Aperio® Imagescope software.

Statistical Analysis

JMP 7 (SAS Institute) and Prism5 (GraphPad) statistical software packages were used for all statistical analyses. In all cases, error bars indicate the standard deviation of at least three multiple biological replicates. For qRT-PCR, standard deviations of Ct values from triplicate reactions were used to determine percent relative error and then propagated using the square root of the sum of squares method.

Supplementary Material

Refer to Web version on PubMed Central for supplementary material.

Acknowledgments

For their invaluable technical assistance during this project, we thank Maria Rojec, Dinah Groesser, Alvin Lo, Sun-Young Lee, Xuefei Tian, and Eva Lee (Lawrence Berkeley National Laboratory). We appreciate also the expertise and help given by Judith Walls and Ed Hubbard (University of California, Davis Center for Comparative Medicine). We express special gratitude also to Michelle Scott of the LBNL flow cytometry and Advanced microscopy facility for her expert technical advice and assistance. Grant support: Innovator award to M.J.B. from the U.S. Department of Defense (W81XWH0810736 and W81XWH12M9532) and in part by National Cancer Institute awards (R37CA064786, R01CA140663, U54CA112970) and by grants from the U.S. Department of Energy, Office of Biological and Environmental Research and Low Dose Scientific Focus Area (contract no. DE-AC02-05CH1123) and the Breast Cancer Research Foundation. The funders had no role in the study design, data collection and analysis, decision to publish or preparation of the manuscript.

References

1. Box, GE.; Draper, NR. Empirical model-building and response surfaces. Vol. 424. Wiley; New York: 1987.
2. Hines WC, Yaswen P, Bissell MJ. Modelling breast cancer requires identification and correction of a critical cell lineage-dependent transduction bias. Nature communications. 2015; 6:6927.10.1038/ncomms7927
3. Wagner KU. Models of breast cancer: quo vadis, animal modeling? Breast Cancer Res. 2004; 6(1): 31–38.10.1186/bcr723 [PubMed: 14680483]
4. Cancer Genome Atlas N. Comprehensive molecular portraits of human breast tumours. Nature. 2012; 490(7418):61–70.10.1038/nature11412 [PubMed: 23000897]
5. O'Brien KM, Cole SR, Tse CK, Perou CM, Carey LA, Foulkes WD, Dressler LG, Geradts J, Millikan RC. Intrinsic breast tumor subtypes, race, and long-term survival in the Carolina Breast Cancer Study. Clin Cancer Res. 2010; 16(24):6100–6110.10.1158/1078-0432.CCR-10-1533 [PubMed: 21169259]
6. Tran B, Bedard PL. Luminal-B breast cancer and novel therapeutic targets. Breast Cancer Res. 2011; 13(6):221.10.1186/bcr2904 [PubMed: 22217398]
7. Ellis MJ, Ding L, Shen D, Luo J, Suman VJ, Wallis JW, Van Tine BA, Hoog J, Goiffon RJ, Goldstein TC, Ng S, Lin L, Crowder R, Snider J, Ballman K, Weber J, Chen K, Koboldt DC, Kandoth C, Schierding WS, McMichael JF, Miller CA, Lu C, Harris CC, McLellan MD, Wendl MC, DeSchryver K, Allred DC, Esserman L, Unzeitig G, Margenthaler J, Babiera GV, Marcom PK, Guenther JM, Leitch M, Hunt K, Olson J, Tao Y, Maher CA, Fulton LL, Fulton RS, Harrison M, Oberkfell B, Du F, Demeter R, Vickery TL, Elhammali A, Piwnica-Worms H, McDonald S,

Watson M, Dooling DJ, Ota D, Chang LW, Bose R, Ley TJ, Piwnica-Worms D, Stuart JM, Wilson RK, Mardis ER. Whole-genome analysis informs breast cancer response to aromatase inhibition. Nature. 2012; 486(7403):353–360.10.1038/nature11143 [PubMed: 22722193]

8. Burdall SE, Hanby AM, Lansdown MR, Speirs V. Breast cancer cell lines: friend or foe? Breast Cancer Res. 2003; 5(2):89–95. [PubMed: 12631387]
9. Kabos P, Finlay-Schultz J, Li C, Kline E, Finlayson C, Wisell J, Manuel CA, Edgerton SM, Harrell JC, Elias A, Sartorius CA. Patient-derived luminal breast cancer xenografts retain hormone receptor heterogeneity and help define unique estrogen-dependent gene signatures. Breast Cancer Res Treat. 2012; 135(2):415–432.10.1007/s10549-012-2164-8 [PubMed: 22821401]
10. DeRose YS, Wang G, Lin YC, Bernard PS, Buys SS, Ebbert MT, Factor R, Matsen C, Milash BA, Nelson E, Neumayer L, Randall RL, Stijleman IJ, Welm BE, Welm AL. Tumor grafts derived from women with breast cancer authentically reflect tumor pathology, growth, metastasis and disease outcomes. Nat Med. 2011; 17(11):1514–1520.10.1038/nm.2454 [PubMed: 22019887]
11. Cottu P, Bieche I, Assayag F, El Botty R, Chateau-Joubert S, Thuleau A, Bagarre T, Albaud B, Rapinat A, Gentien D, de la Grange P, Sibut V, Vacher S, Hatem R, Servely JL, Fontaine JJ, Decaudin D, Pierga JY, Roman-Roman S, Marangoni E. Acquired resistance to endocrine treatments is associated with tumor-specific molecular changes in patient-derived luminal breast cancer xenografts. Clin Cancer Res. 2014; 20(16):4314–4325.10.1158/1078-0432.CCR-13-3230 [PubMed: 24947930]
12. Briand P, Petersen OW, Van Deurs B. A new diploid nontumorigenic human breast epithelial cell line isolated and propagated in chemically defined medium. In Vitro Cell Dev Biol. 1987; 23(3): 181–188. [PubMed: 3558253]
13. Rizki A, Weaver VM, Lee SY, Rozenberg GI, Chin K, Myers CA, Bascom JL, Mott JD, Semeiks JR, Grate LR, Mian IS, Borowsky AD, Jensen RA, Idowu MO, Chen F, Chen DJ, Petersen OW, Gray JW, Bissell MJ. A human breast cell model of preinvasive to invasive transition. Cancer Res. 2008; 68(5):1378–1387. doi:68/5/1378 [pii] 10.1158/0008-5472.CAN-07-2225. [PubMed: 18316601]
14. Soule HD, Maloney TM, Wolman SR, Peterson WD Jr, Brenz R, McGrath CM, Russo J, Pauley RJ, Jones RF, Brooks SC. Isolation and characterization of a spontaneously immortalized human breast epithelial cell line, MCF-10. Cancer Res. 1990; 50(18):6075–6086. [PubMed: 1975513]
15. Park CC, Zhang H, Pallavicini M, Gray JW, Baehner F, Park CJ, Bissell MJ. Beta1 integrin inhibitory antibody induces apoptosis of breast cancer cells, inhibits growth, and distinguishes malignant from normal phenotype in three dimensional cultures and in vivo. Cancer Res. 2006; 66(3):1526–1535. doi:66/3/1526 [pii] 10.1158/0008-5472.CAN-05-3071. [PubMed: 16452209]
16. Dawson PJ, Wolman SR, Tait L, Heppner GH, Miller FR. MCF10AT: a model for the evolution of cancer from proliferative breast disease. The American journal of pathology. 1996; 148(1):313–319. [PubMed: 8546221]
17. Stampfer MR, Bartley JC. Induction of transformation and continuous cell lines from normal human mammary epithelial cells after exposure to benzo[a]pyrene. Proc Natl Acad Sci U S A. 1985; 82(8):2394–2398. [PubMed: 3857588]
18. Stampfer, MR.; LaBarge, MA.; Garbe, JC. Cell and Molecular Biology of Breast Cancer. Springer; 2013. An integrated human mammary epithelial cell culture system for studying carcinogenesis and aging; p. 323-361.
19. Severson PL, Vrba L, Stampfer MR, Futscher BW. Exome-wide mutation profile in benzo[a]pyrene-derived post-stasis and immortal human mammary epithelial cells. Mutat Res Genet Toxicol Environ Mutagen. 2014:775–776. 48–54.10.1016/j.mrgentox.2014.10.011
20. Heppner GH, Miller BE. Tumor heterogeneity: biological implications and therapeutic consequences. Cancer Metastasis Rev. 1983; 2(1):5–23. [PubMed: 6616442]
21. Marusyk A, Tabassum DP, Altrock PM, Almendro V, Michor F, Polyak K. Non-cell-autonomous driving of tumour growth supports sub-clonal heterogeneity. Nature. 2014; 514(7520):54–58.10.1038/nature13556 [PubMed: 25079331]
22. Merlo LM, Pepper JW, Reid BJ, Maley CC. Cancer as an evolutionary and ecological process. Nat Rev Cancer. 2006; 6(12):924–935.10.1038/nrc2013 [PubMed: 17109012]

23. Al-Hajj M, Wicha MS, Benito-Hernandez A, Morrison SJ, Clarke MF. Prospective identification of tumorigenic breast cancer cells. Proc Natl Acad Sci U S A. 2003; 100(7):3983–3988. [PubMed: 12629218]
24. Sheridan C, Kishimoto H, Fuchs RK, Mehrotra S, Bhat-Nakshatri P, Turner CH, Goulet R Jr, Badve S, Nakshatri H. CD44+/CD24- breast cancer cells exhibit enhanced invasive properties: an early step necessary for metastasis. Breast Cancer Res. 2006; 8(5):R59. [PubMed: 17062128]
25. Ponti D, Costa A, Zaffaroni N, Pratesi G, Petrangolini G, Coradini D, Pilotti S, Pierotti MA, Daidone MG. Isolation and in vitro propagation of tumorigenic breast cancer cells with stem/progenitor cell properties. Cancer Res. 2005; 65(13):5506–5511. [PubMed: 15994920]
26. Biddle A, Gammon L, Fazil B, Mackenzie IC. CD44 Staining of Cancer Stem-Like Cells Is Influenced by Down-Regulation of CD44 Variant Isoforms and Up-Regulation of the Standard CD44 Isoform in the Population of Cells That Have Undergone Epithelial-to-Mesenchymal Transition. PLoS One. 2013; 8(2):e57314.10.1371/journal.pone.0057314 [PubMed: 23437366]
27. Graham JD, Mote PA, Salagame U, Balleine RL, Huschtscha LI, Clarke CL. Hormone-responsive model of primary human breast epithelium. Journal of mammary gland biology and neoplasia. 2009; 14(4):367–379.10.1007/s10911-009-9160-6 [PubMed: 19936891]
28. Koren S, Reavie L, Couto JP, De Silva D, Stadler MB, Roloff T, Britschgi A, Eichlisberger T, Kohler H, Aina O, Cardiff RD, Bentires-Alj M. PIK3CA(H1047R) induces multipotency and multi-lineage mammary tumours. Nature. 2015; 525(7567):114–118.10.1038/nature14669 [PubMed: 26266975]
29. Van Keymeulen A, Lee MY, Ousset M, Brohee S, Rorive S, Giraddi RR, Wuidart A, Bouvencourt G, Dubois C, Salmon I, Sotiriou C, Phillips WA, Blanpain C. Reactivation of multipotency by oncogenic PIK3CA induces breast tumour heterogeneity. Nature. 2015; 525(7567):119–123.10.1038/nature14665 [PubMed: 26266985]
30. Bissell MJ, Bartholomew JC, Folkman J, Smith H, Stampfer M. Culture systems for studying malignancy. Cancer Res;(United States). 1979; 39
31. Maley CC, Galipeau PC, Finley JC, Wongsurawat VJ, Li X, Sanchez CA, Paulson TG, Blount PL, Risques RA, Rabinovitch PS, Reid BJ. Genetic clonal diversity predicts progression to esophageal adenocarcinoma. Nat Genet. 2006; 38(4):468–473.10.1038/ng1768 [PubMed: 16565718]
32. Thomasset N, Lochter A, Sympson CJ, Lund LR, Williams DR, Behrendtsen O, Werb Z, Bissell MJ. Expression of autoactivated stromelysin-1 in mammary glands of transgenic mice leads to a reactive stroma during early development. The American journal of pathology. 1998; 153(2):457–467.10.1016/S0002-9440(10)65589-7 [PubMed: 9708806]
33. Zhang P, Lo A, Huang Y, Huang G, Liang G, Mott J, Karpen GH, Blakely EA, Bissell MJ, Barcellos-Hoff MH, Snijders AM, Mao JH. Identification of genetic loci that control mammary tumor susceptibility through the host microenvironment. Scientific reports. 2015; 5:8919.10.1038/srep08919 [PubMed: 25747469]
34. Kim J, Villadsen R, Sorlie T, Fogh L, Gronlund SZ, Fridriksdottir AJ, Kuhn I, Rank F, Wielenga VT, Solvang H, Edwards PA, Borresen-Dale AL, Ronnov-Jessen L, Bissell MJ, Petersen OW. Tumor initiating but differentiated luminal-like breast cancer cells are highly invasive in the absence of basal-like activity. Proc Natl Acad Sci U S A. 2012; 109(16):6124–6129.10.1073/pnas.1203203109 [PubMed: 22454501]
35. Stampfer MR, Garbe J, Nijjar T, Wigington D, Swisshelm K, Yaswen P. Loss of p53 function accelerates acquisition of telomerase activity in indefinite lifespan human mammary epithelial cell lines. Oncogene. 2003; 22(34):5238–5251.10.1038/sj.onc.1206667 [PubMed: 12917625]
36. Cardiff RD, Hubbard NE, Engelberg JA, Munn RJ, Miller CH, Walls JE, Chen JQ, Velasquez-Garcia HA, Galvez JJ, Bell KJ, Beckett LA, Li YJ, Borowsky AD. Quantitation of fixative-induced morphologic and antigenic variation in mouse and human breast cancers. Lab Invest. 2013; 93(4):480–497.10.1038/labinvest.2013.10 [PubMed: 23399853]
37. Labarge MA, Garbe JC, Stampfer MR. Processing of human reduction mammoplasty and mastectomy tissues for cell culture. J Vis Exp. 2013; (71)10.3791/50011
38. Garbe JC, Bhattacharya S, Merchant B, Bassett E, Swisshelm K, Feiler HS, Wyrobek AJ, Stampfer MR. Molecular distinctions between stasis and telomere attrition senescence barriers shown by long-term culture of normal human mammary epithelial cells. Cancer Res. 2009; 69(19):7557–7568. doi:0008-5472.CAN-09-0270 [pii] 10.1158/0008-5472.CAN-09-0270. [PubMed: 19773443]

39. Lim E, Vaillant F, Wu D, Forrest NC, Pal B, Hart AH, Asselin-Labat ML, Gyorki DE, Ward T, Partanen A, Feleppa F, Huschtscha LI, Thorne HJ, Fox SB, Yan M, French JD, Brown MA, Smyth GK, Visvader JE, Lindeman GJ. Aberrant luminal progenitors as the candidate target population for basal tumor development in BRCA1 mutation carriers. Nat Med. 2009; 15(8):907–913. doi:nm.2000 [pii] 10.1038/nm.2000. [PubMed: 19648928]

40. Hines WC, Su Y, Kuhn I, Polyak K, Bissell MJ. Sorting Out the FACS: A Devil in the Details. Cell reports. 2014; 6(5):779–781. [PubMed: 24630040]

41. Wang DY, Fulthorpe R, Liss SN, Edwards EA. Identification of estrogen-responsive genes by complementary deoxyribonucleic acid microarray and characterization of a novel early estrogen-induced gene: EEIG1. Mol Endocrinol. 2004; 18(2):402–411.10.1210/me.2003-0202 [PubMed: 14605097]

42. Toth M, Gervasi DC, Fridman R. Phorbol ester-induced cell surface association of matrix metalloproteinase-9 in human MCF10A breast epithelial cells. Cancer Res. 1997; 57(15):3159–3167. [PubMed: 9242444]

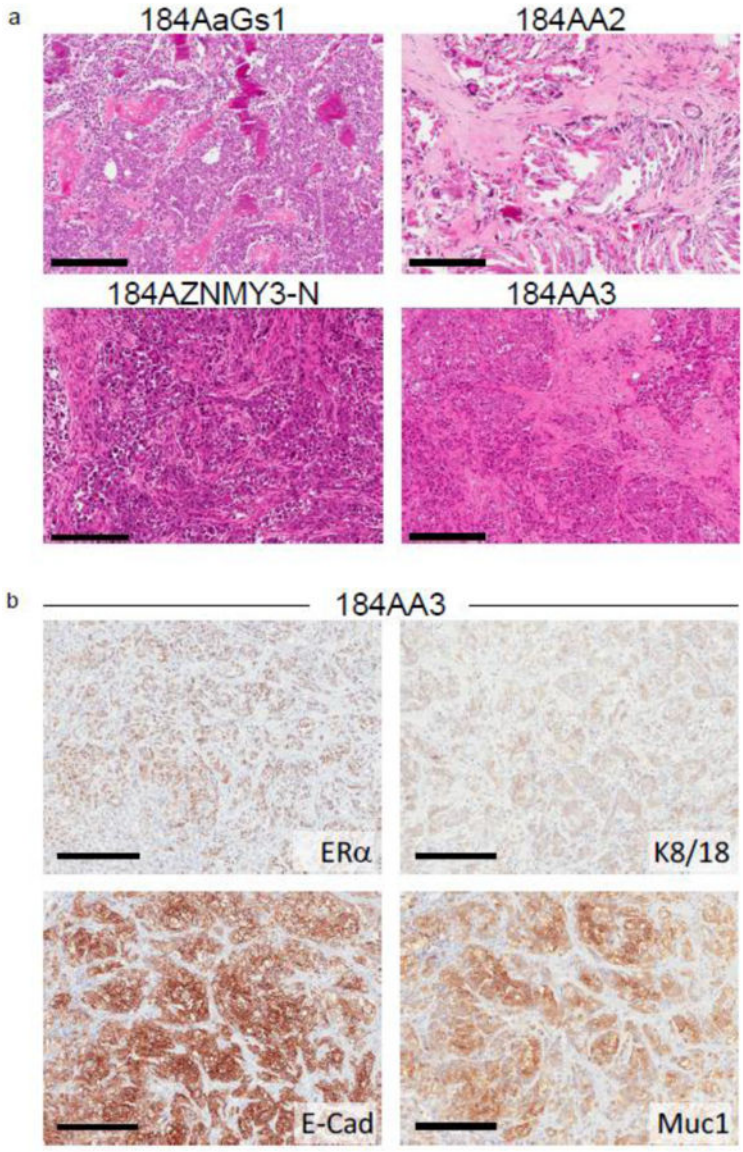

Figure 1. 184AA3 ER+ adenocarcinomas resemble human breast tumors

(a) H&E images of xenografts formed by the 4 tumor producing cell lines in the 184 progression series. Scale bars = 400μm *(b)* Comparison of an 184AA3 xenograft to a clinical breast cancer case. Both are ER^+ adenocarcinomas that contain islands of tumor epithelium expressing luminal markers keratin 18(K18), E-Cadherin (E-Cad), Keratin 8 (K8), keratin 18 (K18), and Muc1. Smooth muscle actin (SMA) and vimentin (Vim) staining emphasizes the epithelial-stromal boundary in the clinical specimen. Keratin 14 (K14) is absent also in the clinical specimen. Scale bars = 200μm.

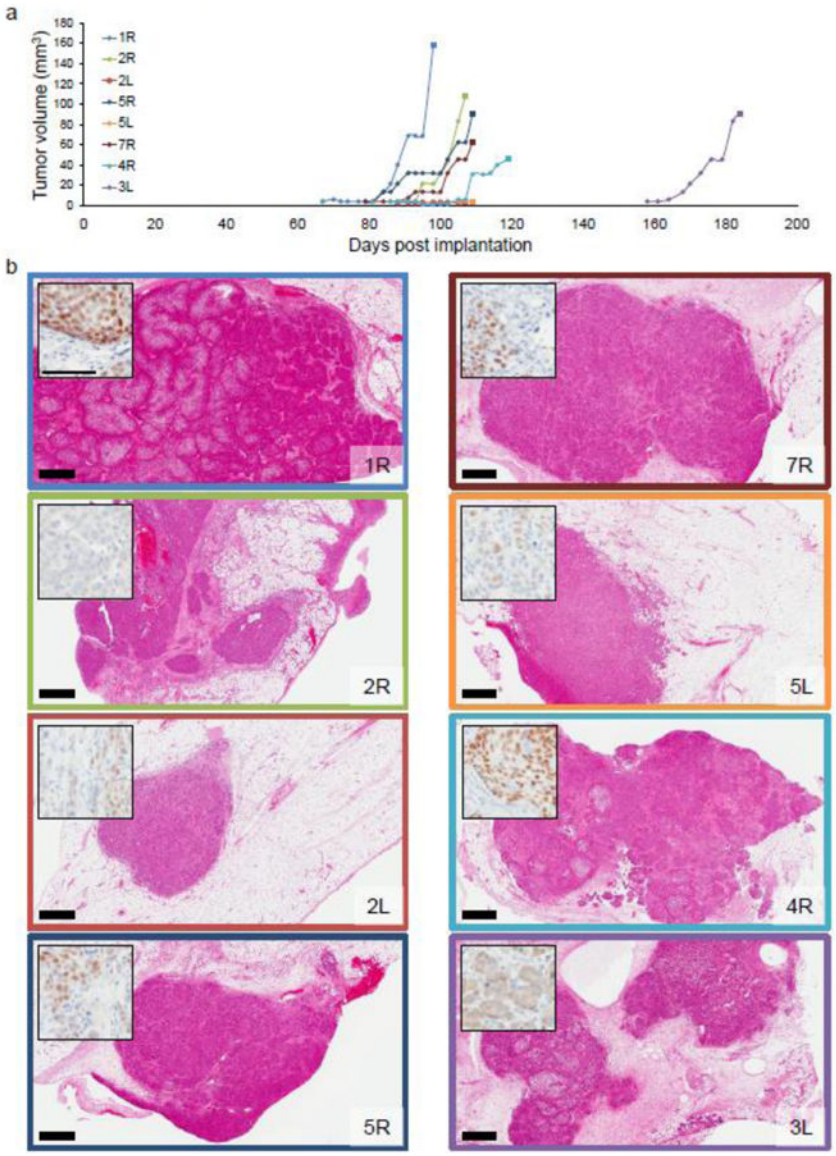

Figure 2. 184AA3 xenograft growth and ERα expression

(a) 184AA3 growth *in vivo*. Tumor volumes of 184AA3 xenografts were calculated from bi-weekly caliper measurements. Each tumor is coded according to the mouse#, and side on which it arose; e.g., '1R' indicates experiment mouse #1, right mammary gland. *(b)* H&E stained sections of 184AA3-derived tumors. Image borders are color-matched to the above growth curves; scale bar = 600μm. Inset: ERα staining with 100μm scale bar.

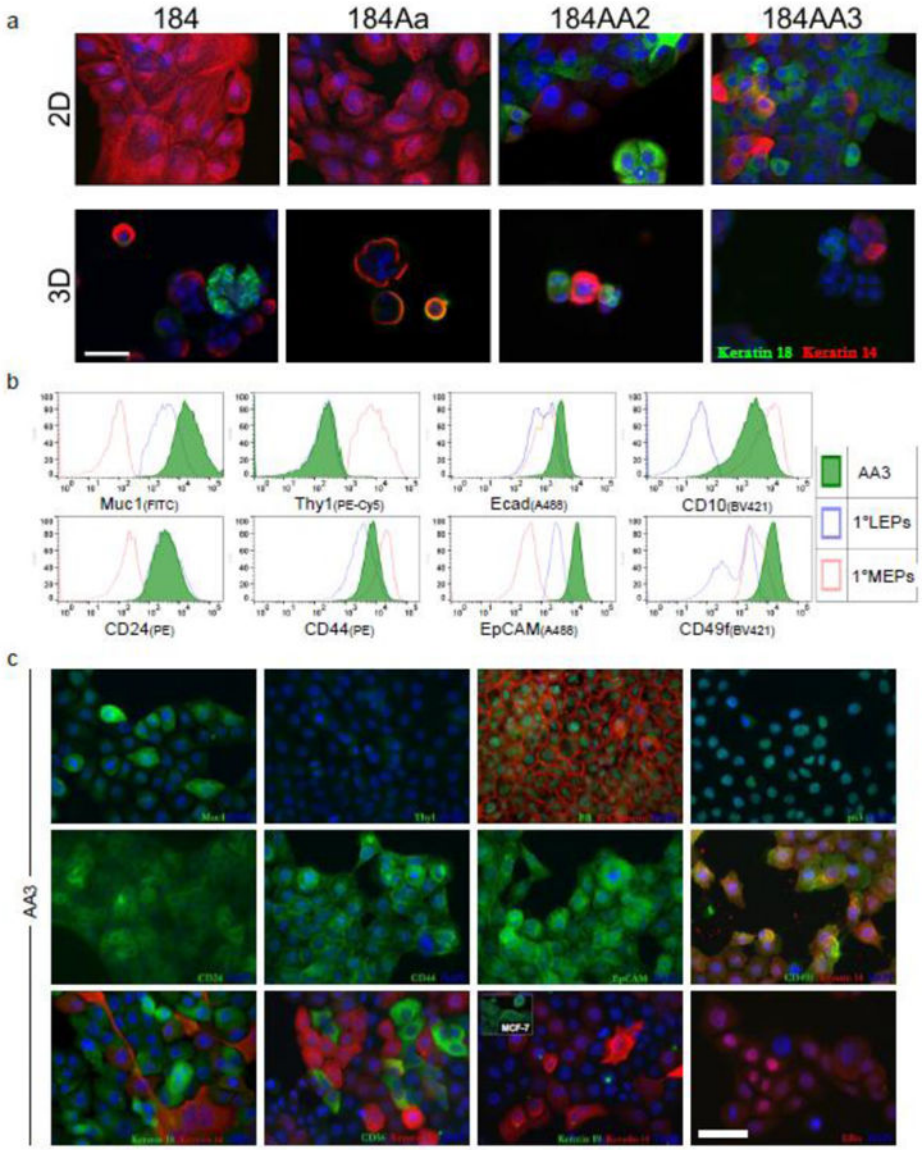

Figure 3. 184AA3 and 184 progression series characterization *in culture*

(a) Keratin 14 and 18 immunostaining of cells within the 184 progression series. Shown are the 184 primary culture (passage 4); 184Aa precursor line; and derivative sister lines 184AA2 and 184AA3, cultured on 2D substratum *(a, top)* and in 3D matrigel *(a, bottom)*; scale bar = 50μm *(b)* Flow cytometry analysis of 184AA3 cells stained with the indicated conjugated antibodies (green-filled histogram plots). Primary luminal (LEPs, blue) and myoepithelial cells (MEPs, red) from reduction mammoplasty organoids serve as reference controls. *(c)* Immunostained 2D cultures of 184AA3 cells; scale bar = 50 μm.

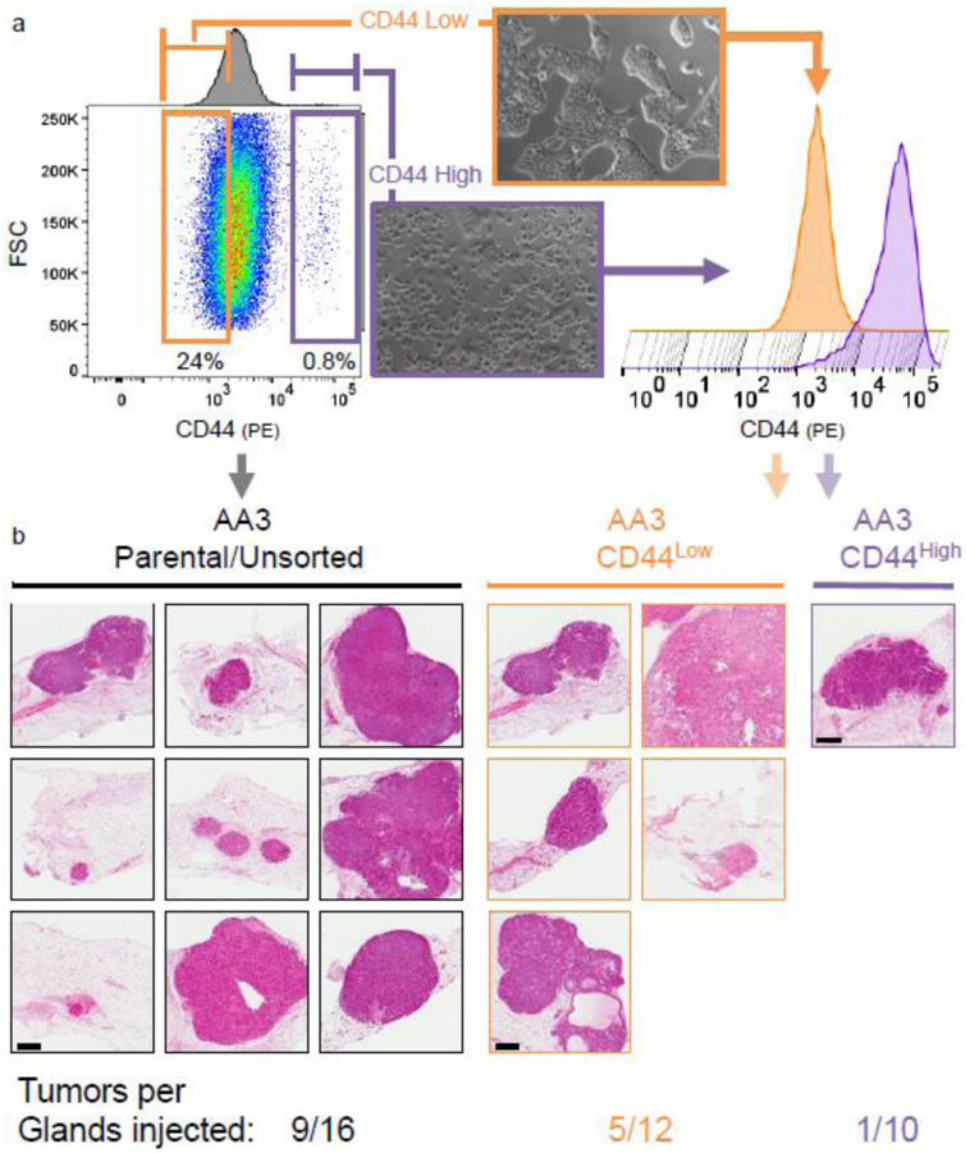

Figure 4. Tumor initiation and culture phenotypes of 184AA3 CD44 subpopulations

(a, *left*) 2D cultures of 184AA3 stained with phycoerythrin (PE) conjugated CD44 antibody and analyzed by flow cytometry. A discreet subpopulation, characterized by their elevated CD44 expression is present. Sorting gates were placed around this 'CD44 High' subpopulation (*purple*) and also around the lowest quartile of CD44 expressing cells, 'CD44 Low' (*orange*). (a, *middle*) morphologies of the FACS sorted cell populations in culture. (a, *histograms on right*) After expansion in culture for 49 days, and immediately prior to NSG xenograft implantation, CD44 expression in the $CD44^{High}$ and $CD44^{low}$ 184AA3 strains was evaluated by flow cytometry. *(b)* H&E sections of derived xenografts from injections of the unsorted parental 184AA3 culture and the $CD44^{Low}$ and $CD44^{High}$ 184AA3 strains, which respectively formed tumors in 9/16 (56%), 5/12(42%), and 1/10(10%) glands. scale bar = 600 μm

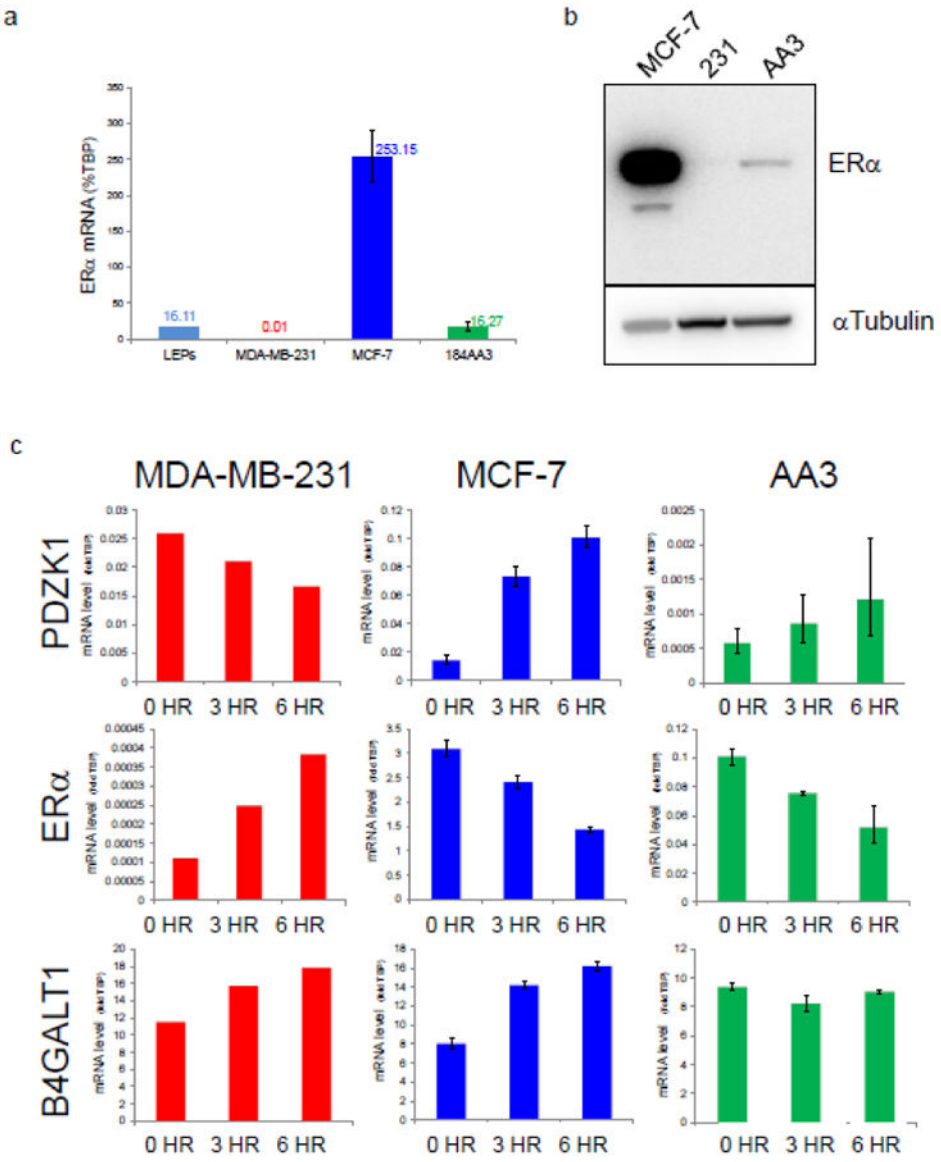

Figure 5. ER expression and functionality in 184AA3 cells

(a) transcript levels of ERα, as measured by qRT-PCR. Values are expressed relative to the internal control gene, TATA box-binding protein (TBP). 2D cultured MCF-7 and MDA-MB-231 breast cancer cell lines, and freshly sorted 'luminal' cells from normal tissue, serve as reference controls. *(b, top)* ERα protein levels in 184AA3, as measured by Western blot. The 66kDa canonical isoform is visible in all three cell lines; the 46kDa isoform is detected in MCF-7 only. *(b, bottom)* αTubulin loading control. *(c)* Gene expression changes resulting from 3-hour and 6-hour estradiol stimulation of 184AA3 and reference cell lines MDA-MB-231 and MCF-7. Transcript levels of PDZK1, ERα, and B4GALT were measured by qRT-PCR and are expressed as fold differences relative to TBP internal control gene.

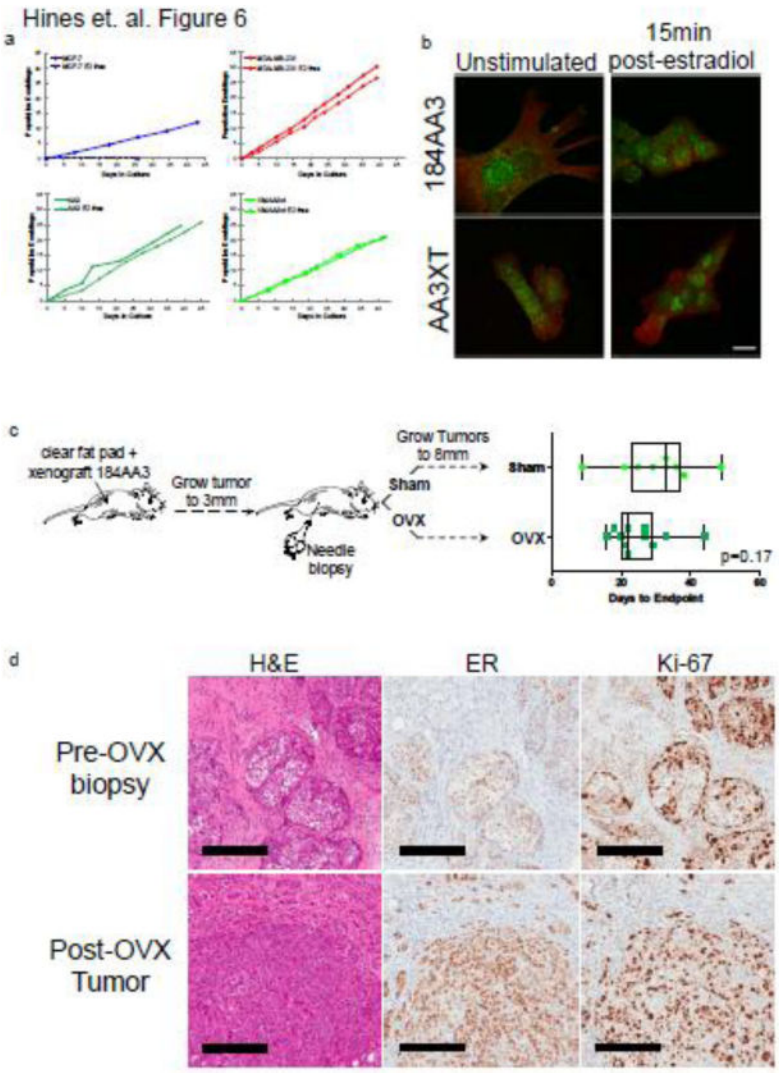

Figure 6. 184AA3 estrogen-independent growth

(a) Growth rates of MCF-7 (blue), MDA-MB-231(red), 184AA3 (dark green) and 184AA3XT (light green) cells cultured in standard medium (solid lines) or in estrogen-free medium (dashed lines). *(b)* ER translocation in 184AA3 and 184AA3XT. Cultures were exposed to estradiol for 15 minutes and then fixed and stained for ER. Scale bar = 10μm *(b)* Effect of ovary removal on 184AA3 tumor growth. 184AA3 cells were xenografted and allowed to grow to 3mm, at which time the tumor was biopsied and mice either ovariectomized or given a sham surgery. After recovery, the mice were monitored until tumors reached 8mm diameter. *(graph on right)* Time taken for tumors to reach the 8mm endpoint (from the time of biopsy, dichotomized by experimental group). There is not sufficient evidence to reject the claim that growth rates between the ovariectomized and sham mice are equivalent (p=0.17, Wilcoxon rank-sum test); it appears the ovaries, and thus ovarian hormones, do not affect 184AA3 tumor growth. *(d)* H&E staining, and ER & Ki-67 immunostained sections of a tumor-biopsy before (Pre-OVX) and 1 week after ovariectomy (Post-OVX tumor). Scale bar = 200μm.

Nuclear repartitioning of galectin-1 by an extracellular glycan switch regulates mammary morphogenesis

Ramray Bhat[a,1,2,3], Brian Belardi[b,1], Hidetoshi Mori[a,c], Peiwen Kuo[d], Andrew Tam[a], William C. Hines[a], Quynh-Thu Le[d], Carolyn R. Bertozzi[e,f,2], and Mina J. Bissell[a,2]

[a]Life Sciences Division, Lawrence Berkeley National Laboratory, Berkeley, CA, 94720; [b]Department of Chemistry, University of California, Berkeley, CA 94720; [c]Department of Pathology, Center for Comparative Medicine, University of California, Davis, CA, 95616; [d]Department of Radiation Oncology, Stanford University School of Medicine, Stanford, CA, 94305; [e]Department of Chemistry, Stanford University, Stanford, CA 94305-4401; and [f]Howard Hughes Medical Institute, Stanford University, Stanford, CA 94305-4401

Co-Contributed by Mina J. Bissell and Carolyn R. Bertozzi, June 16, 2016 (sent for review April 6, 2016; reviewed by Linda G. Baum and Andrew J. Ewald)

Branching morphogenesis in the mammary gland is achieved by the migration of epithelial cells through a microenvironment consisting of stromal cells and extracellular matrix (ECM). Here we show that galectin-1 (Gal-1), an endogenous lectin that recognizes glycans bearing *N*-acetyllactosamine (LacNAc) epitopes, induces branching migration of mammary epithelia in vivo, ex vivo, and in 3D organotypic cultures. Surprisingly, Gal-1's effects on mammary patterning were independent of its glycan-binding ability and instead required localization within the nuclei of mammary epithelia. Nuclear translocation of Gal-1, in turn, was regulated by discrete cell-surface glycans restricted to the front of the mammary end buds. Specifically, α2,6–sialylation of terminal LacNAc residues in the end buds masked Gal-1 ligands, thereby liberating the protein for nuclear translocation. Within mammary epithelia, Gal-1 localized within nuclear Gemini bodies and drove epithelial invasiveness. Conversely, unsialylated LacNAc glycans, enriched in the epithelial ducts, sequestered Gal-1 in the extracellular environment, ultimately attenuating invasive potential. We also found that malignant breast cells possess higher levels of nuclear Gal-1 and α2,6–SA and lower levels of LacNAc than nonmalignant cells in culture and in vivo and that nuclear localization of Gal-1 promotes a transformed phenotype. Our findings suggest that differential glycosylation at the level of tissue microanatomy regulates the nuclear function of Gal-1 in the context of mammary gland morphogenesis and in cancer progression.

galectin-1 | sialic acid | mammary gland | breast cancer | glycobiology

Transmission of information between neighboring cells and their tissue microenvironment is essential for organ morphogenesis and homeostasis. The process of transmission can be spatially separated into an extracellular component, which includes cell–ECM adhesion and soluble ligand binding, and an intracellular component, encompassing phosphorylation networks and transcription programs. This strict division is spanned by transmembrane proteins that relay molecular and mechanical cues through both outside-in and inside-out mechanisms. Recently, a growing number of proteins with distinct functions inside and outside cells have been recognized to subvert this conventional mode of cellular communication via alternative secretion (1). Noncanonically secreted proteins can potentially integrate intracellular and extracellular information, in effect influencing tissue specificity and organogenesis (2).

Galectin-1 (Gal-1), a soluble lectin, lacks a signal peptide but is secreted to the extracellular environment through unconventional transport. Outside the cell, Gal-1 interacts with glycoconjugates, modulating their surface organization and mediating cell–cell and cell–ECM contact (3–5). Within the cell, Gal-1 is found in the cytosol and nucleus, where it has been proposed to play roles in signaling (6) and transcription (7, 8), respectively, that are unrelated to glycan-binding activity (9). To date, no connection has been made between the distinct functions of Gal-1 in different subcellular contexts.

We and others have shown that tissue architecture is a dominant regulator of cancer cell phenotype (10–12). Although glycomic changes such as hypersialylation have long been shown to correlate with cancer cell metastasis (13), how glycans and lectins mechanistically drive the invasive processes during cancer progression remains obscure. Gal-1 is up-regulated in invasive breast cancer (14), which involves epithelial proliferation accompanied by a radical alteration in glandular architecture (10). Normal mammary epithelia also proliferate and migrate within their surrounding stroma during the branching stage of glandular development, albeit in a more controlled manner relative to their transformed counterparts. Accordingly, we sought to determine whether Gal-1 levels are also modulated in this developmental process.

In this paper, we demonstrate that endogenous Gal-1 induces branching of mammary epithelia. By engineering the localization of Gal-1 and the glycan microenvironment in 3D, we show that Gal-1's function in the mammary gland requires nuclear localization, which in turn is regulated by the glycomic signatures of the epithelial microenvironment. Our findings indicate that Gal-1 can directly transmit glycan-encoded information of its surroundings to the nucleus, where it assists in executing a branching

Significance

Malignant cells of breast carcinoma and nonmalignant epithelia of branching mammary glands share the ability to migrate through their surroundings. To form the mammary tree-like architecture, nonmalignant epithelia must migrate in a controlled fashion, integrating cues from their microenvironment, notably, the glycan appendages on extracellular proteins and lipids. Here, we show that Galectin-1, a glycan-binding protein, is able to sense glycan signatures on mammary gland epithelia, transmit this information to epithelial nuclei by direct translocation, and drive branching migration. Nuclear galectin-1 is regulated by the relative levels of α2,6–sialic acids and *N*-acetyllactosamine on extracellular glycans. Similar lectin–glycan signatures were observed in malignant breast cells and suggest cancer cells use this pathway during their invasion.

Author contributions: R.B., B.B., H.M., P.K., Q.-T.L., C.R.B., and M.J.B. designed research; R.B., B.B., and A.T. performed research; P.K., W.C.H., Q.-T.L., C.R.B., and M.J.B. contributed new reagents/analytic tools; R.B., B.B., H.M., A.T., W.C.H., C.R.B., and M.J.B. analyzed data; and R.B., B.B., H.M., P.K., A.T., W.C.H., Q.-T.L., C.R.B., and M.J.B. wrote the paper.

Reviewers: L.G.B., University of California, Los Angeles; and A.J.E., Johns Hopkins University.

The authors declare no conflict of interest.

[1]R.B. and B.B. contributed equally to this work.

[2]To whom correspondence may be addressed. Email: ramray@mrdg.iisc.ernet.in, bertozzi@stanford.edu, or mjbissell@lbl.gov.

[3]Present address: Department of Molecular Reproduction, Development and Genetics, Indian Institute of Science, Bangalore 560012, India.

This article contains supporting information online at www.pnas.org/lookup/suppl/doi:10.1073/pnas.1609135113/-/DCSupplemental.

program. We also confirm our results in transformed breast cells and argue that the spatiotemporal signatures of cell-surface glycans can play crucial and analogous roles in glandular ontogeny and oncogeny.

Results and Discussion

Using immunofluorescence, we assayed for Gal-1 protein in murine mammary glands at distinct stages of development. Gal-1 levels were found to be highest during the early stages of branching morphogenesis (5 wk; 35 d postpartum) (Fig. 1*A* and *SI Appendix*, Fig. S1 show low to moderate levels of Gal-1 at other developmental stages of the mammary gland). Within the glands of 5-wk old mice, Gal-1 expression was highest in epithelial cells at the terminal end bud (TEB), which represents the invading front of the mammary arbor during the branching stage of development (Fig. 1*A*). Gal-1 levels were lower in the quiescent, noninvasive epithelia of mammary ducts even at this stage. Unexpectedly, we found a major difference in Gal-1's subcellular localization in the two microenvironments: high levels of Gal-1 were observed within the nuclei of end-bud epithelia, whereas, in the ductal cells, Gal-1 was largely depleted from their nuclei (Fig. 1*B*).

Culturing primary mammary cells ex vivo within 3D Type-1 collagen (CL-1) scaffolds is an organotypic assay well suited to delineate the roles of proteins expressed predominantly within glandular epithelia during branching and polarization (15). We performed shRNA-based lentiviral knockdown of Gal-1 within organoids from wild-type C57BL/6 and Balb/C mice. In addition, we compared branching in organoids from *Gal-1*$^{-/-}$ mice with their wild-type counterparts. In both cases, knockdown and knockout, we found a significant decrease in branching (Fig. 1 *C–E*). We also observed a significant decrease in branch-point number in carmine-stained mammary glands from 35 d postpartum *Gal-1*$^{-/-}$ mice compared with wild-type controls (*SI Appendix*, Fig. S2). The branching defect was less pronounced in vivo than in ex vivo cultures, which could be explained by the fact that the loss of expression or function of a single protein, no matter how important, is often compensated by other proteins with similar biochemical function (mammals have 15 galectins) and, more importantly, by the maintenance of the architectural integrity.

We next took advantage of a different organotypic 3D culture model that relies on the mammary epithelial cell line, EpH4 (16–19), which is more amenable to genetic manipulations. This culture system was used to probe the influence of the nuclear pool of Gal-1 on epithelial migration and branching. Upon addition of epidermal growth factor, EpH4 cells embedded in CL-1 invade into the gel and form branched structures with high levels

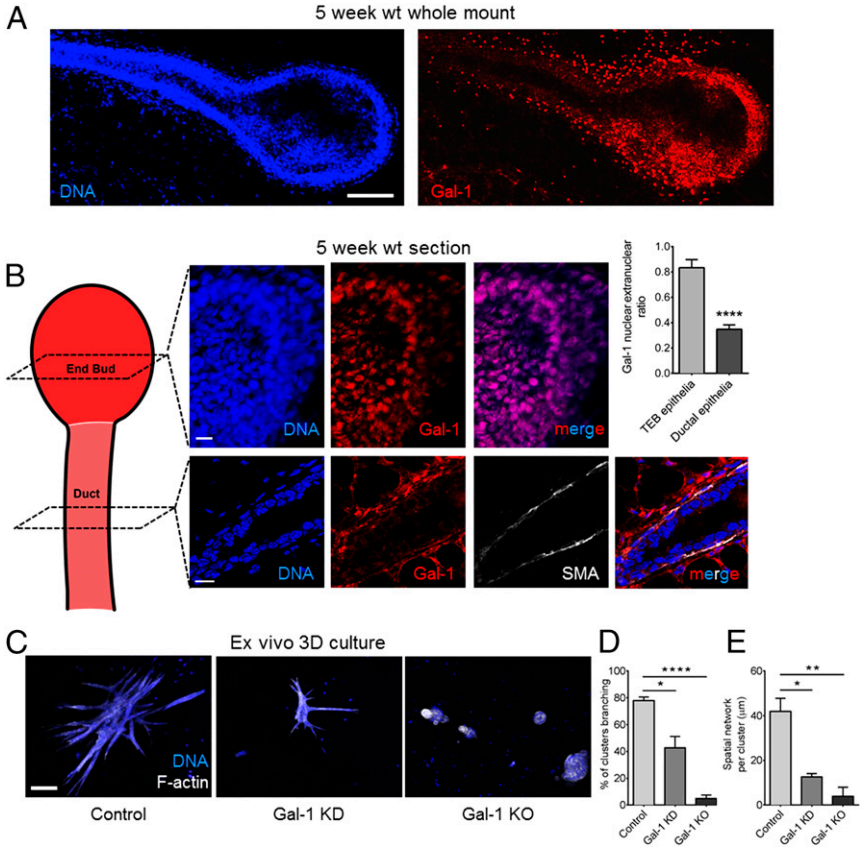

Fig. 1. Gal-1 is essential for mammary branching morphogenesis. (*A*) Immunofluorescence micrographs of a 5-wk murine mammary gland stained with α-Gal-1 antibody (*Right*) and DAPI (*Left*). (See *SI Appendix*, Fig. S1 for control.) (Scale bar, 100 μm.) (*B*) In the end-bud epithelia, Gal-1 is enriched in the nucleus (*Top*), whereas Gal-1 staining in the mammary duct epithelia is mainly extranuclear (*Bottom*). Ductal epithelia were costained for α smooth muscle actin (SMA), a marker of mammary myoepithelial cells. (See *SI Appendix, SI* Materials and Methods for quantification). (Scale bar, 15 μm.) (*C*) Micrographs of organoids cultured in 3D CL-1 and stained for F-actin (depicted in white) and DNA (depicted in blue): control organoids from wild-type (WT) mice (*Left*), organoids from WT mice after Gal-1 knockdown (KD) (*Middle*), and organoids from *Gal-1*$^{-/-}$ mice (*Right*). (Scale bar, 100 μm.) (*D* and *E*) Quantification of branching clusters and spatial network per organoid shows impaired branching upon Gal-1 depletion (20 organoids analyzed per culture). Spatial network is defined as the sum of the branch lengths for each organoid or branching structure. For all bar graphs, error bars represent SEM. Statistical significance is given by $*P < 0.05$; $**P < 0.01$; $****P < 0.0001$.

of Gal-1 in the extensions, similar to primary mammary epithelia grown ex vivo (*SI Appendix*, Fig. S3). Depletion of Gal-1 by shRNA (*SI Appendix*, Fig. S4 *A* and *B*) abrogated branching in 3D cultures (Fig. 2*A*). We rescued the invasive phenotype by adding recombinant human Gal-1 (GAL-1) to EpH4 cells (Fig. 2 *E*–*G*). To probe the effect of Gal-1 subcellular localization on phenotypic rescue, we overexpressed GAL-1 constructs tagged either with a nuclear localization or a nuclear export signal (NLS and NES, respectively; *SI Appendix*, Fig. S5 *A* and *B*). Whereas nuclear resident NLS–GAL-1 rescued branching (Fig. 2 *A*–*C* and *SI Appendix*, Fig. S5*C* for control), cytoplasmic NES–GAL-1 did not (Fig. 2 *A*–*C* and *SI Appendix*, Fig. S5*C* for control).

Endogenous Gal-1 is known to translocate to the extracellular space through unconventional secretion (2, 20). We wondered whether, once extracellular, Gal-1 could traffic back to the nucleus and exert its influence on mammary migration. To address this, we designed a GAL-1 construct bearing a secretion signal peptide (SEC–GAL-1) that should transit to the extracellular space through the classical secretory pathway and, once there, be poised to reenter the cell through Gal-1–dependent uptake. Indeed, overexpressed SEC–GAL-1 was secreted and was able to relocalize to the nucleus and rescue branching (Fig. 2*D*; see *SI Appendix*, Fig. S5 for control and *SI Appendix*, Fig. S6 for nuclear accumulation of SEC–GAL-1 in NLS–mCherry-expressing EpH4 cells). In addition, recombinant Gal-1 added exogenously to mammary cells in 3D culture was detected in nuclei as well as other compartments (*SI Appendix*, Fig. S5*D*). Although these experiments do not suggest a mechanism of Gal-1 reentry into the cell, there are many possible routes by which Gal-1 could traverse the cell membrane. For instance, internalization of Gal-1 by endocytosis, similar to Gal-3 (21), or by flippase activity of glycolipid–Gal-1 complexes (22) are possible candidates for lectin translocation. Collectively, these data suggest that nuclear Gal-1 is necessary for migration and branching and that Gal-1 is able to translocate from the extracellular space to the nucleus.

To pinpoint the microenvironmental context in which Gal-1 localizes to the epithelial nucleus, we cultured EpH4 cells (*i*) in 2D, (*ii*) on CL-1 gels, and (*iii*) on laminin-rich ECM (lrECM) (Fig. 3*A*). In this experiment, CL-1 and lrECM gels approximate an in vivo branching and ductal microenvironment, respectively. In both 2D and on lrECM, where cells form a lumen-containing acinar-like structure, the epithelial nuclei showed sparse Gal-1, whereas, on top of CL-1, mammary epithelia displayed high nuclear Gal-1 levels. Therefore, Gal-1 nuclear localization strongly correlates with a microenvironmental context that is associated with

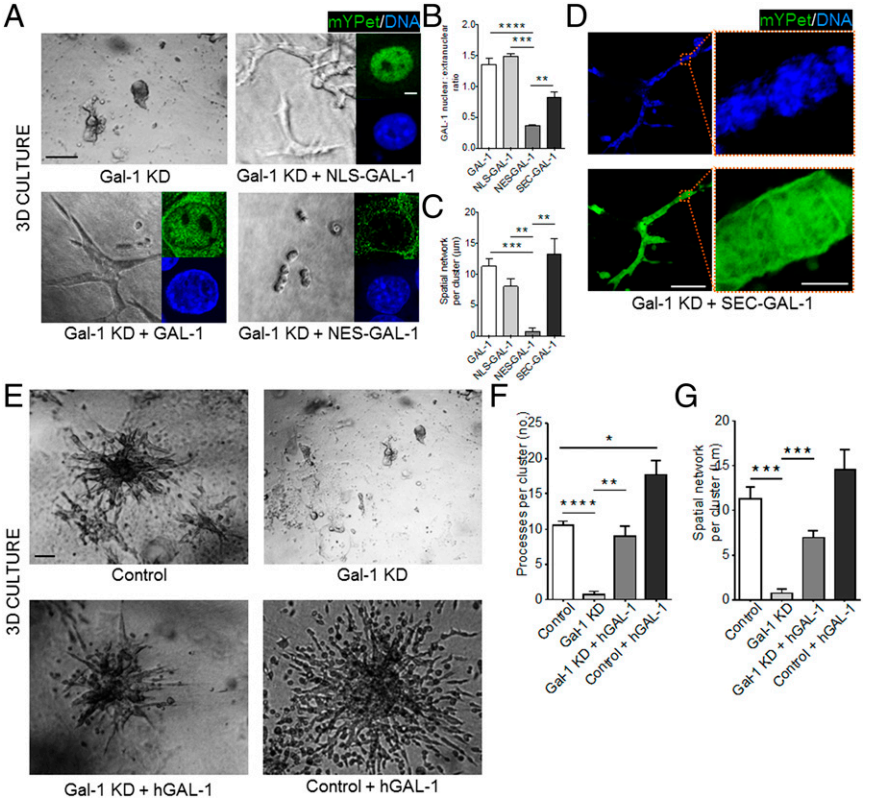

Fig. 2. Nuclear Gal-1 drives mammary epithelial branching and migration in 3D. (*A*) Gal-1 KD EpH4 cells (*Top*, *Left*) ectopically expressing either NLS–GAL-1 (*Top*, *Right*), GAL-1 (*Bottom*, *Left*), or NES–GAL-1 (*Bottom*, *Right*) were cultured in 3D CL-1 gels. Branching was observed only upon expression of GAL-1 or NLS–GAL-1. (Scale bar, 50 μm.) (*Inset*) Fluorescence micrographs indicate the subcellular localization of each mYPet fusion construct [DNA (blue) and mYPet (green)] (see *SI Appendix*, Fig. S5 for construct map and construct controls). (Scale bar, 5 μm.) (*B*) Quantification of GAL-1 nuclear:extranuclear ratio for each of the GAL-1 constructs. (*C*) Quantification of the spatial network per cluster for each of the GAL-1 constructs in 3D (20 clusters analyzed per culture). (*D*) Gal-1 KD EpH4 cells ectopically expressing SEC–GAL-1 branch when cultured in a 3D CL-1 gel (*Left*). (Scale bar, 100 μm.) mYPet fluorescence of SEC–GAL-1 fusion construct is distributed between the extracellular space and the nucleus (*Right*) (see *SI Appendix*, Fig. S5 for construct map and construct controls). (Scale bar, 10 μm.) (*E*) Brightfield micrographs of EpH4 cells (*Top*, *Left*) with Gal-1 KD (*Top*, *Right*), with Gal-1 KD and treatment with recombinant human GAL-1 (*Bottom*, *Left*), and with recombinant human GAL-1 (*Bottom*, *Right*) cultured in 3D CL-1 gels. (Scale bar, 50 μm.) (*F* and *G*) Quantification of the number of processes per branching cluster and the spatial network of each cluster upon endogenous Gal-1 KD and/or treatment with recombinant human GAL-1. For all bar graphs, error bars represent S.E.M. Statistical significance is given by $*P < 0.05$; $**P < 0.01$; $***P < 0.001$; $****P < 0.0001$.

invasive epithelia, i.e., TEB epithelia, and not their quiescent counterparts, i.e., ductal epithelia.

Galectin–glycan binding has previously been reported to influence cell invasion and migration (23). We investigated whether mammary epithelial morphogenesis also requires this activity using a GAL-1 mutant, N46D, which attenuates glycan binding (24). Overexpression of GAL-1 (N46D) in Gal-1–silenced EpH4 cells rescued the branching phenotype in 3D culture similar to wild-type GAL-1 (Fig. 3*B*). Thus, nuclear Gal-1's ability to drive morphogenesis is independent of its sugar-binding activity. Interestingly, GAL-1 (N46D) showed a greater degree of nuclear localization than wild-type Gal-1 when expressed in cells cultured in 2D (Fig. 3*C*).

Our observation above prompted us to consider whether Gal-1's glycan-binding activity might regulate the protein's function by altering its distribution between the nucleus and extracellular microenvironment. To test this idea, we reengineered the microenvironment of the mammary epithelia by adding glycopolymers that mimic ECM glycoproteins to the exterior of the cells (25). We synthesized glycopolymers (GPs) functionalized with multiple Gal-1 ligands (lactose) or control glycan structures (cellobiose) that do not associate with Gal-1. When lactose–GP was added to mammary epithelial cells cultured on top of CL-1 gels, we found a marked decrease in nuclear Gal-1 after 1 d (Fig. 4*A*). In contrast, untreated cells and cells treated with cellobiose–GP showed higher nuclear levels of Gal-1. When added to 3D CL-1 cultures, lactose–GP abrogated branching (Fig. 4*B*). After washing lactose–GP-treated cells, nuclear Gal-1 was undetectable, suggesting that the glycopolymer redistributed Gal-1 to the extracellular space. In contrast, Gal-1 staining was unaltered in branching cultures of cells treated with cellobiose–GP. Similar results were obtained with glycopolymer treatment of EpH4 Gal-1 knockdown cells overexpressing fluorescent GAL-1 fusion protein (*SI Appendix*, Fig. S7).

Our data therefore point to a dynamic reciprocity between the glycan microenvironment and nuclear Gal-1 levels (Fig. 4*C*). When *N*-acetyllactosamine (LacNAc) epitopes are abundant in the extracellular environment, Gal-1's distribution reequilibrates in that direction. In this model, extracellular glycans act as a molecular sink, trapping Gal-1. On the other hand, when Gal-1 is unable to bind extracellular glycan ligands, e.g., GAL-1 (N46D), the partition shifts to a higher abundance of nuclear Gal-1, promoting epithelial invasiveness.

To determine whether this mechanism operates during mammary branching morphogenesis in vivo, fixed mammary gland whole mounts from 35 d postpartum C57BL/6 mice were stained for terminal LacNAc residues using FITC–*Erythrina Crystagalli* lectin (ECL) (26). Fluorescence micrographs revealed strong levels of extracellular LacNAc in ductal regions and relatively sparse levels in TEB epithelia (Fig. 4*D*). Sections of 35-d postpartum mammary gland ducts stained for LacNAc showed strong colocalization with the basement membrane and low levels of extracellular Gal-1 (*SI Appendix*, Fig. S8).

The addition of α2,6–sialic acid (α2,6–SA) residues is known to block Gal-1's binding to LacNAc epitopes (27, 28). To test the effects of sialylation on Gal-1 nuclear localization and mammary branching, we elevated sialoside levels by exogenous addition of peracetylated *N*-acetylmannosamine (Ac_4ManNAc) (29), a metabolic precursor of sialic acid, or by overexpression of UDP–*N*-acetylglucosamine 2-epimerase/*N*-acetylmannosamine kinase (GNE), the rate-limiting enzyme in sialic acid synthesis (*SI Appendix*, Fig. S9 *A–C*) (30). Both approaches led to an increase in α2,6–SA epitopes, as measured by staining with *Sambucus nigra* agglutinin (SNA) (30), as well as an increase in nuclear Gal-1 levels (*SI Appendix*, Fig. S9 *A–C*). shRNA-mediated depletion of GNE in EpH4 cells caused a decrease in branching (*SI Appendix*, Fig. S9*D*). To specifically test the role of α2,6–SA regiochemistry, we either knocked down or overexpressed β-galactoside α2,6–sialyltranferase 1 (ST6Gal1) in EpH4 cells (*SI Appendix*, Fig. S9*E*). We observed lower levels of nuclear Gal-1 in ST6Gal1–knockdown cells and higher levels of nuclear Gal-1 in cells overexpressing ST6GAL1, relative to control cells (Fig. 5*A*). Finally, EpH4 cells depleted in ST6Gal1 and those overexpressing ST6GAL1 showed attenuated and exacerbated branching

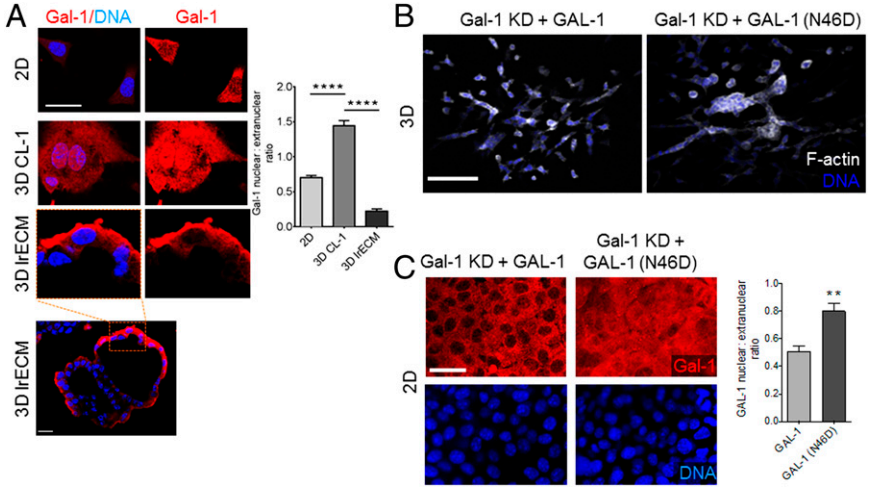

Fig. 3. Glycan recognition by Gal-1 is dispensable for epithelial branching. (*A*) Immunofluorescence micrographs of EpH4 cells cultured in 2D (*Top*), on top of 3D CL-I gel (*Middle*), and on top of 3D lrECM gel (*Bottom Left*: acinar-like architecture with lumen. Scale bar, 20 μm) and stained for Gal-1 (depicted in red) and DNA (depicted in blue). Quantification of Gal-1 nuclear:extranuclear ratio for EpH4 cells cultured in 2D and 3D conditions. (Scale bar, 25 μm.) (*B* and *C*) Fluorescence micrographs of Gal-1 KD EpH4 cells ectopically expressing GAL-1 (*Left*) or GAL-1 (N46D) (*Right*) fusion proteins in 3D (*Top*) or 2D (*Bottom*) and stained for F-actin (depicted in white) and DNA (depicted in blue). Cells expressing GAL-1 (N46D), a mutant with attenuated glycan binding, invade and branch when cultured in 3D. Quantification of GAL-1 nuclear:extranuclear ratio shows GAL-1 (N46D) is concentrated in the nucleus. (Scale bar, 100 μm.) For all bar graphs, error bars represent S.E.M. Statistical significance is given by $^{**}P < 0.01$; $^{****}P < 0.0001$.

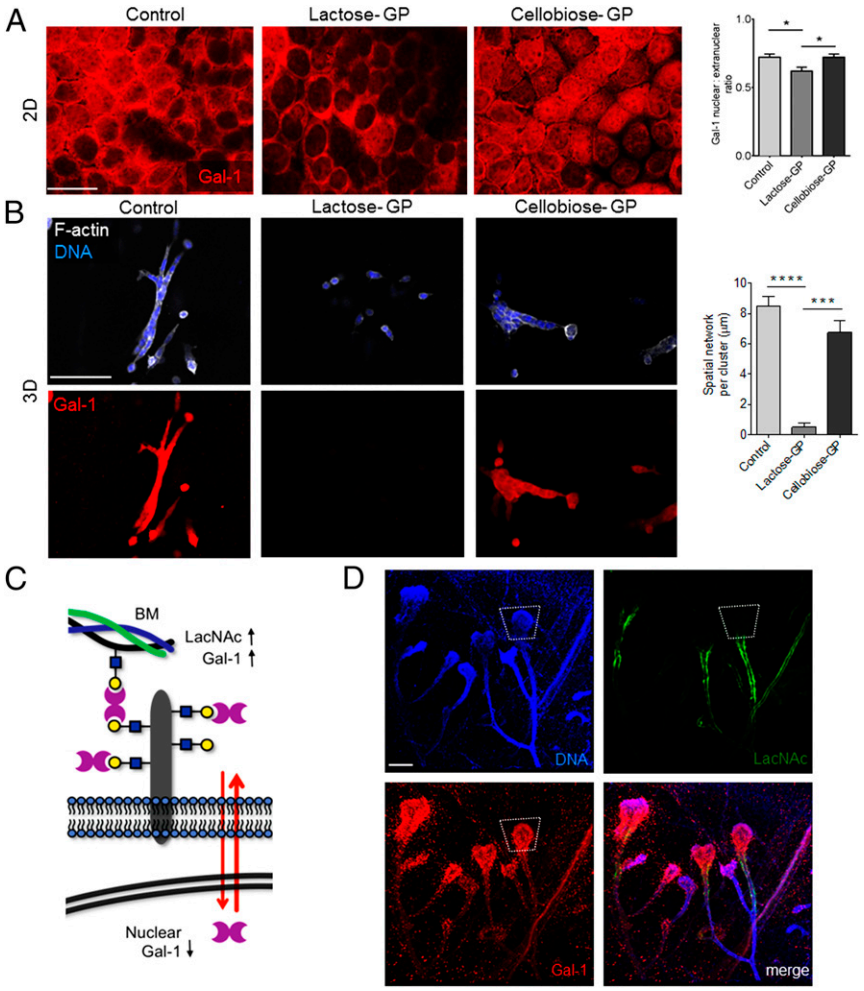

Fig. 4. Extracellular glycans control the nuclear localization of Gal-1. (*A*) Immunofluorescence micrographs of EpH4 cells grown on top of CL-1 gels treated with either soluble lactose–GP, which binds Gal-1, or soluble cellobiose–GP, which does not interact with Gal-1, and stained with an α-Gal-1 antibody (see *SI Appendix*, Fig. S7 for glycopolymer treatment on Gal-1 KD EpH4 cells overexpressing full-length GAL-1). Quantification of the Gal-1 nuclear:extranuclear ratio for EpH4 cells treated with either the lactose–GP or the cellobiose–GP. (Scale bar, 50 μm.) (*B*) Immunofluoresence micrographs of EpH4 cells cultured in 3D CL-1 gel in the presence or absence of either lactose–GP or cellobiose–GP and then washed and stained for F-actin and with DAPI and an α-Gal-1 antibody. Quantification of the spatial network per cluster of EpH4 cells in the presence or absence of GPs. (Scale bar, 100 μm.) (*C*) Model of extracellular glycan patterns regulating nuclear Gal-1 in mammary epithelial cells. In a LacNAc-rich environment containing intact ECM proteins, Gal-1 is mainly concentrated in the extracellular space. (*D*) Immunofluorescence micrographs of murine mammary gland stained with *Erythrina Crystagalli* lectin (ECL) (*Top*, *Right*), which is specific for terminal LacNAc disaccharides, an α-Gal-1 antibody (*Bottom*, *Left*), and DAPI (*Top*, *Left*). LacNAc appears to line the ductal epithelia, whereas Gal-1 is heavily concentrated in the invasive end bud. (*SI Appendix*, Fig. S8 shows colocalization of LacNAc residues and laminin on the surface of ductal epithelia). (Scale bar, 150 μm.) For all bar graphs, error bars represent S.E.M. Statistical significance is given by $*P < 0.05$; $**P < 0.01$; $***P < 0.001$; $****P < 0.0001$.

morphogenesis relative to their control counterparts, respectively (Fig. 5*B*).

Within the whole mounts, α2,6–SA epitopes were enriched at the end buds and absent in the ducts (Fig. 5*D*). These results suggest that LacNAc residues on invading mammary epithelia are capped by α2,6–SA, which negatively regulates binding to Gal-1 (31). Notably, the transcript levels for ST6Gal1, an enzyme that adds α2,6–SA to terminal LacNAc residue, have previously been found to be higher in terminal end buds compared with ductal epithelia (32).

We conclude from the above data that mammary epithelial branching morphogenesis is driven by the dynamics of Gal-1 subcellular localization, which in turn is a sensor of the glycan signature in the epithelial microenvironment. LacNAc, the cognate glycan ligand for Gal-1, acts as a sink to retain Gal-1 in the extracellular milieu. We found high levels of unmodified LacNAc and low nuclear Gal-1 levels in the quiescent ductal epithelia of mammary glands and, reciprocally, extracellular α2,6–SA and nuclear Gal-1 were abundant in the proliferating epithelia at the invading edge of mammary end buds (Fig. 5*C*). Thus, α2,6–sialylation acts as a switch to potentiate Gal-1–mediated mammary morphogenesis.

The molecular mechanism(s) by which nuclear Gal-1 promotes branching and invasion is an intriguing question. In vitro studies have shown that nuclear Gal-1 is involved in pre-mRNA splicing and coexists in a complex with Gemin-4 (7). In accordance with these findings, we observed that Gal-1 localizes to the Gemini bodies of mammary epithelia (*SI Appendix*, Fig. S10*A*), indicating that it may be part of the Gemin-4–containing transcription-regulating complexes (33). shRNA knockdown of Gemin-4 in mammary epithelia (*SI Appendix*, Fig. S10*B*) also abrogated branching. The cells remained alive and formed noninvasive

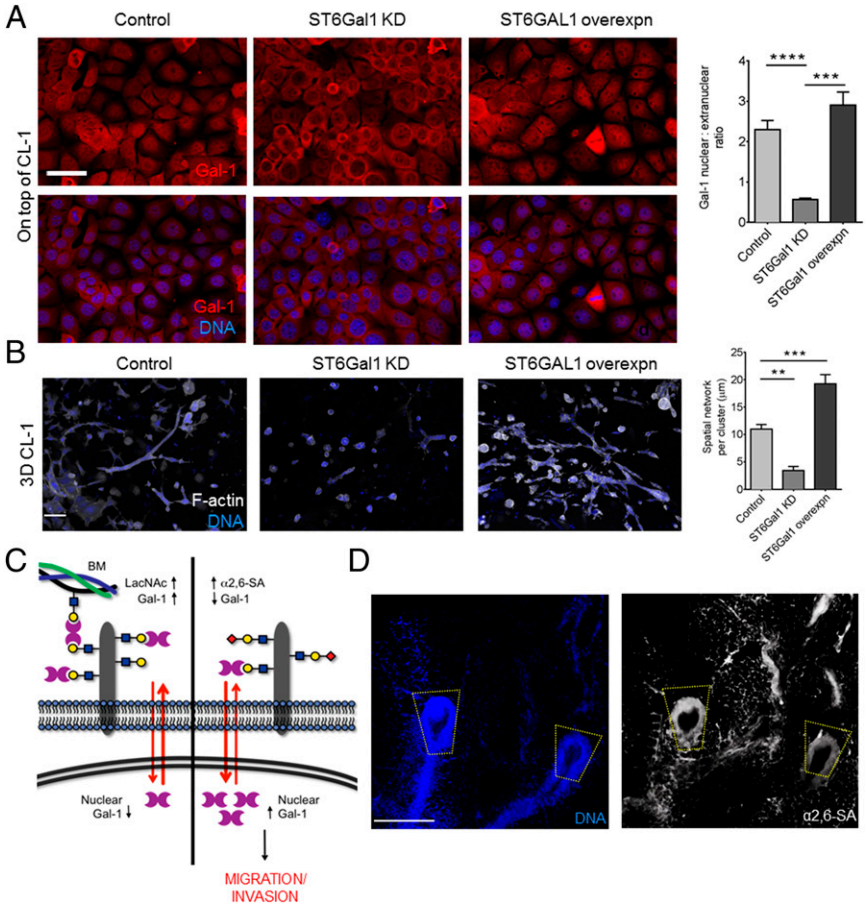

Fig. 5. α2,6–SA regulates Gal-1's nuclear abundance and induction of mammary epithelial morphogenesis. (*A*) Fluorescence micrographs of EpH4 cells cultured on top of CL-1 and stained for Gal-1 (red) and DNA (blue): wild-type cells (*Left*), cells with ST6Gal1 knockdown (*Middle*), and cells overexpressing ST6GAL1 (*Right*) (see *SI Appendix*, Fig. S9*E* Extended Data Fig 9e for α2,6–SA levels of EpH4 cells with ST6Gal1 depletion and overexpression). Quantification of Gal-1 nuclear:extranuclear ratio of EpH4 cells with varying levels of ST6Gal1. (Scale bar, 25 μm.) (*B*) Fluorescence micrographs of EpH4 cells cultured in 3D within CL-1 gels and stained for F-actin (depicted in white) and DNA (depicted in blue): wild-type cells (*Left*), cells with ST6Gal-1 knockdown (*Middle*), and cells overexpressing ST6Gal-1 (*Right*). Quantification of the spatial network per cluster of EpH4 cells with varying levels of ST6Gal1 (50 clusters counted per culture). (Scale bar, 25 μm.) (*C*) Complete model of glycan signatures regulating nuclear Gal-1 in mammary epithelial cells. α2,6–sialylation of LacNAc structures causes Gal-1 to accumulate in the nucleus, resulting in an invasive phenotype (*Right*). (*D*) Fluorescence micrographs of murine mammary gland stained with SNA (*Right*; white) and DAPI (*Left*; blue) show high levels of α2,6–SA residues in the invasive end bud of the mammary gland. (Scale bar, 200 μm.) For all bar graphs, error bars represent S.E.M. Statistical significance is given by $^{**}P < 0.01$; $^{***}P < 0.001$; $^{****}P < 0.0001$.

spherical clusters, phenocopying Gal-1 depletion (*SI Appendix*, Fig. S10*C*). These data suggest that the interaction of Gemin-4 and Gal-1 within the nucleus plays a functional role in mammary epithelial morphogenesis. As well, we found that overexpression of nuclear Gal-1 leads to up-regulation in gene expression of Erk1/2 (*SI Appendix*, Fig. S11), a key signaling node in mammary gland branching (34) and possible target of transcriptional regulation.

Finally, we speculated that our findings were relevant to the acquisition of epithelial invasiveness in breast cancer. We found higher levels of nuclear Gal-1 in malignant epithelia from human invasive ductal carcinoma sections relative to nonmalignant tissues (Fig. 6 *A* and *B*). To examine if our glycan-dependent model may explain this overlooked feature of Gal-1 in breast cancer, we proceeded to stain the tissue for cognate glycan epitopes of Gal-1. We observed low levels of LacNAc and high levels of α2,6–SA in the malignant epithelia, relative to nonmalignant tissue sections (Fig. 6*C*). Other sialylated structures, such as truncated *O*-glycans like sialyl T_N or α2,3–SA on core 1, have previously been linked to breast cancer (35–38). Some of these glycans may also contribute to blocking Gal-1 binding within the malignant glycocalyx by preventing extension of *O*-glycans to terminal LacNAc repeats. The invasive lectin–glycan signatures were also observed by fluorescence in 3D cultures of malignant breast cells (T4-2) in comparison with their isogenic nonmalignant (S1) counterparts (Fig. 6*D*). Moreover, overexpression of NLS–Gal-1 in S1 cells impaired their growth-arrested basoapical polarity (Fig. 6*E*), whereas GAL-1 depletion in malignant T4-2 cells (Fig. 6*F*) arrested their growth and partially restored their polarity (Fig. 6*G*). As previously documented, invasive breast cancer cells show high levels of both Gal-1 (14, 39) and α2,6–SA (40), the modification that masks the ligand of Gal-1 and is associated with mammary epithelial invasiveness (41). Our results seem to reconcile all these observations by linking the nuclear localization of Gal-1 and its ability to induce migration to extracellular α2,6–SA. As well, our finding that Gal-1 translocates to the nucleus of malignant breast cancer cells due to hyper-α2,6–sialylation may be relevant for development of Gal-1 specific inhibitors in breast cancer treatment (42).

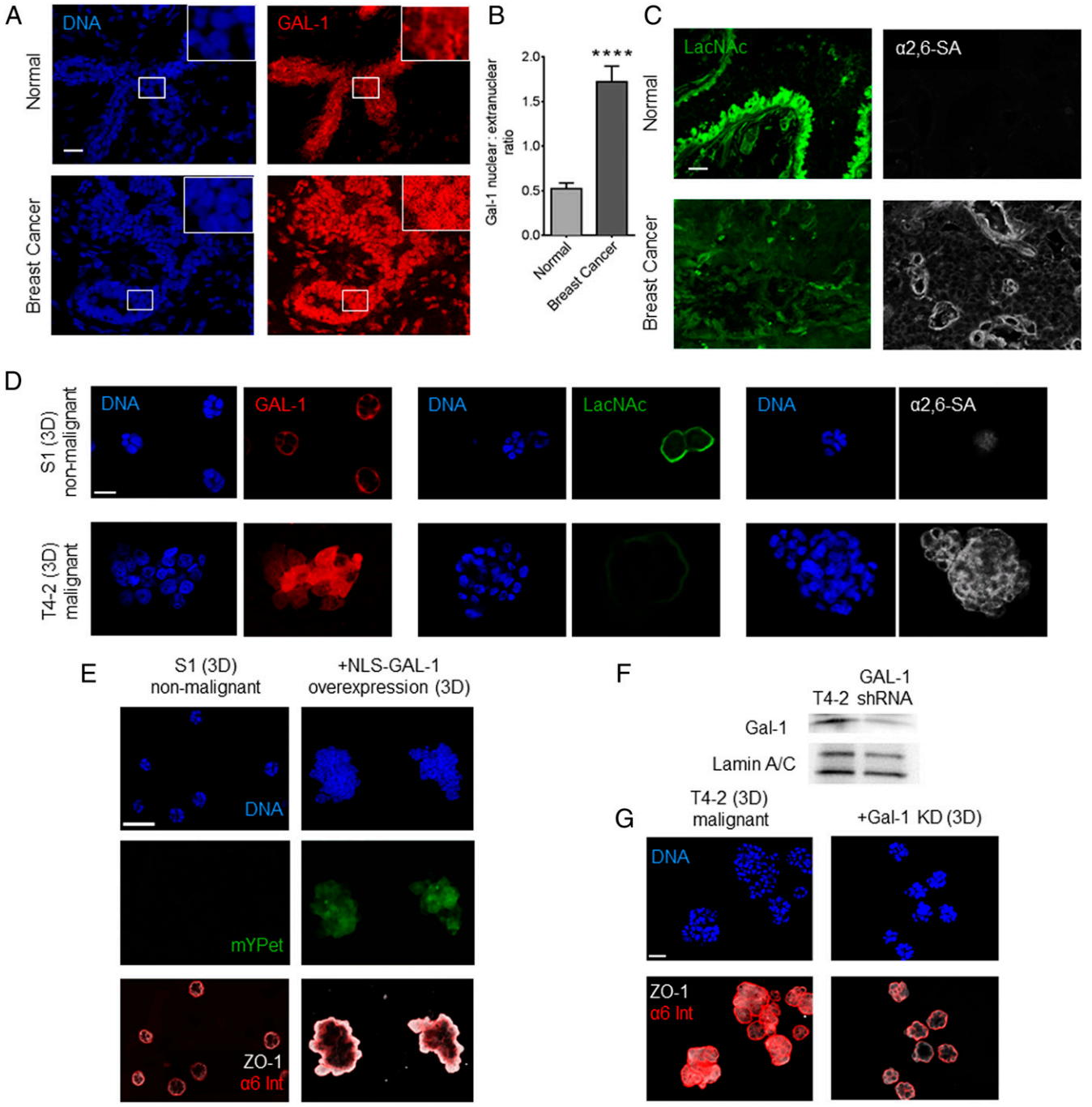

Fig. 6. Malignant breast epithelia possess high levels of nuclear Gal-1 and α2,6–SA and low levels of LacNAc. (*A*) Fluorescence micrographs of sections of normal breast tissue (*Top*) and invasive ductal carcinoma (*Bottom*). The set shows staining for Gal-1 (depicted in red) and DNA (depicted in blue) with insets highlighting single cells for subcellular staining distribution. (Scale bar, 20 μm.) (*B*) Graph showing quantification of nuclear:extranuclear ratio of Gal-1 in breast epithelia from normal and invasive ductal carcinoma tissues. (*C*) Micrographs of normal breast tissue (*Top*) and invasive ductal carcinoma (*Bottom*) showing staining for terminal LacNAc residues (depicted in green, *Left*) and α2,6–SA (depicted in white, *Right*). (Scale bar, 20 μm.) (*D*) Fluorescence micrographs of 3D cultures formed by nonmalignant S1 cells (*Top*) and isogenic malignant T4-2 cells (*Bottom*). Staining for Gal-1 (depicted in red) and DNA (depicted in blue) (*Left*). Staining for terminal LacNAc residues (depicted in green) and DNA (depicted in blue) (*Middle*). Staining for α2,6–SA (depicted in white) and DNA (depicted in blue) (*Right*). (Scale bar, 20 μm.) (*E*) Fluorescence micrographs of 3D cultures of S1 cells, wild-type (*Left*) and overexpressing NLS–GAL-1 (*Right*). S1 cells overexpressing NLS–GAL-1 show loss of growth-arrested phenotype seen in wild-type S1 cells and aberrant basoapical polarity of basal (α6 integrin; depicted in red) and apical (zonula occludens, ZO-1; depicted in white) markers. (Scale bar, 40 μm.) (*F*) Immunoblot showing levels of GAL-1 (*Top*) and Lamin A/C (internal control, *Bottom*) in T4-2 cells with and without shRNA-based knockdown. (*G*) Fluorescence micrographs of 3D cultures of T4-2 cells (*Left*) and T4-2 cells with GAL-1 knockdown (*Right*) showing a recovery of acinar phenotype and basoapical polarity upon GAL-1 knockdown. For bar graphs, error bars represent S.E.M. Statistical significance is given by $^{****}P < 0.0001$. (Scale bar, 20 μm.)

ACKNOWLEDGMENTS. We thank Jason Hudak, Chin Thi, and Angélica Maciel Gomes for helpful discussions and for critical reading of the manuscript. The work from the M.J.B. laboratory has been supported by grants from the US Department of Energy, Office of Biological and Environmental Research, and Low Dose Scientific Focus Area; by multiple grants from the National Cancer Institute; by a grant from the Breast Cancer Research

Foundation; and by two "Innovator awards" from the US Department of Defense. The work from the C.R.B. laboratory was funded by a grant from the NIH (GM059907). The work from the Q.-T.L. laboratory was supported by a grant from the NIH (R01CA161585-05). R.B. was supported by a postdoctoral fellowship from Susan G. Komen for the Cure (KG111229), and B.B. was supported by a National Science Foundation predoctoral fellowship.

1. Nickel W, Rabouille C (2009) Mechanisms of regulated unconventional protein secretion. *Nat Rev Mol Cell Biol* 10(2):148–155.
2. Radisky DC, Stallings-Mann M, Hirai Y, Bissell MJ (2009) Single proteins might have dual but related functions in intracellular and extracellular microenvironments. *Nat Rev Mol Cell Biol* 10(3):228–234.
3. Barondes SH, Cooper DN, Gitt MA, Leffler H (1994) Galectins. Structure and function of a large family of animal lectins. *J Biol Chem* 269(33):20807–20810.
4. Paulson JC, Blixt O, Collins BE (2006) Sweet spots in functional glycomics. *Nat Chem Biol* 2(5):238–248.
5. Bhat R, et al. (2011) A regulatory network of two galectins mediates the earliest steps of avian limb skeletal morphogenesis. *BMC Dev Biol* 11:6.
6. Elad-Sfadia G, Haklai R, Ballan E, Gabius HJ, Kloog Y (2002) Galectin-1 augments Ras activation and diverts Ras signals to Raf-1 at the expense of phosphoinositide 3-kinase. *J Biol Chem* 277(40):37169–37175.
7. Vyakarnam A, Dagher SF, Wang JL, Patterson RJ (1997) Evidence for a role for galectin-1 in pre-mRNA splicing. *Mol Cell Biol* 17(8):4730–4737.
8. Vyakarnam A, Lenneman AJ, Lakkides KM, Patterson RJ, Wang JL (1998) A comparative nuclear localization study of galectin-1 with other splicing components. *Exp Cell Res* 242(2):419–428.
9. Camby I, Le Mercier M, Lefranc F, Kiss R (2006) Galectin-1: A small protein with major functions. *Glycobiology* 16(11):137R–157R.
10. Beliveau A, et al. (2010) Raf-induced MMP9 disrupts tissue architecture of human breast cells in three-dimensional culture and is necessary for tumor growth in vivo. *Genes Dev* 24(24):2800–2811.
11. Bissell MJ, Kenny PA, Radisky DC (2005) Microenvironmental regulators of tissue structure and function also regulate tumor induction and progression: The role of extracellular matrix and its degrading enzymes. *Cold Spring Harb Symp Quant Biol* 70: 343–356.
12. Bissell MJ, Hines WC (2011) Why don't we get more cancer? A proposed role of the microenvironment in restraining cancer progression. *Nat Med* 17(3):320–329.
13. Narayanan S (1994) Sialic acid as a tumor marker. *Ann Clin Lab Sci* 24(4):376–384.
14. Dalotto-Moreno T, et al. (2013) Targeting galectin-1 overcomes breast cancer-associated immunosuppression and prevents metastatic disease. *Cancer Res* 73(3): 1107–1117.
15. Lo AT, Mori H, Mott J, Bissell MJ (2012) Constructing three-dimensional models to study mammary gland branching morphogenesis and functional differentiation. *J Mammary Gland Biol Neoplasia* 17(2):103–110.
16. Reichmann E, Ball R, Groner B, Friis RR (1989) New mammary epithelial and fibroblastic cell clones in coculture form structures competent to differentiate functionally. *J Cell Biol* 108(3):1127–1138.
17. Montesano R, Schaller G, Orci L (1991) Induction of epithelial tubular morphogenesis in vitro by fibroblast-derived soluble factors. *Cell* 66(4):697–711.
18. Hirai Y, et al. (1998) Epimorphin functions as a key morphoregulator for mammary epithelial cells. *J Cell Biol* 140(1):159–169.
19. Mori H, et al. (2013) Transmembrane/cytoplasmic, rather than catalytic, domains of Mmp14 signal to MAPK activation and mammary branching morphogenesis via binding to integrin β1. *Development* 140(2):343–352.
20. Cooper DN, Barondes SH (1990) Evidence for export of a muscle lectin from cytosol to extracellular matrix and for a novel secretory mechanism. *J Cell Biol* 110(5):1681–1691.
21. Lepur A, et al. (2012) Galectin-3 endocytosis by carbohydrate independent and dependent pathways in different macrophage like cell types. *Biochim Biophys Acta* 1820(7):804–818.
22. Seelenmeyer C, et al. (2005) Cell surface counter receptors are essential components of the unconventional export machinery of galectin-1. *J Cell Biol* 171(2):373–381.
23. Rizqiawan A, et al. (2013) Autocrine galectin-1 promotes collective cell migration of squamous cell carcinoma cells through up-regulation of distinct integrins. *Biochem Biophys Res Commun* 441(4):904–910.
24. Voss PG, et al. (2008) Dissociation of the carbohydrate-binding and splicing activities of galectin-1. *Arch Biochem Biophys* 478(1):18–25.
25. Belardi B, O'Donoghue GP, Smith AW, Groves JT, Bertozzi CR (2012) Investigating cell surface galectin-mediated cross-linking on glycoengineered cells. *J Am Chem Soc* 134(23):9549–9552.
26. Wu AM, et al. (2007) Differential affinities of Erythrina cristagalli lectin (ECL) toward monosaccharides and polyvalent mammalian structural units. *Glycoconj J* 24(9): 591–604.
27. Hirabayashi J, et al. (2002) Oligosaccharide specificity of galectins: A search by frontal affinity chromatography. *Biochim Biophys Acta* 1572(2-3):232–254.
28. Stowell SR, et al. (2008) Galectin-1, -2, and -3 exhibit differential recognition of sialylated glycans and blood group antigens. *J Biol Chem* 283(15):10109–10123.
29. Jacobs CL, et al. (2001) Substrate specificity of the sialic acid biosynthetic pathway. *Biochemistry* 40(43):12864–12874.
30. Shibuya N, et al. (1987) The elderberry (Sambucus nigra L.) bark lectin recognizes the Neu5Ac(alpha 2-6)Gal/GalNAc sequence. *J Biol Chem* 262(4):1596–1601.
31. Amano M, Galvan M, He J, Baum LG (2003) The ST6Gal I sialyltransferase selectively modifies N-glycans on CD45 to negatively regulate galectin-1-induced CD45 clustering, phosphatase modulation, and T cell death. *J Biol Chem* 278(9):7469–7475.
32. Kouros-Mehr H, Werb Z (2006) Candidate regulators of mammary branching morphogenesis identified by genome-wide transcript analysis. *Dev Dyn* 235(12): 3404–3412.
33. Pellizzoni L, Charroux B, Rappsilber J, Mann M, Dreyfuss G (2001) A functional interaction between the survival motor neuron complex and RNA polymerase II. *J Cell Biol* 152(1):75–85.
34. Fata JE, et al. (2007) The MAPK(ERK-1,2) pathway integrates distinct and antagonistic signals from TGFalpha and FGF7 in morphogenesis of mouse mammary epithelium. *Dev Biol* 306(1):193–207.
35. Julien S, et al. (2006) ST6GalNAc I expression in MDA-MB-231 breast cancer cells greatly modifies their O-glycosylation pattern and enhances their tumourigenicity. *Glycobiology* 16(1):54–64.
36. Recchi MA, Harduin-Lepers A, Boilly-Marer Y, Verbert A, Delannoy P (1998) Multiplex RT-PCR method for the analysis of the expression of human sialyltransferases: application to breast cancer cells. *Glycoconj J* 15(1):19–27.
37. Picco G, et al. (2010) Over-expression of ST3Gal-I promotes mammary tumorigenesis. *Glycobiology* 20(10):1241–1250.
38. Burchell JM, Mungul A, Taylor-Papadimitriou J (2001) O-linked glycosylation in the mammary gland: Changes that occur during malignancy. *J Mammary Gland Biol Neoplasia* 6(3):355–364.
39. Kreunin P, Yoo C, Urquidi V, Lubman DM, Goodison S (2007) Proteomic profiling identifies breast tumor metastasis-associated factors in an isogenic model. *Proteomics* 7(2):299–312.
40. Recchi MA, et al. (1998) Multiplex reverse transcription polymerase chain reaction assessment of sialyltransferase expression in human breast cancer. *Cancer Res* 58(18): 4066–4070.
41. Lin S, Kemmner W, Grigull S, Schlag PM (2002) Cell surface alpha 2,6 sialylation affects adhesion of breast carcinoma cells. *Exp Cell Res* 276(1):101–110.
42. Ingrassia L, et al. (2006) Anti-galectin compounds as potential anti-cancer drugs. *Curr Med Chem* 13(29):3513–3527.

eLIFE elifesciences.org

RESEARCH ARTICLE

Laminin signals initiate the reciprocal loop that informs breast-specific gene expression and homeostasis by activating NO, p53 and microRNAs

Saori Furuta[1,2†]*, Gang Ren[2], Jian-Hua Mao[1], Mina J Bissell[1]*

[1]Division of Biological Systems and Engineering, Lawrence Berkeley National Laboratory, Berkeley, United States; [2]Department of Cancer Biology, College of Medicine & Life Sciences, University of Toledo Health Science Campus, Toledo, United States

Abstract How mammalian tissues maintain their architecture and tissue-specificity is poorly understood. Previously, we documented both the indispensable role of the extracellular matrix (ECM) protein, laminin-111 (LN1), in the formation of normal breast acini, and the phenotypic reversion of cancer cells to acini-like structures in 3-dimensional (3D) gels with inhibitors of oncogenic pathways. Here, we asked how laminin (LN) proteins integrate the signaling pathways necessary for morphogenesis. We report a surprising reciprocal circuitry comprising positive players: laminin-5 (LN5), nitric oxide (NO), p53, HOXD10 and three microRNAs (miRNAs) — that are involved in the formation of mammary acini in 3D. Significantly, cancer cells on either 2-dimensional (2D) or 3D and non-malignant cells on 2D plastic do not produce NO and upregulate negative players: NFκB, EIF5A2, SCA1 and MMP-9 — that disrupt the network. Introducing exogenous NO, LN5 or individual miRNAs to cancer cells reintegrates these pathways and induces phenotypic reversion in 3D. These findings uncover the essential elements of breast epithelial architecture, where the balance between positive- and negative-players leads to homeostasis.
DOI: https://doi.org/10.7554/eLife.26148.001

***For correspondence:** saori.furuta@utoledo.edu (SF); MJBissell@lbl.gov (MJB)

Present address: †Department of Cancer Biology, College of Medicine & Life Sciences, University of Toledo Health Science Campus, Toledo, OH, United States

Competing interests: The authors declare that no competing interests exist.

Funding: See page 35

Received: 21 February 2017
Accepted: 21 November 2017
Published: 21 March 2018

Reviewing editor: Valerie Horsley, Yale University, United States

Introduction

p53 is an extensively characterized regulator of gene expression in the context of malignant transformation and is aberrant in almost all cancer types. Many p53 studies have been performed in cells cultured in 2D conditions. Despite the extensive literature on p53 and its myriad of functions, little is known about what regulates p53 activity in higher organisms *in vivo* or about how p53 might regulate physiological tissue functions in 3D cultures (***Barcellos-Hoff et al., 1989***; ***Petersen et al., 1992***; ***Bissell et al., 2005***; ***Lee et al., 2007***). ECM proteins, in particular LNs (***Miner and Yurchenco, 2004***), compose another important class of regulators that play a role in glandular tissue morphogenesis. Whether or how these two crucial regulators of gene expression intersect in tissue morphogenesis and homeostasis has not been examined.

To explore the possibility of such an interaction as an element of tissue-specificity, we utilized the HMT3522 cancer progression series of human mammary epithelial cells (MECs) (***Briand et al., 1987***; ***Briand et al., 1996***; ***Rizki et al., 2008***). This unique series comprise both primary normal epithelial cells or non-malignant cells (S1) derived from reduction mammoplasty, and their malignant counterpart (T4-2), which were derived without external oncogenic agents after prolonged cultivation in defined medium that lacked epidermal growth factor (EGF), followed by xenografts in animals (***Briand et al., 1987***). Non-malignant and malignant MECs and organoids are readily distinguished

eLife digest Most animal cells can secrete molecules into their surroundings to form a supportive meshwork of large proteins, called the extracellular matrix. This matrix is connected to the cell membrane through receptors that can transmit signals to the cell nucleus to change the levels of small RNA molecules called microRNAs. These, in turn, can switch genes on and off in the nucleus.

In the laboratory, cells that build breast tissue and glands can be grown in gels containing extracellular matrix proteins called laminins. Under these conditions, 'normal' cells form organized clusters that resemble breast glands. However, if the communication between healthy cells and the extracellular matrix is interrupted, the cells can become disorganized and start to form clumps that resemble tumors, and if injected into mice, can form tumors. Conversely, if the interaction between the extracellular matrix and the cells is restored, each single cancer cell can – despite mutations – be turned into a healthy-looking cell. These cells form a normal-looking tissue through a process called reversion. Until now, it was not known which signals help normal breast tissue to form, and how cancerous cells revert into a 'normal' shape.

To investigate this, Furuta et al. used a unique series of breast cells from a woman who underwent breast reduction. The cells taken from the discarded tissue had been previously grown by a different group of researchers in a specific way to ensure that both normal and eventual cancer cells were from the same individual. Furuta et al. then put these cells in the type of laminin found in extracellular matrix. The other set of cells used consisted of the same cancerous cells that had been reverted to normal-looking cells.

Analysis of the three cell sets identified 60 genes that were turned down in reverted cancer cells to a level found in healthy cells, as well as 10 microRNAs that potentially target these 60 genes. A database search suggested that three of these microRNAs, which are absent in cancer cells, are necessary for healthy breast cells to form organized structures. Using this as a starting point, Furuta et al. discovered a signaling loop that was previously unknown and that organizes breast cells into healthy looking tissue.

This showed that laminins help to produce nitric oxide, an important signaling molecule that activates several specific proteins inside the breast cells and restores the levels of the three microRNAs. These, in turn, switch off two genes that are responsible for activating an enzyme that can chop the laminins. Since the two genes are deactivated in the reverted cancer cells, the laminins remain intact and the cells can form organized structures. These findings suggest that if any of the components of the loop were missing, the cells would start to form cancerous clumps again. Reverting the cancer cells in the presence of laminins, however, could help cancer cells to form 'normal' structures again.

These findings shed new light on how the extracellular matrix communicates with proteins in the nucleus to influence how single cells form breast tissues. It also shows that laminins are crucial for generating signals that regulate both form and function of specific tissues. A better understanding of how healthy and cancerous tissues form and re-form may in the future help to develop new cancer treatments.

DOI: https://doi.org/10.7554/eLife.26148.002

by their colony structures in 3D LN1-rich ECM gels (lrECM) (***Petersen et al., 1992***). Non-malignant mammary cells form polarized colonies resembling normal acini of the breast (***Barcellos-Hoff et al., 1989***), whereas malignant cells form disorganized, tumor-like structures (***Petersen et al., 1992***; ***Lee et al., 2007***; ***Rizki et al., 2008***). However, if the architecture of colonies is restored in LN1 gels by downmodulating receptors such as integrins and EGFR, or other involved oncogenic pathways to a level found in normal cells, every single malignant cell would form polarized growth-arrested colonies – by a process we call phenotypic reversion – through a novel movement we have termed 'coherent angular motion' (CAMo) (***Tanner et al., 2012***).

Here, we aimed to delineate *core* regulators of proper ECM-chromatin communications that establish normal breast acinar architecture, a feature that is aberrant in cancer cells in 3D. Using S1 cells, T4-2 cells and T4-2 cells reverted to 'normal' phenotype (T4-2 Rev) by five different

signaling inhibitors, we identified a subset of 60 genes that had similar expression patterns in S1 and in all of the T4-2 Rev cells (**Bissell et al., 2005**; **Becker-Weimann et al., 2013**), as well as 10 miRNAs that could potentially target these 60 genes. Among the 10 miRNAs, we specifically focused on miR-34c-5p, −30e, and −144, which are dramatically downmodulated in many breast tumors (**Lu et al., 2005**).

Restoration of the miRNA caused phenotypic reversion of T4-2 cells in lrECM. While studying the signaling cascades that involve these three miRNAs, we identified a reciprocal regulatory network – comprising LN1 and LN5, NO, p53, HOXD10, NFκB, the three miRNAs, EIF5A2, SCA1, and MMP-9 – which connects the ECM-laminins and the nuclear transcription factors (TFs), most possibly via a newly discovered nuclear tunnel (**Jorgens et al., 2017**), to execute breast morphogenetic programs. Our results shed light on a completely novel and intricate reciprocal loop for breast acinar morphogenesis through a reiterative activation and suppression of regulatory molecules necessary to maintain the differentiated state in 3D and to prevent malignant conversion.

Results

Identification of miRNAs involved in the formation of mammary acini

Non-malignant S1 cells form apico-basally polarized acini in lrECM while conversely, malignant T4-2 cells form disorganized colonies (**Petersen et al., 1992**). We showed initially that inhibitory antibodies to beta-1 integrin reverted the malignant cells to 'normal' phenotype (**Figure 1a**) (**Weaver et al., 1997**). Inhibiting any of a dozen different oncogenic pathway components, including EGFR, PI3K and MMP-9, could revert breast cancer cells (**Figure 1a–1c**) (**Bissell et al., 2005**; **Beliveau et al., 2010**; **Becker-Weimann et al., 2013**). Such cross-modulation suggested the existence of central common integrators. Array analyses of the five most prominent reverting pathways identified 60 genes that were low in S1, and co-downregulated in T4-2 Rev cells (**Figure 1d**, **Table 1**) (**Bissell et al., 2005**), leading us to suspect that the common regulators would be miRNAs.

miRNA expression profiling of the S1, T4-2, and T4-2 Rev cells in lrECM identified a list of 30 miRNAs, the expression of which was anti-correlated with that of the 60 genes (**Figure 1d**, **Table 2**). Using a miRNA target database (microRNA.org), we predicted miRNAs that could potentially target the 60 genes. By combining these two lists, we chose 10 validated miRNAs (**Figure 2a**) each of which could potentially target at least 10 out of the 60 genes (**Table 3**).

Using published patient sample analyses, we selected three miRNAs: miR-34c-5p, −30e and −144, that were found to be downmodulated significantly in breast tumors and tumor cell lines (**Figure 1—figure supplement 1**)(GSE25464) (**Lu et al., 2005**). By *in situ* hybridization of tissue arrays containing 40 breast tumors vs. normal tissues, we confirmed a significant reduction of the three miRNAs in tumors (**Figure 2b, c**). Re-expression of each of the three miRNAs in T4-2 cells led to dramatic growth inhibition in soft agar (**Figure 2d**, **Figure 2—figure supplement 1b**) and caused phenotypic reversion in lrECM (**Figure 2e**, **Figure 2—figure supplement 1c**). Introduction of each of the three miRNAs into metastatic MDA-MB-231 breast cancer cells also led to severe growth impairment in lrECM (**Figure 2f**, **Figure 2—figure supplement 1d**). These results suggest that the three miRNAs are involved in inhibiting tumor cell growth and, by implication, in the maintenance of non-malignant cell behavior.

EIF5A2 and SCA1 are the targets of the three identified miRNAs

A search of the miRNA target database (microRNA.org) identified EIF5A2 and SCA1 as the only common target genes of the three miRNAs among the 60 genes that were modulated by each of five reverting agents (**Table 4**, **Figure 1**). To validate this, we performed RT-PCR for EIF5A2 and SCA1 in T4-2 cells before and after miRNA expression. Endogenous levels of the two proteins were high in T4-2 cells compared to those in S1 cells, but as expected, were downmodulated in T4-2 Rev cells that were reverted either with a reverting agent or upon restoration of any of the three miRNAs (**Figure 3a**). Thus, each miRNA acted like a reverting agent, similar to the five other reverting agents we have reported on previously (**Figure 3a**; **Figure 1a–c**) (**Bissell et al., 2005**; **Beliveau et al., 2010**; **Becker-Weimann et al., 2013**). Importantly, depletion of either EIF5A2 or SCA1 in T4-2 cells with shRNA (**Figure 3—figure supplement 1a**) also caused phenotypic reversion (**Figure 3b**, **Figure 3—figure supplement 1b**). To ensure that this is not an off-target effect, we

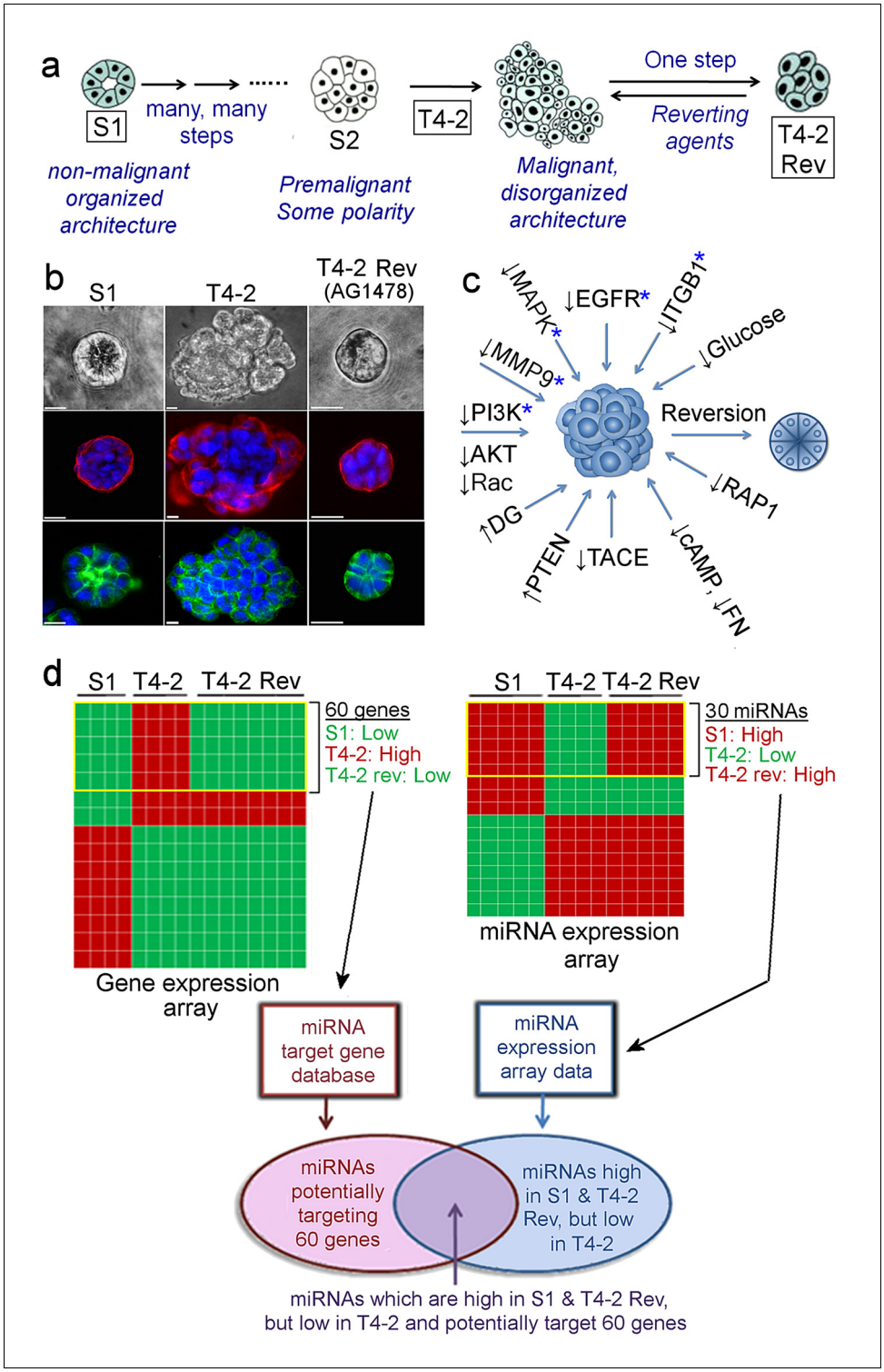

Figure 1. Identification of miRNAs linked to phenotypic reversion of human breast-cancer cells. (**a**) Scheme of progression of non-malignant HMT3522-S1 cells to malignant T4-2 cells and of reversion of T4-2 cells to an S1-like phenotype in the presence of a reverting agent. (**b**) S1, T4-2 and T4-2 Rev cells with AG1478 in lrECM. Cells are stained for integrin α6 (red), β-catenin (green) and nuclei (blue). Scale bars: 20 μm. Replicate experiments (n = 3) were performed, and representative data are shown. (**c**) A scheme of modulation of a single oncogenic pathway for phenotypic reversion of tumor cells. Five pathways chosen for gene and miRNA arrays are indicated with blue asterisks (*). (**d**) Screening miRNAs linked to phenotypic reversion. (Top left) Gene arrays (n = 5, GSE50444 [***Becker-Weimann et al., 2013***]) clustered 60 genes that are downmodulated in S1 and T4-2 Rev

Figure 1 continued on next page

Figure 1 continued

cells compared to T4-2 cells. (Top right) miRNA arrays (n = 4) clustered 30 miRNAs the expression of which was anti-correlated to that of these 60 genes. (Bottom left) A miRNA target database (microRNA.org) predicted miRNAs that could target the 60 genes. Combination of the two lists identified miRNAs that are linked to phenotypic reversion.

DOI: https://doi.org/10.7554/eLife.26148.003

The following figure supplement is available for figure 1:

Figure supplement 1. miR-34c, miR-30e and miR-144 are downregulated in breast cancer.

DOI: https://doi.org/10.7554/eLife.26148.004

restored EIF5A2 and SCA1 in T4-2 cells that were overexpressing the miRNAs. In these T4-2 cells we overexpressed cDNAs of EIF5A2 or SCA1 that lacked miRNA binding sites because the three miRNAs bind only to the 3'UTR of the two target genes (***Table 5***). Overexpression was confirmed by western analysis (***Figure 3—figure supplement 1c***). Restoration of EIF5A2 or SCA1 severely impaired tumor-cell reversion, validating the importance of the inactivation of these two target genes for normal functional differentiation of breast acini (***Figure 3—figure supplement 1d and e***). These results demonstrate that the miRNA database correctly predicted EIF5A2 or SCA1 as the target genes of the three miRNAs.

Reversion of breast tumor cells to normal phenotype requires upregulation of HOXD10 and downregulation of NFκB

To determine the regulators of the three miRNAs, we generated reporter constructs in which the luciferase gene was fused to the miRNA gene promoters, containing 3–0, 2–0 and 1–0 kb regions from the transcription start site (***Figure 3—figure supplement 2a***). The activity of the 1–0 kb region for miR-34c and the 3–0 kb region for both miR-30e and −144 was high in S1 and T4-2 Rev cells, but not in T4-2 cells (***Figure 3c***). In addition, we generated reporter constructs containing non-overlapping 3–2, 2–1 and 1–0 kb fragments of the miRNA promoters from the transcription start site (***Figure 3—figure supplement 2b***). The activity of the 1–0 kb region for miR-34c and the 3–2 kb region for both miR-30e and −144 was high in S1 and T4-2 Rev cells (***Figure 3d***).

To determine which TFs bound to these critical regions, we analyzed the PROMO database (***Farré et al., 2003***) and identified multiple high-confidence binding sites for HOXD10 and NFκB (% dissimilarity <15%; genomic frequency $<1\times10^{-4}$) (***Figure 4—figure supplement 1a***, ***Table 6***) (***Farré et al., 2003***). We had shown previously that overexpression of HOXD10 or downmodulation of NFκB phenotypically reverts T4-2 cells (***Becker-Weimann et al., 2013***; ***Chen et al., 2009***). As predicted, HOXD10 was high in S1 and T4-2 Rev cells compared to T4-2 cells (***Figure 4a***). By contrast, activation of NFκB, as measured by Ser536 phosphorylation of the p65 subunit that causes its nuclear translocation (***Sasaki et al., 2005***), was elevated in T4-2 cells and downmodulated in S1 and T4-2 Rev cells (***Figure 4a***). To show that these two TFs regulate the miRNAs in opposite directions, we generated T4-2 cells that were depleted of either p65 or p50, and its unprocessed precursor, p100, a subunit of NFκB. We also overexpressed HOXD10 in T4-2 cells (***Figure 4—figure supplement 1b***). In all these conditions, the activity of the miRNA promoters was elevated in the same regions as those described above (***Figure 4b***, ***Figure 3—figure supplement 1d***). Northern analysis confirmed the increase of miRNA expression, allowing the formation of basally polarized colonies in lrECM (***Figure 4c and d***, ***Figure 4—figure supplement 1c***), which were analogous to colonies of miRNAs-expressing T4-2 cells (***Figure 2c***). These results highlight the importance of the ratios and balance of different regulatory genes in maintaining normal architecture.

To prove that HOXD10 and NFκB do indeed bind the promoters of the three miRNAs, we performed chromatin immunoprecipitation (ChIP) analyses. We found that HOXD10 bound the promoters of the three miRNAs in S1 and T4-2 Rev cells, but not in T4-2 cells, whereas the NFκB p65 subunit bound the same regions in T4-2 cells, but not in S1 and T4-2 Rev cells (***Figure 4e***, ***Figure 4—figure supplement 1d***).

To ascertain the functional consequence of the above experiment, we used the decoy technology described by Osako et al. (***Osako et al., 2012***). These decoys were derived from their respective binding sequences in each miRNA promoter (***Table 7***). For T4-2 cells, which have a high level of endogenous NFκB (***Figure 4a***), we expressed NFκB decoys; for T4-2 cells that we overexpressed

Table 1. List of 60 genes downregulated in T4-2 revertants to the level found in S1 but unmodulated in T4-2 cells in lrECM (p-value<0.05 was considered significant) (***Rizki et al., 2008***).

Ensembl gene ID	Ensembl transcript ID	Gene name
ENSG00000107796	ENST00000224784	ACTA2
ENSG00000109321	ENST00000264487	AREG
ENSG00000102606	ENST00000317133	ARHGEF7
ENSG00000134107	ENST00000256495	BHLHB2
ENSG00000101189	ENST00000217161	C20ORF20
ENSG00000115009	ENST00000358813	CCL20
ENSG00000161570	ENST00000293272	CCL5
ENSG00000169583	ENST00000224152	CLIC3
ENSG00000165959	ENST00000298912	CLMN
ENSG00000176390	ENST00000324238	CRLF3
ENSG00000105246	ENST00000221847	EBI3
ENSG00000163577	ENST00000295822	EIF5A2
ENSG00000187266	ENST00000222139	EPOR
ENSG00000085832	ENST00000262674	EPS15
ENSG00000124882	ENST00000244869	EREG
ENSG00000197930	ENST00000359133	ERO1L
ENSG00000149573	ENST00000278937	EVA1
ENSG00000141524	ENST00000322933	EVER1
ENSG00000185862	ENST00000330927	EVI2B
ENSG00000180263	ENST00000343958	FGD6
ENSG00000088726	ENST00000314124	FLJ11036
ENSG00000137312	ENST00000259846	FLOT1
ENSG00000100031	ENST00000248923	GGT1
ENSG00000149435	ENST00000286890	GGTLA4
ENSG00000051620	ENST00000058691	HEBP2
ENSG00000178922	ENST00000326220	HT036
ENSG00000172183	ENST00000306072	ISG20
ENSG00000105655	ENST00000357050	ISYNA1
ENSG00000119698	ENST00000304338	KIAA1622
ENSG00000134121	ENST00000256509	L1CAM
ENSG00000110492	ENST00000359803	MDK
ENSG00000146232	ENST00000275015	NFKBIE
ENSG00000008517	ENST00000008180	NK4
ENSG00000157045	ENST00000287706	NTAN1
ENSG00000135124	ENST00000356268	P2R × 4
ENSG00000110218	ENST00000227638	PANX1
ENSG00000145431	ENST00000274071	PDGFC
ENSG00000166289	ENST00000299373	PLEKHF1
ENSG00000083444	ENST00000196061	PLOD
ENSG00000107758	ENST00000342558	PPP3CB
ENSG00000011304	ENST00000350092	PTBP1
ENSG00000073756	ENST00000186982	PTGS2
ENSG00000118508	ENST00000237295	RAB32
ENSG00000013588	ENST00000014914	RAI3

Table 1 continued on next page

Table 1 continued

Ensembl gene ID	Ensembl transcript ID	Gene name
ENSG00000168501	ENST00000307470	RDBP
ENSG00000136643	ENST00000259161	RPS6KC1
ENSG00000124788	ENST00000244769	SCA1
ENSG00000181788	ENST00000312960	SIAH2
ENSG00000136603	ENST00000259119	SKIL
ENSG00000173262	ENST00000340749	SLC2A14
ENSG00000059804	ENST00000075120	SLC2A3
ENSG00000160326	ENST00000291725	SLC2A6
ENSG00000086300	ENST00000338523	SNX10
ENSG00000061656	ENST00000080856	SPAG4
ENSG00000141380	ENST00000269137	SS18
ENSG00000198203	ENST00000251481	SULT1C1
ENSG00000152284	ENST00000282111	TCF7L1
ENSG00000035862	ENST00000262768	TIMP2
ENSG00000125657	ENST00000245817	TNFSF9
ENSG00000115652	ENST00000283148	UXS1

DOI: https://doi.org/10.7554/eLife.26148.007

HOXD10 (***Figure 4—figure supplement 1b***), we employed HOXD10 decoys. Any alteration in the promoter activity after expressing a particular decoy would indicate that the TF was bound and sequestered by the decoy. To test for sequence-specific binding of the TFs, we engineered decoys harboring point mutations in T4-2 cells. The expression of wild-type NFκB decoys, but not mutant decoys, derepressed the promoter activities, showing that the wild-type decoys bound and sequestered NFκB, whereas the mutant decoys did not. The procedure was repeated for HOXD10 with similar conclusions (***Figure 4—figure supplement 1e***). Collectively, these results demonstrate that HOXD10 and NFκB directly bind the specific sequences in miRNA promoters in a mutually exclusive manner to regulate miRNA expression for restoration of breast acinar architecture.

p53 is another essential element in mammary acinar formation and tumor-cell reversion

p53 is a potent inhibitor of NFκB (***Webster and Perkins, 1999***; ***Murphy et al., 2011***). Because p53 activity in tumors is extremely high, it is often assumed that little or no p53 is present in normal tissues. We found appreciable levels of wild-type p53 in the epithelial compartment of sections of normal breast tissues but not in the stroma (***Figure 9—figure supplement 1***). In 3D cultures of S1 and T4-2 Rev cells, we found appreciable levels of Ser20-phosphorylated p53 (pSer20-p53), which stabilizes (***Chehab et al., 1999***) and enhances the transactivation activity of p53 (***Jabbur et al., 2000***). This was also the case when either of the miRNAs were overexpressed in T4-2 cells or when their inhibitory target, EIF5A2 or SCA1, was depleted (***Figure 5a***). The expression of the p53-regulated genes, p21, GADD45 and DRAM, was elevated in S1 and all T4-2 Rev cells (***Figure 5a***).

Whether p53 is both the direct inhibitor of NFκB and an activator of HOXD10 was examined by overexpressing the dominant-negative p53 (DNp53) (***Harvey et al., 1995***) in S1 cells. This particular mutant of p53 was reported to effectively abolish tumor suppression and transcriptional activity of the endogenous wild-type p53, leading to enhanced tumor growth, even in heterozygous mice. In S1 cells that overexpressed DNp53, HOXD10 level plummeted as NFκB activity, measured by Ser536 phosphorylation of the p65 subunit, increased over the levels seen in control S1 cells or S1 cells overexpressing the wild-type p53 (***Figure 5b***).

As expected, expression of DNp53 prevented S1 cells from forming polarized quiescent acini in lrECM (***Figure 5c***, ***Figure 5—figure supplement 1a***). Similarly, RNAi-mediated depletion of the wild-type p53 in S1 or MCF10A cells abrogated acinar formation (***Figure 5d and e***, ***Figure 5—figure***

Table 2. List of 30 miRNAs that were upregulated in S1 and T4-2 revertants and downmodulated in T4-2 in lrECM (p-value<0.05 was considered significant).

Mature ID	Fold regulation S1 vs T4-2	Fold regulation T4 rev vs T4	P value
miR-450b-5p	30.3789	869.8262	0.049943
miR-105	11.1967	783.9313	0.007486
miR-383	52.5275	735.6709	0.042511
miR-432	17.7736	541.6623	0.020574
miR-495	455.6135	510.0813	0.004495
miR-30e	65.4581	228.7297	0.047957
miR-190	48.2236	221.0022	0.044772
miR-369–3 p	14.1069	158.4536	0.041128
miR-323–3 p	13.8486	118.1588	0.015214
miR-127–5 p	10.5195	115.9948	0.005194
miR-330–3 p	39.2603	113.8705	0.044612
miR-382	24.6754	82.0207	0.021385
miR-337–3 p	36.2104	35.2915	0.003663
miR-423–3 p	55.2984	32.9948	0.045694
miR-125b	48.925	29.9434	0.04939
miR-376a	212.9199	11.2032	0.049943
miR-296–5 p	42.5671	8.5618	0.045775
miR-135a	60.0253	7.5379	0.045617
miR-144	1234.0342	7.3743	0.003973
miR-301b	32.1668	7.1892	0.043739
miR-376c	49.8377	6.2803	0.046834
miR-487a	68.5143	6.2243	0.035722
miR-590–3 p	14.4952	5.9622	0.035266
miR-301a	30.8564	5.4045	0.047854
miR-98	33.6103	5.1012	0.041169
miR-34c-5p	31.215	4.8038	0.043702
miR-496	42.8632	3.2108	0.044913
miR-543	74.4569	2.897	0.01967
miR-143	590.5164	2.2076	0.042274
miR-374a	11.1001	1.1926	0.013047

DOI: https://doi.org/10.7554/eLife.26148.008

supplement 1b and c). Furthermore, inhibition of p53 activity with a specific inhibitor, α-pifithrin (***Komarov et al., 1999***), rendered T4-2 cells resistant to phenotypic reversion by any of the reverting agents tested (***Bissell et al., 2005***; ***Lee et al., 2007, 2012***) or by re-expression of any of the three miRNAs (***Figure 5f and g***, ***Figure 5—figure supplement 1d and e***). Likewise, MCF10A cells that overexpressed DNp53, were resistant to reverting agents (***Figure 5h***, ***Figure 5—figure supplement 1f***).

De novo synthesized LN5 is required for acinar morphogenesis

It is known that the basement membrane (BM) of the mammary gland includes not only LN1 but also LN5. To maintain tissue architecture, signaling pathways need to regulate each other directly or indirectly (***Bissell et al., 1982***, ***2005***). We had shown previously that even after placing cells in lrECM, formation of acini and production of milk proteins still required an endogenously formed BM (***Streuli and Bissell, 1990***). Accordingly, we measured the levels of human LNs in the conditioned media (CM) and in cell lysates of S1 and T4-2 cells grown in lrECM. Using a human-specific pan-LN

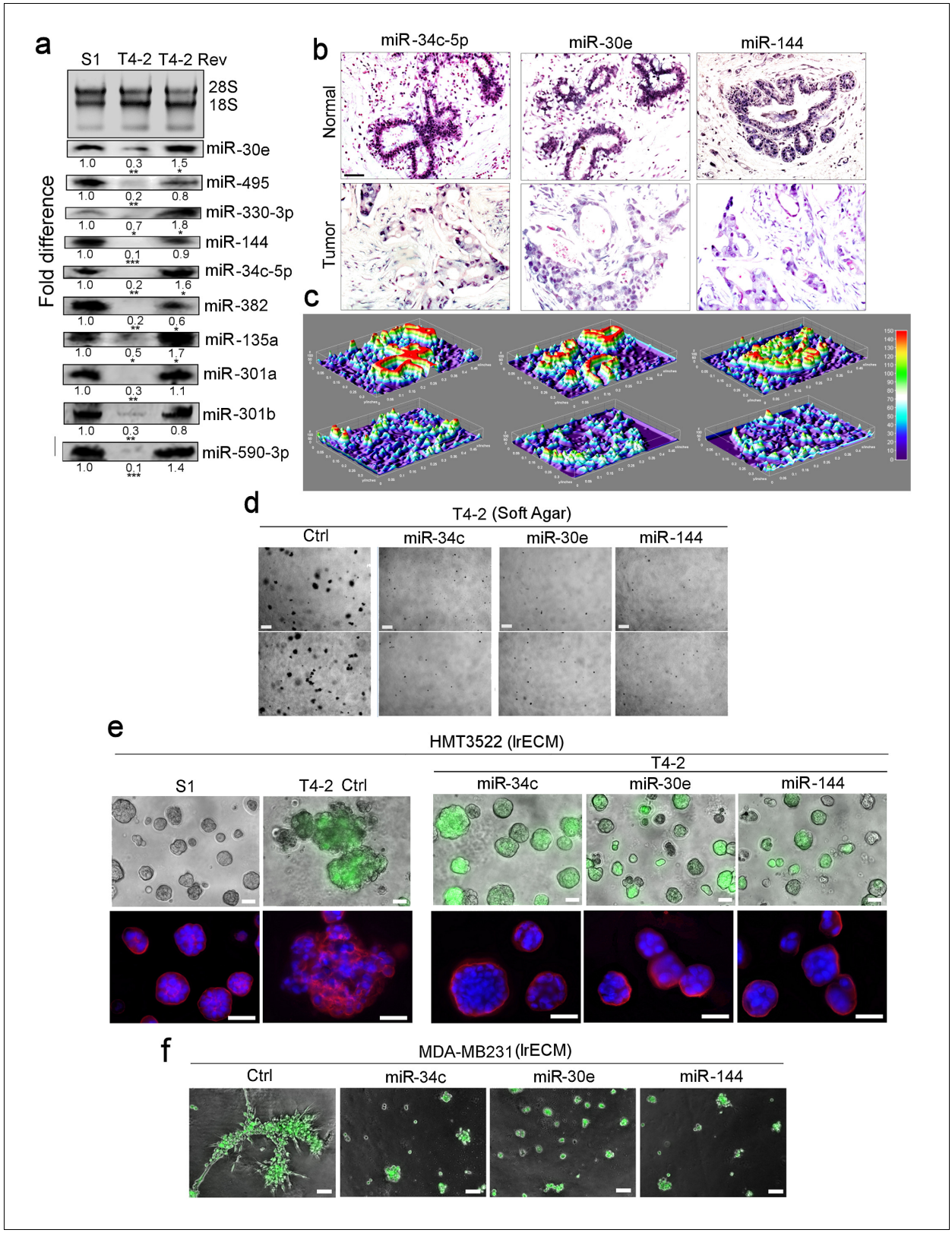

Figure 2. Restoring the expression of miR-34c-5p, −30e or −144 in breast cancer cells induces phenotypic reversion. (**a**) Actual expression pattern of the ten identified miRNAs (***Figure 1***): the levels are at least two-fold higher in S1 and T4-2 Rev cells than in T4-2 cells, as measured by northern analysis. 28S and 18S RNAs were used as internal controls. Fold difference was determined with respect to S1 cells. *p<0.05; **p<0.01; and ***p<0.001. (**b**) *In situ* hybridization of primary human breast tissues showed the abundance of miR-34c-5p, −30e and −144 in normal (top row) compared to tumor

Figure 2 continued on next page

Figure 2 continued

tissues (second row) (n = 3). Nuclei were counterstained with nuclear fast red. (**c**) Heat maps of (**b**) generated by ImageJ. (**d**) T4-2 cells expressing the 3 miRNAs grown in soft agar. See quantification in ***Figure 2—figure supplement 1b***. Two representative images are shown out of 9 samples (**e**) T4-2 cells expressing thethree miRNAs grown in lrECM. (Top) Phase images overlaid with FITI to indicate transduced cells. (Bottom) Red: α6 integrin; blue: DAPI. See quantification in ***Figure 2—figure supplement 1c***. (**f**) MDA-MB231 cells expressing the three miRNAs grown in lrECM. Phase images overlaid with FITI to indicate transduced cells. Scale bars: 20 μm. See quantification of colony sizes in ***Figure 2—figure supplement 1d***. For each analysis, replicate experiments (n = 3) were performed, and representative data are shown.

DOI: https://doi.org/10.7554/eLife.26148.005

The following figure supplement is available for figure 2:

Figure supplement 1. miR-34c, miR-30e and miR-144 are critically involved in tumor-cell reversion.

DOI: https://doi.org/10.7554/eLife.26148.006

antibody, we observed a significant increase in human LNs in both CM and lysates of S1 and T4-2 Rev cells reverted by expression of miRNAs or depletion of the two target genes (***Figure 6—figure supplement 1a***).

Functional LN proteins are heterotrimers of αβγ chains (***Miner and Yurchenco, 2004***). To determine which LN trimers were upregulated, we analyzed the CM of cells grown in lrECM cultures using antibody arrays against human ECM proteins. The α3, β3 and γ2 chains of LN5 were highly elevated in S1 and T4-2 Rev cells that expressed the miRNAs or that were depleted of their two targets. By contrast, parental T4-2 cells did not produce LN5, suggesting that LN5 is only expressed in MECs capable of forming acinar-like polarized structures (***Figure 6—figure supplement 1b–d***). To test the possibility, we depleted one of the LN5 subunits, LAMA3, with shRNA. Loss of LAMA3 abrogated reversion of T4-2 cells with any of the different reverting agents including any of the three miRNAs (***Figure 6a and b***, ***Figure 6—figure supplement 2a, b***). Depletion of LAMA3 could be rescued by addition of ectopic LN5, confirming the specificity of the reaction (***Figure 6a and b***, ***Figure 6—figure supplement 2a and b***).

To follow how LN5 was elevated in acinar formation and tumor cell reversion, we postulated that it could be due to LN5 protein stabilization due to suppression of MMP-9 transcription. We previously had shown that MMP-9, a metalloproteinase secreted to degrade LNs, is elevated in T4-2, but downmodulated in T4-2 Rev cells, leading to stabilization of secreted LNs (***Beliveau et al., 2010***).

Table 3. List of 12 miRNAs that were upregulated in S1 and T4-2 revertants and downmodulated in T4-2, and that could target more than 10 genes among the 60 genes that showed the opposite expression patterns.

Mature ID	Fold regulation T4 vs Control	Fold regulation T4 Rev vs T4	p-value	# Targets / 60 genes	Gene locus	Type	
miR-450b-5p	−30.3789	869.8262	0.000304	15	Xq26.3	Intergenic	
miR-495	−455.6135	510.0813	0.028964	12	14q32.31	Intergenic	
miR-30e*	**−65.4581**	**228.7297**	**0.008983**	**11**	**1p34.2**	**Intronic**	**Down (p<0.05)**
miR-330–3 p	−39.2603	113.8705	0.007481	22	19q13.32	Intronic	
miR-382	−24.6754	82.0207	0.001901	12	14q32.31	Intergenic	
miR-423–3 p	−55.2984	32.9948	0.011304	14	17q11.2	Intronic	
miR-135a	−60.0253	7.5379	0.039409	13	3p21.1	Intergenic	
					12q23.1	Intergenic	
miR-144*	**−1234.0342**	**7.3743**	**0.010599**	**12**	**17q11.2**	**Intergenic**	**Down (p<0.05)**
miR-301b	−32.1668	7.1892	0.028553	16	22q11.21	Intergenic	
miR-590–3 p	−14.4952	5.9622	0.043351	21	7q11.23	Intronic	
miR-301a	−30.8564	5.4045	0.044539	13	17q22	Intronic	
miR-34c-5p*	**−31.215**	**4.8038**	**0.01567**	**10**	**11q23.1**	**Intergenic**	**Down (0 < 0.05)**

*The three miRNAs in **bold** that were the focus of this study.

†p-values were obtained from the array results [GSE2564] (***Petersen et al., 1998***).

DOI: https://doi.org/10.7554/eLife.26148.009

Table 4. List of genes targeted by miR-34c-5p, miR-30e and miR-144 among the cluster of 60 genes that were downmodulated in S1 and T4-2 revertants and upregulated in T4-2.

miR-144 (12 targets)	**miR-30e** (11 targets)	**mir-34c-5p** (10 targets)
		AREG
		BHLHB2
C20ORF20		
CCL20		
EIF5A2	**EIF5A2**	**EIF5A2**
EREG		
ERO1L		ERO1L
	FGD6	
		ISG20
		NK4
	KIAA1622	
L1CAM	L1CAM	
PTBP1		
PTGS2	PTGS2	
	RDBP	RDBP
SCA1 (ATXN1)	**SCA1 (ATXN1)**	**SCA1 (ATXN1)**
SIAH2		SIAH2
	SLC2A14	
	SLC2A3	
	SNX10	SNX10
SS18	SS18	
TIMP2		

DOI: https://doi.org/10.7554/eLife.26148.013

We measured the level of secreted MMP-9 in lrECM cultures and showed that MMP-9 was significantly reduced in T4-2 cells that expressed any of the three miRNAs- or were depleted of the two target genes, EIF5A2 and SCA1 (***Figure 6c***). It had been shown previously that both EIF5A2 and SCA1 lie downstream of the PI3K/AKT pathway and are involved in positive regulation of MMP transcription (***Liu et al., 2000***; ***Park et al., 2013***; ***Khosravi et al., 2014***). We concluded that expression of the miRNAs inactivates both EIF5A2 and SCA1 and thus downmodulates MMP-9 leading to stabilization of LN5.

p53 activation during acinar formation is triggered by LN-induced nitric oxide (NO) production

We searched for possible explanations of how LNs activate p53. In older literature, LN was reported to induce NO production in neuronal and endothelial cells as part of mechanotransduction pathways (***Gloe and Pohl, 2002***; ***Rialas et al., 2000***). As NO is reported to be a potent activator of p53 (***Forrester et al., 1996***; ***Wang et al., 2002***), we hypothesized that LNs might also be instrumental in inducing NO production in breast cells, which in turn would activate p53. We applied purified LN5 (***Figure 7a***) or lrECM (***Figure 7—figure supplement 1a***) to MCF10A cells and observed an increase in pSer20-p53 after 30 min, along with increases in Ser1981-phosphorylated ATM and total level of p14 ARF, the known p53 activators (***Canman et al., 1998***; ***Zhang et al., 1998***). Under the same conditions, Ser1417 phosphorylation of nitric oxide synthase 1 (NOS-1) was also elevated (***Figure 7a***, ***Figure 7—figure supplement 1a***), suggesting its role in NO production. In contrast, DNp53 overexpressed in MCF10A cells was not activated in response to LNs, whereas ATM, p14 ARF and NOS-1 were all activated (***Figure 7a***, ***Figure 7—figure supplement 1a***). When MCF10A cells were treated

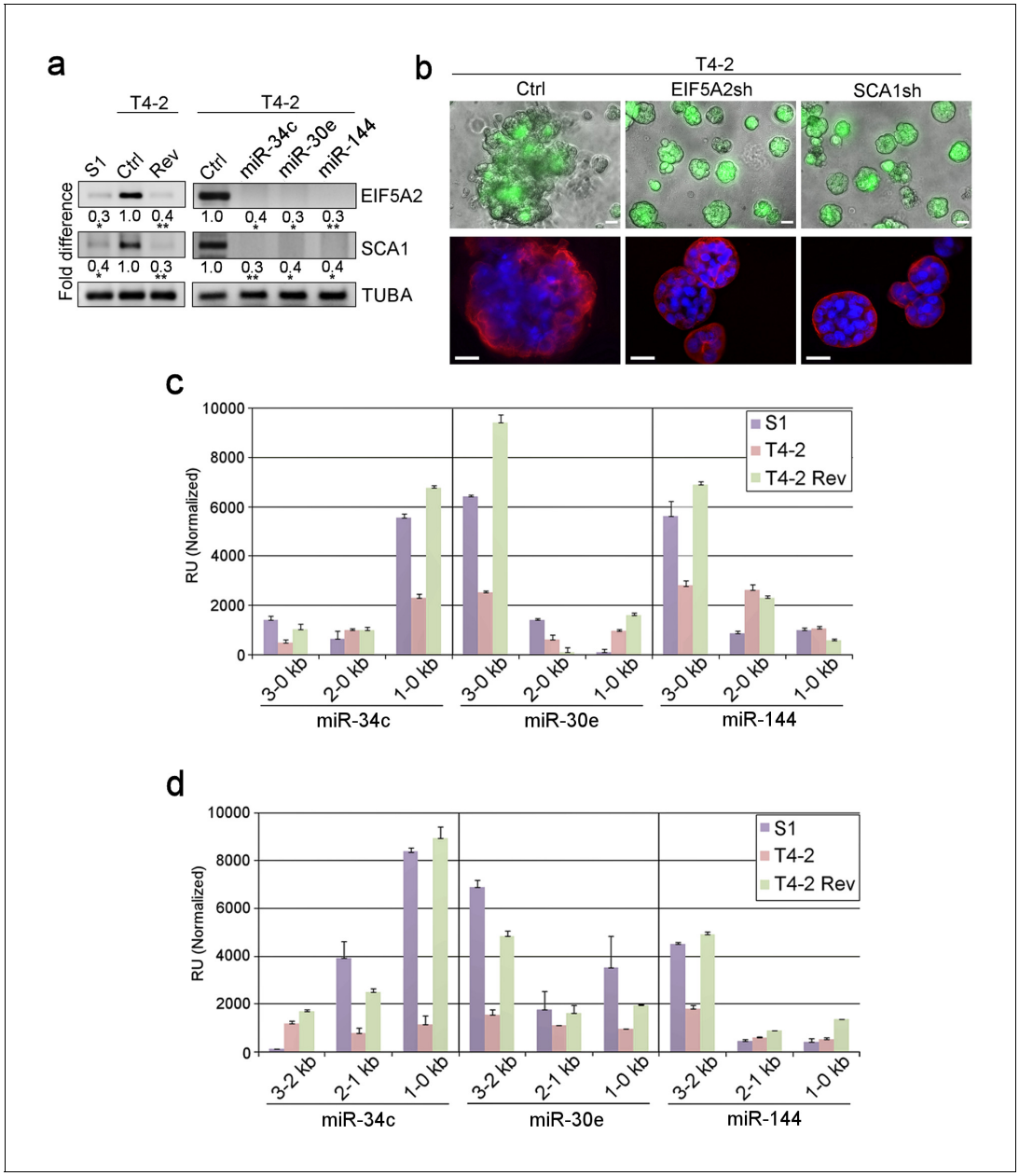

Figure 3. Dissection of miRNA target genes and promoter regulation. (**a**) Representative result of semi-quantitative RT-PCR (n = 3) to determine the levels of EIF5A2 and SCA1 in S1, T4-2 and T4-2 Rev cells (treated with AG1478). Fold difference was determined with respect to the Ctrl T4-2. *p<0.05 and **p<0.01 (**b**) T4-2 cells depleted of EIF5A2 or SCA1 grown in lrECM. (Top) Phase images overlaid with FITI to indicate transduced cells. (Bottom) Red — integrin α6 (red); blue — DAPI. Scale bars: 20 μm. See quantification in ***Figure 3—figure supplement 1b***. (**c**) Activities of different miRNA promoters (n = 3) in S1, T4-2 and T4-2 Rev cells using the promoter constructs shown in ***Figure 3—figure supplement 2a***. Note that a 1–0 kb fragment of miR-34c promoter, a 3–0 kb fragment of miR-30e promoter and a 3–0 kb fragment of miR-144 promoter were activated in the S1 and T4-2 Rev cells. (**d**) Activities of different miRNA promoters (n = 3) in S1, T4-2 and T4-2 Rev cells using the promoter constructs shown in ***Figure 3—figure supplement 2b***. Note that a 1–0 kb fragment of miR-34c promoter,a 3–2 kb fragment of miR-30e promoter and a 3–2 kb fragment of miR-144 promoter were activated in S1 and T4-2 Rev cells. Data are represented as mean ± SEM. For each analysis, replicate experiments (n = 3) were performed, and representative data are shown.

DOI: https://doi.org/10.7554/eLife.26148.010

The following figure supplements are available for figure 3:

Figure supplement 1. Identification of the downstream targets of the three miRNAs and generation of the promoter constructs of the miRNA genes.

DOI: https://doi.org/10.7554/eLife.26148.011

Figure supplement 2. Scheme of reporter constructs derived from the promoter regions of the three miRNAs genes.

Figure 3 continued on next page

Figure 3 continued

DOI: https://doi.org/10.7554/eLife.26148.012

with a NOS inhibitor, L-NAME, that inhibits NO production, LN5-mediated activation of p53, as well as of ATM and p14 ARF, were severely impaired (***Figure 7b***).

We measured the level of NO in CM after addition of LNs using a fluorescence probe, DAN, against NO metabolites. S1 and MCF10A cells produced NO as a function of time in response to LN5 or lrECM (***Figure 7c and d***). By contrast, T4-2 cells failed to do so (***Figure 7c and d***). Addition of another ECM protein collagen-1 (COL1) did not induce NO production by S1 or MCF10A cells (***Figure 7e***), suggesting a unique role of LNs. We then monitored the intracellular NO level after addition of lrECM using a fluorescence probe DAF-FM DA. NO level peaked at around 1 hr after lrECM addition and declined thereafter in S1 and MCF10A cells, whereas it remained low in T4-2 cells (***Figure 7f***, ***Figure 7—figure supplement 1b***).

To confirm the biological relevance of NO production by MECs, we stained 3D colonies for S-nitrosocysteine (SNOC), an indicator of NO production (***Gould et al., 2013***) and localization (***Iwakiri et al., 2006***). S1 acini showed strong basolateral SNOC staining, whereas T4-2 cells showed weak and dispersed staining. However, T4-2 Rev cells restored the strong basolateral SNOC staining analogous to S1, suggesting the recovery of NO production upon phenotypic reversion (***Figure 7g***, ***Figure 7—figure supplement 1c***). We then stained normal (n = 8) vs. cancerous (n = 32) breast tissue sections for SNOC. Normal mammary epithelia were distinctively stained for SNOC, whereas the majority of tumor samples were only weakly and diffusely stained [positive staining (intensity >+1): 8/8 vs. 8/32, respectively] (***Figure 7h***). These results support the relevance of NO production to the biology of the normal breast.

NO is critical for mammary acinar formation and gland morphogenesis

NO is known to play a role in the differentiation and morphogenesis of neurons, muscles and immune cells (***Rialas et al., 2000***; ***Stamler and Meissner, 2001***; ***Niedbala et al., 2002***). To test the involvement of NO in mammary morphogenesis, we inhibited NO production with L-NAME in two different non-malignant breast epithelial cells; this led to the formation of disorganized proliferative structures in lrECM (***Figure 8a and b***, ***Figure 8—figure supplement 1a and b***). Alternatively, the induction of NO production in T4-2 cells with a NO donor, SNAP, induced phenotypic reversion (***Figure 8c***, ***Figure 8—figure supplement 1c***). Also, application of L-NAME to T4-2 cells, even in the presence of a reverting agent (e.g., an inhibitor of EGFR or β1 integrin) (***Bissell et al., 2003***), abrogated phenotypic reversion in lrECM (data not shown). To determine whether the activity of NO is necessary for human mammary gland morphogenesis, we monitored the alveologenesis of breast organoids treated with L-NAME in *ex vivo* 3D cultures. L-NAME treatment dramatically reduced the percentage of colonies capable of alveologenesis (vehicle-treated: 28% vs. L-NAME-treated: 1.2%) (***Figure 8d***, ***Videos 1*** and ***2***).

We tracked movement of L-NAME-treated S1 cells in lrECM for 48 hr by live cell imaging. We and others have shown previously that acinar forming non-malignant breast cells undergo CAMo in

Table 5. Predicted binding sites of three miRNAs at 3′UTR of SCA1 and EIF5A2.

miRNA	Seed	miRNA binding site in 3′UTR of mRNA
SCA1		
hsa-miR-34c	GGCAGUG	691, 913, 6461
hsa-miR-30e	GUAAACA	3588, 4308, 4603, 4770, 5440, 6092, 6233
hsa-miR-144	GAUAUCA	47, 987, 1113, 1160, 4557, 5426, 6267
EIF5A2		
hsa-miR-34c	GGCAGUG	297, 802, 2656
hsa-miR-30e	GUAAACA	3264, 3312, 3525, 3652, 3643, 4113
hsa-miR-144	GAUAUCA	2642, 2742, 2977, 4123, 4541, 4570

DOI: https://doi.org/10.7554/eLife.26148.014

Table 6. miRNA promoter regions harboring binding sites of TFs, NFκB (p65) and HOXD10.

						Frequency (random expectancy x 10^{-3})	
miRNA promoter	**TXN bound**	**Start nt from TSS**	**End nt from TSS**	**String**	**Dissimilarity (%)**	**Equally**	**Query**
miR-34c	RelA	−787	−778	AGGGAATCAA	14	1×10^{-5}	1×10^{-5}
		−769	−760	TGGGAAGTTT	11	3×10^{-5}	5×10^{-5}
		−427	−418	TGGGAACCTT	11	4×10^{-5}	3×10^{-5}
		−64	−55	TGGGAAGCCG	13	4×10^{-5}	4×10^{-5}
		−56	−47	CGCTTTCCCA	12	5×10^{-5}	4×10^{-5}
		-3	6	GGGGAATGAG	13	3×10^{-5}	3×10^{-5}
	HOXD10	−864	−855	AGTTTGTATT	10	1×10^{-4}	2×10^{-4}
		−385	−376	CCCTTCTATT	12	3×10^{-5}	4×10^{-5}
miR-30e	RelA	−2888	−2879	GATATTCCCA	2	6×10^{-6}	5×10^{-6}
	HOXD10	−2553	−2544	TGGTTGTATT	10	1×10^{-4}	2×10^{-4}
		−2230	−2221	GCGTGATATT	11	1×10^{-4}	1×10^{-4}
		−2122	−2113	TTTTTTTATT	4	1×10^{-5}	4×10^{-5}
		−1967	−1967	TACTCATATT	9	1×10^{-4}	2×10^{-4}
miR-144	RelA	−3207	−3198	AGGGAATTTG	10	5×10^{-5}	5×10^{-5}
	HOXD10	−2850	−2841	AATAGAATGA	10	1×10^{-4}	2×10^{-4}
		−2715	−2706	AATACAAAAA	10	1×10^{-4}	2×10^{-4}
		−2412	−2403	CCATATTATT	11	1×10^{-4}	1×10^{-4}
		−2336	−2327	AATAAGAGTA	7	5×10^{-5}	7×10^{-5}
		−2312	−2303	ATTTATTATT	10	1×10^{-4}	2×10^{-4}

DOI: https://doi.org/10.7554/eLife.26148.017

lrECM, whereas cancer cells exhibit random amoeboid motion (***Tanner et al., 2012***; ***Wang et al., 2013***). S1 cells treated with L-NAME are defective in CAMo and form disorganized masses (***Figure 8e***, ***Videos 3*** and ***4***).

LN5 activates p53 phosphorylation and p53 activates LN5 transcription

We showed above that NO production in response to lrECM is critical for p53 activation and the formation of mammary acini (***Figures 7a–g*** and ***8a–e***). This process involves *de novo* synthesized LN5 (***Figure 6a and b***). We also showed that p53 upregulates the expression of HOXD10 and downregulates activation of NFκB. This dual action allows expression of the three miRNAs that inhibit TFs, SCAI and EIF5A2, to downmodulate MMP-9 expression. The result is inhibition of laminin protein degradation, leading to the closure of the morphogenetic loop (***Figure 9a***).

To demonstrate reciprocity in 3D, we selected the interaction between p53 and LN5, where a single manipulation at any part of the cycle allowed integration of all the pathways examined, PROMO analysis of the promoter of *LAMA3* chain of LN5 revealed over 20 high-confidence p53 binding sites within 1 kb length of the CpG island around the transcription start site (% dissimilarity <8%; genomic frequency $<1\times10^{-3}$) (***Figure 9b***, ***Table 8***) (***Farré et al., 2003***). Consistently, LAMA3 expression in S1 cells, could be abrogated by p53 inhibition with α-pifithrin (***Figure 9c***, ***Figure 9—figure supplement 1a***), whereas ectopic addition of LN5 or lrECM, elevated *LAMA3* transcription (***Figure 9d***, ***Figure 9—figure supplement 1b***) in parallel to the activation of wild-type p53 (***Figure 7a***, ***Figure 7—figure supplement 1a***).

To see whether there is a correlation between the wild-type p53 and LAMA3 levels *in vivo*, we performed immunohistochemical analyses of primary breast tissues using antibodies against the wildtype p53 (Clone pAb1620) and LAMA3 (Clone 546215). All normal breast tissue sections were stained strongly with both antibodies (***Figure 9—figure supplement 1c***). The reciprocity between LN5 and wild-type p53 remains strong even as cells progress to malignancy. The levels of the two proteins fell in parallel in the tumor samples ($R = 0.51$, $p<0.0001$, $n = 117$) (***Figure 9e***).

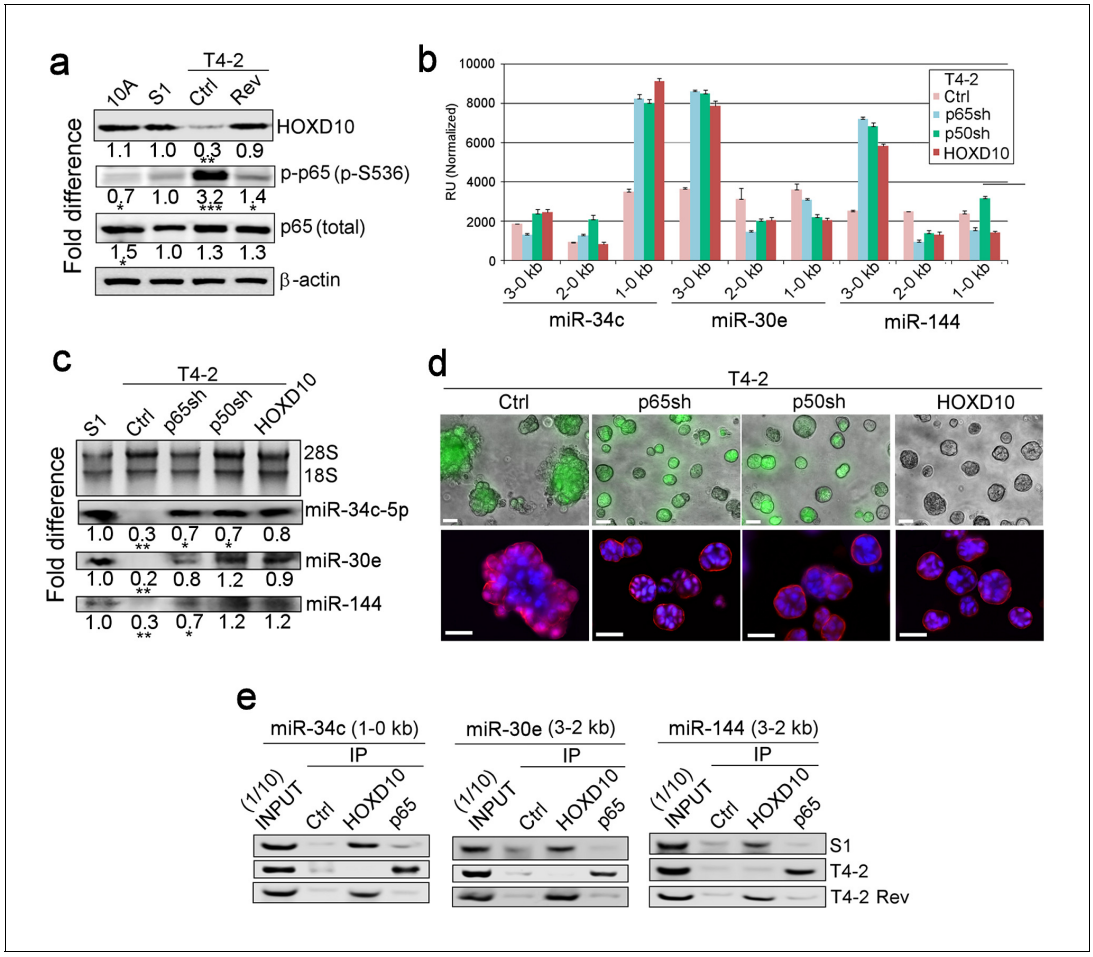

Figure 4. HOXD10 and NFκB regulate expression of the three miRNAs in opposite directions. (**a**) Representative western blot result (n = 3) for HOXD10 level, phosphorylation of p65 subunit of NFκB (p-p65, S536), and total p65 level in MCF10A, S1, T4-2 and T4-2 Rev (treated with AG1478) cells. Fold difference was determined with respect to S1 cells. *p<0.05 and ***p<0.001. Note the opposing patterns of HOXD10 and p-p65 levels. (**b**) Activities of different miRNA promoters (n = 3) in Ctrl, P65sh-, p50sh- or HOXD10-expressing T4-2 cells. Note that a 1–0 kb fragment of miR-34c promoter, a 3–0 kb fragment of miR-30e promoter and a 3–0 kb fragment of miR-144 promoter (the same regions activated in S1 and T4-2 Rev cells, ***Figure 3—figure supplement 2a***) were activated in p65sh-, p50sh- or HOXD10-expressing T4-2 cells. Data are represented as mean ± SEM. (**c**) Representative northern blot result (n = 3) for the expression of miR-34c-5p, miR-30e and miR-144 in Ctrl, p65sh-, p50sh- or HOXD10-expressing T4-2 cells. 28S and 18S serve as loading controls. Please note that for miR-30e and miR-144, both the sense (5 p) and antisense strands (3 p) are involved. *p<0.05 and **p<0.01. (**d**) Ctrl, p65sh-, p50sh- or HOXD10-expressing T4-2 cells grown in lrECM. (Top) Phase images overlaid with FITI to indicate transduced cells. (Bottom) red — integrin α6; blue — DAPI. Scale bars: 20 μm. See the quantification in ***Figure 4—figure supplement 1c***. (**e**) Representative result for ChIP analysis (n = 3) for the binding of HOXD10 and the NFκB p65 subunit on the miRNA promoters. Note that binding of HOXD10 and p65 to the mRNA promoters are mutually exclusive. See the quantification in ***Figure 4—figure supplement 1e***. For each analysis, replicate experiments (n = 3) were performed, and representative data are shown.

DOI: https://doi.org/10.7554/eLife.26148.015

The following figure supplement is available for figure 4:

Figure supplement 1. HOXD10 and NFκB positively and negatively regulate the miRNA expression, respectively.

DOI: https://doi.org/10.7554/eLife.26148.016

The essential and prominent steps of the acinar circuitry are shown in the schematic presented in ***Figure 10***.

Discussion

The ability to phenotypically revert breast cancer cells by inhibiting a single signaling pathway in 3D lrECM has provided us with the means to identify additional major signaling pathways that must

Table 7. Decoy sequences of NFκB and HOXD10 for each miRNA promoter.

miRNA promoter	TXN bound	Start from TSS	End from TSS	Predicted binding sequence	Wt decoy sequence (5′ → 3′) (Ds DNA)	Mt decoy sequence (5′→ 3′) (Ds DNA)	Transfected T4-2 cells
	Scramble				F TTGCCGTACCTGACTTAGCC		
					R GGCTAAGTCAGGTACGGCAA		
miR-34c	NFκB	−787	−778	AGGGAATCAA	F CCTTGAAAGGGAATCAATCC	F CCTTGAAAtGtAcTaAcTCC	Ctrl (pDCF1)
					R GGATTGATTCCCTTTCAAGG	R GGAgTtAgTaCaTTTCAAGG	
		−769	−760	TGGGAAGTTT	F CCTTGAATGGGAAGTTTTCC	F CCTTGAATtGtAcGgTgTCC	Ctrl (pCDF1)
					R GGAAAACTTCCCATTCAAGG	R GGAcAcCgTaCaATTCAAGG	
		−427	−418	TGGGAACCTT	F CCTTGAATGGGAACCTTTCC	F CCTTGAATtGtAcCaTgTCC	Ctrl (pCDF1)
					R GGAAAGGTTCCCATTCAAGG	R GGAcAtGgTaCaATTCAAGG	
		−64	−55	TGGGAAGCCG	F CCTTGAATGGGAAGCCGTCC	F CCTTGAATtGtAcGaCtTCC	Ctrl (pCDF1)
					R GGACGGCTTCCCATTCAAGG	R GGAAGtCgTaCaATTCAAGG	
		−56	−47	CGCTTTCCCA	F CCTTGAACGCTTTCCCATCC	F CCTTGAACtCgTgCaCcTCC	Ctrl (pCDF1)
					R GGATGGGAAAGCGTTCAAGG	R GGAgGtGcAcGaGTTCAAGG	
		-3	6	GGGGAATGAG	F CCTTGAAGGGGAATGAGTCC	F CCTTGAAGtGtAcTtAtTCC	HOXD10/ pCDF1
					R GGACTCATTCCCCTTCAAGG	R GGAaTaAgTaCaCTTCAAGG	
	HOXD10	−864	−855	AGTTTGTATT	F CCTTGAAAGTTTGTATTTCC	F CCTTGAAAtTgTtTcTgTCC	HOXD10/ pCDF1
					R GGAAATACAAACTTTCAAGG	R GGAcAgAaAcAaTTTCAAGG	
		−385	−376	CCCTTCTATT	F CCTTGAACCCTTCTATTTCC	F CCTTGAACaCgTaTcTgTCC	HOXD10/ pCDF1
					R GGAAATAGAAGGGTTCAAGG	R GGAcAgAtAcGtGTTCAAGG	
miR-30e	NFκB	−2888	−2879	GATATTCCCA	F CCTTGAAGATATTCCCATCC	F CCTTGAAGcTcTgCaCcTCC	Ctrl (pCDF1)
					R GGATGGGAATATCTTCAAGG	R GGAgGtGcAgAgCTTCAAGG	
	HOXD10	−2553	−2544	TGGTTGTATT	F CCTTGAATGGTTGTATTTCC	F CCTTGAATtGgTtTcTgTCC	HOXD10/ pCDF1
					R GGAAATACAACCATTCAAGG	R GGAcAgAaAcCaATTCAAGG	
		−2230	−2221	GCGTGATATT	F CCTTGAAGCGTGATATTTCC	F CCTTGAAGaGgGcTcTgTCC	HOXD10/ pCDF1
					R GGAAATATCACGCTTCAAGG	R GGAcAgAgCcCtCTTCAAGG	
		−2122	−2113	TTTTTTTATT	F CCT TGAATTTTTTTATTTCC	F CCTTGAATgTgTgTcTgTCC	HOXD10/ pCDF1
					R GGAAATAAAAAAATTCAAGG	R GGAcAgAcAcAcATTCAAGG	
		−1967	−1967	TACTCATATT	F CCTTGAATACTCATATTTCC	F CCTTGAATcCgCcTcTgTCC	HOXD10/ pCDF1
					R GGAAATATGAGTATTCAAGG	R GGAcAgAgGcGgATTCAAGG	
miR-144	NFκB	−3207	−3198	AGGGAATTTG	F CCTTGAAAGGGAATTTGTCC	F CCTTGAAAtGtAcTgTtTCC	Ctrl (pCDF1)
					R GGACAAATTCCCTTTCAAGG	R GGAaAcAgTaCaTTTCAAGG	
	HOXD10	−2850	−2841	AATAGAATGA	F CCTTGAAAATAGAATGATCC	F CCTTGAAAcTcGcAgGcTCC	HOXD10/ pCDF1
					R GGATCATTCTATTTTCAAGG	R GGAgCcTgCgAgTTTCAAGG	
		−2715	−2706	AATACAAAAA	F CCTTGAAAATACAAAAATCC	F CCTTGAAAcTcCcAcAcTCC	HOXD10/ pCDF1
					R GGATTTTTGTATTTTCAAGG	R GGAgTgTgGgAgTTTCAAGG	
		−2412	−2403	CCATATTATT	F CCTTGAACCATATTATTTCC	F CCTTGAACaAgAgTcTgTCC	HOXD10/ pCDF1
					R GGAAATAATATGGTTCAAGG	R GGAcAgAcTcTtGTTCAAGG	

Table 7 continued on next page

Table 7 continued

miRNA promoter	TXN bound	Start from TSS	End from TSS	Predicted binding sequence	Wt decoy sequence (5′ → 3′) (Ds DNA)	Mt decoy sequence (5′→ 3′) (Ds DNA)	Transfected T4-2 cells
		−2336	−2327	AATAAGAGTA	F CCTTGAAAATAAGAGTATCC	F CCTTGAAAcTcAtAtTcTCC	HOXD10/ pCDF1
					R GGATACTCTTATTTTCAAGG	R GGAgAaTaTgAgTTTCAAGG	
		−2312	−2303	ATTTATTATT	F CCTTGAAATTTATTATTTCC	F CCTTGAAAgTgAgTcTgTCC	HOXD10/ pCDF1
					R GGAAATAATAAATTTCAAGG	R GGAcAgAcTcAcTTTCAAGG	

Note: the transcription factor binding sites are underlined, whereas mutated nucleotides are indicated in lower case.

DOI: https://doi.org/10.7554/eLife.26148.018

integrate for the formation of 'phenotypically normal' human breast acini (***Weaver et al., 1997***; ***Muschler et al., 2002***; ***Beliveau et al., 2010***; ***Bissell and Hines, 2011***; ***Lee et al., 2012***; ***Tanner et al., 2012***; ***Becker-Weimann et al., 2013***). Here, we set out to develop a blueprint for how the breast cells interpret their interactions with the ECM proteins LN1 and LN5. The LNs trigger the signaling cascade leading to reciprocal communications between the ECM and TFs essential for mammary morphogenesis.

To do this, we used a unique breast cancer progression series, HMT3522: non-malignant S1, malignant T4-2 and T4-2 reverted to non-malignant phenotype (using five signaling inhibitors of oncogenic pathways, where addition of single inhibitors could revert the malignant phenotype). We observed that, although T4-2 Rev cells have similar phenotypes, their gene expression patterns were very different (***Becker-Weimann et al., 2013***). Nevertheless, a comparison of the gene arrays of the five T4-2 revertants identified a group of 60 similar genes that are also expressed in S1 cells (***Figure 1d***) (***Becker-Weimann et al., 2013***). This led us to propose that the common denominator of reversion had to contain a number of miRNAs that regulate this gene subset. We thus devised miRNA expression arrays and identified 10 miRNAs that fit the above category (***Figure 2a***). This result, together with the literature search (***Lu et al., 2005***) and our analysis of miRNA expression in normal- vs. cancerous- breast tissues (***Figure 2b***), identified three miRNAs (miR-34c-5p, −30e, and −144) that were shown to be severely downmodulated in primary breast tumors (***Figure 2b and c***, ***Figure 2—figure supplement 1***) (***Lu et al., 2005***). As expected, restoration of any of these three miRNAs in T4-2 cells led to phenotypic reversion in lrECM (***Figure 2e***). We utilized these miRNAs as the focal starting point to dissect the fundamental reciprocal pathways necessary for the formation and maintenance of breast tissue architecture.

It has been long known that diverse biological activities in development are regulated by tissue–tissue and tissue–microenvironment interactions and signaling (***Wessells, 1977***; ***Chiquet-Ehrismann et al., 1986***; ***Howlett and Bissell, 1993***; ***Hogan, 1999***; ***Bhat and Bissell, 2014***). During development, different cell types communicate and coordinate with each other through negative and positive feedback regulations. Within a given tissue, there are also negative and positive operators that must be regulated constantly to maintain homeostasis and quiescence as we demonstrated here. In addition, similar to movements that are being discovered in the formation of embryos during development (***Haigo and Bilder, 2011***), tissue formation starts with cells moving within a soft microenvironment such as lrECM, as we and others observed for mammary acini; we termed this 'coherent angular motion' (***Tanner et al., 2012***). CAMo creates polarity and adhesion by interacting with exogenous ECM to lay down its own endogenous tissue-specific ECM (***Tanner et al., 2012***).

The balance and integration of the different signaling pathways and dynamic interactions between epithelial cells and the ECM drive the remodeling of the ECM, including formation of the BM that helps to anchor the epithelia (***Weaver et al., 2002***) and that protects the cells within the tissues from apoptosis. Such changes in the ECM regulate cell proliferation, survival, migration, shape and adhesion, ultimately sculpting and maintaining tissue architecture (***Wessells, 1977***; ***Chiquet-Ehrismann et al., 1986***; ***Howlett and Bissell, 1993***; ***Hogan, 1999***; ***Bhat and Bissell, 2014***; ***Haigo and Bilder, 2011***; ***Weaver et al., 2002***; ***Daley and Yamada, 2013***). There are important

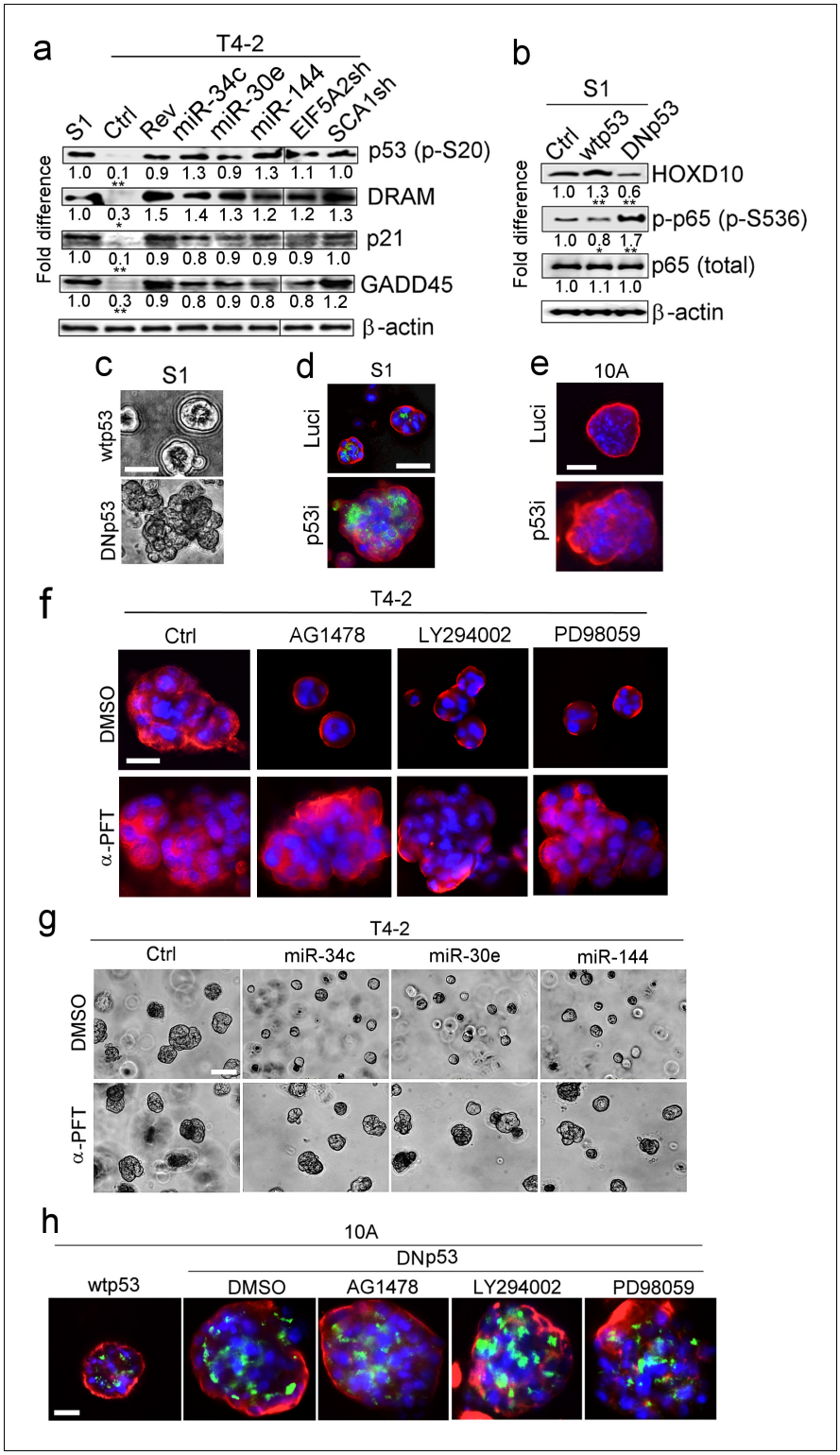

Figure 5. p53 activation is another requirement for tumor-cell reversion by the miRNAs. (**a**) Representative result of western analysis (n = 3) for the level and activation of proteins in the p53 pathway [p53 (p-Ser20), DRAM, p21 and GADD45] in S1, T4-2 and T4-2 Rev cells. T4-2 Rev cells include those treated with AG1478, those expressing the three miRNAs and those depleted of the two target genes (EIF5A2 and SCA1). Fold difference was determined with respect to S1 cells. *p<0.05 and **p<0.01. (**b**) Representative result of western analysis (n = 3) for the activities of HOXD10 and p65 (p-p65) in Ctrl S1 cells and in S1 cells that were overexpressing the wild-type (wt) or dominant-negative mutant (DN) p53. Note the opposing effects of wtp53 or DNp53 expression on HOXD10 vs.

Figure 5 continued on next page

Figure 5 continued

p-p65. Fold difference was determined with respect to Ctrl S1. *p<0.05 and **p<0.01. (**c**) Representative image for S1 cells overexpressing wtp53 (top) or DNp53 (bottom) grown in lrECM. Ctrl S1 cells were un-transduced. See the quantification of 3D colony size in ***Figure 5—figure supplement 1a***. (**d**) Representative image for Ctrl S1 (top) and S1 cells depleted of p53 (bottom) grown in lrECM. Red — α6, green; apical marker GM130. See the confirmation of p53 depletion and quantification of the 3D colony size in ***Figure 5—figure supplement 1b***. (**e**) Representative image for Ctrl MCF10A cells (top) and MCF10A cells depleted of p53 (bottom) grown in lrECM. See the confirmation of p53 depletion and quantification of the 3D colony size in ***Figure 5—figure supplement 1c***. (**f**) Representative image of 3D morphologies of T4-2 cells co-treated with a reverting agent [AG1478 (EGFR inhibitor), LY294002 (PI3K inhibitor) or PD98059 (MEK inhibitor)] along with p53 inhibitor α-pifithrin (α-PFT). Note that α-PFT treatment abrogated reversion of T4-2 cells. See the quantification of 3D colony size in ***Figure 5—figure supplement 1d***. (**g**) Representative image of 3D morphologies of miRNA-overexpressing T4-2 cells co-treated with a reverting agent [AG1478 (EGFR inhibitor), LY294002 (PI3K inhibitor) or PD98059 (MEK inhibitor)] along with p53 inhibitor α-pifithrin (α-PFT). Note that α-PFT treatment abrogated the reversion of T4-2 cells after expressing miRNAs. See the quantification of the 3D colony size in ***Figure 5—figure supplement 1e***. (**h**) Representative image of 3D morphologies of DNp53-expressing MCF10A cells treated with a reverting agent [AG1478 (EGFR inhibitor), LY294002 (PI3K inhibitor) or PD98059 (MEK inhibitor)]. Note that DNp53-expressing cells are more proliferative, fail to form acini and are resistant to a reverting agent. See the quantification of the 3D colony size in ***Figure 5—figure supplement 1f***. Red — integrin α6; green — Golgi marker, GM130; and blue — DAPI. Scale bars: 20 μm. For each analysis, replicate experiments (n = 3) were performed, and representative data are shown.

DOI: https://doi.org/10.7554/eLife.26148.019

The following figure supplement is available for figure 5:

Figure supplement 1. p53 activation is essential for acinar formation and tumor-cell reversion.

DOI: https://doi.org/10.7554/eLife.26148.020

differences, however, between developmental processes and tissue maintenance and renewal (***Howlett and Bissell, 1993***; ***Hogan, 1999***; ***Bhat and Bissell, 2014***; ***Daley and Yamada, 2013***). Unlike the signaling pathways in development, the stability of the differentiated state does not appear to be hierarchical. Instead, it reflects the balance between growth and differentiation, between the negative and positive signaling pathways, and between the formation of a BM and the destruction of ECM by degrading enzymes that determines the stability of the differentiated state in the tissues.

Another novel finding here is that NO is a pivotal player in reciprocal cell–ECM interactions in breast morphogenesis, but tumor cells produce only a small amount of NO unless the architecture is re-established and the cells have reverted to a 'dormant state' (***Figure 7c–e and g***). This is a mimicry of differentiation-dependent tissue architecture. These findings demonstrate that NO production is a mechanistic link between proper architecture and proper function in breast tissues. Please see also the accompanying paper of ***Ricca et al., 2018***, which describes how the reversion of T4-2 cells induced by a short period of compression in laminin is also mediated by NO production.

There are a few papers in the literature on connections between LN1 and NO in other tissues (***Rialas et al., 2000***; ***Gloe et al., 1999***), and there are other reports of activation of p53 by high levels of exogenous NO (***Forrester et al., 1996***; ***Gordon et al., 2001***; ***Wang et al., 2003***). To our knowledge, however, there are no reports of endogenous NO as a critical link in the formation of mammary epithelium and its role in stability of the tissue architecture.

It is crucial to note that the levels of NO produced endogenously in response to LNs in our studies, as well as the exogenous NO levels required for the reciprocal loop we describe here, are at least *500-fold lower* than those used in the literature (***Forrester et al., 1996***; ***Gloe et al., 1999***; ***Gordon et al., 2001***). As stated long ago, differences in quantity of such magnitudes becomes a change in quality and hence have appreciable consequence (***Bissell, 1981***).

NO has been reported to play an important role during lactation. Increased levels of NO are produced by the mammary gland of postpartum mammals (***Akçay et al., 2002***). NO promotes blood flow and the nutrient uptake of mammary glands for milk production (***Kim and Wu, 2009***). NO is also proposed to facilitate milk ejection by inducing contraction of myoepithelial cells (MEPs) in mammary glands as well as smooth muscle cells in the stroma (***Iizuka et al., 1998***; ***Adriance et al., 2005***; ***Tezer et al., 2012***). In addition, NO is secreted into the breast milk as an essential component

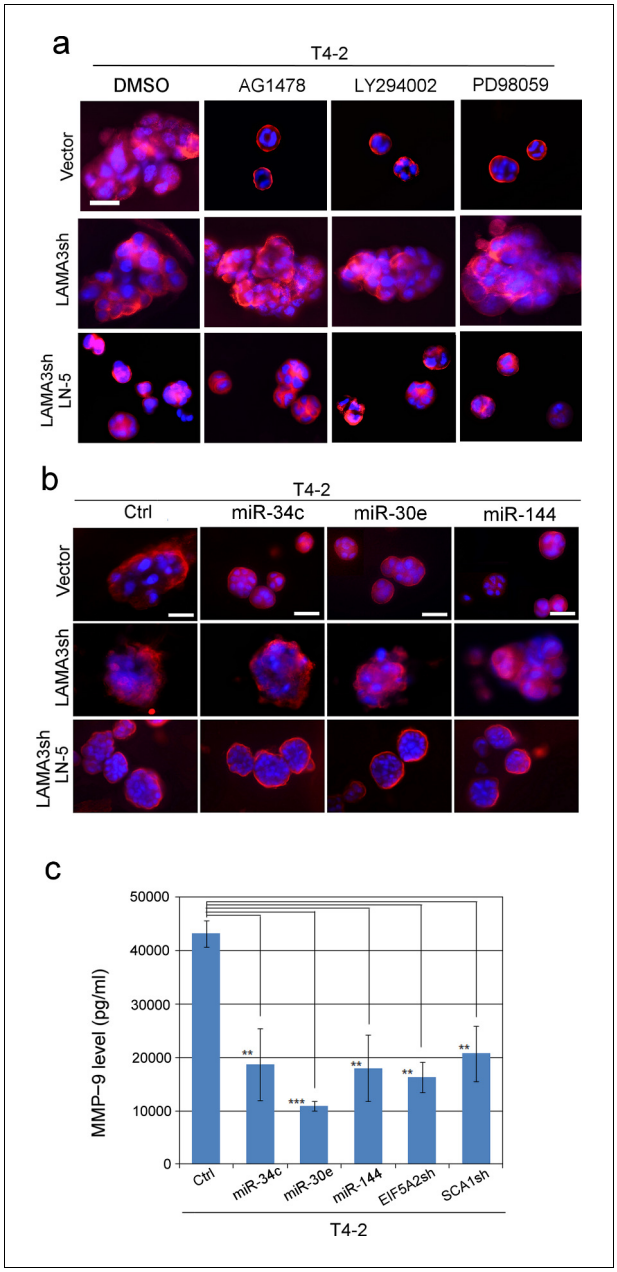

Figure 6. MMP-9 degrades LN5 and prevents tumor-cell reversion; miRNAs' ability to revert T4-2 cells is connected to inhibition of MMP-9 and the rescue of LN5. (**a**) Representative images of repricate experiments (n = 3) of 3D morphologies of T4-2 cells (vector, LAMA3sh, LAMA3sh + LN5) reverted with a reverting agent, AG1478, LY294002 or PD98059. See the quantification of the 3D colony size in ***Figure 6—figure supplement 2a***. Note that the depletion of LAMA3 abrogated the reverting effect, which was rescued by ectopic addition of LN5 (1 μg/ml). Red — α6 integrin; blue — DAPI. Scale bars: 20 μm. (**b**) Representative images of replicate experiments (n = 3) of 3D morphologies of T4-2 cells (vector, LAMA3sh, LAMA3sh + LN5) overexpressing individual miRNAs. See the quantification of the 3D colony size in ***Figure 6—figure supplement 2b***. Note that the depletion of LAMA3 abrogated the reverting effect of the miRNAs, which was rescued by ectopic addition of LN5. (**c**) The mean MMP-9 level (n = 9) in the CM of T4-2 cells, T4-2 cells expressing one of the three miRNAs or T4-2 cells depleted of the two target genes, EFI5A2 and SCA1, was determined 24 hr after addition of lrECM (5% Matrigel). The concentration of MMP-9 was determined using the MMP-9 standard. Data represented as mean ± SEM. **p<0.01 and ***p<0.001.

DOI: https://doi.org/10.7554/eLife.26148.021

The following figure supplements are available for figure 6:

Figure 6 continued on next page

Figure 6 continued

Figure supplement 1. LN5 expression is upregulated in T4-2 cells overexpressing the three miRNAs or depleted of their target genes.

DOI: https://doi.org/10.7554/eLife.26148.022

Figure supplement 2. LN5 expression is required for reversion of tumor cells in 3D.

DOI: https://doi.org/10.7554/eLife.26148.023

for immunity in neonatal growth (***Hord et al., 2011***). Using 3D cultures and *ex vivo* cultures of human mammary glands, we showed here that NO also plays additional and significant roles in breast morphogenesis (***Figure 8a, b and d***).

Importantly, NO production was specific to LNs and was not induced by collagen (***Figure 7c-e***). We and others had shown previously that LNs and COL1 elicit opposite actions on epithelia (***Gudjonsson et al., 2002***; ***Oktay et al., 2000***; ***Chamoux et al., 2002***). We showed here that LNs activate NOS-1 (***Figure 7a***, ***Figure 7—figure supplement 1a***), supporting previous observations by others that NOS-1 is expressed in the mammary tissue at appreciable levels — in particular in MEPs during pregnancy and lactation in humans (***Tezer et al., 2012***) and rodents (***Iizuka et al., 1998***; ***Islam et al., 2009***; ***Wockel et al., 2005***). As the molecule that appears to be responsible for linking LNs to NOS-1, we speculate the involvement of the LN receptor, dystroglycan (DG), which is known to form a multi-protein complex involving LNs and NOS-1, in mediating the mechanotransduction of muscle cells (***Rando, 2001***; ***Garbincius and Michele, 2015***). We had shown previously that DG also plays a critical signaling role in breast epithelial cells (***Muschler et al., 2002***). DG anchors the BM protein, in particular LNs, to the cell surface, allowing for LN polymerization and transduction of signals for the formation of polarized colonies (***Weir et al., 2006***). Such DG–LN interaction is impaired in different types of cancer cells and correlates with poorer patient prognosis (***Akhavan et al., 2012***; ***Esser et al., 2013***).

Form and function are maintained in adult organs throughout most of the life of the organism, despite constant mutations and damage from environmental assaults and aging. To maintain the correct tissue function throughout the lifetime of the organisms, signaling pathways have to integrate in order to prevent chaos and malfunction. Evolution has packed much wisdom and specificity onto the ECM, which appears to instruct the chromatin to change shape and thus also gene expression, as seen in ***Figure 4e***. When cells on flat surfaces receive LNs, not only their shape, but also many of their signaling pathways are altered (***Figure 1***) (***Bissell et al., 2005***); growth must stop in many tissues (***Spencer et al., 2011***; ***Fiore et al., 2017***) and differentiation and cell death must be coordinated. It is now clear that narratives that are based solely on linear and irreversible regulatory dynamics cannot satisfactorily explain the reality *in vivo* (***Hogan, 1999***). It is also clear that, at the last analysis, it is the 3D architecture of the tissue itself that is the message (***Hagios et al., 1998***).

Materials and methods

Cell lines

Cell lines of the HMT3522 breast cancer progression series (S1 and T4-2) were provided by O.W. Petersen (Laboratory of Tumor Endocrinology, The Fibiger Institute, Copenhagen, Denmark) (***Briand et al., 1996***). The cell lines were authenticated by genome sequencing by the provider. Mycoplasma testing was negative. MCF10A cells were obtained from the Karmanos Cancer Institute (Detroit, MI, USA) under a Material Transfer Agreement. The cell lines was authenticated by the provider. Mycoplasma testing was negative.

Cell culture and reagents

The isogenic cell lines of the HMT3522 human breast cancer progression series, non-malignant S1 and malignant T4-2 cells, were maintained as described previously (***Briand et al., 1996***). This cell line series was established in an attempt to recapitulate the stochastic and prolonged nature of breast cancer progression by continuously culturing S1 cells, derived from reduction mammoplasty, in the absence of serum, followed by EGF removal and injection into mice, to give rise to T4-2 cells (***Briand et al., 1996***). For 3D culture experiments, S1 and T4-2 cells were seeded at the density of

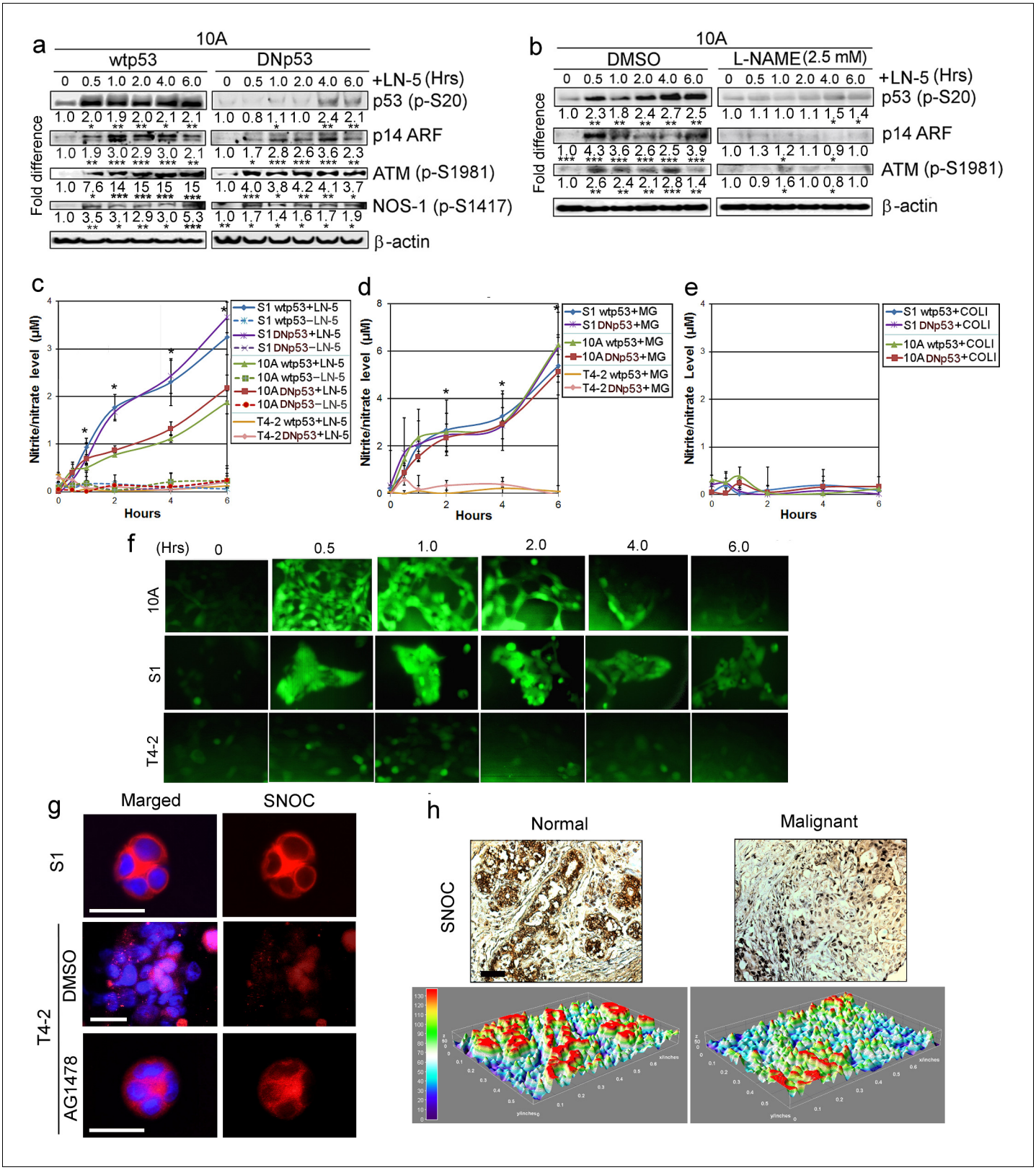

Figure 7. LNs activate p53 through production of NO. (**a**) Representative results of western analysis (n = 3) for MCF10A cells expressing either wtp53 or DNmtp53, showing the level of activated p53 (p-Ser20) after addition of exogenous LN5 (1 μg/ml). Other lanes indicate the levels of p14 ARF and activation of ATM and NOS-1 after LN5 addition. Fold differences were determined first by normalization with respect to β-actin and then by normalization with respect to the value at time 0. *p<0.05; **p<0.01 and ***p<0.001. See similar results after the addition of Matrigel (5%) in ***Figure 7—***

Figure 7 continued on next page

Figure 7 continued

figure supplement 1a. (**b**) Representative results of western analysis (n = 3) showing the levels of activation of ATM, p14 ARF and p53 in the absence or the presence of an NO inhibitor, L-NAME. (**c–e**) The mean level of NO metabolites (nitrite or nitrate, n = 9) in CM after addition of LN5 (1 μg/ml) (**c**), lrECM (5% Matrigel) (**d**) or COL1 (500 μg/ml) (**e**); please note that this amount is equivalent to the total protein level of 5% Matrigel. Nitrite or nitrate level was determined with a fluorescent probe DAN using the nitrite/nitrate standard. Data are represented as mean ± SEM. *p<0.05. Note that S1 and MCF10A cells, but not T4-2 cells, produced NO in response to LN5 (**c**) and lrECM (**d**), irrespective of whether they express wild-type or mutant p53. (**e**) COL1 did not induce NO production. (**f**) Representative images (n = 3) showing the level of intracellular NO in MCF10A, S1 and T4-2 cells after addition of 5% MG, as determined with a fluorescent NO probe DAF-FM DA. See the quantification of NO level in ***Figure 7—figure supplement 1b***. (**g**) Representative images (n = 3) of S-nitrosocysteine (SNOC, NO indicator)-stained HMT3522 cells (S1, T4-2 and T4-2 Rev cells with AG1478) in lrECM cultures for 1 wk. Note that SNOC was enriched in the basolateral surface of S1 and T4-2 Rev cells, whereas it was weakly diffused in T4-2 cells treated with DMSO. Red —SNOC; blue — nuclei. Scale bars: 20 μm. (**h**) Representative images of normal (n = 8) vs. cancerous (n = 32) breast tissues stained for SNOC presented as IHC (top) and heat map of surface plot (bottom). Positive staining (intensity >+1): 8/8 for normal vs. 8/32 for cancerous tissues. Scale bars: 50 μm.

DOI: https://doi.org/10.7554/eLife.26148.024

The following figure supplement is available for figure 7:

Figure supplement 1. Acinar-forming breast cells produce NO in response to LNs.

DOI: https://doi.org/10.7554/eLife.26148.025

2.5×10^4 cells/cm^2 and 1.8×10^4 cells/cm^2, respectively, in growth factor reduced Matrigel (Corning, NY, USA) and maintained for 10 days with the addition of fresh medium on alternate days. For T4-2 reversion, EGFR inhibitor AG1478 (EMD Millipore, Burlington, MA, USA) was used at 350 nM, PI3K inhibitor LY294002 at 8 μM, and MEK inhibitor PD98059 at 20 μM (***Lee et al., 2012***). For p53 inhibition, 30 μM α-PFT (α-pifithrin, Sigama-Aldrich, St. Louis, MO, USA) was used. For inhibition of NO production, cells were treated with 2.5 mM L-NAME (N_ω-Nitro-L-arginine methyl ester hydrochloride, Sigma- Aldrich); for induction of NO production, 10 μM SNAP (S-Nitroso-N-acetyl-DL-penicillamine, Sigma- Aldrich) was used.

miRNA array

miRNA expression profiling was performed using the RT^{2}miRNA PCR Array System (Qiagen, Inc. USA, Germantown, MD, USA) on the MyiQ Single-Color Real-Time PCR platform (Bio-Rad, Hercules, CA, USA). Briefly, 1.0×10^6 cells were grown in 1.2 ml Matrigel in 30 mm-plates for 10 days (for T4-2 Rev, 350 nM AG1478 was added). The medium was removed and cells were scraped off from the dish with 2 ml phosphate-buffered saline (PBS) with 5 mM EDTA. Cells were spun down to harvest pellets, which were repetitively washed with ice-cold PBS + EDTA until the Matrigel was dissolved. The total RNA was extracted with 1 ml Trizol (Life Technologies) and purified with an RNeasy plus mini kit (Qiagen, Inc, USA) according to the manufacturers' protocols. cDNA was generated from 4 μg of RNA using the RT^{2}miRNA First Strand Kit (SABiosciences), mixed with SYBR Green Master Mix (SABioseicences) and loaded onto an array with 98 wells. Real-time PCR was performed according to the manufacturer's instructions, and data analysis was performed using the manufacturer's PCR Array Data Analysis Web Portal (Qiagen, Inc, USA).

Northern analysis

Northern analysis of miRNAs was performed using the DIG detection system from Roche. Briefly, 1.0×10^6 cells/30-mm plate were grown in 1.2 ml Matrigel in triplicates for 10 days (for T4-2 Rev, 350 nM AG1478 was added). Cells were scraped off from the dish with PBS with 5 mM EDTA, spun down and washed with PBS + EDTA until the Matrigel was dissolved. The total RNA was extracted with 1 ml Trizol (ThermoFisher Scientific, Waltham, MA, USA). 20 μg of RNA was separated by denaturing polyacrylamide TBE-Urea gel electrophoresis (ThermoFisher Scientific) and electroblotted onto Bright-Star nylon membrane (Ambion) with 0.5% TBE for 2 hr. The membrane was rinsed in 2xSSC buffer, UV cross-linked at 120 mJ/cm^2, dried and stored between filter papers. LNA-modified DNA oligonucleotides complementary to the mature miRNA sequences (***Table 9***) were obtained from IDT and DIG-labeled using the DIG Oligonucleotide Tailing Kit (Roche Diagnostics, USA, Indianapolis, IN, USA). Using DIG Easy Hyb (Roche Diagnostics, USA), the membrane was prehybridized and hybridized with DIG-labeled probe at room temperature overnight. The membrane was washed

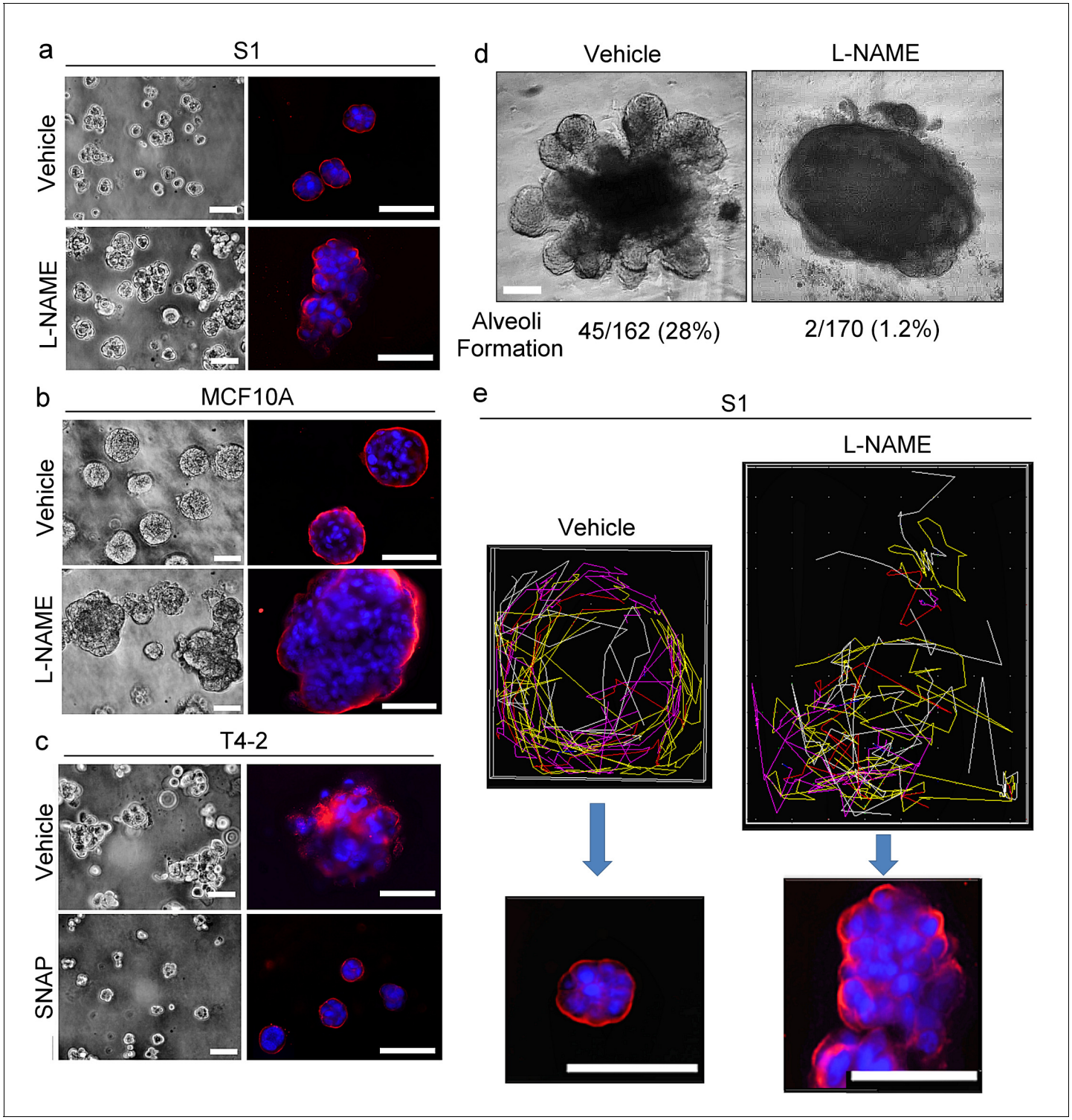

Figure 8. NO is involved critically in breast acinar formation and mammary gland morphogenesis. (**a–b**) Representative images (n = 3) of S1 (**a**) and MCF10A (**b**) cells grown in lrECM in the absence (vehicle only) or presence of an NO inhibitor, L-NAME (2.5 mM). Scale bars: 20 μm. (**c**) Representative image (n = 3) of T4-2 cells grown in lrECM in the absence (vehicle only) or presence of an NO donor, SNAP (10 μM). (**a–c**) (Left) Phase images. (Right) Cells stained for integrin α6 (red) and nuclei (blue). Scale bars: 20 μm. See the quantification of colony size in ***Figure 8—figure supplement 1a–c***. (**d**) Representative images of *ex vivo* cultures of normal human mammary gland organoids grown in lrECM for 1 week. The numbers of organoids that underwent alveologenesis were 45 out of 162 vehicle-treated, and only 2 out of 170 L-NAME-treated organoids. (**e**) (Top) Representative result (n = 5) of tracking analysis for the movement of S1 cells during 48 hr of growth in lrECM in the absence (vehicle only) or presence of L-NAME. (Bottom) Representative image of the colonies (n = 5) formed by cells after respective treatments for 10 days. Red — integrin α6; blue —nucleus. Scale bars: 50

Figure 8 continued on next page

Figure 8 continued

µm. Note that vehicle-treated S1 cells moved in a coherent rotatory fashion in a confined area, whereas L-NAME-treated S1 cells moved in a disorganized fashion in a larger area.

DOI: https://doi.org/10.7554/eLife.26148.026

The following figure supplement is available for figure 8:

Figure supplement 1. NO is critical for breast cells to form growth-arrested colonies in 3D.

DOI: https://doi.org/10.7554/eLife.26148.027

in 10xSSC + 0.1% SDS four times and processed for DIG detection using the DIG Luminescent Detection Kit (Roche) according to the manufacturer's protocol.

miRNA *in situ* hybridization (ISH)

miRNA *in situ* hybridization (ISH) was performed using the miRCURY LNA miRNA ISH Optimization kit for formalin-fixed paraffin embedded (FFPE) tissues (Qiagen, Inc, USA) and double-DIG-labeled detection probes for miR-34c-5p, miR-30e and miR-144 (EXIQON) on breast cancer tissue arrays containing paraffin-embedded sections of normal and malignant (stages II and III) tissues (US Biomax, Inc, Rockville, MD, USA). Briefly, the tissue slides were heated at 60˚C for 1 hr, deparaffinized in xylene and hydrated in alcohol series (100% to 70%). Slides were deproteinated with proteinase K for 20 min, fixed in 4% paraformaldehyde for 10 min and washed with 0.2% glycine in PBS for 5 min. Then, slides were incubated in imidazole buffer (0.13 M 1-methylimidazole, 300 mM NaCl, pH 8.0) for 10 min twice, in EDC solution (0.16M 1-ethyl-3-[3-dimethylaminopropyl] carbodiimide [EDC], pH 8.0) for 1.5 hr and washed with 0.2% glycine in PBS. Then, slides were dehydrated in an alcohol series (70% to 100%), hybridized with heat-denatured probes at room temperature overnight, and processed for DIG detection according to the manufacturer's protocol (Qiagen, Inc, USA). The slides were counterstained with Nuclear Fast Red and mounted with permount. Photomicrographs were taken with the Zeiss Axioskop Imaging Platform and Axion Vision software (Version 4.7).

miRNA expression constructs

Lentivector-based precursor constructs for miR-34c-5p, miR-30e and miR-144 co-expressing copGFP were obtained from System Biosciences Palo Alto, CA, USA, and the virus particles to express each miRNA were produced according to the manufacturer's guideline.

Gene-overexpressing lentiviral constructs

For construction of HOXD10-overexpressing lentivirus, the full-length human HOXD10 cDNA clone was obtained from Open Biosystems (Lafayette, CO, USA, Clone ID: 7262455). For construction of p53-overexpressing lentivirus, both wild-type and dominant-negative (A135V) p53 expression plasmids were obtained from Clontech. The coding region was PCR-amplified using the respective primers (***Table 9***). The PCR product was ligated into the *Ascl*/*EcoR*1 site (for HOXD10) or the *BamHI*/*EcoR*1 site (for p53) of the PCDF1-MCS2-EF1-puro lentiviral vector (System Biosciences). For the SCA1- and EIF5A2-overexpression lentivirus construct, the cDNA clones were obtained from Origene (Rockville, MD, USA, Cat#RC222862 and Cat#RC206249, respectively) and cloned into PCDF1-MCS2-EF1-puro lentiviral vector at the *BamHI*/*EcoR*1 site using the Gibson assembly system and a DNA assembly kit (Cat# E5520S, NEB) with the primers designed on the NEB Builder Assembly Tool website as shown in ***Table 9***.

Gene knockdown by shRNA

For shRNA production, a double-stranded DNA oligonucleotide was generated from the respective sequences (***Table 9***). Sense and antisense oligonucleotides were annealed and ligated into *Bam*H1/*Eco*R1 site of pGreen puro lentival vector which co-expresses copGFP (System Biosciences).

Lentivirus production and transduction

Lentivirus production and transduction of target cells were conducted following the guideline by System Biosciences. Briefly, lentivirus vector and packaging plasmid mix (System Biosciences) were transfected into 293FT cells (ThermoFisher Scientific) using Lipofectamine 2000. After 48 hr, medium

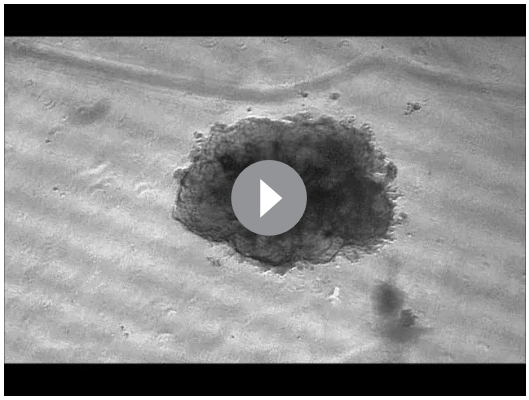

Video 1. Representative movie of alveologenesis of normal human mammary gland organoids in *ex vivo* 3D culture for 2 weeks.
DOI: https://doi.org/10.7554/eLife.26148.028

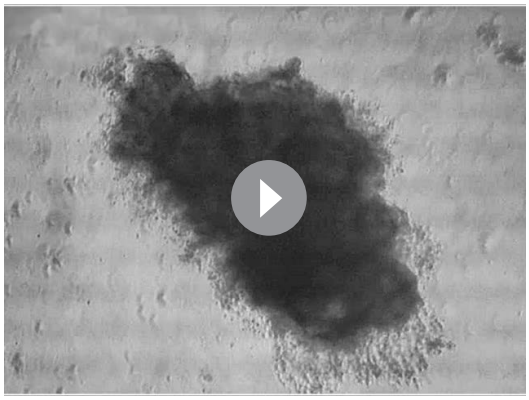

Video 2. Representative movie of impaired alveologenesis of L-NAME-treated normal human mammary gland organoids in *ex vivo* 3D culture for 2 weeks.
DOI: https://doi.org/10.7554/eLife.26148.029

was harvested, filtered and used to infect target cells with the addition of polybrene (10 µg/ml). The medium was replaced after 24 hr. At 72 hr post-infection, puromycin (0.5 µg/ml) was added for selection and maintained throughout the culturing period.

RT-PCR

One million cells were grown in 1.2 ml Matrigel on a 30-mm plate for 10 days (for T4-2 Rev, 350 nM AG1478 was added). The medium was removed and cells were scraped off from the dish with 2 ml PBS with 5 mM EDTA. They were then spun down to harvest the cell pellet and repeatedly washed with PBS + EDTA until Matrigel was dissolved. The total RNA was extracted with 1 ml Trizol (ThermoFisher Scientific). cDNA was synthesized from 2 µg RNA using the SuperScript Double-Stranded cDNA Synthesis Kit (Invitrogen) and served as a template for PCR amplification with the respective primers (***Table 9***).

Immunofluorescence staining

Immunofluorescence was performed as described previously (***Weaver et al., 1997***). Samples were incubated with primary antibody for 2 hr at room temperature in a humidified chamber. After intensive washing (three times, 15 min each) in 0.1% BSA, 0.2% Triton-X 100, 0.05% Tween 20, 0.05% NaN3 in PBS, fluorescence-conjugated secondary antibodies (Molecular Probes) were added for 1 hr at room temperature. Nuclei were stained with 0.5 ng/ml DAPI.

Soft agar assay

One percent agar was mixed with the equivalent volume of 2x DMEM/F12 medium supplemented with all the additives necessary for culturing T4-2 cells (***Briand et al., 1996***) plus 20% FBS and 2% penicillin or streptomycin. 1 ml of the agar solution was poured into a 35 mm plate in triplicate and solidified. 0.7% agar solution equilibrated to 40˚C was mixed with 2x growth medium and breast cancer cells at 7000 cells/ml and poured onto the base agar at 1 ml/plate. The solidified agar was covered with 500 µl growth medium and maintained in a 37˚C humidified incubator for 14 d. The plates were stained with 0.01% crystal violet for 30 min, and colonies were counted under a dissecting microscope.

Luciferase reporter assay

For generation of miRNA reporter constructs, the promoter regions of miRNA genes were obtained by PCR-amplifying BAC genomic clones [miR-34c (Ch11), PR11-794P6; miR-30e (Ch1), RP11-576N9; miR-144 (Ch17), RP11-832J20] using the respective primers (***Table 9***) and inserted into the pGL3 luciferase expression vector. Cells seeded at 5×10^5 cells/60-mm plate were transfected with 7 µg

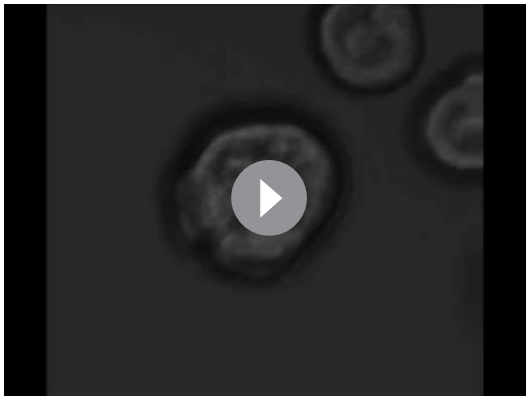

Video 3. Representative time-lapse movie of S1 cells undergoing coherent axial rotation in lrECM culture for 48 hr.
DOI: https://doi.org/10.7554/eLife.26148.030

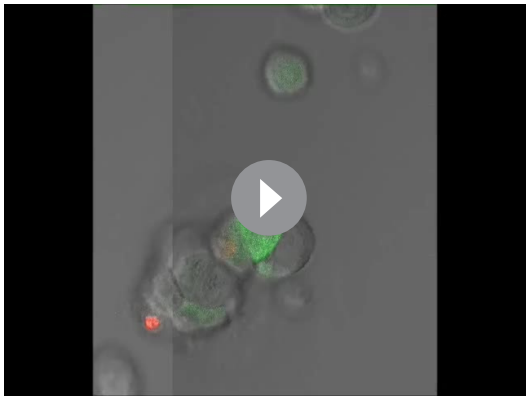

Video 4. Representative time-lapse movie of L-NAME-treated S1 cells undergoing stochastic amoeboid movement in lrECM culture for 48 hr.
DOI: https://doi.org/10.7554/eLife.26148.031

of luciferase reporter and 0.5 µg of β-galactosidase plasmids using Xfect transfection reagent according to the manufacturer's protocol (Clontech, Mountain View, CA, USA). After 24 hr post transfection, the medium was replaced with the fresh medium containing 5% Matrigel and cells were maintained for another 24 hr (for T4-2 Rev, 350 nM AG1478 was added). Luciferase and β-galactosidase reporter activities were measured using a reporter assay kit (Promega, Madison, WI, USA).

Decoy analysis

Wild-type miRNA decoy sequences (***Table 7***) were derived from the binding sites of NFκB or HOXD10 within the miRNA promoters predicted by AlGGEN PROMO software (see below). The sequence-specific binding of the two TFs was tested using mutant decoys (***Table 7***) that had point mutations in their core binding sequences. The forward and reverse oligonucleotides of decoys at 100 µM each were annealed in Duplex buffer (Integrated DNA Technologies, Coralville, IA, USA, CAT#11-05-01-12), and the same group of decoys was pooled. T4-2 cells were plated at 0.5×10^5/12 wells the day before transfection. NFκB decoys (scramble, WT or MT), along with miRNA promoters fused to luciferase (see above), were transfected into control T4-2 cells that had a high endogenous level of NFκB. HOXD10 decoys (scramble, WT or MT), along with promoter constructs, were transfected into T4-2 cells that overexpressed HOXD10. Transfection was performed with 1 µl XFect transfection reagent (Clontech, cat# 631318), 1.5 µg of promoter DNA and 200 nM of decoy oligonucleotides according to the manufacturer's protocol. Cells were harvested at 48 hr post transfection. The luciferase activity was analyzed using the Bright-Glo Luciferase assay system (E2610, Promega) according to the manufacturer's protocol, and the activity was normalized using protein concentration.

Analysis of transcription factor (TF) binding sites

TF binding sites within the promoter regions were predicted by AlGGEN PROMO software (http://alggen.lsi.upc.es/cgi-bin/promo_v3/promo/promoinit.cgi?dirDB=TF_8.3) (***Farré et al., 2003***). The feasibility of these predicted sites was indicated as the 'Dissimilarity' to the canonical sequence (0% as the best match). The significance of the predicted site was indicated as the 'Frequency' in the genomic background ('Random Expectancy' (RE) value x 10^{-3}) (***Farré et al., 2003***).

Chromatin Immunoprecipitation (ChIP)

ChIP assays were performed as described by ***Saccani et al. (2001)*** with a minor modification. Cells were plated at 2×10^6/100-mm plate and maintained overnight. Then, cells were maintained in the fresh medium containing 5% Matrigel for 24 hr (for T4-2 Rev, 350 nM AG1478 was added). Cells placed in fresh medium with 1% formaldehyde for 10 min, scraped off from the dish with PBS and processed for nuclear extraction. Chromatins were sonicated to ~500 bp fragments and

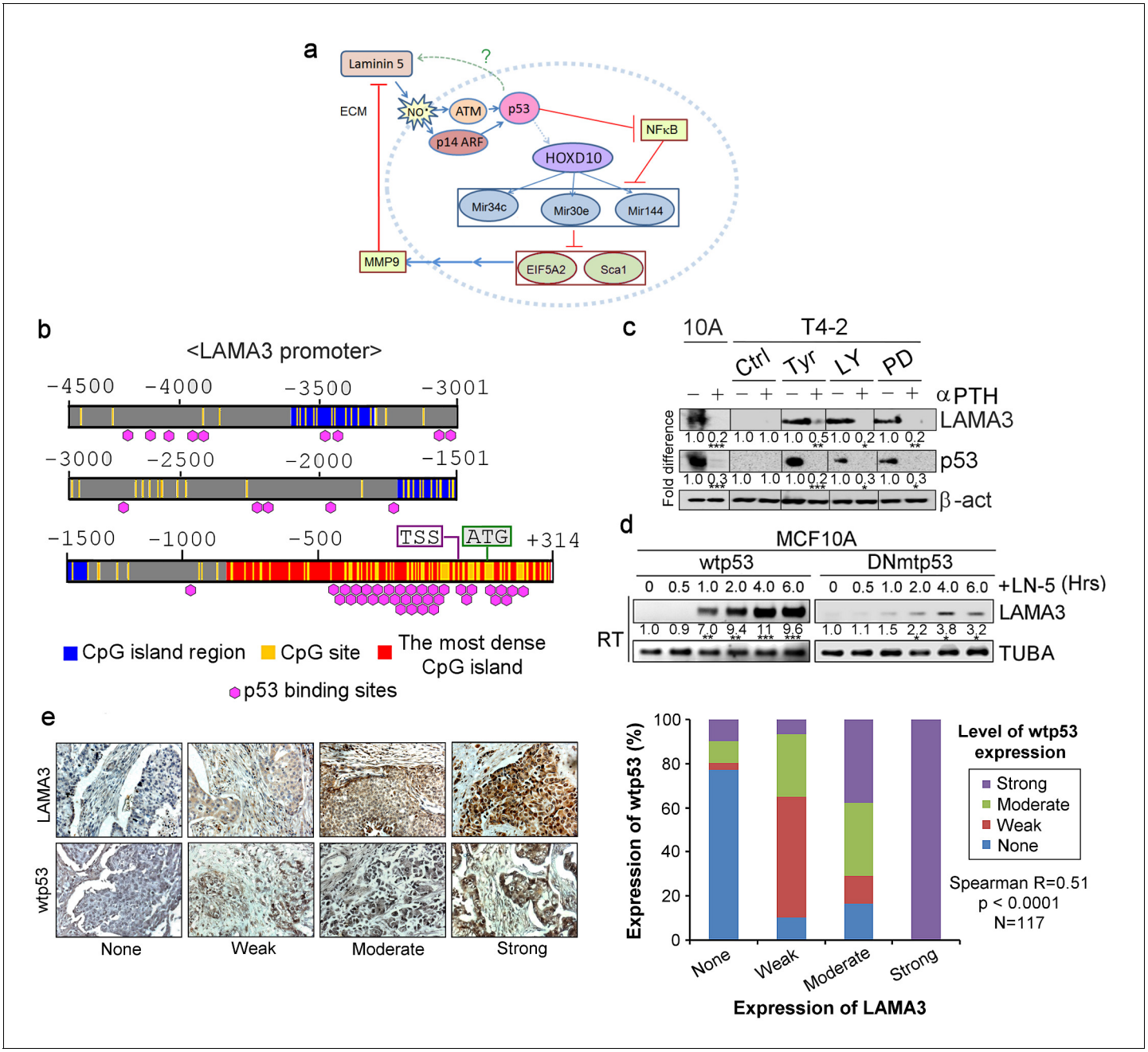

Figure 9. Activated p53 in turn upregulates expression of the endogenous alpha chain of LN5. (**a**) A schematic of the morphogenetic loop dissected to date with a predicted feedback loop between p53 and LN5. (**b**) The promoter region of the *LAMA3* gene contained the CpG island that harbors numerous p53-binding sites around the transcription start site (TSS). (**c**) Representative result of western analysis (n = 3) for LAMA3 expression in T4-2 cells treated with a reverting agent (AG1478, LY294002 or PD98059) in the absence or presence of a p53 inhibitor, α-PFT. β-actin serves as a loading control. Fold difference was determined with respect to the Ctrl T4-2. *p<0.05; **p<0.01 and ***p<0.001. For each analysis, replicate experiments (n = 3) were performed, and representative data are shown. (**d**) Representative result of RT-PCR analysis (n = 3) showing that exogenous LN5 (1 μg/ml) upregulated *LAMA3* transcription in MCF10A cells expressing wild-type p53, but not in cells expressing DNp53. α-tubulin (TUBA) was used as a control. Fold difference was determined with respect to time 0. *p<0.05; **p<0.01 and ***p<0.001. (**e**) (Left) Representative images of the IHC staining of breast cancer tissues (n = 117) for LAMA3 and wild-type p53. (Right) Correlation analysis between LAMA3 expression and wild-type p53 expression in breast tumors.

DOI: https://doi.org/10.7554/eLife.26148.032

The following figure supplement is available for figure 9:

Figure supplement 1. LAMA3 expression depends on p53 activation.

DOI: https://doi.org/10.7554/eLife.26148.033

Table 8. LAMA3 promoter regions harboring binding sites of p53.

						Frequency (random expectancy x 10^{-3})	
Promoter	**TXN bound**	**Start nt from TSS**	**End nt from TSS**	**String**	**Dissimilarity (%)**	**Equally**	**Query**
LAMA3	p53	−4245	−4239	TGAGCCC	8.8	2×10^{-3}	2×10^{-3}
		−4143	−4137	GGGCAGA	1.7	9×10^{-4}	8×10^{-4}
		−4063	−4057	TCTGCCC	1.7	9×10^{-4}	8×10^{-4}
		−3597	−3591	GGTGCCC	4	1×10^{-3}	1×10^{-3}
		−3585	−3579	CACGCCC	3.3	1×10^{-3}	1×10^{-3}
		−3451	−3445	GGCGCCC	7.4	1×10^{-3}	1×10^{-3}
		813	819	ACTGCCC	3.5	1×10^{-3}	1×10^{-3}
		−4547	−4541	CTTGCCC	0.2	9×10^{-4}	7×10^{-4}
		−3094	−3088	TGAGCC	6.7	2×10^{-3}	2×10^{-3}
		−2804	−2798	CACGCCC	3.3	1×10^{-3}	1×10^{-3}
		−2718	−2712	TCTGCCC	1.7	9×10^{-4}	8×10^{-4}
		−2347	−2341	CCAGCCC	3.7	1×10^{-3}	1×10^{-3}
		−2328	−2322	GGGCTCT	8.5	3×10^{-4}	2×10^{-4}
		−1914	−1908	GTCGCCC	6.4	1×10^{-3}	1×10^{-3}
		−1798	−1792	ACCGCCC	6.8	2×10^{-3}	2×10^{-3}
		−948	−942	GTCGCCC	6.4	1×10^{-3}	9×10^{-4}
		−437	−431	TCTGCCC	1.7	9×10^{-4}	8×10^{-4}
		−420	−414	GGGCGGC	6.1	1×10^{-3}	1×10^{-3}
		−374	−368	GGGCGGC	3.5	1×10^{-3}	1×10^{-3}
		−355	−349	GGGCGCG	4.6	6×10^{-4}	4×10^{-4}
		−342	−336	CTGGCCC	4.3	6×10^{-4}	4×10^{-4}
		−325	−319	GGGCCGC	6.9	2×10^{-3}	2×10^{-3}
		−314	−308	GGGCGGG	3.3	1×10^{-3}	1×10^{-3}
		−310	−304	GGGCAGG	0	9×10^{-4}	7×10^{-4}
		−296	−290	GGGCACA	3	1×10^{-3}	1×10^{-3}
		−256	−250	GCAGCCC	6.5	1×10^{-3}	9×10^{-4}
		−236	−230	TCAGCCC	5.5	1×10^{-3}	1×10^{-3}
		−223	−217	TCTGCCC	1.7	9×10^{-4}	8×10^{-4}
		−183	−177	TCAGCCC	5.5	1×10^{-3}	1×10^{-3}
		−1127	−1121	GGGCGCC	7.4	1×10^{-3}	1×10^{-3}
		−126	−120	GGCGCCC	7.4	1×10^{-3}	1×10^{-3}
		−96	−90	GGGCCAA	6	1×10^{-3}	1×10^{-3}
		−85	−79	GGGCGGG	3.3	1×10^{-3}	1×10^{-3}
		−75	−69	GGGCGGG	3.3	1×10^{-3}	1×10^{-3}
		−70	−64	GGGCGGG	3.3	1×10^{-3}	1×10^{-3}
		−65	−59	GGGCGCA	6.4	1×10^{-3}	1×10^{-3}
		−40	−34	GGGCGGC	6.1	1×10^{-3}	1×10^{-3}
		−24	−18	GGGCGGC	6.1	1×10^{-3}	1×10^{-3}
		1	7	GGGCCAG	4.3	6×10^{-4}	4×10^{-4}
		7	13	GGGCAGC	2.8	1×10^{-3}	1×10^{-3}
		45	51	GGGCGCG	4.6	6×10^{-4}	4×10^{-4}
		101	107	GGGCGTG	3.3	1×10^{-3}	1×10^{-3}
		155	161	TGAGCCC	6.7	2×10^{-3}	2×10^{-3}

Table 8 continued on next page

Table 8 continued

Promoter	TXN bound	Start nt from TSS	End nt from TSS	String	Dissimilarity (%)	Frequency (random expectancy x 10^{-3}) Equally	Query
		160	166	CCGGCCC	4.1	1×10^{-3}	1×10^{-3}
		216	222	GGGCGGG	3.3	1×10^{-3}	1×10^{-3}
		200	206	GGGCGGG	3.3	1×10^{-3}	1×10^{-3}
		206	212	GGGCGGC	6.1	1×10^{-3}	1×10^{-3}
		220	226	AAAGCCC	7.2	1×10^{-3}	1×10^{-3}
		236	242	GGGCTGC	6.5	1×10^{-3}	1×10^{-3}
		251	257	GGGCGCG	4.6	6×10^{-4}	4×10^{-4}

DOI: https://doi.org/10.7554/eLife.26148.034

immunoprecipitated with control rabbit IgG, HOXD10 and p65 antibodies at 4°C overnight. Chromatin-antibody complexes were washed with buffer 1 [0.1% SDS, 0.5% Triton X-100, 2 mM EDTA, 20 mM Tris-HCl (pH 8.0), 150 mM NaCl], buffer 2 [0.1% SDS, 2 mM EDTA, 20 mM Tris-HCl (pH 8.0), 500 mM NaCl] then TE buffer [10 mMTris-HCl (pH 8.0) 1 mM EDTA]. After reversal of cross-linking by heating at 65°C overnight, immunoprecipitated chromatin was subjected to PCR reaction for ~300 bp fragments around HOXD10/NFκB binding sites in miRNA promoters (miR-34c: −1 ~ 0 kb, miR-30e: −3~−2 kb, miR-144: −3~−2 kb) with the appropriate primers (***Table 9***).

Protein array

The relative abundance of the secreted laminin chains was determined with ImmunoCruz Cell Adhesion-2 MicroArray (sc-200006, Santa Cruz Biotechnologies, Santa Cruz, CA, USA) according to the manufacturer's protocol. Briefly, cells were plated at 2×10^6/100-mm plate and maintained overnight. Cells were maintained in the fresh medium containing 5% Matrigel for 24 hr. The CM was harvested and spun to remove the Matrigel drip. The medium was concentrated to 1 ml using Amicon Ultra-15 centrifugal filter units (3 kDa cut off, Millipore). The protein concentration was determined with DC Protein Assay reagent (Bio-Rad) and normalized to 1 mg/ml. 250 µg protein was labeled with Cy3 dye (Cy3 Mono-Reactive Dye Pack, GE Healthcare, Milwaukee, WI, USA). The labeled protein was dissolved in 1.5 ml desalting buffer, and unbound dye was removed by using Amicon Ultra-15 centrifugal filter units that concentrated the protein to 500 µl. The labeled protein was hybridized with array slides, and slides were scanned and analyzed by the CruzScan Scanning service (sc-200215, Santa Cruz).

Immunohistochemistry

Breast cancer tissue arrays containing 150 paraffin-embedded sections of normal and malignant tissues with pathological information (stages I through III) were obtained from US Biomax, Inc (BR1503b). Slides were deparaffinized, hydrated, and treated with antigen unmasking solutions (Vector Laboratories, Inc.). After being blocked with 0.3% H_2O_2 and nonimmune goat serum, sections were incubated at room temperature with an antibody against S-nitrosocysteine (Abcam, Cambridge, MA, USA, clone HY8E12), human LAMA3 (R&D Systems, Minneapolis, MN, USA, , clone 546215) or wild-type human p53 (EMD Millipore, clone pAb1620) and link antibodies, followed by peroxidase-conjugated streptavidin complex and diaminobenzidine tetrahydroxy chloride solution as the peroxidase substrate (Vector Laboratories, Burlingame, CA, USA). The sections were counterstained with hematoxylin. Photomicrographs were taken with the Zeiss Axioskop Imaging platform and Axion Vision software (Version 4.7).

MMP-9 measurement

MMP-9 secreted into CM was measured using the MMP-9 ELISA Kit (ThermoFisher Scientific) according to the manufacturer's protocol. Assay samples were prepared in the dark. Briefly, cells were plated at 1×10^6/60-mm plate and maintained overnight. Cells were maintained in 2 ml of the fresh medium containing 5% Matrigel for 24 hr. The CM was harvested and spun to remove the

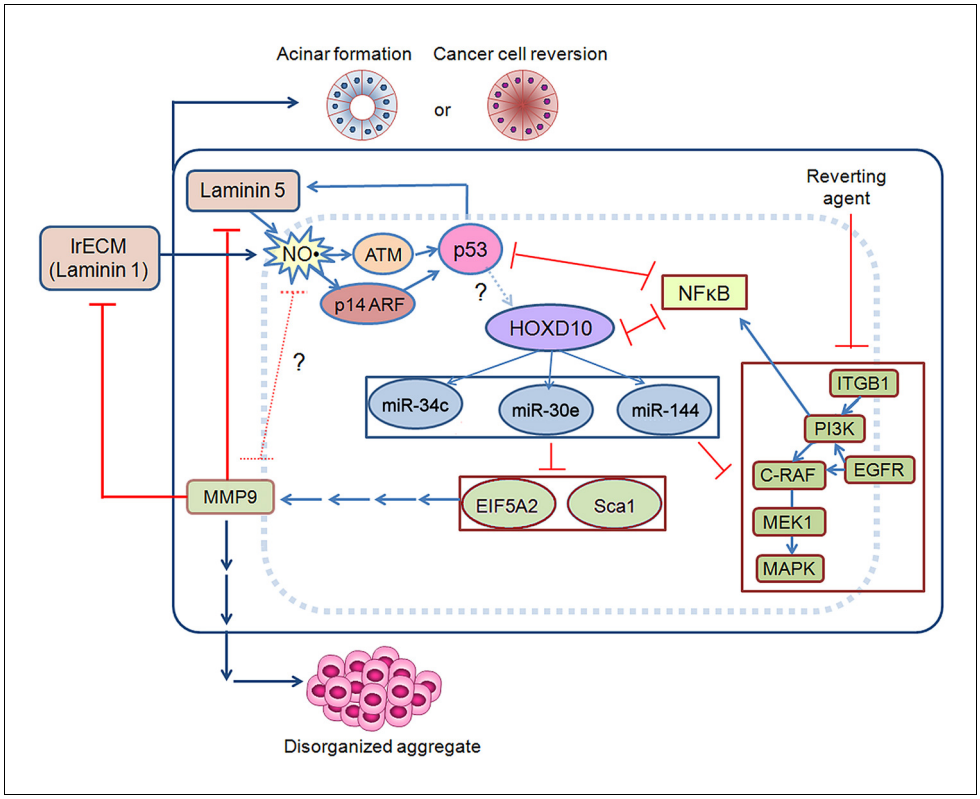

Figure 10. Schematic for acinar morphogenesis and phenotypic reversion of tumor cells in response to LN1 or LN5.

DOI: https://doi.org/10.7554/eLife.26148.035

Matrigel drip. The cleared CM was diluted 100-fold and analyzed for MMP-9 concentration using MMP-9 standards based on the optical density values at 450 nm.

Nitrite/nitrate measurement

To quantify the cumulative level of NO produced, the more stable oxidation product nitrite/nitrate was measured using the Measure-IT High-Sensitivity Nitrite Assay Kit (ThermoFisher Scientific) according to the manufacturer's protocol. Assay samples were prepared in the dark. Briefly, cells were plated at 1×10^6/60-mm plate and maintained overnight. Cells were maintained in 2 ml of the fresh medium containing 5% Matrigel for the designated time periods. The CM was harvested and spun to remove the Matrigel drip. 10 µl of the cleared CM was analyzed for nitrite concentration using nitrite standards at the excitation/emission maxima of 340/410 nm.

Detection of NO production in live cells

To capture a snap shot of NO level in live cells after laminin addition, a dye DAF-FM DA (4-amino-5-methylamino-2',7'-difluorofluorescein diacetate, ThermoFisher Scientific) was used according to the manufacturer's protocol. The signal intensity/area/cell was measured with ImageJ.

Breast tissues and *ex vivo* 3D organoid cultures

Breast tissues from reduction mammoplasties were obtained from the Cooperative Human Tissue Network (CHTN), a program funded by the National Cancer Institute. All specimens were collected with patient consent and were reported negative for proliferative breast disease by board-certified pathologists. Use of these anonymous samples was granted exemption status by the University of California at Berkeley Institutional Review Board according to the Code of Federal Regulations 45 CFR 46.101. Upon receipt, the tissues were rinsed with PBS, minced and incubated overnight with 0.1% collagenase as previously described (with gentle agitation) (***Hines et al., 2015***). The resulting

Table 9. List of oligonucleotide sequences of molecules listed in the manuscript.

Northern probes	
miR-450b-5p	5′-TAT TCA GGA ACA TAT TGC AAA A-3′
miR-495	5′-AAG AAG TGC ACC ATG TTT GTT T-3′
miR-30e	5′-CTT CCA GTC AAG GAT GTT TAC A-3′
miR-330–3 p	5′-TCT CTG CAG GCC GTG TGC TTT GC-3′
miR-382	5′-CGA ATC CAC CAC GAA CAA CTT C-3′
miR-423–3 p	5′-ACT GAG GGG CCT CAG ACC GAG CT-3′
miR-135a	5′-TCA CAT AGG AAT AAA AAG CCA TA-3′
miR-144	5′-AGT ACA TCA TCT ATA CTG TA-3′
miR-301b	5′-GCT TTG ACA ATA TCA TTG CAC TG-3′
miR-590–3 p	5′-ACT AGC TTA TAC ATA AAA TTA-3′
miR-301a	5′-GCT TTG ACA ATA CTA TTG CAC TG-3′
miR-34c-5p	5′-GCA ATC AGC TAA CTA CAC TGC CT-3′
RT-PCR	
EIF5A2	
FW	5′-ATG GCA GAC GAA ATT GAT TTC ACT A-3′
RV	5′-CTC ATT GCA CAC ATG ACA GAC-3′
SCA1	
FW	5′-ACG GTC ATT CAG ACC ACA CA-3′
RV	5′-CAG GGT TGA AGT TCT CGC TC-3′
ITGB1	
FW	5′-CGC CGC GCG GAA AAG ATG AAT-3′
RV	5′-TGG GCT GGT GCA GTT CTG TTC A-3′
c-RAF	
FW	5′-CGA CCC ACA GTG GAC GAT CCA G-3′
RV	5′-AGA TAA TGC TGG CCG ACT GGC CT-3′
MEK1	
FW	5′-AAG GGA ATC CCG GGC TGC CGA A-3′
RV	5′-GCC ATC GCT GTA GAA CGC ACC A-3′
MAPK	
FW	5′-GCA CCG TGA CCT CAA GCC TTC-3′
RV	5′-CAC CGA TGT CTG AGC ACG TCC AG-3′
LAMA3	
FW 5′-GAT GGC TCA GGC ATA TGT GTT-3′	
RV 5′-CTG GCC ATT GCT GTT ACA ACT-3′	
TUBA	
FW	5′-TGA CCT GAC AGA ATT CCA GAC CA-3′
RV	5′-GCA TTG ACA TCT TTG GGA ACC AC-3′
shRNA (target sequence underlined; *Bam*H1/*Eco*R1 cohesive ends italicized)	
EIF5A2sh	
Sense	5′-*GAT CCG* CTG CCA GAA GGT GAA CTA GCT TCC TGT CAG ATA TAT CTC TCC TTC CAC ACT TTT TG-3′
Antisense	5′-*AAT TCA* AAA ACT GCC AGA AGG TGA ACT AGT CTG ACA GGA AGT ATA TCT CTC CTT CCA CAC G-3′
ScaIsh	

Table 9 continued on next page

Table 9 continued

Northern probes	
Sense	5′-*GAT CCG* AAC CTG AAG AAC GGC TCT CTT CCT GTC AGA AGA GCC GTT CTT CAG GTT CTT TTT *G*-3′
Antisense	5′-*AAT TCA* AAA AGA ACC TGA AGA ACG GCT CTT CTG ACA GGA AGA GAG CCG TTC TTC AGG TTC *G*-3′
p65sh	
Sense	5′-*GAT CCG* GAC ATA TGA GAC CTT CAA CTT CCT GTC AGA TTG AAG GTC TCA TAT GTC CTT TTT *G*-3′
Antisense	5′-*AAT TCA* AAA AGG ACA TAT GAG ACC TTC AAT CTG ACA GGA AGT TGA AGG TCT CAT ATG TCC *G*-3′
p50/p100sh	
Sense	5′-*GAT CCG* AGC TAA TCC GCC AAG CAG CTT CCT GTC AGA CTG CTT GGC GGA TTA GCT CTT TTT *G*-3′
Antisense	5′-*AAT TCA* AAA AGA GCT AAT CCG CCA AGC AGT CTG ACA G GA AGC TGC TTG GCG GAT TAG CTC *G*-3′
LAMA3sh	
Sense	5′-*GAT CCG* GAG TCC TTC TGG ATT ACC CTT CCT GTC AGA GGT AAT CCA GAA GGA CTC CTT TTT *G*-3′
Antisense	5′-*AAT TCA* AAA AGG AGT CCT TCT GGA TTA CCT CTG ACA GGA AGG GTA ATC CAG AAG GAC TCC *G*-3′
Overexpressing constructs	
HOXD10	
FW	5′-CGG CAG *GCG CGC* CGC CAC CAT GTC CTT TCC CAA CAG CTC TCC T-3′ (*Asc*I site italicized)
RV	5′-CCG GCC *GAA TTC* CTA AGA AAA CGT GAG GTT GGC GGT CAG-3′ (*EcoR*1 site italicized)
p53	
FW	5′-GAT CTC *GGA TCC* GCC ACC ATG GAG GAG CCG CAG TCA GAT CCT AGC-3′ (*BamH*1 site italicized)
RV	5′-TAC AG*G AAT TC*T CAG TCT GAG TCA GGC CCT TCT GTC TTG AAC ATG-3′ (*EcoR*1 site italicized)
ATXN1 and EIF5A2	
FW	5′-TCT AGA GCC CGG GCG CGC CGG CCG CCG CGA TCG CCA TG-3′
RV	5-′′GCA GAT CCT TCG CGG CCG CGT TAA ACC TTA TCG TCG TCA TCC TTG TAA TCC AGG ATA TCA TTT GC-3′
miRNA reporter constructs (*Mlu*1/*Xho*1 sites italicized)	
miR-34c	
3–0 kb	
FW	5′-GAC TA*C GCG* TAC CGC TGG CAG TTC ATT TTA GCT C-3′ (*Mlu*1 site italicized)
RV	5′-GAC T*CT CGA* GCT AGA AGA TGG AGG CCC AGA TTC TTG AGA C-3′ (*Xho*1 site italicized)
2–0 kb	
FW	5′-GAC TA*C GCG* TCT TGG CTT CCT CCT AGT CAT CAA CCT-3′ (*Mlu*1 site italicized)
RV	5′-GAC T*CT CGA* GTC TGA TCT AGC AGG AGG GAC AAA GAG-3′ (*Xho*1 site italicized)
1–0 kb	
FW	5′-GAC TA*C GCG* TTC CCT TCA CTA TGG GGT GTA CAG AAC-3′ (*Mlu*1 site italicized)
RV	5′-GAC T*CT CGA* GCT AGA AGA TGG AGG CCC AGA TTC TTG AGA C-3′ (*Xho*1 site italicized)
3–2 kb	
FW	5′-GAC TA*C GCG* TTT ATA AAA ACC GCT GGC AGT TCA TTT TAG C-3′ (*Mlu*1 site italicized)
RV	5′-GAC T*CT CGA* GAG GAG GAA GCC AAG AAG AGT GTA GAA AAC A-3′ (*Xho*1 site italicized)
2–1 kb	
FW	5′-GAC TA*C GCG* TCT ATT CTC CCA CCT CAG CC TCC AAG TAG-3′ (*Mlu*1 site italicized)
RV	5′-GAC T*CT CGA* GCT GTA CAC CCC ATA GTG AAG GGA AAG AAA C-3′ (*Xho*1 site italicized)

Table 9 continued on next page

Table 9 continued

Northern probes	
miR-30e	
3–0 kb	
FW	5′-GAC T*AC GCG* T*GC* CAC CAT GCC CGG CTA A-3′ (*Mlu*1 site italicized)
RV	5′-GAC T*CT CGA* G*GG* GAG CTC GAG ATC TGA GTT TTG ACC-3′ (*Xho*1 site italicized)
2–0 kb	
FW	5′-GAC T*AC GCG* T*CT* GGT CTT GAA CTC CTG ACC TCG TCA T-3′ (*Mlu*1 site italicized)
RV	5′-GAC T*CT CGA* G*TT* CGG GAG CTC GAG ATC TGA GTT TTG-3′ (*Xho*1 site italicized)
1–0 kb	
FW	5′-GAC T*AC GCG* T*TT* AGA TCT GGG TAC AGA TGA AGG AAT TGA GAC TCC-3′ (*Mlu*1 site italicized)
RV	5′-GAC T*CT CGA* G*TT* CGG GAG CTC GAG ATC TGA TGG TTG-3′ (*Xho*1 site italicized)
3–2 kb	
FW	5′-GAC T*AC GCG* T*CT* TTT TGA ACT CCA GCA GCA CAT GAA CTA T-3′ (*Mlu*1 site italicized)
RV	5′-GAC T*CT CGA* G*GG* CCT TGT TTT GAC CAA TGA AAT ATG AGT A-3′ (*Xho*1 site italicized)
2–1 kb	
FW	5′-GAC T*AC GCG* T*CT* GGT CTT GAA CTC CTG ACC TCG TCA T-3′ (*Mlu*1 site italicized)
RV	5′-GAC T*CT CGA* G*AC* ACT TGA CTT CAG GGA GTC TCA ATT CCT T-3′ (*Xho*1 site italicized)
miR-144	
3–0 kb	
FW	5′-GAC T*AC GCG* T*CT* CAC TAT AAG ACT CGG GCC AAG CAC TTC-3′ (*Mlu*1 site italicized)
RV	5′-GAC T*CT CGA* G*GC* CAG TTG TGG TGG CAT GTG-3′ (*Xho*1 site italicized)
2–0 kb	
FW	5′-GAC T*AC GCG* T*GT* TGC CCA GGC TGG AGT ACA ATA GGA T-3′ (*Mlu*1 site italicized)
RV	5′-GAC T*CT CGA* G*AA* TTA GCC AGT TGT GGT GGC ATG TG-3′ (*Xho*1 site italicized)
1–0 kb	
FW	5′-GAC T*AC GCG* T*GT* ACT GGG GAG GCA GAG GAA TGG AAG-3′ (*Mlu*1 site italicized)
RV	5′-GAC T*CT CGA* G*AA* TTA GCC AGT TGT GGT GGC ATG TG-3′ (*Xho*1 site italicized)
3–2 kb	
FW	5′-GAC T*AC GCG* T*CC* TAT TCC TAG CGG GTT TGT GCA TAG AG-3′ (*Mlu*1 site italicized)
RV	5′-GAC T*AG ATC* T*CT* GGG CAA CAA GAG CAA AAC TGG ATC-3′ (*Bgl*1I site italicized)
2–1 kb	
FW	5′-GAC T*AC GCG* T*CC* CAG GCT GGA GTA CAA TAG GAT GAT CT-3′ (*Mlu*1 site italicized)
RV	5′-GAC T*CT CGA* G*GC* CCA GGG CTG TTT TCC TGG ATA TT-3′ (*Xho*1 site italicized)
ChIP	
miR-34c (−1~0 kb)	
FW	5′-GTG TCA GCA ATG GGT GCT CTA-3′
RV	5′-CCA GAG GAG GTG AGA CTT GAG-3′
miR-30e (−3~−2 kb)	
FW	5′-GAG GCA GTC TGA GAT ATT CCC-3′
RV	5′-CTG CAG CAT AAC ATG CTA GCT-3′
miR-144 (−3~−2 kb)	
FW	5′-CTG TGA TGA GGA CAA CAG TAA-3′
RV	5′-ATC CCC CTA CCT CAG CCT CTC-3′

DOI: https://doi.org/10.7554/eLife.26148.036

divested tissue fragments (organoids) were rinsed with PBS and collected by centrifugation (100 g × 2 min). Lactiferous ducts and terminal ductal lobular units (TDLU) were individually isolated using a micromanipulator and drawn glass needles using a screw-actuated micrometer driven hamilton syringe for suction/injection pressure. Single organoids were subsequently embedded in 50% growth factor reduced Matrigel (BD Biosciences) and overlayed with M87 growth medium. At 2 hr post seeding, medium was refreshed with L-NAME (NO inhibitor) containing medium at 5 mM. Cells were incubated at 37°C/5% CO_2. Medium was refreshed every other day for the length of the experiment (14 d).

Live cell imaging and cell tracking

Three-dimensional live cell imaging was performed using a Zeiss LSM 710 Meta confocal microscope and Zen Version 8.1 software. Cells were mixed with lrECM, seeded and covered along with complete growth media in a Lab-Tek 4-well chambered coverglass 2 hr prior to image capturing. Samples were placed in a 37 °C humidified microscope stage incubator with 5% CO_2. Images of 512 × 512 pixels in XY coordinates with a maximum Z-axis displacement of 75 µm were acquired using a 0.8 NA 20 × air objective at one frame/second. Images were captured successively at 20 min intervals for 48 hr. Samples were simultaneous excited by the 488 nm light (argon ion laser) at a power of <3% maximum and 546 nm light (a solid-state laser) at a power of <10% maximum. A secondary dichroic mirror was used in the emission pathway to separate the red (band-pass filters 560–575 nm) and green (band-pass filters 505–525 nm) channels. Gain was set between 100 and 180. Processed data were imported into Imaris (Bitplane, South Windsor, CT, USA), and nuclei were modeled (detection diameter: 5,800~6,500 nm). The nuclei were tracked over time using the tracking function of Imaris with the maximum distance of 2,500–20,000 nm and the maximum gap size of 1.

Statistics

Unless otherwise indicated, statistical analyses were performed using Graph Pad Prism Version 5 software and an unpaired two-tailed Student's t-test for parametric tests and Spearman correlation analysis for non-parametric tests. P-values of 0.05 or less were considered significant. Average results of multiple experiments (n > 3) are presented as the arithmetic mean ± SEM.

Acknowledgements

We thank all members of the Bissell Laboratory for constructive comments. In particular, we would like to thank Dr Curt Hines, Kremena Karagyozova and Kate Thi for providing normal human breast tissues and preparing *ex vivo* organotypic cultures. We also would like to thank Drs. Eva Lee and Alvin Lo in the Bissell laboratory and Samantha Metzger and Matthew Bommarito in the Furuta laboratory for their excellent technical support. The authors thank Dr Sun-Young Lee for helping with accuracy of the galley and additional suggestions for improvement. The authors thank Sarah J Lee for her excellent administrative assistance with the many changes required during the final stages of manuscript preparation and galley proofing. This work was supported by grants from the US Department of Defense Innovator Expansion Award (W81XWH0810736); Breast Cancer Research Foundation (BCRF); multiple grants from the NCI (R01CA064786; U01CA143233, U54CA112970 and U54CA143836 – Bay Area Physical Sciences Oncology Center) to MJB; and in part by the University of Toledo Department of Cancer Biology Startup Fund and an Ohio Cancer Research Grant (Project #: 5017) to SF.

Additional information

Funding

Funder	Grant reference number	Author
Ohio Cancer Research	5017	Saori Furuta
National Cancer Institute	R01CA064786	Mina J Bissell
U.S. Department of Defense	W81XWH0810736	Mina J Bissell

Breast Cancer Research Foundation		Mina J Bissell
National Cancer Institute	U01CA143233	Mina J Bissell
National Cancer Institute	U54CA112970	Mina J Bissell
National Cancer Institute	U54CA143836	Mina J Bissell

The funders had no role in study design, data collection and interpretation, or the decision to submit the work for publication.

Author contributions

Saori Furuta, Conceptualization, Data curation, Formal analysis, Funding acquisition, Investigation, Visualization, Methodology, Writing—original draft, Project administration, Writing—review and editing; Gang Ren, Data curation, Performed the experiments for revision, Acquired and analysed data; Jian-Hua Mao, Data curation, Formal analysis, Writing—review and editing, Performed statistical analyses and provided primary tissues; Mina J Bissell, Conceptualization, Resources, Supervision, Funding acquisition, Writing—original draft, Project administration, Writing—review and editing

Author ORCIDs

Saori Furuta https://orcid.org/0000-0003-1121-0487
Mina J Bissell http://orcid.org/0000-0001-5841-4423

Decision letter and Author response

Decision letter https://doi.org/10.7554/eLife.26148.043
Author response https://doi.org/10.7554/eLife.26148.044

Additional files

Supplementary files

- Transparent reporting form

DOI: https://doi.org/10.7554/eLife.26148.037

Major datasets

The following previously published dataset was used:

Author(s)	Year	Dataset title	Dataset URL	Database, license, and accessibility information
Becker-Weimann S, Bissell MJ, Onodera Y, Rizki A	2013	Gene expression in organized and disorganized human breast epithelial cells	https://www.ncbi.nlm.nih.gov/geo/query/acc.cgi?acc=GSE50444	Publicly available at the NCBI Gene Expression Omnibus (accession no: GSE50444)

References

Adriance MC, Inman JL, Petersen OW, Bissell MJ. 2005. Myoepithelial cells: good fences make good neighbors. *Breast Cancer Research* **7**:190–197. DOI: https://doi.org/10.1186/bcr1286, PMID: 16168137

Akçay F, Aksoy H, Memisoğullari R. 2002. Effect of breast-feeding on concentration of nitric oxide in breast milk. *Annals of Clinical Biochemistry* **39**:68–69. DOI: https://doi.org/10.1258/0004563021901595, PMID: 11853194

Akhavan A, Griffith OL, Soroceanu L, Leonoudakis D, Luciani-Torres MG, Daemen A, Gray JW, Muschler JL. 2012. Loss of cell-surface laminin anchoring promotes tumor growth and is associated with poor clinical outcomes. *Cancer Research* **72**:2578–2588. DOI: https://doi.org/10.1158/0008-5472.CAN-11-3732, PMID: 22589276

Barcellos-Hoff MH, Aggeler J, Ram TG, Bissell MJ. 1989. Functional differentiation and alveolar morphogenesis of primary mammary cultures on reconstituted basement membrane. *Development* **105**:223–235. PMID: 2806122

Becker-Weimann S, Xiong G, Furuta S, Han J, Kuhn I, Akavia UD, Pe'er D, Bissell MJ, Xu R. 2013. NFkB disrupts tissue polarity in 3D by preventing integration of microenvironmental signals. *Oncotarget* **4**:2010–2020. DOI: https://doi.org/10.18632/oncotarget.1451, PMID: 24243820

Beliveau A, Mott JD, Lo A, Chen EI, Koller AA, Yaswen P, Muschler J, Bissell MJ. 2010. Raf-induced MMP9 disrupts tissue architecture of human breast cells in three-dimensional culture and is necessary for tumor growth in vivo. *Genes & Development* **24**:2800–2811. DOI: https://doi.org/10.1101/gad.1990410, PMID: 21159820

Bhat R, Bissell MJ. 2014. Of plasticity and specificity: dialectics of the micro- and macro-environment and the organ phenotype. *Wiley Interdisciplinary Reviews. Membrane Transport and Signaling* **3**:147–163. DOI: https://doi.org/10.1002/wdev.130, PMID: 24678448

Bissell MJ, Hall HG, Parry G. 1982. How does the extracellular matrix direct gene expression? *Journal of Theoretical Biology* **99**:31–68. DOI: https://doi.org/10.1016/0022-5193(82)90388-5, PMID: 6892044

Bissell MJ, Hines WC. 2011. Why don't we get more cancer? A proposed role of the microenvironment in restraining cancer progression. *Nature Medicine* **17**:320–329. DOI: https://doi.org/10.1038/nm.2328, PMID: 21383745

Bissell MJ, Kenny PA, Radisky DC. 2005. Microenvironmental regulators of tissue structure and function also regulate tumor induction and progression: the role of extracellular matrix and its degrading enzymes. *Cold Spring Harbor Symposia on Quantitative Biology* **70**:343–356. DOI: https://doi.org/10.1101/sqb.2005.70.013, PMID: 16869771

Bissell MJ, Rizki A, Mian IS. 2003. Tissue architecture: the ultimate regulator of breast epithelial function. *Current Opinion in Cell Biology* **15**:753–762. DOI: https://doi.org/10.1016/j.ceb.2003.10.016, PMID: 14644202

Bissell MJ. 1981. The differentiated state of normal and malignant cells or how to define a "normal" cell in culture. *International Review of Cytology* **70**:27–100. PMID: 7228573

Briand P, Nielsen KV, Madsen MW, Petersen OW. 1996. Trisomy 7p and malignant transformation of human breast epithelial cells following epidermal growth factor withdrawal. *Cancer Research* **56**:2039–2044. PMID: 8616848

Briand P, Petersen OW, Van Deurs B. 1987. A new diploid nontumorigenic human breast epithelial cell line isolated and propagated in chemically defined medium. *In Vitro Cellular & Developmental Biology* **23**:181–188. DOI: https://doi.org/10.1007/BF02623578, PMID: 3558253

Canman CE, Lim DS, Cimprich KA, Taya Y, Tamai K, Sakaguchi K, Appella E, Kastan MB, Siliciano JD. 1998. Activation of the ATM kinase by ionizing radiation and phosphorylation of p53. *Science* **281**:1677–1679. DOI: https://doi.org/10.1126/science.281.5383.1677, PMID: 9733515

Chamoux E, Narcy A, Lehoux JG, Gallo-Payet N. 2002. Fibronectin, laminin, and collagen IV as modulators of cell behavior during adrenal gland development in the human fetus. *The Journal of Clinical Endocrinology & Metabolism* **87**:1819–1828. DOI: https://doi.org/10.1210/jcem.87.4.8359, PMID: 11932324

Chehab NH, Malikzay A, Stavridi ES, Halazonetis TD. 1999. Phosphorylation of Ser-20 mediates stabilization of human p53 in response to DNA damage. *PNAS* **96**:13777–13782. DOI: https://doi.org/10.1073/pnas.96.24.13777, PMID: 10570149

Chen A, Cuevas I, Kenny PA, Miyake H, Mace K, Ghajar C, Boudreau A, Bissell MJ, Bissell M, Boudreau N. 2009. Endothelial cell migration and vascular endothelial growth factor expression are the result of loss of breast tissue polarity. *Cancer Research* **69**:6721–6729. DOI: https://doi.org/10.1158/0008-5472.CAN-08-4069, PMID: 19654314

Chiquet-Ehrismann R, Mackie EJ, Pearson CA, Sakakura T. 1986. Tenascin: an extracellular matrix protein involved in tissue interactions during fetal development and oncogenesis. *Cell* **47**:131–139. DOI: https://doi.org/10.1016/0092-8674(86)90374-0, PMID: 2428505

Daley WP, Yamada KM. 2013. ECM-modulated cellular dynamics as a driving force for tissue morphogenesis. *Current Opinion in Genetics & Development* **23**:408–414. DOI: https://doi.org/10.1016/j.gde.2013.05.005, PMID: 23849799

Esser AK, Miller MR, Huang Q, Meier MM, Beltran-Valero de Bernabé D, Stipp CS, Campbell KP, Lynch CF, Smith BJ, Cohen MB, Henry MD. 2013. Loss of LARGE2 disrupts functional glycosylation of α-dystroglycan in prostate cancer. *Journal of Biological Chemistry* **288**:2132–2142. DOI: https://doi.org/10.1074/jbc.M112.432807, PMID: 23223448

Farré D, Roset R, Huerta M, Adsuara JE, Roselló L, Albà MM, Messeguer X. 2003. Identification of patterns in biological sequences at the ALGGEN server: PROMO and MALGEN. *Nucleic Acids Research* **31**:3651–3653. DOI: https://doi.org/10.1093/nar/gkg605, PMID: 12824386

Fiore A, Spencer VA, Mori H, Carvalho HF, Bissell MJ, Bruni-Cardoso A. 2017. Laminin-111 and the level of nuclear actin regulate epithelial quiescence via exportin-6. *Cell reports* **19**:2102–2115. DOI: https://doi.org/10.1016/j.celrep.2017.05.050, PMID: 28591581

Forrester K, Ambs S, Lupold SE, Kapust RB, Spillare EA, Weinberg WC, Felley-Bosco E, Wang XW, Geller DA, Tzeng E, Billiar TR, Harris CC. 1996. Nitric oxide-induced p53 accumulation and regulation of inducible nitric oxide synthase expression by wild-type p53. *PNAS* **93**:2442–2447. DOI: https://doi.org/10.1073/pnas.93.6.2442, PMID: 8637893

Garbincius JF, Michele DE. 2015. Dystrophin-glycoprotein complex regulates muscle nitric oxide production through mechanoregulation of AMPK signaling. *PNAS* **112**:13663–13668. DOI: https://doi.org/10.1073/pnas.1512991112, PMID: 26483453

Gloe T, Pohl U. 2002. Laminin binding conveys mechanosensing in endothelial cells. *Physiology* **17**:166–169. DOI: https://doi.org/10.1152/nips.01381.2001, PMID: 12136046

Gloe T, Riedmayr S, Sohn HY, Pohl U. 1999. The 67-kDa laminin-binding protein is involved in shear stress-dependent endothelial nitric-oxide synthase expression. *Journal of Biological Chemistry* **274**:15996–16002. DOI: https://doi.org/10.1074/jbc.274.23.15996, PMID: 10347148

Gordon SA, Abou-Jaoude W, Hoffman RA, McCarthy SA, Kim YM, Zhou X, Zhang XR, Simmons RL, Chen Y, Schall L, Ford HR. 2001. Nitric oxide induces murine thymocyte apoptosis by oxidative injury and a p53-dependent mechanism. *Journal of leukocyte biology* **70**:87–95. PMID: 11435490

Gould N, Doulias PT, Tenopoulou M, Raju K, Ischiropoulos H. 2013. Regulation of protein function and signaling by reversible cysteine S-nitrosylation. *Journal of Biological Chemistry* **288**:26473–26479. DOI: https://doi.org/10.1074/jbc.R113.460261, PMID: 23861393

Gudjonsson T, Rønnov-Jessen L, Villadsen R, Rank F, Bissell MJ, Petersen OW. 2002. Normal and tumor-derived myoepithelial cells differ in their ability to interact with luminal breast epithelial cells for polarity and basement membrane deposition. *Journal of cell science* **115**:39–50. PMID: 11801722

Hagios C, Lochter A, Bissell MJ. 1998. Tissue architecture: the ultimate regulator of epithelial function? *Philosophical Transactions of the Royal Society B: Biological Sciences* **353**:857–870. DOI: https://doi.org/10.1098/rstb.1998.0250, PMID: 9684283

Haigo SL, Bilder D. 2011. Global tissue revolutions in a morphogenetic movement controlling elongation. *Science* **331**:1071–1074. DOI: https://doi.org/10.1126/science.1199424, PMID: 21212324

Harvey M, Vogel H, Morris D, Bradley A, Bernstein A, Donehower LA. 1995. A mutant p53 transgene accelerates tumour development in heterozygous but not nullizygous p53-deficient mice. *Nature Genetics* **9**:305–311. DOI: https://doi.org/10.1038/ng0395-305, PMID: 7773294

Hines WC, Yaswen P, Bissell MJ. 2015. Modelling breast cancer requires identification and correction of a critical cell lineage-dependent transduction bias. *Nature Communications* **6**:69727. DOI: https://doi.org/10.1038/ncomms7927, PMID: 25896888

Hogan BL. 1999. Morphogenesis. *Cell* **96**:225–233. DOI: https://doi.org/10.1016/S0092-8674(00)80562-0, PMID: 9988217

Hord NG, Ghannam JS, Garg HK, Berens PD, Bryan NS. 2011. Nitrate and nitrite content of human, formula, bovine, and soy milks: implications for dietary nitrite and nitrate recommendations. *Breastfeeding Medicine* **6**:393–399. DOI: https://doi.org/10.1089/bfm.2010.0070, PMID: 20958096

Howlett AR, Bissell MJ. 1993. The influence of tissue microenvironment (stroma and extracellular matrix) on the development and function of mammary epithelium. *Epithelial Cell Biology* **2**:79–89. PMID: 8353596

Iizuka T, Sasaki M, Oishi K, Uemura S, Koike M. 1998. The presence of nitric oxide synthase in the mammary glands of lactating rats. *Pediatric Research* **44**:197–200. DOI: https://doi.org/10.1203/00006450-199808000-00010, PMID: 9702914

Islam MS, Matsumoto M, Tsuchida K, Oka T, Kanouchi H, Suzuki S. 2009. Immunohistochemical localization of nitric oxide synthase (NOS) in mouse mammary gland during reproductive cycle. *Journal of Veterinary Medical Science* **71**:945–949. DOI: https://doi.org/10.1292/jvms.71.945, PMID: 19652483

Iwakiri Y, Satoh A, Chatterjee S, Toomre DK, Chalouni CM, Fulton D, Groszmann RJ, Shah VH, Sessa WC. 2006. Nitric oxide synthase generates nitric oxide locally to regulate compartmentalized protein S-nitrosylation and protein trafficking. *PNAS* **103**:19777–19782. DOI: https://doi.org/10.1073/pnas.0605907103, PMID: 17170139

Jabbur JR, Huang P, Zhang W. 2000. DNA damage-induced phosphorylation of p53 at serine 20 correlates with p21 and Mdm-2 induction in vivo. *Oncogene* **19**:6203–6208. DOI: https://doi.org/10.1038/sj.onc.1204017, PMID: 11175334

Jorgens DM, Inman JL, Wojcik M, Robertson C, Palsdottir H, Tsai WT, Huang H, Bruni-Cardoso A, López CS, Bissell MJ, Xu K, Auer M. 2017. Deep nuclear invaginations are linked to cytoskeletal filaments - integrated bioimaging of epithelial cells in 3D culture. *Journal of Cell Science* **130**:177–189. DOI: https://doi.org/10.1242/jcs.190967, PMID: 27505896

Khosravi S, Wong RP, Ardekani GS, Zhang G, Martinka M, Ong CJ, Li G. 2014. Role of EIF5A2, a downstream target of Akt, in promoting melanoma cell invasion. *British Journal of Cancer* **110**:399–408. DOI: https://doi.org/10.1038/bjc.2013.688, PMID: 24178756

Kim SW, Wu G. 2009. Regulatory role for amino acids in mammary gland growth and milk synthesis. *Amino Acids* **37**:89–95. DOI: https://doi.org/10.1007/s00726-008-0151-5, PMID: 18683019

Komarov PG, Komarova EA, Kondratov RV, Christov-Tselkov K, Coon JS, Chernov MV, Gudkov AV. 1999. A chemical inhibitor of p53 that protects mice from the side effects of cancer therapy. *Science* **285**:1733–1737. DOI: https://doi.org/10.1126/science.285.5434.1733, PMID: 10481009

Lee GY, Kenny PA, Lee EH, Bissell MJ. 2007. Three-dimensional culture models of normal and malignant breast epithelial cells. *Nature Methods* **4**:359–365. DOI: https://doi.org/10.1038/nmeth1015, PMID: 17396127

Lee SY, Meier R, Furuta S, Lenburg ME, Kenny PA, Xu R, Bissell MJ. 2012. FAM83A confers EGFR-TKI resistance in breast cancer cells and in mice. *Journal of Clinical Investigation* **122**:3211–3220. DOI: https://doi.org/10.1172/JCI60498, PMID: 22886303

Liu E, Thant AA, Kikkawa F, Kurata H, Tanaka S, Nawa A, Mizutani S, Matsuda S, Hanafusa H, Hamaguchi M. 2000. The Ras-mitogen-activated protein kinase pathway is critical for the activation of matrix metalloproteinase secretion and the invasiveness in v-crk-transformed 3Y1. *Cancer Research* **60**:2361–2364. PMID: 10811109

Lu J, Getz G, Miska EA, Alvarez-Saavedra E, Lamb J, Peck D, Sweet-Cordero A, Ebert BL, Mak RH, Ferrando AA, Downing JR, Jacks T, Horvitz HR, Golub TR. 2005. MicroRNA expression profiles classify human cancers. *Nature* **435**:834–838. DOI: https://doi.org/10.1038/nature03702, PMID: 15944708

Miner JH, Yurchenco PD. 2004. Laminin functions in tissue morphogenesis. *Annual Review of Cell and Developmental Biology* **20**:255–284. DOI: https://doi.org/10.1146/annurev.cellbio.20.010403.094555, PMID: 15473841

Murphy SH, Suzuki K, Downes M, Welch GL, De Jesus P, Miraglia LJ, Orth AP, Chanda SK, Evans RM, Verma IM. 2011. Tumor suppressor protein (p)53, is a regulator of NF-kappaB repression by the glucocorticoid receptor. *PNAS* **108**:17117–17122. DOI: https://doi.org/10.1073/pnas.1114420108, PMID: 21949408

Muschler J, Levy D, Boudreau R, Henry M, Campbell K, Bissell MJ. 2002. A role for dystroglycan in epithelial polarization: loss of function in breast tumor cells. *Cancer research* **62**:7102–7109. PMID: 12460932

Niedbala W, Wei XQ, Campbell C, Thomson D, Komai-Koma M, Liew FY. 2002. Nitric oxide preferentially induces type 1 T cell differentiation by selectively up-regulating IL-12 receptor beta 2 expression via cGMP. *PNAS* **99**:16186–16191. DOI: https://doi.org/10.1073/pnas.252464599, PMID: 12451176

Oktay K, Karlikaya G, Akman O, Ojakian GK, Oktay M. 2000. Interaction of extracellular matrix and activin-A in the initiation of follicle growth in the mouse ovary. *Biology of Reproduction* **63**:457–461. DOI: https://doi.org/10.1095/biolreprod63.2.457, PMID: 10906050

Osako MK, Nakagami H, Morishita R. 2012. Development and modification of decoy oligodeoxynucleotides for clinical application. *Advances in Polymer Science = Fortschritte Der Hochpolymeren-Forschung* **249**:49–60.

Park J, Al-Ramahi I, Tan Q, Mollema N, Diaz-Garcia JR, Gallego-Flores T, Lu HC, Lagalwar S, Duvick L, Kang H, Lee Y, Jafar-Nejad P, Sayegh LS, Richman R, Liu X, Gao Y, Shaw CA, Arthur JSC, Orr HT, Westbrook TF, et al. 2013. RAS-MAPK-MSK1 pathway modulates ataxin 1 protein levels and toxicity in SCA1. *Nature* **498**:325–331. DOI: https://doi.org/10.1038/nature12204, PMID: 23719381

Petersen OW, Rønnov-Jessen L, Howlett AR, Bissell MJ. 1992. Interaction with basement membrane serves to rapidly distinguish growth and differentiation pattern of normal and malignant human breast epithelial cells. *PNAS* **89**:9064–9068. DOI: https://doi.org/10.1073/pnas.89.19.9064, PMID: 1384042

Petersen OW, Rønnov-Jessen L, Weaver VM, Bissell MJ. 1998. Differentiation and cancer in the mammary gland: shedding light on an old dichotomy. *Advances in Cancer Research* **75**:135–161. PMID: 9709809

Rando TA. 2001. The dystrophin-glycoprotein complex, cellular signaling, and the regulation of cell survival in the muscular dystrophies. *Muscle & Nerve* **24**:1575–1594. DOI: https://doi.org/10.1002/mus.1192, PMID: 11745966

Rialas CM, Nomizu M, Patterson M, Kleinman HK, Weston CA, Weeks BS. 2000. Nitric oxide mediates laminin-induced neurite outgrowth in PC12 cells. *Experimental Cell Research* **260**:268–276. DOI: https://doi.org/10.1006/excr.2000.5017, PMID: 11035921

Ricca BL, Venugopalan G, Furuta S, Tanner K, Orellana WA, Reber CD, Brownfield DG, Bissell MJ, Fletcher DA. 2018. Transient external force induces phenotypic reversion of malignant epithelial structures via nitric oxide signaling. *eLife*:e26161. DOI: https://doi.org/10.7554/eLife.26161

Rizki A, Weaver VM, Lee SY, Rozenberg GI, Chin K, Myers CA, Bascom JL, Mott JD, Semeiks JR, Grate LR, Mian IS, Borowsky AD, Jensen RA, Idowu MO, Chen F, Chen DJ, Petersen OW, Gray JW, Bissell MJ. 2008. A human breast cell model of preinvasive to invasive transition. *Cancer Research* **68**:1378–1387. DOI: https://doi.org/10.1158/0008-5472.CAN-07-2225, PMID: 18316601

Saccani S, Pantano S, Natoli G. 2001. Two waves of nuclear factor kappaB recruitment to target promoters. *The Journal of Experimental Medicine* **193**:1351–1360. DOI: https://doi.org/10.1084/jem.193.12.1351, PMID: 11413190

Sasaki CY, Barberi TJ, Ghosh P, Longo DL. 2005. Phosphorylation of RelA/p65 on serine 536 defines an I{kappa}B{alpha}-independent NF-{kappa}B pathway. *Journal of Biological Chemistry* **280**:34538–34547. DOI: https://doi.org/10.1074/jbc.M504943200, PMID: 16105840

Spencer VA, Costes S, Inman JL, Xu R, Chen J, Hendzel MJ, Bissell MJ. 2011. Depletion of nuclear actin is a key mediator of quiescence in epithelial cells. *Journal of Cell Science* **124**:123–132. DOI: https://doi.org/10.1242/jcs.073197, PMID: 21172822

Stamler JS, Meissner G. 2001. Physiology of nitric oxide in skeletal muscle. *Physiological Reviews* **81**:209–237. DOI: https://doi.org/10.1152/physrev.2001.81.1.209, PMID: 11152758

Streuli CH, Bissell MJ. 1990. Expression of extracellular matrix components is regulated by substratum. *The Journal of Cell Biology* **110**:1405–1415. DOI: https://doi.org/10.1083/jcb.110.4.1405, PMID: 2182652

Tanner K, Mori H, Mroue R, Bruni-Cardoso A, Bissell MJ. 2012. Coherent angular motion in the establishment of multicellular architecture of glandular tissues. *PNAS* **109**:1973–1978. DOI: https://doi.org/10.1073/pnas.1119578109, PMID: 22308439

Tezer M, Ozluk Y, Sanli O, Asoglu O, Kadioglu A. 2012. Nitric oxide may mediate nipple erection. *Journal of Andrology* **33**:805–810. DOI: https://doi.org/10.2164/jandrol.111.014951, PMID: 22207705

Wang H, Lacoche S, Huang L, Xue B, Muthuswamy SK. 2013. Rotational motion during three-dimensional morphogenesis of mammary epithelial acini relates to laminin matrix assembly. *PNAS* **110**:163–168. DOI: https://doi.org/10.1073/pnas.1201141110, PMID: 23248267

Wang X, Michael D, de Murcia G, Oren M. 2002. p53 Activation by nitric oxide involves down-regulation of Mdm2. *Journal of Biological Chemistry* **277**:15697–15702. DOI: https://doi.org/10.1074/jbc.M112068200, PMID: 11867628

Wang X, Zalcenstein A, Oren M. 2003. Nitric oxide promotes p53 nuclear retention and sensitizes neuroblastoma cells to apoptosis by ionizing radiation. *Cell Death & Differentiation* **10**:468–476. DOI: https://doi.org/10.1038/sj.cdd.4401181, PMID: 12719724

Weaver VM, Lelièvre S, Lakins JN, Chrenek MA, Jones JC, Giancotti F, Werb Z, Bissell MJ. 2002. beta4 integrin-dependent formation of polarized three-dimensional architecture confers resistance to apoptosis in normal and malignant mammary epithelium. *Cancer Cell* **2**:205–216. DOI: https://doi.org/10.1016/S1535-6108(02)00125-3, PMID: 12242153

Weaver VM, Petersen OW, Wang F, Larabell CA, Briand P, Damsky C, Bissell MJ. 1997. Reversion of the malignant phenotype of human breast cells in three-dimensional culture and in vivo by integrin blocking antibodies. *The Journal of Cell Biology* **137**:231–245. DOI: https://doi.org/10.1083/jcb.137.1.231, PMID: 9105051

Webster GA, Perkins ND. 1999. Transcriptional cross talk between NF-kappaB and p53. *Molecular and Cellular Biology* **19**:3485–3495. DOI: https://doi.org/10.1128/MCB.19.5.3485, PMID: 10207072

Weir ML, Oppizzi ML, Henry MD, Onishi A, Campbell KP, Bissell MJ, Muschler JL. 2006. Dystroglycan loss disrupts polarity and beta-casein induction in mammary epithelial cells by perturbing laminin anchoring. *Journal of Cell Science* **119**:4047–4058. DOI: https://doi.org/10.1242/jcs.03103, PMID: 16968749

Wessells N. 1977. *Interaction in Development*. Menlo Park: W.A. Benjamin, Inc.

Wockel A, Baum O, Planitzer G, Rothen-Rutishauser B, Gossrau R, Abou-Dakn M. 2005. Constitutive coexpression of nitric oxide synthase-1 and soluble guanylyl cyclase in myoepithelial cells of mammary glands in mice. *Cells Tissues Organs* **180**:178–184. DOI: https://doi.org/10.1159/000088246, PMID: 16260864

Zhang Y, Xiong Y, Yarbrough WG. 1998. ARF promotes MDM2 degradation and stabilizes p53: ARF-INK4a locus deletion impairs both the Rb and p53 tumor suppression pathways. *Cell* **92**:725–734. DOI: https://doi.org/10.1016/S0092-8674(00)81401-4, PMID: 9529249

JCB Journal of Cell Biology

ARTICLE

Fibronectin rescues estrogen receptor α from lysosomal degradation in breast cancer cells

Rocío G. Sampayo[1,2,3], Andrés M. Toscani[4], Matthew G. Rubashkin[5], Kate Thi[6], Luciano A. Masullo[7,8], Ianina L. Violi[7], Jonathon N. Lakins[5], Alfredo Cáceres[9], William C. Hines[6], Federico Coluccio Leskow[4], Fernando D. Stefani[7,8], Dante R. Chialvo[10], Mina J. Bissell[6], Valerie M. Weaver[5], and Marina Simian[1,3]

Estrogen receptor α (ERα) is expressed in tissues as diverse as brains and mammary glands. In breast cancer, ERα is a key regulator of tumor progression. Therefore, understanding what activates ERα is critical for cancer treatment in particular and cell biology in general. Using biochemical approaches and superresolution microscopy, we show that estrogen drives membrane ERα into endosomes in breast cancer cells and that its fate is determined by the presence of fibronectin (FN) in the extracellular matrix; it is trafficked to lysosomes in the absence of FN and avoids the lysosomal compartment in its presence. In this context, FN prolongs ERα half-life and strengthens its transcriptional activity. We show that ERα is associated with β1-integrin at the membrane, and this integrin follows the same endocytosis and subcellular trafficking pathway triggered by estrogen. Moreover, ERα⁺ vesicles are present within human breast tissues, and colocalization with β1-integrin is detected primarily in tumors. Our work unravels a key, clinically relevant mechanism of microenvironmental regulation of ERα signaling.

Introduction

Estrogen receptor α (ERα) is a transcription factor present in different adult tissues such as mammary gland, ovaries, uterus, and brain (Couse et al., 1997; Han et al., 2013). It regulates cell proliferation, migration, and survival. In the breast in particular, ERα controls mammary development and plays a key role in tumor growth. Therefore, understanding what regulates ERα activation and shutdown is fundamental for cell biology. ERα action can be blocked with tamoxifen (the most widely used selective ER modulator), although one third of breast cancer patients develop resistance, with ERα regaining activity (Nardone et al., 2015; Jeselsohn et al., 2017). The causes of this resistance are still unclear.

So far, the main proposed mechanism for ERα signaling shutdown is estrogen-induced ERα degradation. Estrogen binding to ERα induces its nuclear translocation. Once in the nucleus, ERα binds to its target promoters and is then ubiquitylated and subsequently degraded in cytosolic proteasomes. Therefore, ERα's half-life decreases from 4 to 2 h in the presence of estrogens. The pool of ERα attached to the plasma membrane by reversible S-palmitoylation on cysteine 447 (Acconcia et al., 2005; Marino et al., 2006; Adlanmerini et al., 2014) has been suggested to follow different degradation dynamics (La Rosa et al., 2012). Whether membrane-bound ERα has transcriptional activity is still a matter of debate (Levin, 2009). Understanding how membrane and cytoplasmic ERα are regulated in breast cancer is crucial to develop strategies to overcome resistance to endocrine therapy.

The ECM plays a key role in cell fate, and evidence is accumulating that it modulates response to therapy in breast cancer as well (Ghajar and Bissell, 2008; Correia and Bissell, 2012). We previously described that ECM components affect the response of breast cancer cells to tamoxifen (Pontiggia et al., 2012). In particular, we found that fibronectin (FN), which correlates with lower survival when levels are increased (Yao et al., 2007; Helleman et al., 2008), induces tamoxifen resistance in breast

[1]Universidad de Buenos Aires, Instituto de Oncología "Ángel H. Roffo", Área Investigación, Buenos Aires, Argentina; [2]Universidad de Buenos Aires, Facultad de Ciencias Exactas y Naturales, Departamento de Fisiología y Biología Molecular y Celular, Ciudad Universitaria, Buenos Aires, Argentina; [3]Universidad Nacional de San Martín, Instituto de Nanosistemas, Campus Miguelete, San Martín, Argentina; [4]Universidad de Buenos Aires, Facultad de Ciencias Exactas y Naturales, Departamento de Química Biológica, IQUIBICEN UBA-CONICET y Universidad Nacional de Luján, Departamento de Ciencias Básicas, Buenos Aires, Argentina; [5]Center for Bioengineering and Tissue Regeneration, Department of Surgery, University of California, San Francisco, San Francisco, CA; [6]Division of Biological Systems and Engineering, Lawrence Berkeley National Laboratory, Berkeley, CA; [7]Centro de Investigaciones en Bionanociencias, Consejo Nacional de Investigaciones Científicas y Técnicas, Buenos Aires, Argentina; [8]Departamento de Física, Facultad de Ciencias Exactas y Naturales, Universidad de Buenos Aires, Buenos Aires, Argentina; [9]Instituto de Investigación Médica Mercedes y Martín Ferreyra, Córdoba, Argentina; [10]Center for Complex Systems and Brain Sciences, Escuela de Ciencia y Tecnología, Universidad Nacional de San Martín and Consejo Nacional de Investigaciones Científicas y Tecnológicas, San Martín, Argentina.

Correspondence to Rocío G. Sampayo: ro.sampayo@gmail.com; Marina Simian: marsimian@gmail.com.

cancer cells when bound to β1-integrin, its surface receptor. Therefore, we hypothesized that FN–β1-integrin pathway might have a direct effect on ERα signaling, modifying its response to hormone treatment.

We used two well-known cellular models of ERα-positive human breast adenocarcinoma: MCF7 and T47D. These cell lines have been widely used and validated for the study of ERα activity because primary culture of normal or tumor human breast tissues leads to the loss of ERα expression (Graham et al., 2009; Hines et al., 2016). We demonstrate that FN prolongs ERα half-life and strengthens its transcriptional activity. Mechanistically, we show that upon treatment with 17β-estradiol (E_2), membrane ERα is endocytosed and travels in these vesicles through the cytoplasm and into the nucleus. In the absence of FN, it is degraded in lysosomes after 60 min of treatment. When FN is present, these endosomes escape lysosomal degradation, and ERα is localized in RAB11$^+$ vesicles, typically involved in recycling. Using superresolution microscopy and coimmunoprecipitation assays, we found that ERα and β1-integrin colocalize at the plasma membrane and are endocytosed together after stimulation with E_2. In these vesicles, β1-integrin is also degraded upon 60 min of treatment with E_2, unless FN is present. We propose that FN-bound β1-integrin, following its recycling pathway, drags these ERα–β1-integrin$^+$ vesicles back to the plasma membrane, thus bypassing the lysosomal compartment. We show that these endosomes are present in normal and tumor human breast tissues, although only tumor samples showed positive colocalization between ERα and β1-integrin. This indicates that the mechanism of ERα overactivation dependent on its association with FN–β1-integrin pathway would be particularly active within tumors. In light of these findings, we strongly suggest that a novel therapeutic strategy designed to interfere with the cross talk between FN and ERα signaling pathways would resensitize patients to endocrine therapy.

Results

FN modulates ERα degradation and transcriptional activity

Given that we have previously shown that FN induces resistance to anti-estrogenic therapy (Pontiggia et al., 2012), we wondered whether FN has a direct effect on ERα activity. Research on ERα activity and dynamics in culture is challenging because primary culture of ERα-positive normal tissues and tumors leads to the loss of ERα expression (Hines et al., 2016). Therefore, we used two well-characterized human ERα-positive breast adenocarcinoma cell lines, MCF7 and T47D, that allowed us to modulate and study ERα regulation in culture. We first performed luciferase reporter assays with a construction that allowed us to measure ERα activity mediated by the estrogen response element (ERE). We found that, when cells are seeded on FN, this receptor has a stronger transcriptional activity in the presence of E_2, compared with its activity on the control substrate (BSA; Fig. 1 a). To study the mechanism through which FN regulates ERα activity, we analyzed the effect of FN on ERα degradation. We found that when cells are seeded on BSA, ERα completely localizes in the nucleus after 15 min of treatment with E_2 (Fig. 1 b). Knowing that E_2 triggers ERα degradation, reducing ERα mean expression after 60 min (Reid et al., 2003), we increased the treatment time and found that as expected, total ERα levels drop after stimulation with E_2 in cells seeded on BSA (Fig. 1 c). When cells are seeded on FN, ERα is also completely localized in the nucleus after 15 min of treatment with E_2 (Fig. 1 d). However, we found that after a longer treatment with the hormone (>60 min), FN inhibits E_2-induced ERα degradation (Fig. 1 e). We confirmed these observations by immunofluorescence, showing a more intense signal of nuclear ERα after treatment with E_2 in cells seeded on FN compared with BSA (Fig. S1, a and b). Similar results were obtained using T47D cells (Fig. S1, c–f). These data indicate that FN inhibits E_2-stimulated ERα degradation. Of note, total ERα levels are increased when cells are seeded on FN even in the absence of E_2, indicating that FN might also alter basal ERα degradation dynamics (Reid et al., 2003). Interestingly, when we performed ultracentrifugation to separate cytoplasmic and membrane fractions, we observed that membrane ERα follows a dynamics similar to cytoplasmic ERα (Fig. S1, g–j).

Moreover, we further tested the effect of FN on ERα shuttling kinetics. As shown in Fig. 1 f, E_2 stimulates ERα nuclear localization, reaching its maximum after 8 min of treatment. These kinetics are not affected by the presence of FN (Fig. 1 g). However, upon 20 min of treatment, it can be already observed that degradation of both nuclear and cytoplasmic ERα is reduced when cells are seeded on FN. Altogether, these data indicate that FN modulates ERα degradation but does not alter ERα shuttling dynamics to the nucleus.

ERα is degraded in lysosomes and can be rescued by FN

We next tested whether FN was inhibiting E_2-triggered proteasomal degradation of ERα, the best-characterized degradation pathway of this receptor. We found that upon E_2 stimulation for 60 min, inhibition of the proteasomal pathway with bortezomib (BZ) increases ERα levels even in the presence of FN (Fig. 2 a), suggesting that FN would inhibit a different mechanism of ERα degradation. Because FN has been found to modulate lysosomal degradation of membrane proteins (Caswell et al., 2009; Dozynkiewicz et al., 2012), we next asked whether ERα could be degraded in lysosomes upon E_2 stimulation. Blocking the passage of late endosomes to lysosomes by inhibiting V-ATPase with bafilomycin-A1 (BAF; Li et al., 2013) impaired ERα degradation after 60 min of treatment with E_2, in cells seeded on BSA (Fig. 2 b). To further test that ERα is degraded in lysosomes after E_2 treatment, we expressed GFP-tagged Rab7, a well-known small GTPase that determines the passage of late endosomes to lysosomes (Vanlandingham and Ceresa, 2009). As shown in Fig. 2 c, E_2 treatment triggers ERα colocalization with Rab7. Pearson's and Manders' correlation coefficients (PCCs and MCCs, respectively) were used to quantify the degree of colocalization observed between these proteins in each analyzed field as previously described (Dunn et al., 2011). The overall significance level of colocalization was calculated from these coefficients for each condition. A shorter treatment with E_2 (15 min) revealed an increase in ERα localization closer to the Rab7 compartment, although practically no colocalization with Rab7$^+$ endosomes was observed (Fig. S1 k, top), indicating that a longer treatment is necessary for ERα$^+$ vesicle localization to lysosomes.

We next investigated the effect of FN on E_2-induced ERα lysosomal degradation and found that ERα does not colocalize with

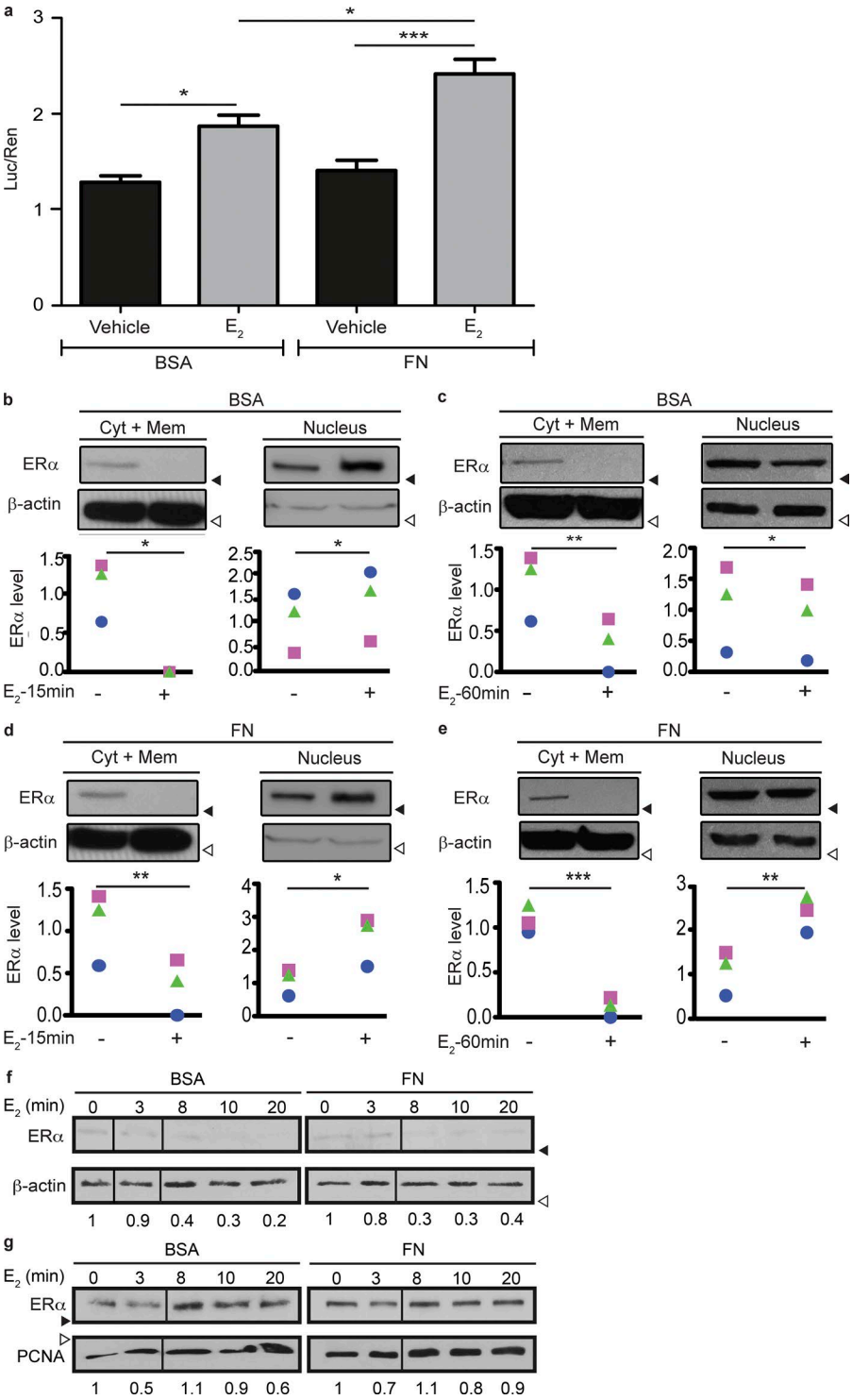

Figure 1. **FN stimulates ERα's transcriptional activity. (a)** Luciferase assay in MCF7 cells transiently transfected with pTK-ERE-Luc and pTK-Renilla, seeded on BSA or FN and treated for 14 h as indicated. Data are represented as mean ± SD. Differences between groups were analyzed by two-way ANOVA followed by Bonferroni contrasts adjusted for multiple comparisons (n = 3 replicates). **(b and c)** Top: Western blot of a subcellular fractionation of MCF7 cells seeded on BSA and treated for 15 min (b) or 60 min (c) as indicated. Blotting antibodies are shown on the left. Bottom: densitometry. For each subcellular fraction, shown is the ERα/β-actin density ratio normalized to the mean control group. Each symbol represents a different experiment. Differences between groups were analyzed by a one-tailed paired Student's t test (n = 3 replicates). **(d and e)** Top: Western blot of a subcellular fractionation of MCF7 cells seeded on FN and treated for 15 (d) or 60 min (e) as indicated. Blotting antibodies are shown on the left. Bottom: Densitometry. For each subcellular fraction, shown is the ERα/β-actin density ratio normalized to the mean control group. Each symbol represents a different experiment. **(f)** Western blot of the cytosolic + membrane fraction of MCF7 cells seeded on BSA or FN and treated with E_2 for the indicated times. Below the blots, the ERα/β-actin density ratio is shown, normalized to the control group. **(g)** Western blot of the nuclear fraction of MCF7 cells seeded on BSA or FN and treated with E_2 for the indicated times. Below the blots, the ERα/PCNA density ratio is shown, normalized to the control group. Differences between groups were analyzed by one-tailed paired Student's t test (n = 3 replicates). *, P < 0.05; **, P < 0.01; ***, P < 0.001. Shown data are representative of at least three independent experiments. Black arrowheads indicate positions of 50-kD markers. White arrowheads indicate positions of 37-kD markers. Treatments: ethanol (vehicle) or 10^{-8} M E_2.

Rab7 after 60 min (Fig. 2, e and f) or 15 min (Fig. S1 k, bottom) treatment in the presence of FN. These data indicate that FN is rescuing ERα from being degraded in the lysosomal compartment. We confirmed these results with LAMP-1, a lysosomal marker, which shows that after 60 min of treatment with E_2, ERα colocalizes with LAMP-1 when cells are seeded on BSA, and this is reverted when cells are seeded on FN (Fig. S1 l).

To ensure that ERα signals observed in these assays correspond in fact with ERα, we checked the specificity of this antibody. We used the epitope this antibody was raised against as a blocking peptide and obtained no ERα signal in Western blot or immunofluorescence assays (Fig. S1, m and n). Moreover, knockdown of ERα significantly reduces the signal obtained with this antibody proving that it specifically recognizes this protein (Fig. S1 o).

ERα is rapidly endocytosed after estrogen treatment

We next asked whether ERα was present in endosomes that could end up in lysosomes upon E_2 stimulation and whether this was

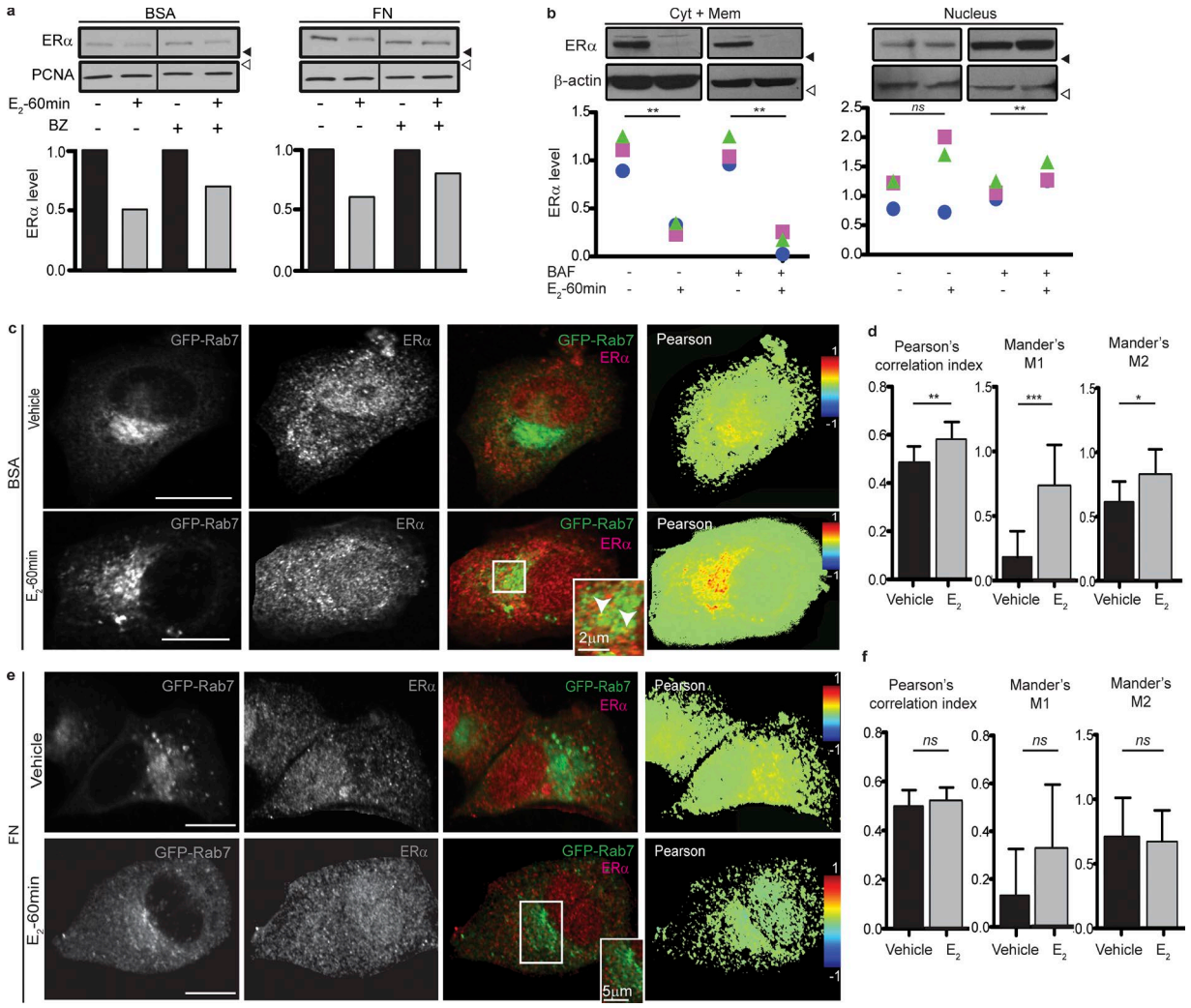

Figure 2. **ERα is degraded in lysosomes and rescued by FN. (a)** Top: Western blot of T47D cells seeded on BSA or FN pretreated with BZ 8nM or its vehicle (saline) for 4 h and treated as indicated. Bottom: Densitometry. For each subcellular fraction, the mean ERα/β-actin density ratio is shown normalized to the mean control group. **(b)** Top: Western blot of a subcellular fractionation of T47D cells pretreated for 90 min with 25 nM BAF or its vehicle (DMSO) and then treated for 60 min with 10^{-8} M E_2 or its vehicle (ethanol). Blotting antibodies are shown on the left. Bottom: Densitometry. For each experimental condition, the ERα/β-actin density ratio is shown, normalized to the mean control group. Each symbol represents a different experiment. Differences between groups were analyzed by one-tailed paired Student's *t* test (n = 3 replicates). **(c)** Confocal images of T47D cells expressing GFP-Rab7 seeded on BSA treated for 60 min with vehicle or E_2, and stained for ERα. In the inset, arrows indicate points of colocalization. **(d)** Quantification of c. For each experimental condition, Pearson's correlation index and Manders' coefficients (M1 and M2) were calculated within the areas of colocalization using Fiji. Data are represented as mean ± SD. Differences between groups were analyzed by one-tailed Student's *t* test (per replicate: Pearson's: $n_{vehicle}$ = 11 fields, n_{E2} = 12 fields; Manders': $n_{vehicle}$ = 8 fields, n_{E2} = 9 fields). **(e)** Confocal images of T47D cells expressing GFP-Rab7 seeded on FN treated for 60 min with vehicle or E_2, and stained for ERα. **(f)** Quantification of e. For each experimental condition, Pearson's correlation index and Manders' coefficients (M1 and M2) were calculated within the areas of colocalization using Fiji. Data are represented as mean ± SD. Differences between groups were analyzed by one-tailed Student's *t* test (per replicate: $n_{vehicle}$ = 9 fields, n_{E2} = 7 fields). Treatments: ethanol (vehicle) or 10^{-8} M E_2, 8 nM BZ. *, P < 0.05; **, P < 0.01; ***, P < 0.001. Shown data are representative of at least three independent experiments. Black arrowheads indicate positions of 50-kD markers. White arrowheads indicate positions of 37-kD markers. Bars, 10 μm (unless otherwise indicated).

an FN-induced event. We found that ERα is present in vesicle-like punctae after treatment with E_2 for 15 min, regardless of the presence of FN (Fig. 3, a and b). To confirm that E_2 was inducing rapid endocytosis in these cells, we stained them for EEA1, an early endosomal marker, and found that the size of EEA1$^+$ vesicles is dramatically increased after a 15-min treatment with E_2 (Fig. 3, c and d). Moreover, ERα colocalizes with EEA1 upon E_2 treatment (Fig. S2 a). Interestingly, we found that EEA1$^+$ endosomes are strongly localized in the nuclear membrane with this treatment (Fig. 3, e and f). We stained these cells with Lamin B1, a nuclear envelope marker, or with propidium iodide and performed 3D reconstructions to confirm that EEA1 colocalizes with Lamin B1, although EEA1$^+$ endosomes do not seem to enter the nucleus (Fig. S2, b and c). This finding led us to hypothesize that these endosomes could be carrying ERα straight into the nucleus, where it would exert its action, analogous to the way signaling endosomes carry neurotransmitters along neuronal axons (Delcroix et al., 2003; Cosker et al., 2008; Cosker and Segal, 2014). To investigate whether nuclear localization of ERα was in fact endocytosis dependent, we studied the effects of low temperatures on ERα

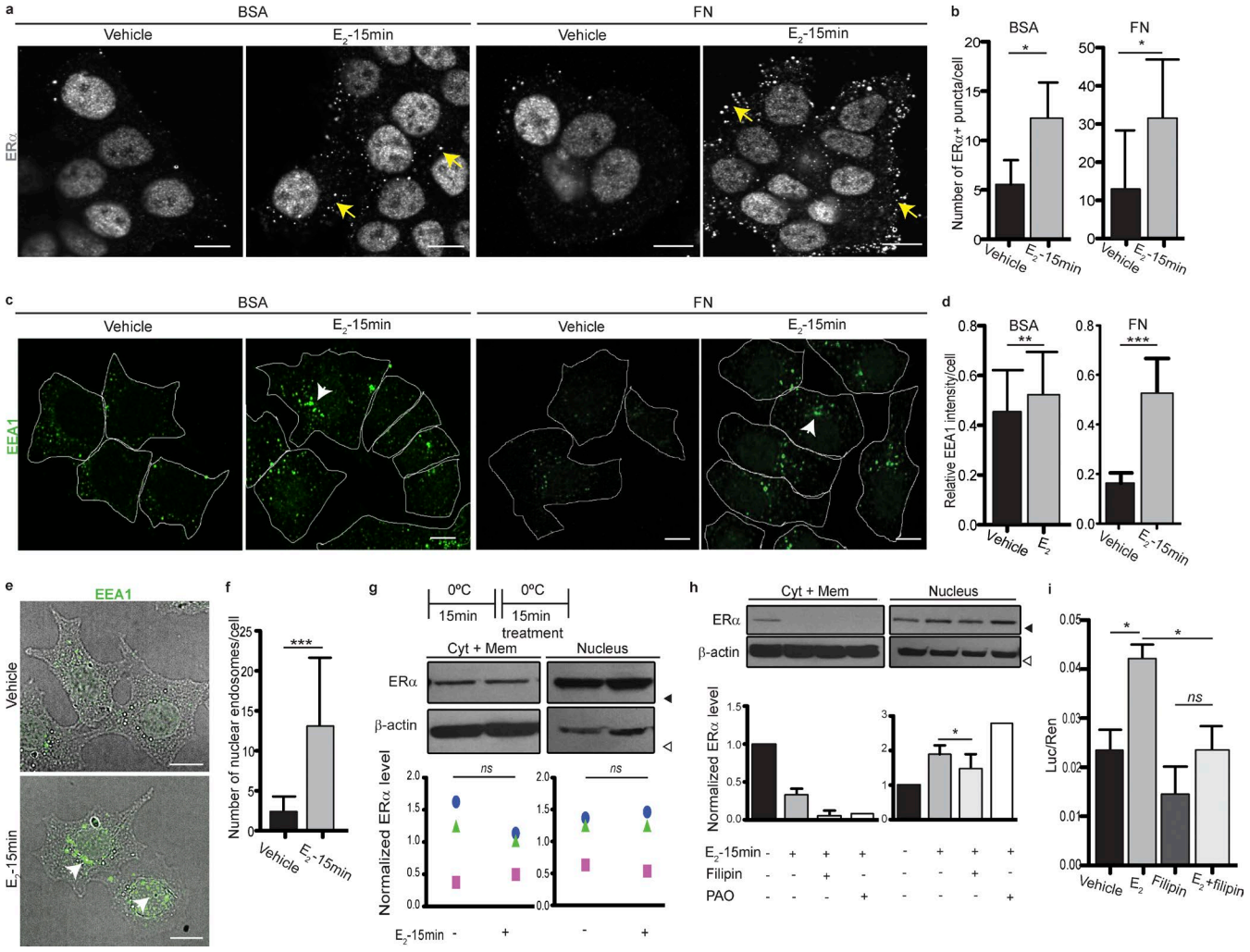

Figure 3. **E_2 stimulates endocytosis of vesicles containing ERα. (a)** Confocal images of MCF7 cells seeded on BSA (left) or FN (right) treated for 15 min as indicated and stained for ERα. Arrows indicate ERα⁺ endosomes. **(b)** Quantification of a. For each experimental condition, structures of ∼200-nm diameter (10–15 pixels) were quantified using Fiji. Shown is the number of ERα⁺ puncta per cell. Differences between groups were analyzed by one-tailed Student's *t* test (per replicate: BSA: $n_{vehicle}$ = 81 cells, n_{E2} = 87 cells; FN: $n_{vehicle}$ = 50 cells, n_{E2} = 64 cells). **(c)** Confocal images of MCF7 cells seeded on BSA (left) or FN (right) treated for 15 min as indicated and stained for EEA1. Cells are delineated in white. Arrows indicate early endosomes. **(d)** Quantification of c. For each experimental condition, shown is EEA1 intensity (mean gray value) per cell calculated using Fiji relative to the highest intensity recorded. Differences between groups were analyzed by one-tailed Student's *t* test (per replicate: BSA: n_{EtOH} = 68 cells; n_{E2} = 39 cells; FN: n_{EtOH} = 94 cells; n_{E2} = 108 cells). **(e)** Confocal images of MCF7 cells seeded on FN treated for 15 min as indicated and stained for EEA1. Merges between differential interference contrast (DIC) microscopy and the green channel are shown. Arrows indicate early endosomes present either in the nuclear membrane or inside the nucleus. **(f)** Quantification of e. For each experimental condition, structures of 10–15 pixels in diameter were quantified using Fiji. Shown is the number of nuclear early endosomes per cell. It was calculated as the total number of EEA1⁺ vesicles in the nuclear membrane or inside the nucleus, per cell. Differences between groups were analyzed by one-tailed Student's *t* test (per replicate: n_{EtOH} = 59 cells; n_{E2} = 54 cells). **(g)** Top: Outline of the protocol followed and Western blot of a subcellular fractionation of MCF7 cells treated as indicated. Blotting antibodies are shown on the left. Bottom: Densitometry. For each subcellular fraction, shown is the ERα/β-actin density ratio normalized to the mean control group. Each symbol represents a different experiment. Differences between groups were analyzed by one-tailed paired Student's *t* test (*n* = 3 replicates). **(h)** Top: Western blot of a subcellular fractionation of MCF7 cells treated for 15 min as indicated. Blotting antibodies are shown on the left. Bottom: Densitometry. For each subcellular fraction, shown is the ERα/β-actin density ratio normalized to the control group. Differences between groups were analyzed by one-tailed paired Student's *t* test (*n* = 3 replicates). **(i)** Luciferase assay in MCF7 cells transiently transfected with pTK-ERE-Luc and pTK-Renilla and treated for 14 h as indicated. Differences between groups were analyzed by two-way ANOVA followed by Bonferroni contrasts adjusted for multiple comparisons (*n* = 3 replicates). Data are represented as mean ± SD. *, P < 0.05; **, P < 0.01; ***, P < 0.001. Treatments: ethanol (vehicle) or 10^{-8} M E_2, 2.5 µg/ml filipin, 5 µM PAO. Shown data are representative of at least three independent experiments. Black arrowheads indicate positions of 50-kD markers. White arrowheads indicate positions of 37-kD markers. Bars, 10 µm.

subcellular shuttling. This treatment should immediately block both membrane events: endocytosis and ATP-dependent vesicle trafficking (Letoha et al., 2003). We found that chilling cells to 0°C completely blocks subcellular shuttling of ERα (Fig. 3 g), which is consistent with a static plasma membrane. We confirmed that the effect of low temperatures was reversible because prechilling the cells does not affect ERα shuttling (Fig. S2 d).

There are two main mechanisms of integrin endocytosis: clathrin dependent and clathrin independent (Mayor and Pagano, 2007). Among clathrin-independent mechanisms, the

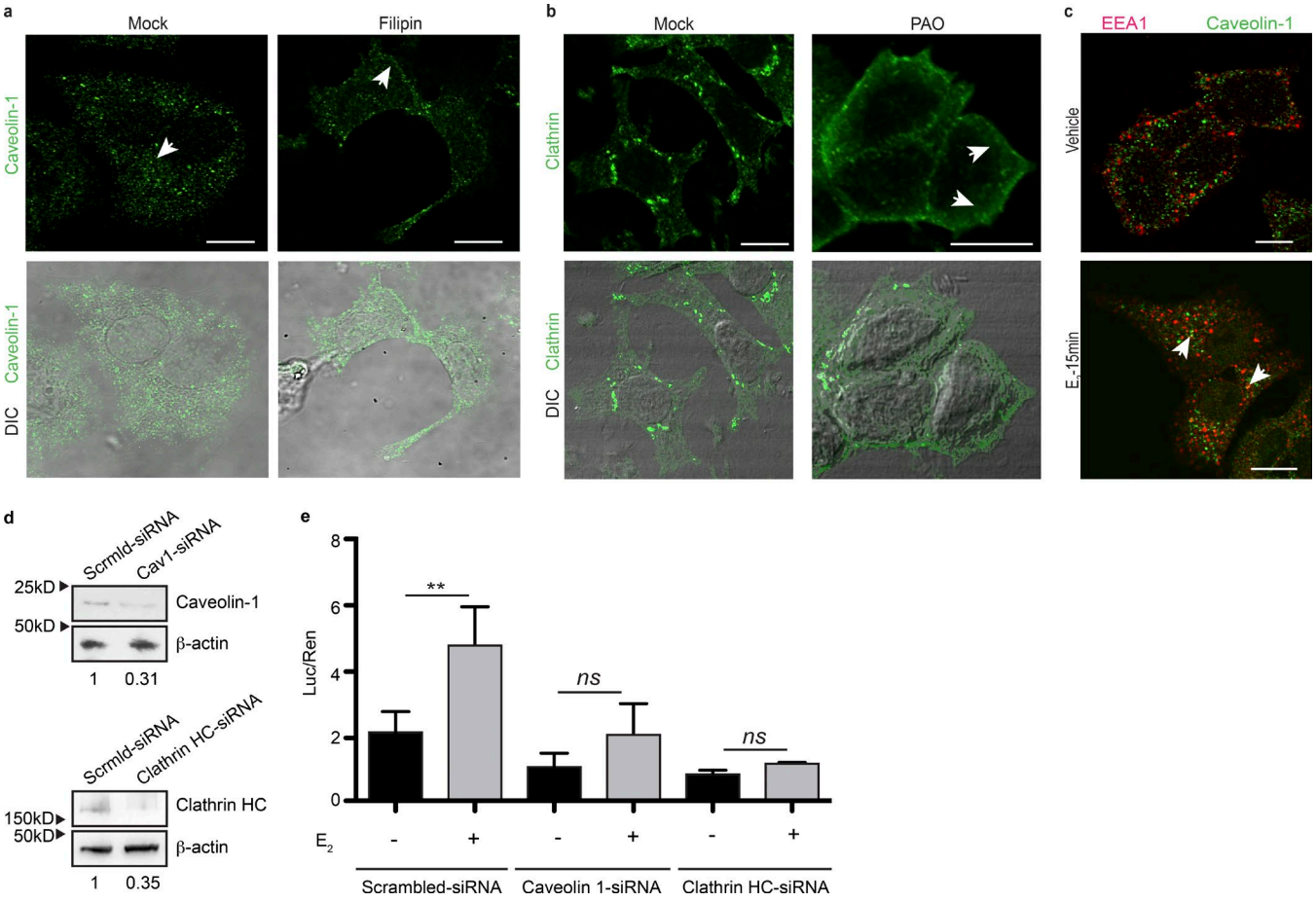

Figure 4. **ERα is endocytosed through a caveolin 1–dependent pathway. (a)** Top: Confocal images of MCF7 cells treated for 15 min as indicated and stained for caveolin 1. Bottom: Merge between caveolin 1 signal and differential interference contrast (DIC) images. Arrows indicate internal or peripheral localization of caveolin 1. **(b)** Top: Confocal images of MCF7 cells, treated for 15 min as indicated, and stained for clathrin. Bottom: Merge between caveolin 1 signal and DIC images. Arrows indicate internal or peripheral localization of clathrin. **(c)** Confocal images of MCF7 cells treated for 15 min as indicated and stained for caveolin 1 or EEA1. Arrows indicate regions of colocalization between the two markers. **(d)** Western blots of MCF7 cells transfected with siRNAs against caveolin 1, clathrin HC, or scrambled for 48 h. Blotting antibodies are shown on the right. Fold change relative to scrambled siRNA is shown on the bottom. **(e)** Luciferase assay in MCF7 cells transiently transfected with pTK-ERE-Luc and pTK-Renilla and the respective siRNAs and treated for 14 h as indicated. Differences between groups were analyzed by two-way ANOVA followed by Bonferroni contrasts adjusted for multiple comparisons ($n = 3$ replicates). Data are represented as mean ± SD. **, $P < 0.01$. Shown data are representative of at least three independent experiments performed. Treatments: ethanol (vehicle) or 10^{-8} M E_2, 2.5 µg/ml filipin, 5 µM PAO. Bars, 10 µm.

best described is the caveolin-dependent pathway. Given that ERα is known to interact with caveolin 1 and 3 (Schlegel et al., 1999; Chung et al., 2009), we hypothesized that ERα would be endocytosed through a caveolin-dependent mechanism in the presence of E_2. To test this, we used filipin, a specific inhibitor of caveolin-mediated endocytosis/membrane recycling, and found that it inhibits E_2-stimulated ERα nuclear translocation (Fig. 3 h). The inhibition of clathrin-mediated endocytosis with phenylarsine oxide (PAO) does not affect ERα shuttling dynamics (Fig. 3 h). We next assessed the effect of filipin treatment on ERα transcriptional activity, performing luciferase reporter assays with a construction that allowed us to measure ERα activity mediated by the ERE. As expected, we found that E_2 is not able to induce ERα transcriptional activity in the presence of filipin, supporting the finding that ERα endocytosis has a major effect in gene transcription (Fig. 3 i). We verified the specific action of filipin and PAO through the inhibition of their canonical endocytosis substrates (Fig. 4, a and b). Together with these results, we found that caveolin 1 colocalizes with EEA1 in the cytoplasm upon 15 min of treatment with E_2 (Fig. 4 c). We further tested the effect of caveolin 1 knockdown on ERα action and found that it inhibits its ERα transcriptional activity, similarly to what we found with its pharmacological inhibitor (Fig. 4, d and e). Interestingly, we found that clathrin knockdown also impairs ERα transcriptional activity (Fig. 4, d and e). This suggests that clathrin might also play at least a partial role in ERα dynamics. Altogether, these data indicate that E_2 induces caveolin-mediated ERα endocytosis in cells seeded on BSA or FN.

ERα⁺ colocalizes with Rab11 in the presence of FN

Internalized endosomes typically avoid lysosomal degradation if recycled to the plasma membrane (Gould and Lippincott-Schwartz, 2009). Therefore, we explored whether FN promoted the recycling of ERα⁺ endosomes, therefore inhibiting

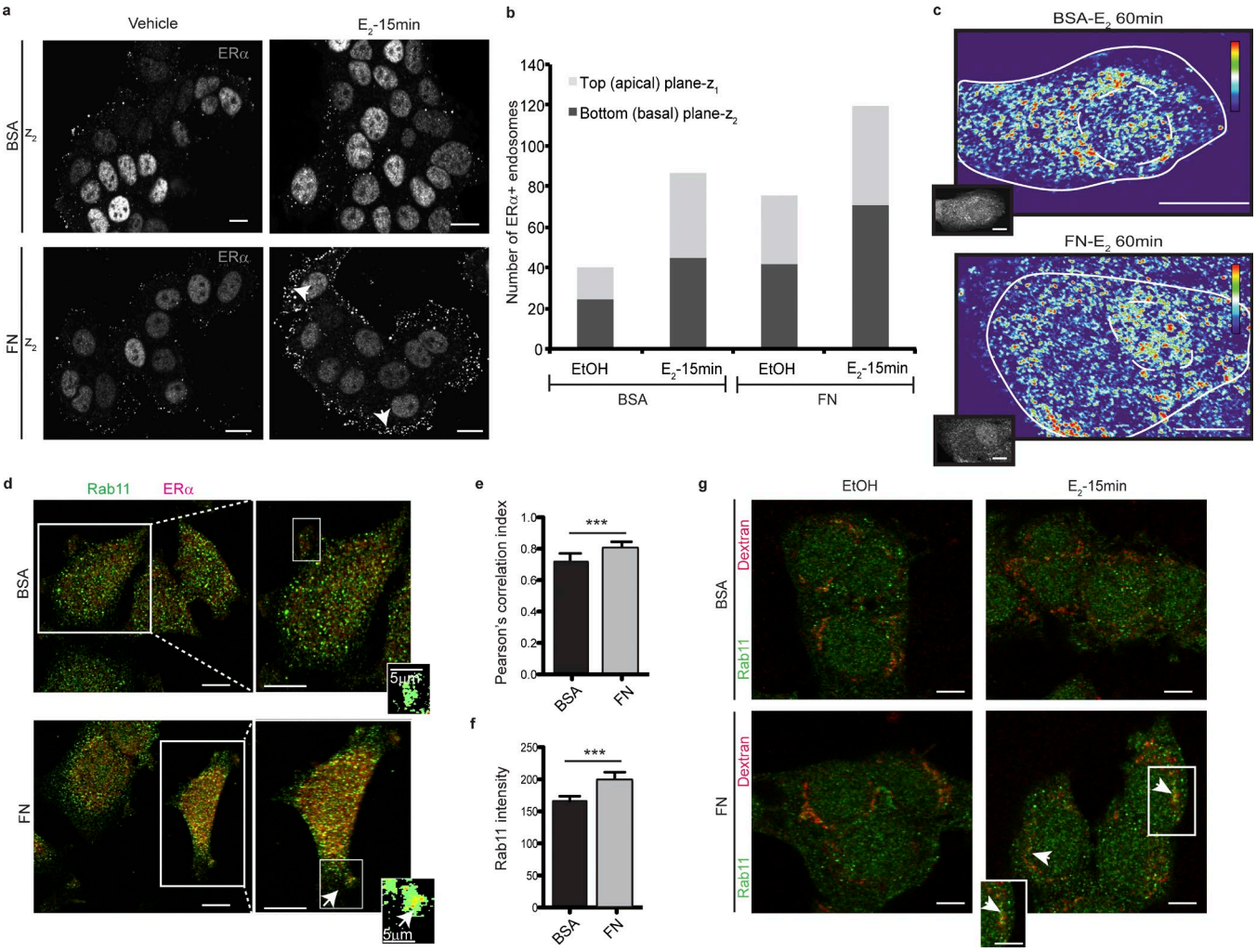

Figure 5. **ERα⁺ is localized in Rab11⁺ vesicles in the presence of FN. (a)** Images of confocal microscopy of MCF7 cells seeded on BSA or FN treated for 15 min as indicated and stained for ERα. Panels show the cytoplasmic/plasma membrane (basal) plane (z2). Nuclear/cytoplasmic (apical) plane (z1) is shown in Fig. S3 b. White arrows indicate ERα⁺ vesicles determined as punctae of 10–15 pixels in diameter (~200 nm). **(b)** Quantification of a. Apical (nuclear/cytoplasmic) versus basal (cytoplasmic/plasma membrane) distribution of ERα⁺ vesicles. Structures of 10–15 pixels in diameter were quantified using Fiji. Mean number of endosomes in each fraction and for each condition is shown. **(c)** Heatmaps of T47D cells seeded on BSA or FN treated for 60 min as indicated and stained for ERα. Cells are outlined in white. Dashed line outlines the nucleus. Intensity bars are shown on the right (red, maximum pixel intensity; blue, minimum pixel intensity). Original images are shown in the insets. **(d)** Images of confocal microscopy of MCF7 cells seeded on BSA or FN treated for 60 min with E_2 and stained for ERα and Rab11. Arrows indicate areas of colocalization within filopodia. Pearson's colocalization maps are shown in the insets. **(e)** Quantification of d. For each experimental condition, Pearson's correlation index was calculated within filopodia protrusions using Fiji. Differences between groups were analyzed by one-tailed Student's *t* test (per replicate: n_{BSA} = 16 fields, n_{FN} = 15 fields). **(f)** Quantification of d. For each experimental condition, overall Rab11 intensity was calculated using Fiji. Data are represented as mean ± SD. Differences between groups were analyzed by one-tailed Student's *t* test (per replicate: n_{BSA} = 5 fields, n_{FN} = 4 fields). **(g)** Images of confocal microscopy of MCF7 cells seeded on BSA or FN treated for 15 min with E_2 in the presence of dextran-CF543 and stained for Rab11. Arrows indicate areas of colocalization between the two fluorophores. Higher magnification is shown in the inset. ***, P < 0.001. Shown data are representative of at least three independent experiments. Treatments: ethanol (vehicle) or 10^{-8} M E_2. Bars, 10 µm (unless otherwise indicated).

its lysosomal degradation induced by E_2. We found that, when cells are seeded on FN and treated with E_2 for 15 min, there is a larger proportion of ERα⁺ vesicles closer to the basal plane (ventral membrane) than when cells are seeded on BSA as shown in Figs. 5 (a and b) and S2 e. Consistent with these findings, after a longer treatment with E_2, ERα distribution in the cytoplasm is peripheral when cells are seeded on FN compared with a more centered distribution on BSA (Fig. 5 c). These data suggest that in the presence of FN, ERα⁺ vesicles are more likely to be found closer to the plasma membrane than to the lysosomal–perinuclear compartment.

To further explore whether ERα⁺ vesicles are more likely to be redirected to the plasma membrane in the presence of FN, we costained the cells with the recycling marker Rab11 (Grant and Donaldson, 2009). Rab11 is mostly localized in the perinuclear region and is further transported to the cell periphery to participate in membrane fusion when recycling is active (Cox et al., 2000; Takahashi et al., 2012). We found that the degree of colocalization of ERα with Rab11 is highest when cells are seeded on FN, particularly at the membrane tips, indicating that ERα is more likely to be localized in Rab11⁺ vesicles under these conditions (Fig. 5, d and e). Together with this, overall intensity of

Rab11 is higher in the presence of FN, suggesting that this pathway is enhanced either by the presence of more Rab11⁺ vesicles or by an increased size of these vesicles (Fig. 5, d and f).

We further tested the effect of E_2 on endocytosis using dextran (10 kD) conjugated with a red fluorophore. We found that a 15-min treatment with E_2 induces strong dextran endocytosis that also colocalizes with EEA1 (Fig. S2, f–h). In addition, we found that dextran colocalizes with Rab11 when cells are seeded on FN, suggesting that it is more frequently localized in Rab11⁺ vesicles in this condition (Fig. 5 g). Moreover, we measured the amount of dextran present in the supernatant after E_2 treatment and found that it is significantly higher when cells are seeded on FN, further suggesting that dextran would be more likely to be recycled in the presence of FN (Fig. S2 i).

ERα is associated to β1-integrin in estrogen-triggered endosomes

To gain insight into the possible mechanism responsible for triggering ERα localization in Rab11⁺ vesicles on cells seeded on FN after E_2 treatment, we explored the possibility that upon endocytosis, ERα⁺ endosomes might contain integrins that, if engaged with FN, would trigger membrane recycling, therefore making the whole complex avoid lysosomal degradation (Caswell et al., 2009; Sung and Weaver, 2011; Dozynkiewicz et al., 2012; De Franceschi et al., 2015). Because we have previously found that FN-induced endocrine resistance is mediated by β1-integrin (Pontiggia et al., 2012), we asked whether this could be the bona fide integrin associated with ERα at the plasma membrane and, therefore, present in E_2-induced endosomes. We performed total internal reflection fluorescence microscopy (TIRFM), which allows the detection only of those fluorophores localized on the ventral plasma membrane, at the cell–substrate interphase. This assay showed that β1-integrin and ERα colocalize at the ventral membrane in MCF7 cells (Fig. 6, a and b; and Video 1). For β1-integrin detection, live-staining technique was used to intensely detect integrin present in the periphery of the cell, although it does not stain cytoplasmic integrin. Therefore, most of the colocalization structures were found at the periphery of the cell, where further colocalization analysis was run as described previously (Dunn et al., 2011). We also found colocalization structures in T47D cells (Fig. S3 a). As a positive control, colocalization between β1-integrin and its well-known partner FAK was assayed with TIRFM, and a similar colocalization pattern was found (Fig. S3 b).

Consistent with these results, coimmunoprecipitation experiments showed that ERα and β1-integrin immunoprecipitate together (Figs. 6 c and S3, c and d). Moreover, we found that β1-integrin has a sequence of five amino acids (LXXLL) within the cytoplasmic-proximal region of its transmembrane domain that is present among all steroid hormone receptor coactivators such as steroid receptor coactivator 1 (SRC1; Fig. 6 d; Mak et al., 1999). Indeed, this conserved motif called NR-box is known to be sufficient to mediate the interaction of coactivators with nuclear receptors such as ERα. For ERα in particular, this interaction is established within its helix 12 in the AF-2 domain (Heery et al., 1997; Savkur and Burris, 2004). In addition, we found that only β1- and β3-integrins contain this sequence (Fig. 6 d), and remarkably, these two integrins share several extracellular ligands and moreover are known to have transmembrane and cytoplasmic domains that are functionally interchangeable (Solowska et al., 1991). Fig. 6 e shows our proposed model for ERα–β1-integrin interaction. Further analyses needed to confirm ERα–β1-integrin physical association are being conducted at our laboratory.

We further investigated whether β1-integrin followed the same endocytosis/degradation pathway as ERα. We found that as with ERα, 60-min treatment with E_2 generates a strong reduction in β1-integrin levels (Figs. 6 f and S3 e). As shown in Fig. 5 f, E-cadherin levels remain unchanged after this treatment, indicating that E_2-induced endocytosis and posterior degradation is specific for certain plasma membrane proteins spatially associated with ERα. As expected, when cells were seeded on FN, this ECM protein rescued β1 integrin from E_2-induced degradation (Figs. 6 g and S3 f).

Using the antibody feeding technique, we followed β1-integrin internalization dynamics and found that 15-min treatment with E_2 stimulates the internalization of β1-integrin (Fig. S3, g and h). This technique allows the detection of β1-integrin⁺ endosomes in a cleaner manner, making it possible to see a small fraction of them without the background signal from cytoplasmic β1-integrin. Along with this, β1-integrin and ERα colocalize in a proportion of E_2-induced endosomes (Fig. 6, h and i). Moreover, β1-integrin shows a strong colocalization with Rab11 after stimulation with E_2 in cells plated on FN, indicating that as with ERα, β1-integrin is largely localized in Rab11⁺ vesicles under these conditions (Fig. 6, j and k). As another control, cells negative for ERα (such as MDA-MB-231) do not exhibit alterations in β1-integrin levels after prolonged treatment with E_2 (Fig. S3, i and j), suggesting that E_2-induced β1-integrin degradation is in fact mediated by ERα.

Estrogen treatment stimulates ERα–β1-integrin clustering

To investigate the interaction between ERα and β1-integrin in higher detail, we performed two-color superresolution microscopy using stochastic optical reconstruction microscopy (STORM; Rust et al., 2006; Bates et al., 2007). Fig. 7 a shows representative STORM images taken in regions of the filopodia of MCF7 cells.

Two-color STORM is a fairly new technique, and therefore there is no consensus yet on the optimal method to quantify correlations between biomolecules. PCC or MCC indices have been used to measure the degree of cooccurrence of the two colors in the same pixel within very small areas of the image where physical colocalization happens (He et al., 2015; Johnson et al., 2016). In principle, the changes in the association between any pair of biomolecules can be estimated by three pairwise quantities: mutual distances between their domains, relative densities, and spatial heterogeneity. We started by analyzing the images using a recently published method (Bermudez-Hernandez et al., 2017) that accounts for two of these quantities: mutual distances and densities. Fig. 7 b shows the results for this interaction factor (IF) between β1-integrin and ERα calculated for control and treated cells. As shown by this index, there are regions with low colocalization (<0.1) and others with higher correlation (>0.4). In fact,

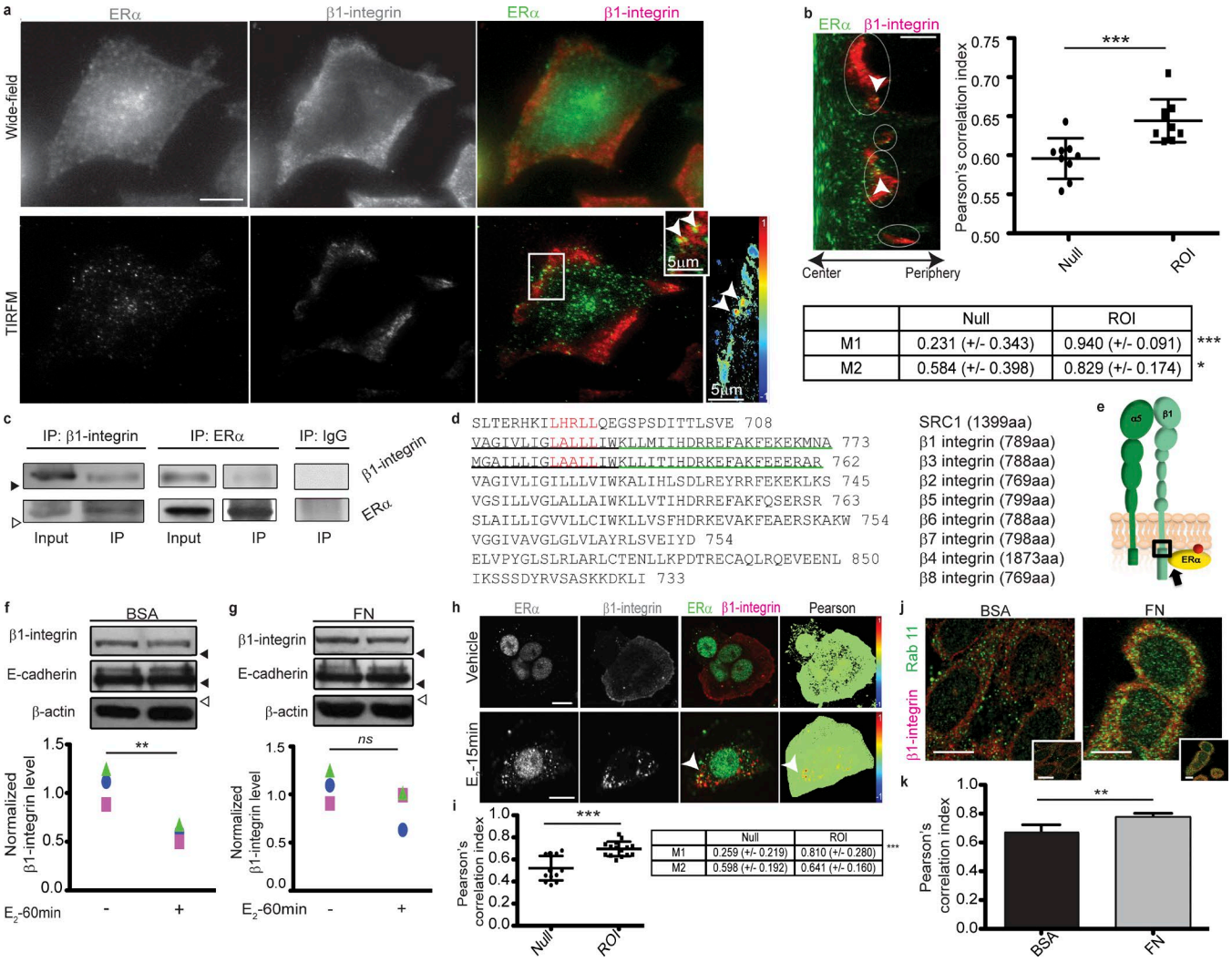

	Null	ROI	
M1	0.231 (+/- 0.343)	0.940 (+/- 0.091)	***
M2	0.584 (+/- 0.398)	0.829 (+/- 0.174)	*

	Null	ROI	
M1	0.259 (+/- 0.219)	0.810 (+/- 0.280)	***
M2	0.598 (+/- 0.192)	0.641 (+/- 0.160)	

Figure 6. **ERα is spatially associated with β1-integrin and they are endocytosed together. (a)** Widefield (top) and TIRFM (bottom) images of a coimmunofluorescence in MCF7 cells, using antibodies against β1-integrin (live-stained) and ERα. In the inset, white arrowheads indicate points of colocalization. Pearson's correlation maps corresponding with the white box shown on the right. White arrowheads indicate points of positive Pearson's correlation. **(b)** Quantification of a. Top left: Polar transformation of TIRFM images was performed using Fiji to align areas of the cell periphery where colocalization is found. For each experimental condition, Pearson's correlation index and Manders' coefficients (M1 and M2) were calculated within the areas of colocalization (ROI) and compared with random areas without colocalization (Null), using Fiji. For Pearson's correlation, datasets are plotted and mean ± SD are shown on the graph. For Manders' coefficients, the table shows mean and SD for each dataset. Differences between groups were analyzed by one-tailed Student's *t* test (per replicate: Pearson's: n_{null} = 9 fields, n_{ROI} = 9 fields; Manders': n_{null} = 14 fields, n_{ROI} = 9 fields). **(c)** Western blot of a coimmunoprecipitation in MCF7 cells, using antibodies against β1-integrin or ERα. Blotting antibodies are shown on the right. Input, whole lysate. IP, immunoprecipitated fraction. **(d)** ClustalW alignment of the eight β-integrins present in humans. The sequence of SRC1 is shown on top. NR-box motif is indicated in red. On the sequences of β1-integrin and β3-integrin, underlined in black is the region corresponding with their transmembrane domain, and in green is their cytoplasmic domain. The topology was predicted using the algorithm TMpred from the website ExPASy and the algorithm from the website TOPCONS. **(e)** Cartoon showing β1-integrin structure and putative interaction site with ERα. Black box indicates the localization of NR-box motif (LXXLL) within β1-integrin transmembrane domain. Red dot shows ERα palmitoylation site, and the arrow indicates where its helix 12 would be localized within the AF-2 domain. **(f and g)** Top: Western blot of total lysates of MCF7 cells, seeded on BSA (f) or FN (g) and treated for 60 min as indicated. Blotting antibodies are shown on the left. Bottom: Densitometry. For each experimental condition, shown is the β1-integrin/β-actin density ratio normalized to the mean control group. Each symbol represents a different experiment. Differences between groups were analyzed by one-tailed paired Student's *t* test (n = 3 replicates). **(h)** Confocal images of MCF7 cells treated for 15 min as indicated and stained for β1-integrin (live stained) and ERα. Arrows indicate points of colocalization. Corresponding Pearson's correlation maps are shown on the right, respectively. White arrows indicate points of positive Pearson's correlation. **(i)** Quantification of h. For each experimental condition, Pearson's correlation index and Manders' coefficients (M1 and M2) were calculated within the areas of colocalization (ROI) and compared with random areas without colocalization (Null) using Fiji. For Pearson's correlation, datasets are plotted and mean ± SD are shown on the graph. For Manders' coefficients, the table shows mean and SD for each dataset. Differences between groups were analyzed by one-tailed Student's *t* test (per replicate: Pearson's: n_{null} = 14 fields, n_{ROI} = 15 fields; Manders': n_{null} = 10 fields, n_{ROI} = 11 fields). **(j)** Confocal images of MCF7 cells seeded on BSA or FN treated with E_2 for 15 min and stained for β1-integrin and Rab11. Full images are shown in the insets. **(k)** Quantification of j. For each experimental condition, Pearson's correlation index was calculated within the areas of colocalization using Fiji. Data are represented as mean ± SD. Differences between groups were analyzed by a one-tailed Student's *t* test (per replicate: n_{BSA} = 4 fields, n_{FN} = 4 fields). *, P < 0.05; **, P < 0.01; ***, P < 0.001. Shown data are representative of at least three independent experiments. Black arrowheads indicate positions of 100-kD markers. White arrowheads indicate positions of 50-kD markers. Treatments: ethanol (vehicle) or 10^{-8} M E_2. Bars, 10 µm (unless otherwise indicated).

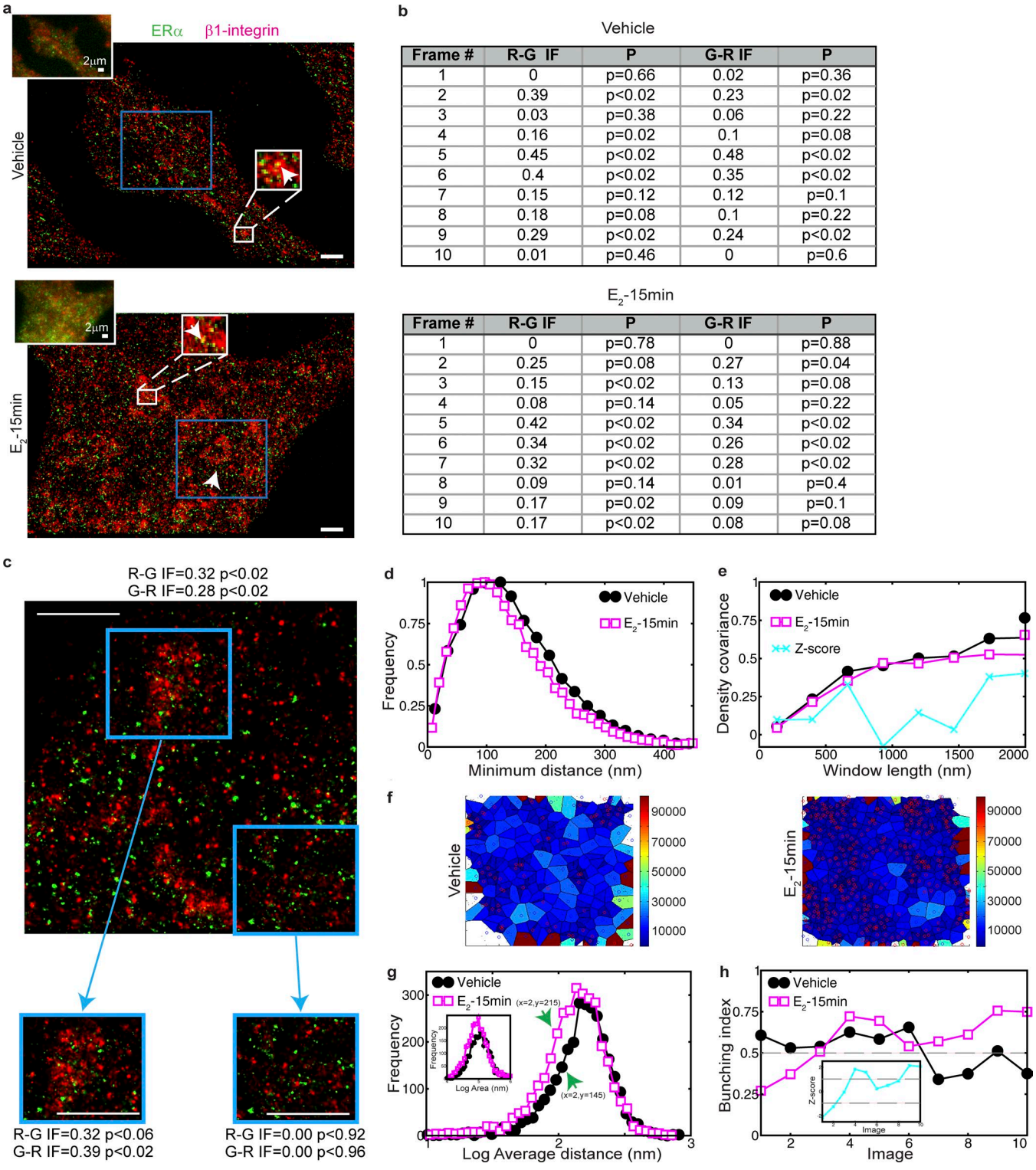

Figure 7. **Effect of E_2 treatment on the conditional distribution of ERα versus β1-integrin. (a)** Images from STORM of filopodia of MCF7 cells treated as indicated for 15 min and stained for ERα or β1-integrin. Insets in the top left corners show the same images taken with widefield microscopy. Inside the zoomed areas, arrows show regions of superposition of the two markers (yellow pixels). Blue squares outline representative areas of 500 × 500 pixels used for subsequent analyses. In the treated cell, arrow inside the blue square shows a region of dense clustering between ERα and β1-integrin. **(b)** Tables showing the IF calculated as described previously (Bermudez-Hernandez et al., 2017) for 10 representative frames of filopodia of MCF7 cells under control (top) or treated (bottom) conditions. R-G, red–green correlation; G-R, green–red correlation. Red, β1-integrin; green, ERα. **(c)** IF calculated for one treated cell (frame 7) and for two sub-ROIs of this frame, showing how this index changes between areas of different β1-integrin/ERα densities. Bars 2 µm. **(d)** Histogram for normalized frequencies of MD between β1-integrin and ERα in filopodia of MCF7 cells among all the analyzed frames for each condition. For each domain detected, centroids were identified, and MDs were calculated from each β1-integrin to its nearest ERα domain throughout each 500 × 500–pixel frame. Frequencies were normalized to the highest value. The graph shows a slight shift toward smaller MDs for treated cells. **(e)** Mean density covariance between ERα and β1-integrin

this method shows a high variability depending on where the region of interest (ROI) is chosen as shown in Fig. 7 c. Therefore, based on this IF, one conclusion would be that there is no difference between control and treated cells, ignoring any change in β1-integrin/ERα clustering that could have occurred in specific domains of the filopodia of these cells. Indeed, this index, similarly to PCCs and MCCs, is biased toward studying the cooccurrence of the two colors in the same pixel, which makes sense for diffraction-limited microscopy but is not enough for the resolution that STORM offers (20–30 nm).

This calls for alternative ways to incorporate the heterogeneities of the distribution of the proteins in this analysis. Therefore, we implemented a numerical estimation of the changes in the three quantities to describe the interaction between ERα and β1-integrin. To facilitate the analysis, these calculations were done using only the centroids of each domain, a simplification further justified by the fact that the sizes of the domains of both proteins were shown to be invariant between the different conditions analyzed (see Fig. S4 e).

Of the three pairwise quantities, the simplest one is the estimation of the minimum distance (MD) calculated over all pairs of ERα and β1-integrin molecules. The first analyses from these datasets reveal that the overall mean MD between ERα and β1-integrin is ∼100 nm (Fig. S4 a), clearly below the diffraction limit. This indicates that these molecules are probably part of the same subcellular nanodomain and that their localization is not well resolved by conventional diffraction-limited microscopy. Using this approach, we also investigated whether distribution of ERα and β1-integrin was affected by 15-min treatment with E_2. Overall, of all frames, we found a small shift toward smaller MD for treated cells (Fig. 7 d). However, when comparing individual frames, we observed that this shift was in the other direction in three of the 10 treated frames analyzed, suggesting that this overall difference is not significant and is highly dependent on the analyzed frame.

The second pairwise quantity estimates the covariation of densities, which is computed as the number of domains per unit area (for each ERα and β1-integrin). The functional association of these two molecules was investigated by computing their covariation as a function of increasing areas. The densities of the two proteins in fact covary, denoted by a positive linear regression coefficient between their densities as shown on the graph of Fig. S4 b. This covariation is shown to be statistically significant when tested against a null model constructed by randomizing the spatial positions of the centroids. This indicates that ERα and β1-integrin exhibit some degree of spatial cooccurrence and that such localization cannot be simply attributed to a random process (as indicated by the values of the z scores in the inset in Fig. S4 b). With this tool, we further sought to explore whether the density covariance was influenced by E_2 treatment. In this case, we found no significant difference between control and treated cells (Fig. 7 e).

Finally, the third analysis considers the spatial spread of both molecules, which seems highly heterogeneous. Specifically, we computed the ratio between the two densities (number of ERα centroids over number of β1-integrin centroids) inside a square ROI of a given size. An example of that heterogeneity is presented (for ROI side length = 50 nm) in Fig. S4 c. The revealed heterogeneity calls for caution when reporting overall means because they might not be representative of changes that are very important in one cell but negligible in others. For that reason, we decided to explore a novel measure with the potential to avoid the limitations. The idea is very simple and uses a Voronoi transformation of the ERα receptor centroid positions (Nicovich et al., 2017). This mathematical transformation identifies a "shell" containing all the points in space that are closer to a given ERα protein than to any other ERα protein. After the transformation, the analysis estimates the size of the shells as well as their β1-integrin contents, i.e., the number, distance, and distribution of β1-integrin centroids inside each shell.

Two examples of the Voronoi transformation (control and treated cells) are presented in Fig. 7 f, where the size of the shells are labeled with colors: centroids of each ERα domain with empty circles and locations of the β1-integrin centroids with full black circles. For each frame, we computed in each shell the average distance (AD) of all β1-integrins to the ERα centroid (notice that this is different from the previous computation that only accounted

domains. Each frame was divided into square ROI of different sizes (window lengths ranging from 130 nm [10 pixels] to 2,000 nm [150 pixels] in side length). For each ROI size, the densities of ERα and β1-integrin were obtained, and the correlation coefficient (C) between these densities was calculated for all datasets. The mean of C among all the control (black full circles) or treated (pink empty squares) cells was plotted as a function of the window side length. Light-blue crosses show the z score (defined by the difference between the mean of the control group (for each window) and the mean of the treated group, and further divided by the square root of the sum of the SD of each group normalized by *n*). Thus, because the z score expresses, in units of SD, the distance between the two distributions, one may safely conclude that here there is no significant difference in density covariance between control and treated cells. **(f)** Two examples of a Voronoi partition for control (left) or treated (right) cells using the centroids of the ERα domains to compute the transformation. Colors indicated in the color bar on the right represent the size of each Voronoi shell (in square nanometers). Black small dots indicate the location of the centroids for β1-integrin domains. Empty big circles indicate the centroids of ERα domains; red circles denote those ERα that have β1-integrins closer than 160 nm, and blue circles indicate those ERα that have β1-integrins further than 160 nm away on the mean. The examples in these panels reveal a clear difference in ERα–β1-integrin bunching between control and treated conditions. **(g)** Histogram of frequencies for the ADs from each ERα centroid to the β1-integrins inside its Voronoi shell among all the analyzed data for each condition (note the semilog axis for presentation purposes). The graph shows a shift toward smaller distances for treated cells. Green arrows indicate as an example a region of the plot where the difference between treated and control fields is almost double. The inset shows the histogram for frequencies of the areas of the Voronoi regions among all the analyzed fields for each condition, demonstrating that treated cells present also relatively smaller Voronoi shells. **(h)** Graph of the bunching index for each cell, which is the ratio between the number of shells (normalized) that contains mean ERα–β1-integrin distances smaller than a threshold value of 160 nm. We named it bunching index as it quantifies the proportion of ERα–β1-integrin complexes among all the domains localized. Control image 1 and E_2-treated image 4 are the ones represented in f. Inset shows the z score, which was calculated as the difference between each bunching index for the treated cell and the mean of the bunching indexes for the control group divided by the SD of the control group. Z score results demonstrate for six cells a significant difference (abs[z score] >1) in the bunching index between control and treated cells. In all plots, control cells are represented with black full circles and treated cells with pink empty squares. Treatments: ethanol (vehicle) or 10^{-8} M E_2.

for the MD). From the analysis of such transformations, we found that the AD of all β1-integrins to their corresponding ERαs inside each shell is different between control and treated cells. This is shown in Fig. 7 g, where the AD distributions for vehicle and treatment are plotted. Note that for relatively long AD values, the two estimations are similar; however, shorter ADs are more frequent for the treated cells than for the control ones. In other words, despite the heterogeneity, there are more ERαs having at least one β1-integrin close by. In particular, the region between 50 and 300 nm of ERα-to–β1-integrin distances shows the most significant shift between control and treated cells, revealing that these distances are more frequent after a 15-min treatment with E_2. These distances are compatible with the typical sizes of early endosomes (Luzio et al., 2007; Su et al., 2016), which further supports our data showing that ERα and β1-integrin are internalized upon E_2 treatment. In addition, the sizes of Voronoi shells are also reduced by E_2 treatment, suggesting that ERs are more tightly packed together (Fig. 7 g, inset).

To account for the observed heterogeneity between different trials, particularly in treated cells, we developed an index to measure the statistical relevance of the differences between the mean of the control group and each treated cell individually, in that way revealing the intrinsic differences between treated ones (Fig. 7 h). We computed the ratio of Voronoi shells containing an AD less than a threshold value (we chose 160 nm, suggested by the mode value of AD in Fig. 7 g and also related to the most frequent size of early endosomes between 100 and 200 nm) over the total number of shells. This index, termed "bunching index," is supposed to reflect for each experiment the tendency seen in Fig. 7 g for short distances.

As Fig. 7 h shows, a number of treated cells present a significantly higher bunching index than the control ones. Interestingly, there are a couple of E_2-treated cells that showed the opposite effect. This could represent the different kinetics with which each cell responds to E_2. After E_2 treatment, ERα–β1-integrin clustering that can be observed in most of the treated cells would be the first step preceding caveolin-dependent internalization as has been extensively shown previously (Mayor et al., 1994; Upla et al., 2004; Bacia et al., 2005). Conversely, faster-responding cells might have already internalized most of the endosomes containing ERα–β1-integrin clusters that would therefore not be present anymore in the membrane region analyzed, explaining why some treated cells showed fewer ERα–β1-integrin clusters than control ones.

Moreover, we studied whether size or number of ERα or β1-integrin domains were affected by the treatment and found there is no significant effect on these variables (Fig. S4, d–f). Interestingly, sizes of these domains are scale free, i.e., they are well represented by a power law distribution, as often happens in many biological systems (Fig. S4 e; Honerkamp-Smith et al., 2009). We also verified that STORM clearly reveals nuclear accumulation of ERα upon E_2 treatment as shown in Fig. S5 (a and b).

ERα–β1-integrin complexes are present in tumor and normal human samples

To further explore whether ERα endocytosis takes place within human tissues, we analyzed normal human tissues from reduction mammoplasties and tumor samples from patients with mammary adenocarcinoma. We found that ERα is present in endosome-like bodies in both normal and tumor samples (Fig. 8, a and b). Sizes of the vesicles observed are compatible with early endosomal vesicles (<500 nm), late endosomes (>600 nm), or multivesicular bodies (>1 µm; Luzio et al., 2007; Su et al., 2016). We confirmed these observations using the ERα antibody typically used for clinical analysis (clone SP1) to stain different sections of the same samples used in Fig. 8 a. This antibody reveals ERα$^+$ endosomes in both normal and tumor tissues (Fig. S5, c and d).

Interestingly, ERα colocalizes with β1-integrin in several areas of the analyzed tumor samples, showing a higher degree of colocalization compared with normal tissues (Fig. 8, a and c). Remarkably, membrane localization of ERα in the tumor samples is higher than in normal tissues; this might account for the increased degree of colocalization with β1-integrin within these samples.

To further explore the clinical relevance of ERα–β1-integrin association, we analyzed TCGA data through cBioPortal (Cerami et al., 2012; Gao et al., 2013) and found that alterations in ERα (*ESR1*) and β1-integrin (*ITGB1*) genes present a tendency to be mutually exclusive in breast cancer (Fig. 8 d). As has been intensely studied, alterations that affect the same pathway tend to not co-occur in the same patient (Cancer Genome Atlas Network, 2012; Ciriello et al., 2012). Therefore, mutual exclusivity would be further evidence indicating that ERα and β1-integrin signaling have a close relationship. Moreover, breast cancer patients with genetic alterations in *ESR1* or *ITGB1* have decreased survival (Fig. 8 e).

These preliminary clinical findings reveal that even though ERα$^+$ vesicles are present in both normal and tumor tissues, ERα and β1-integrin might only be co-endocytosed within tumors. Therefore, FN-induced strengthening of ERα signaling would be a tumor-specific phenomenon, which further suggests this pathway as a target for new antitumor therapies.

Discussion

In this study, we demonstrate by biochemical approaches and high-resolution microscopy that E_2 induces endocytosis of ERα by a mechanism involving caveolin 1. In the presence of FN, ERα avoids lysosomal degradation and is localized in Rab11$^+$ recycling endosomes. We found that ERα is functionally associated with β1-integrin at the plasma membrane of breast tumor cells. We show that β1-integrin follows the same endocytosis/degradation dynamics in the presence of E_2 and would be responsible for dragging ERα to Rab11$^+$ vesicles in the presence of FN, avoiding lysosomal degradation. In this context, FN has a direct, positive impact on ERα's transcriptional activity. ERα$^+$ vesicles are present within human breast tissues, and colocalization with β1-integrin is detected primarily in tumors. The mechanism we describe in this study unravels a new level of regulation of cancer cell signaling by the ECM and provides a putative target for new treatments directed to resensitize patients to endocrine therapy.

We found that upon E_2 treatment, activated membrane ERα is endocytosed in a caveolin-dependent manner and travels in

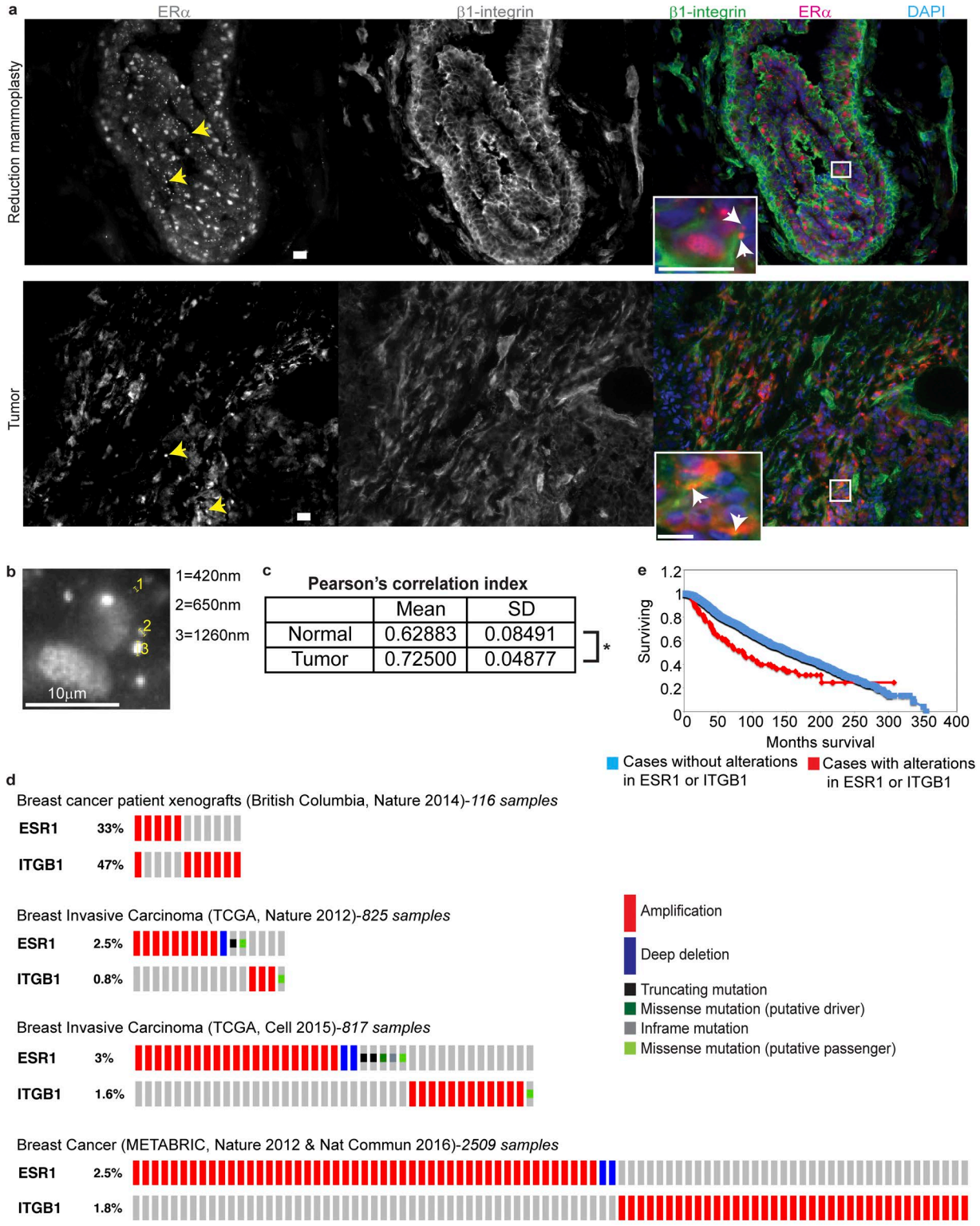

Figure 8. **Endosomes containing ERα are present in normal and tumor human breast tissues. (a)** Top: Confocal images of a normal human breast tissue (reduction mammoplasty; sample N211) stained for ERα (HC-20 clone), β1-integrin, and DAPI. In the inset, arrows indicate the presence of ERα⁺ endosomes. Similar results were obtained in the four different specimens analyzed. Bottom: Confocal images of a human breast tumor (Luminal A subtype adenocarcinoma; sample T171) stained for ERα (HC-20 clone), β1-integrin, and DAPI. Yellow arrows indicate ERα⁺ endosomes. In the inset, arrows indicate the presence of ERα⁺ endosomes. Similar results were obtained in the three different specimens analyzed. **(b)** Magnification from the inset shown in panel a (top). Diameters of ER⁺ vesicles are shown on the right. **(c)** Table showing mean and SD of Pearson's correlation index calculated for the overall colocalization between ERα and β1-integrin. Differences between groups were analyzed by two-tailed Student's *t* test (per replicate: n_{normal} = six fields; n_{tumor} = seven fields). **(d)** OncoPrint from http://www.cbioportal.org (Cerami et al., 2012; Gao et al., 2013) showing the alterations found in ERα (*ESR1*) and β1-integrin (*ITGB1*) genes in different patients obtained from the search in four different datasets: British Columbia, Nature 2014 (Eirew et al., 2015); TCGA, Nature 2012 (Cancer Genome Atlas Network, 2012);

endosomes through the cytoplasm and into the nucleus. In addition, inhibition of clathrin also impairs ERα transcriptional activity, suggesting that the clathrin-dependent pathway might be also, at least partially, involved in ERα endocytosis. The shuttling of plasma membrane proteins into the nucleus through endosomes has been described for other endosomal proteins (Chaumet et al., 2015) and transmembrane receptors such as FGF (Małecki et al., 2004). A mechanism for E_2-induced ERα endocytosis has been proposed for ERα-positive neurons (Kisler et al., 2013). We propose that binding of E_2 to ERα would occur at the plasma membrane so that at least a proportion of hormones could exert their action without actually crossing through the membrane. We show in this study that E_2-induced endosomes containing ERα can also be targeted to lysosomes, where ERα is degraded. Therefore, we propose that E_2-induced lysosomal degradation of ERα is a relevant mechanism of desensitization to E_2. However, this mechanism is lost when cells are in a FN-rich matrix, where ERα escapes lysosomal degradation and its transcriptional activity is enhanced. We present evidence indicating that FN promotes ERα localization in Rab11$^+$ vesicles that would therefore inhibit its lysosomal degradation.

As with other membrane proteins such as caveolin 1 and membrane-associated proteins such as integrin-linked kinase (Schlegel et al., 1999; Acconcia et al., 2006; Chung et al., 2009), ERα colocalizes with β1-integrin in plasma membrane structures. Through high-resolution microscopy and coimmunoprecipitation analyses, we show evidence of a close association between these proteins that would be mediated by the NR-box that we identified within the β1-integrin sequence. Ongoing experiments in our laboratory are aiming to confirm the physical association between these two proteins and the domains involved.

Through STORM superresolution microscopy, we showed that ERα and β1-integrin are present in the same nanodomains within the filopodia and, moreover, are organized in structures of size consistent with early endosomes. In addition, STORM revealed that ERα–β1-integrin clustering is incremented upon E_2 treatment, further supporting the presented evidence that indicates that ERα–β1-integrin complexes are endocytosed together upon E_2 treatment. Membrane β1-integrin could be in both its active (high-affinity) or inactive (low-affinity) conformations, each of which normally undergo different endocytosis/recycling pathways (De Franceschi et al., 2015). Inactive β1-integrins are rapidly recycled to the cell membrane to form protrusions such as lamellipodia and filopodia, following a fast recycling pathway. Active β1-integrins are less efficiently recycled and are targeted to the Rab7 compartment (Arjonen et al., 2012). However, in the presence of FN, ligand-occupied active β1-integrins are rapidly recycled from the lysosomal compartment to the rear of the cell, keeping their active conformation. Interestingly, this process occurs specifically in cancer cells and is a way by which cells remodel their ECM (Dozynkiewicz et al., 2012). Therefore, we propose that E_2 induces internalization of at least active β1-integrins associated with ERα (Fig. 9). In the absence of FN, active β1-integrin and ERα are directed to the lysosomal compartment, where both proteins are degraded. However, when FN is present, ligand-occupied active β1-integrin would be recycled to the plasma membrane in Rab11$^+$ vesicles, carrying ERα with it and inhibiting its lysosomal degradation (Fig. 9). The role of integrins as masters of endosomal trafficking has been also demonstrated for other receptors and cargos such as VEGFR2 and lipid rafts (Caswell et al., 2009). In this context, an FN-rich matrix represents a double advantage for breast tumor cell survival because it triggers proliferative signals transduced through β1-integrin (Han and Roman, 2006; Moreno-Layseca and Streuli, 2014) and also intensifies E_2 signaling. Ongoing experiments in our laboratory are aiming to determine whether E_2 affects active and inactive β1-integrins differently.

Several functions have been associated with membrane ERα and are mainly related to nonclassic (extranuclear) ERα signaling pathways (Levin, 2009). However, some authors have begun to suggest that there is a direct link between membrane ERα and its classic nuclear activity (Pedram et al., 2002; La Rosa et al., 2012). Our results provide a link between genomic and nongenomic effects of E_2 through the activity of membrane-bound ERα. We show evidence suggesting that membrane ERα travels in endosomes into the nucleus, where it would also have transcriptional (genomic) activity. The evidence of the signaling pathway shown in this study is, to our knowledge, the first demonstration of the previously suggested hypothesis of an active mechanism responsible for E_2 shuttling into the nucleus (Pietras and Szego, 1984; Razandi et al., 2002). Further analyses are needed to unravel whether membrane ERα dimerizes within these endosomes and at which stage of its subcellular shuttling.

Endocytosis and subsequent degradation of ERα in lysosomes described in this study is a novel pathway of subcellular signaling and negative feedback induced by E_2. Totta et al. (2014, 2015) recently proposed that membrane-bound ERα could be degraded in lysosomes as well as in the proteasomal compartment. However, the authors did not demonstrate what membrane events take place in response to E_2, leading to ERα internalization and further lysosomal degradation. In this study, we show robust evidence of this phenomenon, describing how this process is regulated and what is the response of the membrane proteins involved. However, it still remains to be elucidated how ERα enters the lysosomal lumen for its degradation. In this sense, it has been proposed that the molecular pump LAMP-2, which has been shown to interact with ERα, would be responsible for allowing its uptake into the lysosomal lumen (Totta et al., 2014; Wang and Robbins, 2014). The signal that triggers ERα lysosomal degradation after prolonged exposure to E_2 and whether this mechanism requires ERα's previous translocation to the nucleus are still unknown.

TCGA, Cell 2015 (Ciriello et al., 2015); and Nature 2012 and Nature Communications 2016 (Pereira et al., 2016). **(e)** Kaplan–Meier plot of the overall survival of patients with alterations in *ESR1* or *ITGB1* genes using thelargest and newest dataset available in http://www.cbioportal.org (Breast Cancer-METABRIC; Cerami et al., 2012; Gao et al., 2013). Significance level after the log-rank test is shown in the plot. *, P < 0.05; **, P < 0.01; ***, P < 0.001. Bars, 20 µm (unless otherwise indicated). The results shown in this study are in whole or part based on data generated by the TCGA Research Network: http://cancergenome.nih.gov/.

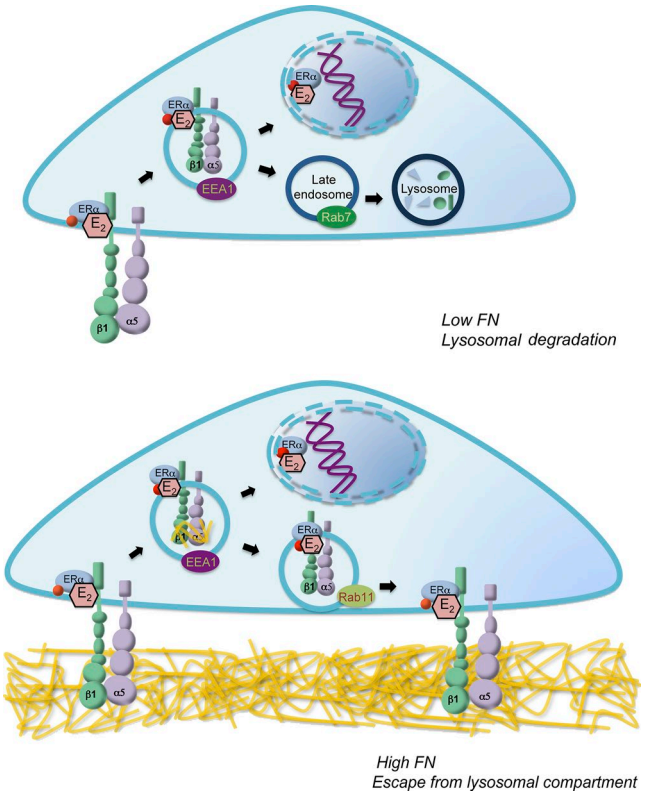

Figure 9. **Model for endocytic transport of ERα and β1-integrin regulated by FN in breast cancer cells.** Estrogens induce rapid endocytosis of membrane ERα–β1-integrin complexes, generating EEA1⁺ vesicles. In the absence of FN, vesicles containing β1-integrin and ERα could either fuse to the nuclear membrane where ERα exerts its action or follow the lysosomal pathway, where ERα colocalizes with Rab7. After 60 min, ERα and β1-integrin are degraded in lysosomes and the signal ends. In the presence of FN, ERα and β1-integrin are localized in Rab11⁺ vesicles, suggesting that they might be recycled and therefore avoid the lysosomal pathway. ERα and β1-integrin levels are maintained over time and the cycle continues, keeping ERα transcriptionally active.

The finding that FN strengthens ERα activity suggests that tumor-like stromas would enhance ERα's activity. FN has been shown to be incremented within cancer cells (Nam et al., 2010; Bae et al., 2013) and is known to contact breast epithelial cells when the normal structure of the basement membrane is disrupted, which occurs during malignant transformation (Ghajar and Bissell, 2008; Lu et al., 2011, 2012). Within tumors, not only ECM composition changes but also its stiffness (Acerbi et al., 2015). Therefore, it is tempting to speculate that not only the presence of FN but also the distorted tissue architecture in stiff substrates (i.e., more cell-substrate contacts, loss of cell apical-basal polarity) might affect ERα degradation in tumors. The loss of normal cellular polarity and subcellular compartmentalization might lead to a different frequency of ERα–β1-integrin interactions in tumor cells. Indeed, we show that although ERα⁺ endosomes are present in normal as well as tumor human samples, ERα colocalizes with β1-integrin fundamentally in tumors. These data are consistent with studies showing that high levels of FN and β1-integrin in breast tumors are associated with lower survival (Yao et al., 2007; Helleman et al., 2008). Moreover, clinical data of breast cancer patients from TCGA databases show that alterations in ERα and β1-integrin genes are mutually exclusive, suggesting that they might be implicated in the same signaling pathway. In addition, alterations in these genes correlate with decreased survival. The findings presented in this study have direct therapeutic implications for breast cancer as blocking FN-dependent activation of ERα, potentially by inhibiting the interaction between ERα and β1-integrin, arises as a novel target for new therapies. This would be a breakthrough approach to overcome endocrine resistance induced by the ECM in breast cancer.

Materials and methods

Cell culture

MCF7 and T47D cell lines were purchased from ATCC and regularly checked for mycoplasma. These cell lines were routinely maintained in DMEM/F12 cell culture medium (Sigma-Aldrich) supplemented with 10% FBS (Internegocios) and gentamicin, in a humidified 5% CO_2/air atmosphere. Serial passages were performed by treatment of 80% confluent monolayers with 0.25% trypsin (Invitrogen) and 0.02% EDTA in Ca^{2+}-free and Mg^{2+}-free PBS.

Reagents

E_2 was purchased from Sigma-Aldrich; BAF and BSA from Santa Cruz Biotechnology; and FN from EMD Millipore. Filipin and PAO, both from Sigma-Aldrich, were provided by C. Davio (Universidad de Buenos Aires, Buenos Aires, Argentina). BZ was purchased from Velcade; Lipofectamine 2000 from Thermo Fisher Scientific; LyoVec transfection reagent InvivoGen; phalloidin from Sigma-Aldrich, and DAPI from Research Organics.

DNA constructs and RNA interference sequences

GFP-Rab7 expression construct was a gift from C. Arregui (Universidad de San Martin, Buenos Aires, Argentina; Hernández et al., 2006). Plasmid pTK-ERE-luc containing five copies of the ERE upstream of the luciferase cassette was a gift from C. Jordan (University of Texas, Houston, TX). pTK-renilla was purchased from Promega.The constructs were verified by sequencing. siRNA/Stealth against ERα was purchased from Invitrogen as the following sequences: sense 5′-CAGAGGCUCUCAAACUAUAAAGAAA-3′, and antisense 5′-UUUCUUUAUAGUUUGAGAGCCUCUG-3′. siRNA against caveolin 1 (sc-29241), siRNA against clathrin–heavy chain (HC; sc-35067), and scrambled siRNA (sc-37007) were purchased from Santa Cruz Biotechnology.

Antibodies

The following antibodies were used in this study and were purchased from Santa Cruz Biotechnology unless otherwise noted (including dilutions/amounts used for immunofluorescence, Western blot [WB], and immunoprecipitation [IP]): ERα (HC-20 rabbit; 1:100 immunofluorescence, 1:200 WB; 3 µg IP), ERα (F-10 mouse; 3 µg IP), β1-integrin (LM534 mouse; 1:100 immunofluorescence; EMD Millipore), β1-integrin (M-106 rabbit; 1:300 WB; 3 µg IP), E-cadherin (H-108 rabbit; 1:1,000 WB), β-actin (C4 mouse; 1:10,000 WB), Rab11 (H-87 rabbit; 1:200 WB), Rab7 (sc-376362 mouse; 1:100 immunofluorescence), and caveolin 1 (sc-53564

mouse; 1:600 immunofluorescence; 1:200 WB). LAMP-1 (ab25630 mouse; 1:20 immunofluorescence), clathrin (ab2731 mouse; 1:500 immunofluorescence), and Lamin B1 (ab133741 rabbit; 1:243 immunofluorescence) were purchased from Abcam; and clathrin-HC (clone 23 mouse; 610500; 1:1,000 WB) was purchased from BD. HC-20 peptide was purchased from Santa Cruz Biotechnology. Secondary antibodies used for WB (1:5,000) were goat anti–mouse HRP-conjugated (AP308P) and goat anti–rabbit HRP conjugated (AP132P) purchased from EMD Millipore. Secondary antibodies used for immunofluorescence (1:500) were goat anti–mouse and goat anti–rabbit Alexa Fluor 488–, 555–, and 647–conjugated antibodies, all purchased from Thermo Fisher Scientific.

Subcellular fractionation

1,000,000 cells were seeded in 60-mm cell culture dishes (Greiner-Bio-One) coated with FN (2 µg/cm^2 in PBS) in regular culture medium. Culture dishes coated with BSA (2 µg/cm^2 in PBS) were used as control. After 16 h, cells were washed three times with PBS, and culture medium was changed to phenol red–free DMEM/F12 plus 1% charcoal-stripped FBS and left in the incubator for another 24 h. Cells were then treated with 10^{-8} M E_2 at 37°C for the indicated times and washed twice with PBS, and protein extracts were prepared by homogenizing fresh cells on ice in subcellular fractionation buffer (250 mM sucrose, 20 mM Hepes, pH 7.4, 10 mM KCl, 1.5 mM $MgCl_2$, 1 mM EDTA, and 1 mM EGTA; Abcam). The Abcam subcellular fractionation protocol was followed. Briefly, cells were centrifuged at 720 *g* to obtain the nuclear pellet, and the supernatant was recentrifuged at 3,000 *g* to obtain the cytoplasmic and membrane fraction. After two further ultracentrifugations, cytosolic and membrane fractions were obtained. These fractions were subsequently analyzed by SDS-PAGE followed by Western blotting with the indicated antibodies. Efficiency of nuclear/cytoplasmic separation was verified using nuclear-specific protein H2A.X (Fig. S5 e). E-cadherin was used to verify the efficiency of membrane purification (Fig. S1, g–j).

Western blot

Protein extracts from whole cells were prepared by scraping the culture dishes on ice with radioimmunoprecipitation assay (RIPA) buffer (50 mM Tris, pH 8.0, containing 150 mM NaCl, 0.1% SDS, 0.5% deoxycholate, and 1% NP-40) containing protease inhibitors (40 µM phenylmethylsulfonyl fluoride, 5 µg/ml leupeptin, 50 µg/ml aprotinin, and 200 µM orthovanadate). Protein extracts form subcellular fractions were obtained as described above. Protein concentration was measured using the Bradford method (Bradford, 1976). After adding sample buffer containing β-mercaptoethanol, samples were heated at 95°C for 5 min. 50 µg of each sample was then run in SDS-PAGE minigels and transferred to polyvinylidene difluoride membranes (Amersham Biosciences). Membranes were blocked for 1 h at RT in 5% fat-free milk in Tris-buffered saline plus 0.1% Tween-20 (TBST). Primary antibodies were prepared in blocking medium and incubated at 4°C overnight. After washing with TBST, membranes were incubated with secondary antibodies for 1 h at RT. Signal was detected with an enhanced chemiluminescence kit (ECL; Amersham Biosciences). Densitometry was performed using the gel analyzer plugin of Fiji (ImageJ; National Institutes of Health; Schindelin et al., 2012) and the plugin Gels. The standard process with this software was to select the ROI in each lane individually and then plot the intensity measurements. The area under the curve was quantified, which represents the final intensity for each band. The intensities were further analyzed as has been extensively reported previously (Degasperi et al., 2014; McDonough et al., 2015). We then normalized each intensity value to the intensity measured for β-actin in the corresponding lane for each one of the three repetitions of the experiment. The three results for the density ratio of the control group were then averaged, and each ratio was normalized to the control mean, so that the control value will be 1 with its correspondent SD.

Membrane fluidity reduction, endocytosis/membrane recycling blockade, and lysosomal inhibition

For membrane fluidity reduction, a 15-min pretreatment of chilling cells at 0°C followed by a treatment with E_2 at 0°C or 37°C was performed. For endocytosis/membrane recycling blockade, filipin (2.5 µg/ml), or PAO (5 µM) were administrated together with E_2 for the indicated times. For lysosomal inhibition, a 90-min pretreatment with BAF (25 nM) at 37°C was done. After these treatments, subcellular fractionation and Western blot were performed as described above.

Dextran endocytosis assay

We followed the protocol described previously for substrate endocytosis/recycling (Gillespie et al., 2013). Briefly, cells were seeded at 80% confluence in 24-well plates. After 16 h, cells were washed three times with PBS and serum-starved for 24 h. Cells were then treated with 10^{-8} M E_2 or its vehicle for 15 min at 37°C. Then 10 µg/ml dextran-CF543 (80111; Biotium) was added, and cells were left at 37°C for another 10 min. Subsequently, cells were washed once with cold serum-free medium and twice with 0.2 M sodium acetate, pH 4.5, and washed again once with cold serum-free medium. For the chase, cells were incubated another 15 min at 37°C with serum-free medium. After the chase, the medium was recovered before washing one more time with 0.2 M sodium acetate, pH 4.5. Fluorescence from acid washes and medium was measured on a FilterMax F3 Multi-Mode Microplate-Reader (Molecular Devices) at 535/595-nm absorption/emission.

IP

The protocol described by Bonifacino et al. (2001) was followed with slight modifications. Briefly, fresh cells were lysed with weak RIPA buffer. 3 µg antibody was preincubated with protein A/G agarose beads (Santa Cruz Biotechnology) with gentle mixing for 1 h at RT. Antibody–bead complexes were then mixed overnight at 4°C with 500 µg protein. After several washes with weak RIPA, samples were analyzed by SDS-PAGE followed by Western blotting with the indicated antibodies.

Luciferase assay

100,000 cells per well were seeded in 48-well culture dishes coated or not coated with FN (2 µg/cm^2) in the presence of

LyoVec–DNA complexes (50:1). DNA constructs pTK-Renilla and pTK-ERE-Luc were used in a 10:1 ratio. After 18 h, cells were washed three times with PBS, and culture medium was changed to phenol red–free DMEM/F12 plus 1% charcoal-stripped FBS and left in the incubator for another 24 h. Cells were then incubated in the presence of 10^{-8} M E_2 at 37°C for 14 h. Dual-luciferase reporter assay system kit (Promega) was used to reveal luciferase or renilla signals, following the instructions described by the manufacturer.

Immunofluorescence and confocal microscopy

50,000 cells were seeded on glass coverslips (Marienfeld) in 24-well plates coated with BSA or FN (2 µg/cm^2) in regular culture medium. After 16 h, cells were washed three times with PBS, and culture medium was changed to phenol red–free DMEM/F12 plus 1% charcoal-stripped FBS and left in the incubator for 24 h. Cells were then treated with 10^{-8} M E_2 for the indicated times. When cells were transfected before this treatment, 3×10^4 cells were seeded on glass coverslips in 24-well plates covered or uncovered with FN (2 µg/cm^2) in regular culture medium. After 16 h, cells were transfected using Lipofectamine 2000, following the protocol described by the manufacturer. Briefly, culture medium was replaced by OptiMEM (Thermo Fisher Scientific), and cells were incubated for 24 h with lipofectamine–DNA (5:1) complexes. Treatment was then administered as described above. For immunofluorescence staining, the protocol described by Debnath et al. (2003) was followed with slight modifications. In brief, cells were fixed for 20 min at RT with 4% PFA in PBS and permeabilized with 0.1% Triton X-100 in PBS for 10 min at 4°C, then blocked for 90 min at RT with immunofluorescence buffer (130 mM NaCl, 7 mM Na_2HPO_4, 3.5 mM NaH_2PO_4, 7.7 mM NaN_3, 0.1% BSA, 0.2% Triton X-100, and 0.05% Tween-20) plus 10% goat serum. They were subsequently stained with the indicated primary antibodies (prepared in blocking medium) overnight at 4°C, followed by incubation with the secondary antibodies for 1 h at RT. For β1-integrin staining, when indicated, cells were live-stained: antibody was prepared in the culture medium, and cells were incubated with it for 1 h in the incubator. They were subsequently fixed and further stained as described above. For β1-integrin endocytosis assay, after live-staining, cells were treated with 10^{-8} M E_2 for 15 min and then fixed and permeabilized with 0.1% Triton X-100 in PBS for 20 min at 37°C. Secondary antibodies were incubated for 1 h at RT. Coverslips were mounted using Mowiol 4–88 (Sigma-Aldrich). Widefield images were acquired using a Nikon Eclipse TE 2000-S inverted microscope with a Nikon Plan Fluor 20×/0.50-NA objective at RT using a Nikon Digital Sight DS-Fi1 camera and the acquisition software NIS-Elements (Nikon) and processed with Fiji. Confocal images were acquired using an Olympus FV-1000 inverted confocal microscope with an Olympus 60×/1.20-NA UPLAN Apochromat water objective, at RT, using the acquisition software Olympus FluoView v.5.0 and processed with Fiji. For colocalization analyses, PCCs and MCCs were calculated within the desired areas of the images as described previously (Dunn et al., 2011). Briefly, PCC is a useful statistic to quantify colocalization, with values range from 1 for two images whose fluorescence intensities are perfectly and linearly related to −1 for two images whose fluorescence intensities are perfectly but inversely related to one another. Values near zero reflect distributions of probes that are uncorrelated with one another. In the images shown, red color indicates a value of 1 for the PCC, and blue indicates a value of −1. The formula for PCC for a typical image consisting of red and green channels is

$$\mathrm{PCC} = \frac{\sum_i (R_i - \bar{R}) \times (G_i - \bar{G})}{\sum_i (R_i - \bar{R})^2 \times \sum_i (G_i - \bar{G})^2},$$

where R_i and G_i refer to the intensity values of the red and green channels, respectively, of pixel i, and $\bar{R}$ and $\bar{G}$ refer to the mean intensities of the red and green channels, respectively, across the entire image. We calculated it for each analyzed frame using the Colocalization colormap plugin for Fiji. Although PCC provides an effective statistic for measuring overall association of two probes in an image, MCC is useful to measure the fraction of one protein that colocalizes with a second protein. For two probes, denoted as R and G, two different MCC values are derived, M_1, the fraction of R in compartments containing G, and M_2, the fraction of G in compartments containing R. These coefficients are simply calculated as

$$M_1 = \frac{\sum_i R_{i,\mathrm{colocal}}}{\sum_i R_i},$$

where $R_{i,\mathrm{colocal}} = R_i$ if $G_i > 0$ and $R_{i,\mathrm{colocal}} = 0$ if $G_i = 0$ and

$$M_2 = \frac{\sum_i G_{i,\mathrm{colocal}}}{\sum_i G_i},$$

where $G_{i,\mathrm{colocal}} = G_i$ if $R_i > 0$ and $G_{i,\mathrm{colocal}} = 0$ if $R_i = 0$. We calculated these coefficients for each analyzed frame using the Coloc 2 plugin for Fiji.

3D rendering from z stacks was performed using Fiji and the plugin 3D Viewer. This plugin performs the 3D reconstitution from which we recorded the videos and images shown in this paper.

Verification of antibody specificity

Every antibody used in this paper was chosen based on its wide usage in the literature. In particular, the antibody used to detect ERα has been used in >200 papers (Gao et al., 2015; Arnal et al., 2017). β1-integrin antibodies used throughout this paper have also been widely used in the literature (Tiwari et al., 2011; Waxmonsky and Conner, 2013; Long et al., 2016). In the case of the antibody used to detect ERα, the most thoroughly used in the present paper, its specificity was tested for Western blot and immunofluorescence. For immunoneutralization assays, ERα antibody (clone HC-20; Santa Cruz Biotechnology) was preincubated for 90 min at 4°C with HC-20 peptide (Santa Cruz Biotechnology) or its control before using it in the blotting membranes from MCF7 cell lysates or for immunofluorescence of these cells. Considering that each antibody has two HC-20 epitopes and that an excess (at least 10-fold) of the peptide is needed to ensure efficient blocking (Skliris et al., 2009), the amount of blocking peptide used was calculated as

$$\mathrm{mol\,HC\text{-}20\,peptide} = [2 * (\mathrm{mol\,ER\alpha\,antibody})] * 10.$$

However, the specificity of this antibody was further confirmed by knocking down endogenous ERα in MCF7 cells, with the specific siRNA described above, followed by its detection through Western blot to evaluate the loss of the ERα signal.

TIRFM

This technique is based in the formation of an evanescent electromagnetic field generated when the incident light is totally internally reflected at the glass–water interface. The evanescent field decays exponentially from the interface and thus only illuminates fluorophores that are close to the glass. Therefore, it is used to selectively detect molecules localized in the ventral plasma membrane, within a radius of ∼100 nm from the glass surface (Ambrose, 1956; Axelrod, 1981, 2001). 300,000 cells were seeded on BSA- or FN-coated (2 µg/cm^2) 25-mm coverslips in six-well plates. After 16 h, cells were live-stained for β1-integrin as explained for confocal microscopy, or fixed with 4% PFA/4% sucrose and stained with the antibody against ERα. Coverslips were mounted in PBS on the stage of a fully motorized Nikon TE2000-E inverted microscope equipped for widefield and TIRFM. In all cases, cells were visualized through a TIRF 60×/1.45-NA water objective, at RT, and imaged using an ORCA II ER charge-coupled device (CCD) camera controlled by the MetaMorph software (Molecular Devices). Images were then processed with the software Fiji. For TIRFM, cells were illuminated using a 488-nm argon laser. Evanescent wave penetration depth was calculated to be ∼210 nm using the following parameters: 488 nm as λ, 1.52 as n_1, 1.33 as n_2, and 62° as the incident light beam angle. For image processing, when indicated, polar transformation was performed using Fiji and the plugin Polar Transformer (https://imagej.nih.gov/ij/plugins/polar-transformer.html). This transformation takes an input image in a Cartesian space and transforms it into polar coordinates. This transformation is useful for "unwrapping" images with a generally round object. As a consequence of this transformation, if the image has a visible background, the four angles of the original can be often seen as four triangle-like shapes to the right of the transformed image (giving rise to five black arches, which is the color of the underlying background).

STORM

Setup

The STORM microscope is custom-built on an Olympus IX-73 inverted microscope. Two continuous-wave lasers of wavelength 642 nm (2RU-VFL-P-1500-642; MPB Communications) and 532 nm (Ventus 532; Laser Quantum) and output power of 1.5 W are used for fluorescence excitation/deactivation (van de Linde et al., 2011), and a 405-nm continuous-wave, 50-mW laser (RGB Photonics Lambda Mini) is used for fluorescence reactivation. The lasers are combined with dichroic mirrors (LM01-552-25 and LM01-427-25; Semrock), magnified, and then focused to the back focal plane of the oil-immersion objective Olympus Plan Apochromat 60× NA 1.42. A multiband dichroic mirror (Di03-R 405/488/532/635-t1 25 × 36; Semrock) is used for decoupling of the fluorescence emission of the sample from the laser excitation. Further blocking of the illumination lasers is performed with a multi-edge notch filter (NF03-405/488/532/635E-25; Semrock). The emission light is further divided into two channels with a longpass dichroic (zt647rdc; Chroma) and expanded with a 2× telescope so that the pixel size of the electron-multiplying CCD camera (Andor iXon3 897) matches an optimal value for single-molecule localization, in this case a pixel size of 133 nm. Both channels are filtered with appropriate emission dichroics for Alexa Fluor 565 and 647 (Semrock 582/75 BrightLine HC and Chroma ET700/75m) and imaged side by side into the same electron-multiplying CCD camera (Andor ixon3 897) by using a D-shaped mirror.

A motorized platform is used to laterally displace the illumination (two mirrors and lens), focusing at the back focal plane of the objective. This allows to switch among conventional widefield, HILO, and TIRF illumination. To prevent defocusing within the relatively long STORM imaging acquisition, the setup is equipped with a custom-built focus stabilization system that senses the total internal reflection of an IR diode laser at the interface between the coverslip and the sample and then actuates by mechanically correcting the objective's axial position. The camera, lasers, motorized parts of the microscope, and focus stabilization system are controlled and integrated with Tormenta, open-source, free Python software for fluorescence microscopy control and measurements (Barabas et al., 2016).

Data acquisition

Cells cultured on 18-mm coverslips were placed in a holder, and imaging was performed in 50 mM Tris, pH 8, 10 mM NaCl buffer, at RT. The imaging buffer was supplemented with 10% wt/vol glucose, 100 mM 2-mercaptoethylamine, 1 µg/ml glucose oxidase (Sigma-Aldrich), and 0.5 µg/ml catalase (Sigma-Aldrich) as oxygen scavenging system.

Before STORM imaging, conventional fluorescence images of the ROI were acquired by setting the excitation laser intensity to 1–5 W cm^{-2}. STORM data acquisition was then started by changing the excitation lasers' intensity to 5–15 kW cm^{-2}, thus inducing on-off switching of the fluorescent marker in the tens of milliseconds time range. A camera rate of 20 Hz was found appropriate considering both Alexa Fluor 647 and 565 switching times. Throughout the whole acquisition, the activation 405-nm laser power (1–10 µW cm^{-2}) was increased manually in steps whenever the density of single-molecule events decreased below ∼1–2 molecules per frame. Typically, 15,000 frames were recorded to assure a high density of localizations.

To correct for chromatic aberrations, the two channels were calibrated using fluorescent nanoparticles emitting in both channels (TetraSpeck microspheres; Thermo Fisher Scientific). An affine matrix was computed as the best transformation that matches the location of the beads in both channels (Hartley and Zisserman, 2004). Only calibrations resulting in an error <10 nm were used. A preprocessing background subtraction step is performed to match the background level of both channels for subsequent analysis. The localization analysis and the rendering of the final superresolved image were performed with ThunderSTORM software (Ovesný et al., 2014).

Data analysis

MatLab software (release 2014a; MathWorks) was used to analyze all the images using codes developed by our laboratory to study distribution of distances, densities, and architecture of the proteins imaged by STORM as described for each corresponding figure.

Human breast tissues

Breast tissues from reduction mammoplasties and tumors were acquired from the Cooperative Human Tissue Network, a program funded by the National Cancer Institute. All specimens were collected with patient consent; reduction mammoplasties were reported negative for proliferative breast disease by board-certified pathologists. Use of anonymous samples was granted exemption status by the University of California, Berkeley, Institutional Review Board in accordance with the Code of Federal Regulations 45 CFR 46.101.

Statistical analysis

All statistical analyses were performed using SPSS (IBM SPSS Statistics for Mac OS X, v.23.0; IBM Corp.) or Prism 5 (v.5.0c for Mac OS X; GraphPad Software). To detect differences between media, we used Student's *t* test when comparing between two media. For multiple contrasts, we used two-way ANOVA followed by Bonferroni contrast adjusted for multiple comparisons. Statistical tests and the corresponding contrasts used for each assay are indicated in the figure legends.

Online supplemental material

Fig. S1 shows that FN stabilizes ERα and verifies specificity of the antibodies used. Fig. S2 provides further evidence that ERα is endocytosed in the presence of E_2. Fig. S3 confirms that ERα and β1-integrin colocalize at the plasma membrane and are internalized upon treatment with E_2 in both MCF7 and T47D cells. Fig. S4 shows the conditional distribution of ERα and β1-integrin and its statistical properties from superresolution microscopy analyses. Fig. S5 shows the nuclear localization of ERα through STORM and provides evidence for ERα$^+$ endosomes in human breast tissues using the antibody typically used for clinical analysis (clone SP1). Video 1 provides a 3D render to show that ERα and β1-integrin colocalize in membrane structures in breast tumor cells.

Acknowledgments

We gratefully acknowledge Dr. Carlos Arregui for the gift of GFP-Rab7 expression construct. We also acknowledge Dr. Carlos Davio for providing us with the endocytosis inhibitors. We thank the scientific and technical support provided by the members of the Institute of Oncology "Ángel H. Roffo."

This work was supported by the following grants to M. Simian: Susan G. Komen for the Cure (BCTR0600341), Agencia Nacional de Promoción Científica y Tecnológica (PICT2008-0325/Préstamo BID), Instituto Nacional del Cáncer Ministerio de Salud de la Nación (2015), Fundación Florencio Fiorini, and the Consejo Nacional de Investigaciones Científicas y Técnicas. In addition, the work was supported by a grant from U.S. Department of Defense to M.J. Bissell (W81XWH0810736) and the Breast Cancer Research Foundation to M.J. Bissell as well as a Department of Defense grant to V.M. Weaver (W81XWH-13-1-0216) and a grant from the National Institutes of Health/National Cancer Institute to V.M. Weaver (R01CA192914; Weaver/Seewaldt). We also thank Consejo Nacional de Investigaciones Científicas y Técnicas for the doctoral fellowship awarded to R.G. Sampayo and the Fulbright Association and the Fundación Bunge y Born for the fellowship awarded to R.G. Sampayo.

The authors declare no competing financial interests.

Author contributions: R.G. Sampayo and M. Simian conceived the project; R.G. Sampayo and M. Simian designed experimental approaches; R.G. Sampayo performed most of the experiments and analyzed all the data; R.G. Sampayo and A.M. Toscani developed TIRFM and confocal microscopy analyses; A.M. Toscani also helped in the experimental design; A. Cáceres provided expertise in high-resolution microscopy and the tools to develop TIRFM experiments; M.G. Rubashkin and J.N. Lakins provided technical support for developing confocal and high-resolution microscopy; K. Thi and W.C. Hines performed immunofluorescence staining and imaging of human samples; W.C. Hines also provided key advice for manuscript preparation; F.C. Leskow provided experimental advice and insightful ideas on data interpretation and contributed to the confocal microscopy analyzes; L.A. Masullo, I.L. Violi, and F.D. Stefani provided the necessary equipment to perform STORM, helped to carry out the measurements, and contributed in the elaboration of the superresolution section of this manuscript; D.R. Chialvo provided the numerical tools applied in this study to analyze superresolution microscopy images, performed the analysis with R.G. Sampayo, and contributed in the elaboration of the superresolution section of this manuscript; M.J. Bissell and V.M. Weaver provided expertise in ECM biology, conceptual advice, and experimental support; V.M. Weaver provided expertise in biophysics of cell–matrix interaction; R.G. Sampayo and M. Simian wrote the paper. All authors read and extensively critiqued the manuscript.

Submitted: 9 March 2017
Revised: 20 December 2017
Accepted: 3 May 2018

References

Acconcia, F., P. Ascenzi, A. Bocedi, E. Spisni, V. Tomasi, A. Trentalance, P. Visca, and M. Marino. 2005. Palmitoylation-dependent estrogen receptor alpha membrane localization: Regulation by 17beta-estradiol. *Mol. Biol. Cell.* 16:231–237. https://doi.org/10.1091/mbc.e04-07-0547

Acconcia, F., B. Manavathi, J. Mascarenhas, A.H. Talukder, G. Mills, and R. Kumar. 2006. An inherent role of integrin-linked kinase-estrogen receptor alpha interaction in cell migration. *Cancer Res.* 66:11030–11038. https://doi.org/10.1158/0008-5472.CAN-06-2676

Acerbi, I., L. Cassereau, I. Dean, Q. Shi, A. Au, C. Park, Y.Y. Chen, J. Liphardt, E.S. Hwang, and V.M. Weaver. 2015. Human breast cancer invasion and aggression correlates with ECM stiffening and immune cell infiltration. *Integr. Biol.* 7:1120–1134. https://doi.org/10.1039/C5IB00040H

Adlanmerini, M., R. Solinhac, A. Abot, A. Fabre, I. Raymond-Letron, A.L. Guihot, F. Boudou, L. Sautier, E. Vessières, S.H. Kim, et al. 2014. Mutation of the palmitoylation site of estrogen receptor α in vivo reveals tissue-specific roles for membrane versus nuclear actions. *Proc. Natl. Acad. Sci. USA.* 111:E283–E290. https://doi.org/10.1073/pnas.1322057111

Ambrose, E.J. 1956. A surface contact microscope for the study of cell movements. *Nature.* 178:1194. https://doi.org/10.1038/1781194a0

Arjonen, A., J. Alanko, S. Veltel, and J. Ivaska. 2012. Distinct recycling of active and inactive β1 integrins. *Traffic.* 13:610–625. https://doi.org/10.1111/j.1600-0854.2012.01327.x

Arnal, J.F., F. Lenfant, R. Metivier, G. Flouriot, D. Henrion, M. Adlanmerini, C. Fontaine, P. Gourdy, P. Chambon, B. Katzenellenbogen, and J. Katzenellenbogen. 2017. Membrane and nuclear estrogen receptor alpha actions: From tissue specificity to medical implications. *Physiol. Rev.* 97:1045–1087. https://doi.org/10.1152/physrev.00024.2016

Axelrod, D. 1981. Cell-substrate contacts illuminated by total internal reflection fluorescence. *J. Cell Biol.* 89:141–145. https://doi.org/10.1083/jcb.89.1.141

Axelrod, D. 2001. Total internal reflection fluorescence microscopy in cell biology. *Traffic.* 2:764–774. https://doi.org/10.1034/j.1600-0854.2001.21104.x

Bacia, K., P. Schwille, and T. Kurzchalia. 2005. Sterol structure determines the separation of phases and the curvature of the liquid-ordered phase in model membranes. *Proc. Natl. Acad. Sci. USA.* 102:3272–3277. https://doi.org/10.1073/pnas.0408215102

Bae, Y.K., A. Kim, M.K. Kim, J.E. Choi, S.H. Kang, and S.J. Lee. 2013. Fibronectin expression in carcinoma cells correlates with tumor aggressiveness and poor clinical outcome in patients with invasive breast cancer. *Hum. Pathol.* 44:2028–2037. https://doi.org/10.1016/j.humpath.2013.03.006

Barabas, F.M., L.A. Masullo, and F.D. Stefani. 2016. Tormenta: An open source Python-powered control software for camera based optical microscopy. *Rev. Sci. Instrum.* 87:126103. https://doi.org/10.1063/1.4972392

Bates, M., B. Huang, G.T. Dempsey, and X. Zhuang. 2007. Multicolor super-resolution imaging with photo-switchable fluorescent probes. *Science.* 317:1749–1753. https://doi.org/10.1126/science.1146598

Bermudez-Hernandez, K., S. Keegan, D.R. Whelan, D.A. Reid, J. Zagelbaum, Y. Yin, S. Ma, E. Rothenberg, and D. Fenyö. 2017. A method for quantifying molecular interactions using stochastic modelling and super-resolution microscopy. *Sci. Rep.* 7:14882. https://doi.org/10.1038/s41598-017-14922-8

Bonifacino, J.S., E.C. Dell'Angelica, and T.A. Springer. 2001. Immunoprecipitation. Curr. Protoc. Immunol. Chapter 8:Unit 8 3.

Bradford, M.M. 1976. A rapid and sensitive method for the quantitation of microgram quantities of protein utilizing the principle of protein-dye binding. *Anal. Biochem.* 72:248–254. https://doi.org/10.1016/0003-2697(76)90527-3

Cancer Genome Atlas Network. 2012. Comprehensive molecular portraits of human breast tumours. *Nature.* 490:61–70. https://doi.org/10.1038/nature11412

Caswell, P.T., S. Vadrevu, and J.C. Norman. 2009. Integrins: masters and slaves of endocytic transport. *Nat. Rev. Mol. Cell Biol.* 10:843–853. https://doi.org/10.1038/nrm2799

Cerami, E., J. Gao, U. Dogrusoz, B.E. Gross, S.O. Sumer, B.A. Aksoy, A. Jacobsen, C.J. Byrne, M.L. Heuer, E. Larsson, et al. 2012. The cBio cancer genomics portal: An open platform for exploring multidimensional cancer genomics data. *Cancer Discov.* 2:401–404. https://doi.org/10.1158/2159-8290.CD-12-0095

Chaumet, A., G.D. Wright, S.H. Seet, K.M. Tham, N.V. Gounko, and F. Bard. 2015. Nuclear envelope-associated endosomes deliver surface proteins to the nucleus. *Nat. Commun.* 6:8218. https://doi.org/10.1038/ncomms9218

Chung, T.H., S.M. Wang, J.Y. Liang, S.H. Yang, and J.C. Wu. 2009. The interaction of estrogen receptor alpha and caveolin-3 regulates connexin43 phosphorylation in metabolic inhibition-treated rat cardiomyocytes. *Int. J. Biochem. Cell Biol.* 41:2323–2333. https://doi.org/10.1016/j.biocel.2009.06.001

Ciriello, G., E. Cerami, C. Sander, and N. Schultz. 2012. Mutual exclusivity analysis identifies oncogenic network modules. *Genome Res.* 22:398–406. https://doi.org/10.1101/gr.125567.111

Ciriello, G., M.L. Gatza, A.H. Beck, M.D. Wilkerson, S.K. Rhie, A. Pastore, H. Zhang, M. McLellan, C. Yau, C. Kandoth; TCGA Research Network, et al. 2015. Comprehensive Molecular Portraits of Invasive Lobular Breast Cancer. *Cell.* 163:506–519. https://doi.org/10.1016/j.cell.2015.09.033

Correia, A.L., and M.J. Bissell. 2012. The tumor microenvironment is a dominant force in multidrug resistance. *Drug Resist. Updat.* 15:39–49. https://doi.org/10.1016/j.drup.2012.01.006

Cosker, K.E., and R.A. Segal. 2014. Neuronal signaling through endocytosis. *Cold Spring Harb. Perspect. Biol.* 6:a020669. https://doi.org/10.1101/cshperspect.a020669

Cosker, K.E., S.L. Courchesne, and R.A. Segal. 2008. Action in the axon: Generation and transport of signaling endosomes. *Curr. Opin. Neurobiol.* 18:270–275. https://doi.org/10.1016/j.conb.2008.08.005

Couse, J.F., J. Lindzey, K. Grandien, J.A. Gustafsson, and K.S. Korach. 1997. Tissue distribution and quantitative analysis of estrogen receptor-alpha (ERalpha) and estrogen receptor-beta (ERbeta) messenger ribonucleic acid in the wild-type and ERalpha-knockout mouse. *Endocrinology.* 138:4613–4621. https://doi.org/10.1210/endo.138.11.5496

Cox, D., D.J. Lee, B.M. Dale, J. Calafat, and S. Greenberg. 2000. A Rab11-containing rapidly recycling compartment in macrophages that promotes phagocytosis. *Proc. Natl. Acad. Sci. USA.* 97:680–685. https://doi.org/10.1073/pnas.97.2.680

Debnath, J., S.K. Muthuswamy, and J.S. Brugge. 2003. Morphogenesis and oncogenesis of MCF-10A mammary epithelial acini grown in three-dimensional basement membrane cultures. *Methods.* 30:256–268. https://doi.org/10.1016/S1046-2023(03)00032-X

De Franceschi, N., H. Hamidi, J. Alanko, P. Sahgal, and J. Ivaska. 2015. Integrin traffic: The update. *J. Cell Sci.* 128:839–852. https://doi.org/10.1242/jcs.161653

Degasperi, A., M.R. Birtwistle, N. Volinsky, J. Rauch, W. Kolch, and B.N. Kholodenko. 2014. Evaluating strategies to normalise biological replicates of Western blot data. *PLoS One.* 9:e87293. https://doi.org/10.1371/journal.pone.0087293

Delcroix, J.D., J.S. Valletta, C. Wu, S.J. Hunt, A.S. Kowal, and W.C. Mobley. 2003. NGF signaling in sensory neurons: Evidence that early endosomes carry NGF retrograde signals. *Neuron.* 39:69–84. https://doi.org/10.1016/S0896-6273(03)00397-0

Dozynkiewicz, M.A., N.B. Jamieson, I. Macpherson, J. Grindlay, P.V. van den Berghe, A. von Thun, J.P. Morton, C. Gourley, P. Timpson, C. Nixon, et al. 2012. Rab25 and CLIC3 collaborate to promote integrin recycling from late endosomes/lysosomes and drive cancer progression. *Dev. Cell.* 22:131–145. https://doi.org/10.1016/j.devcel.2011.11.008

Dunn, K.W., M.M. Kamocka, and J.H. McDonald. 2011. A practical guide to evaluating colocalization in biological microscopy. *Am. J. Physiol. Cell Physiol.* 300:C723–C742. https://doi.org/10.1152/ajpcell.00462.2010

Eirew, P., A. Steif, J. Khattra, G. Ha, D. Yap, H. Farahani, K. Gelmon, S. Chia, C. Mar, A. Wan, et al. 2015. Dynamics of genomic clones in breast cancer patient xenografts at single-cell resolution. *Nature.* 518:422–426. https://doi.org/10.1038/nature13952

Gao, J., B.A. Aksoy, U. Dogrusoz, G. Dresdner, B. Gross, S.O. Sumer, Y. Sun, A. Jacobsen, R. Sinha, E. Larsson, et al. 2013. Integrative analysis of complex cancer genomics and clinical profiles using the cBioPortal. *Sci. Signal.* 6:pl1. https://doi.org/10.1126/scisignal.2004088

Gao, W.W., R.Q. Xiao, B.L. Peng, H.T. Xu, H.F. Shen, M.F. Huang, T.T. Shi, J. Yi, W.J. Zhang, X.N. Wu, et al. 2015. Arginine methylation of HSP70 regulates retinoid acid-mediated RARβ2 gene activation. *Proc. Natl. Acad. Sci. USA.* 112:E3327–E3336. https://doi.org/10.1073/pnas.1509658112

Ghajar, C.M., and M.J. Bissell. 2008. Extracellular matrix control of mammary gland morphogenesis and tumorigenesis: Insights from imaging. *Histochem. Cell Biol.* 130:1105–1118. https://doi.org/10.1007/s00418-008-0537-1

Gillespie, E.J., C.L. Ho, K. Balaji, D.L. Clemens, G. Deng, Y.E. Wang, H.J. Elsaesser, B. Tamilselvam, A. Gargi, S.D. Dixon, et al. 2013. Selective inhibitor of endosomal trafficking pathways exploited by multiple toxins and viruses. *Proc. Natl. Acad. Sci. USA.* 110:E4904–E4912. https://doi.org/10.1073/pnas.1302334110

Gould, G.W., and J. Lippincott-Schwartz. 2009. New roles for endosomes: From vesicular carriers to multi-purpose platforms. *Nat. Rev. Mol. Cell Biol.* 10:287–292. https://doi.org/10.1038/nrm2652

Graham, J.D., P.A. Mote, U. Salagame, R.L. Balleine, L.I. Huschtscha, and C.L. Clarke. 2009. Hormone-responsive model of primary human breast epithelium. *J. Mammary Gland Biol. Neoplasia.* 14:367–379. https://doi.org/10.1007/s10911-009-9160-6

Grant, B.D., and J.G. Donaldson. 2009. Pathways and mechanisms of endocytic recycling. *Nat. Rev. Mol. Cell Biol.* 10:597–608. https://doi.org/10.1038/nrm2755

Han, S.W., and J. Roman. 2006. Fibronectin induces cell proliferation and inhibits apoptosis in human bronchial epithelial cells: Pro-oncogenic effects mediated by PI3-kinase and NF-kappa B. *Oncogene.* 25:4341–4349. https://doi.org/10.1038/sj.onc.1209460

Han, X., K.K. Aenlle, L.A. Bean, A. Rani, S.L. Semple-Rowland, A. Kumar, and T.C. Foster. 2013. Role of estrogen receptor α and β in preserving hippocampal function during aging. *J. Neurosci.* 33:2671–2683. https://doi.org/10.1523/JNEUROSCI.4937-12.2013

Hartley, R.I., and A. Zisserman. 2004. Multiple View Geometry in Computer Vision. Chapter 4. Cambridge University Press, Cambridge, UK.

He, Y., Y. Ren, B. Wu, B. Decourt, A.C. Lee, A. Taylor, and D.M. Suter. 2015. Src and cortactin promote lamellipodia protrusion and filopodia formation and stability in growth cones. *Mol. Biol. Cell.* 26:3229–3244. https://doi.org/10.1091/mbc.e15-03-0142

Heery, D.M., E. Kalkhoven, S. Hoare, and M.G. Parker. 1997. A signature motif in transcriptional co-activators mediates binding to nuclear receptors. *Nature.* 387:733–736. https://doi.org/10.1038/42750

Helleman, J., M.P. Jansen, K. Ruigrok-Ritstier, I.L. van Staveren, M.P. Look, M.E. Meijer-van Gelder, A.M. Sieuwerts, J.G. Klijn, S. Sleijfer, J.A.

Foekens, and E.M. Berns. 2008. Association of an extracellular matrix gene cluster with breast cancer prognosis and endocrine therapy response. *Clin. Cancer Res.* 14:5555–5564. https://doi.org/10.1158/1078-0432.CCR-08-0555

Hernández, M.V., M.G. Sala, J. Balsamo, J. Lilien, and C.O. Arregui. 2006. ER-bound PTP1B is targeted to newly forming cell-matrix adhesions. *J. Cell Sci.* 119:1233–1243. https://doi.org/10.1242/jcs.02846

Hines, W.C., I. Kuhn, K. Thi, B. Chu, G. Stanford-Moore, R. Sampayo, J.C. Garbe, M. Stampfer, A.D. Borowsky, and M.J. Bissell. 2016. 184AA3: A xenograft model of ER+ breast adenocarcinoma. *Breast Cancer Res. Treat.* 155:37–52. https://doi.org/10.1007/s10549-015-3649-z

Honerkamp-Smith, A.R., S.L. Veatch, and S.L. Keller. 2009. An introduction to critical points for biophysicists; observations of compositional heterogeneity in lipid membranes. *Biochim. Biophys. Acta.* 1788:53–63. https://doi.org/10.1016/j.bbamem.2008.09.010

Jeselsohn, R., C. De Angelis, M. Brown, and R. Schiff. 2017. The evolving role of the estrogen receptor mutations in endocrine therapy-resistant breast cancer. *Curr. Oncol. Rep.* 19:35. https://doi.org/10.1007/s11912-017-0591-8

Johnson, J.L., J. He, M. Ramadass, K. Pestonjamasp, W.B. Kiosses, J. Zhang, and S.D. Catz. 2016. Munc13-4 is a Rab11-binding protein that regulates Rab11-positive vesicle trafficking and docking at the plasma membrane. *J. Biol. Chem.* 291:3423–3438. https://doi.org/10.1074/jbc.M115.705871

Kisler, K., R.H. Chow, and R. Dominguez. 2013. Fluorescently-labeled estradiol internalization and membrane trafficking in live N-38 neuronal cells visualized with total internal reflection fluorescence microscopy. *J. Steroids Horm. Sci.* https://doi.org/10.4172/2157-7536.S12-002

La Rosa, P., V. Pesiri, G. Leclercq, M. Marino, and F. Acconcia. 2012. Palmitoylation regulates 17β-estradiol-induced estrogen receptor-α degradation and transcriptional activity. *Mol. Endocrinol.* 26:762–774. https://doi.org/10.1210/me.2011-1208

Letoha, T., S. Gaál, C. Somlai, A. Czajlik, A. Perczel, and B. Penke. 2003. Membrane translocation of penetratin and its derivatives in different cell lines. *J. Mol. Recognit.* 16:272–279. https://doi.org/10.1002/jmr.637

Levin, E.R. 2009. Plasma membrane estrogen receptors. *Trends Endocrinol. Metab.* 20:477–482. https://doi.org/10.1016/j.tem.2009.06.009

Li, X., A.G. Garrity, and H. Xu. 2013. Regulation of membrane trafficking by signalling on endosomal and lysosomal membranes. *J. Physiol.* 591:4389–4401. https://doi.org/10.1113/jphysiol.2013.258301

Long, K., L. Moss, L. Laursen, L. Boulter, and C. ffrench-Constant. 2016. Integrin signalling regulates the expansion of neuroepithelial progenitors and neurogenesis via Wnt7a and Decorin. *Nat. Commun.* 7:10354. https://doi.org/10.1038/ncomms10354

Lu, P., K. Takai, V.M. Weaver, and Z. Werb. 2011. Extracellular matrix degradation and remodeling in development and disease. *Cold Spring Harb. Perspect. Biol.* 3:a005058. https://doi.org/10.1101/cshperspect.a005058

Lu, P., V.M. Weaver, and Z. Werb. 2012. The extracellular matrix: A dynamic niche in cancer progression. *J. Cell Biol.* 196:395–406. https://doi.org/10.1083/jcb.201102147

Luzio, J.P., P.R. Pryor, and N.A. Bright. 2007. Lysosomes: Fusion and function. *Nat. Rev. Mol. Cell Biol.* 8:622–632. https://doi.org/10.1038/nrm2217

Mak, H.Y., S. Hoare, P.M. Henttu, and M.G. Parker. 1999. Molecular determinants of the estrogen receptor-coactivator interface. *Mol. Cell. Biol.* 19:3895–3903. https://doi.org/10.1128/MCB.19.5.3895

Małecki, J., J. Wesche, C.S. Skjerpen, A. Wiedłocha, and S. Olsnes. 2004. Translocation of FGF-1 and FGF-2 across vesicular membranes occurs during G1-phase by a common mechanism. *Mol. Biol. Cell.* 15:801–814. https://doi.org/10.1091/mbc.e03-08-0589

Marino, M., P. Ascenzi, and F. Acconcia. 2006. S-palmitoylation modulates estrogen receptor alpha localization and functions. *Steroids.* 71:298–303. https://doi.org/10.1016/j.steroids.2005.09.011

Mayor, S., and R.E. Pagano. 2007. Pathways of clathrin-independent endocytosis. *Nat. Rev. Mol. Cell Biol.* 8:603–612. https://doi.org/10.1038/nrm2216

Mayor, S., K.G. Rothberg, and F.R. Maxfield. 1994. Sequestration of GPI-anchored proteins in caveolae triggered by cross-linking. *Science.* 264:1948–1951. https://doi.org/10.1126/science.7516582

McDonough, A.A., L.C. Veiras, J.N. Minas, and D.L. Ralph. 2015. Considerations when quantitating protein abundance by immunoblot. *Am. J. Physiol. Cell Physiol.* 308:C426–C433. https://doi.org/10.1152/ajpcell.00400.2014

Moreno-Layseca, P., and C.H. Streuli. 2014. Signalling pathways linking integrins with cell cycle progression. *Matrix Biol.* 34:144–153. https://doi.org/10.1016/j.matbio.2013.10.011

Nam, J.M., Y. Onodera, M.J. Bissell, and C.C. Park. 2010. Breast cancer cells in three-dimensional culture display an enhanced radioresponse after coordinate targeting of integrin alpha5beta1 and fibronectin. *Cancer Res.* 70:5238–5248. https://doi.org/10.1158/0008-5472.CAN-09-2319

Nardone, A., C. De Angelis, M.V. Trivedi, C.K. Osborne, and R. Schiff. 2015. The changing role of ER in endocrine resistance. *Breast.* 24(Suppl 2):S60–S66. https://doi.org/10.1016/j.breast.2015.07.015

Nicovich, P.R., D.M. Owen, and K. Gaus. 2017. Turning single-molecule localization microscopy into a quantitative bioanalytical tool. *Nat. Protoc.* 12:453–460. https://doi.org/10.1038/nprot.2016.166

Ovesný, M., P. Křížek, J. Borkovec, Z. Svindrych, and G.M. Hagen. 2014. ThunderSTORM: A comprehensive ImageJ plug-in for PALM and STORM data analysis and super-resolution imaging. *Bioinformatics.* 30:2389–2390. https://doi.org/10.1093/bioinformatics/btu202

Pedram, A., M. Razandi, M. Aitkenhead, C.C. Hughes, and E.R. Levin. 2002. Integration of the non-genomic and genomic actions of estrogen. Membrane-initiated signaling by steroid to transcription and cell biology. *J. Biol. Chem.* 277:50768–50775. https://doi.org/10.1074/jbc.M210106200

Pereira, B., S.F. Chin, O.M. Rueda, H.K. Vollan, E. Provenzano, H.A. Bardwell, M. Pugh, L. Jones, R. Russell, S.J. Sammut, et al. 2016. The somatic mutation profiles of 2,433 breast cancers refines their genomic and transcriptomic landscapes. *Nat. Commun.* 7:11479. https://doi.org/10.1038/ncomms11479

Pietras, R.J., and C.M. Szego. 1984. Specific internalization of estrogen and binding to nuclear matrix in isolated uterine cells. *Biochem. Biophys. Res. Commun.* 123:84–91. https://doi.org/10.1016/0006-291X(84)90383-8

Pontiggia, O., R. Sampayo, D. Raffo, A. Motter, R. Xu, M.J. Bissell, E.B. Joffé, and M. Simian. 2012. The tumor microenvironment modulates tamoxifen resistance in breast cancer: A role for soluble stromal factors and fibronectin through β1 integrin. *Breast Cancer Res. Treat.* 133:459–471. https://doi.org/10.1007/s10549-011-1766-x

Razandi, M., P. Oh, A. Pedram, J. Schnitzer, and E.R. Levin. 2002. ERs associate with and regulate the production of caveolin: Implications for signaling and cellular actions. *Mol. Endocrinol.* 16:100–115. https://doi.org/10.1210/mend.16.1.0757

Reid, G., M.R. Hübner, R. Métivier, H. Brand, S. Denger, D. Manu, J. Beaudouin, J. Ellenberg, and F. Gannon. 2003. Cyclic, proteasome-mediated turnover of unliganded and liganded ERalpha on responsive promoters is an integral feature of estrogen signaling. *Mol. Cell.* 11:695–707. https://doi.org/10.1016/S1097-2765(03)00090-X

Rust, M.J., M. Bates, and X. Zhuang. 2006. Sub-diffraction-limit imaging by stochastic optical reconstruction microscopy (STORM). *Nat. Methods.* 3:793–795. https://doi.org/10.1038/nmeth929

Savkur, R.S., and T.P. Burris. 2004. The coactivator LXXLL nuclear receptor recognition motif. *J. Pept. Res.* 63:207–212. https://doi.org/10.1111/j.1399-3011.2004.00126.x

Schindelin, J., I. Arganda-Carreras, E. Frise, V. Kaynig, M. Longair, T. Pietzsch, S. Preibisch, C. Rueden, S. Saalfeld, B. Schmid, et al. 2012. Fiji: An open-source platform for biological-image analysis. *Nat. Methods.* 9:676–682. https://doi.org/10.1038/nmeth.2019

Schlegel, A., C. Wang, B.S. Katzenellenbogen, R.G. Pestell, and M.P. Lisanti. 1999. Caveolin-1 potentiates estrogen receptor alpha (ERalpha) signaling. *J. Biol. Chem.* 274:33551–33556. https://doi.org/10.1074/jbc.274.47.33551

Skliris, G.P., B.G. Rowan, M. Al-Dhaheri, C. Williams, S. Troup, S. Begic, M. Parisien, P.H. Watson, and L.C. Murphy. 2009. Immunohistochemical validation of multiple phospho-specific epitopes for estrogen receptor alpha (ERalpha) in tissue microarrays of ERalpha positive human breast carcinomas. *Breast Cancer Res. Treat.* 118:443–453. https://doi.org/10.1007/s10549-008-0267-z

Solowska, J., J.M. Edelman, S.M. Albelda, and C.A. Buck. 1991. Cytoplasmic and transmembrane domains of integrin β 1 and β 3 subunits are functionally interchangeable. *J. Cell Biol.* 114:1079–1088. https://doi.org/10.1083/jcb.114.5.1079

Su, Q.P., W. Du, Q. Ji, B. Xue, D. Jiang, Y. Zhu, J. Lou, L. Yu, and Y. Sun. 2016. Vesicle size regulates nanotube formation in the cell. *Sci. Rep.* 6:24002. https://doi.org/10.1038/srep24002

Sung, B.H., and A.M. Weaver. 2011. Regulation of lysosomal secretion by cortactin drives fibronectin deposition and cell motility. *Bioarchitecture.* 1:257–260. https://doi.org/10.4161/bioa.1.6.19197

Takahashi, S., K. Kubo, S. Waguri, A. Yabashi, H.W. Shin, Y. Katoh, and K. Nakayama. 2012. Rab11 regulates exocytosis of recycling vesicles at the plasma membrane. *J. Cell Sci.* 125:4049–4057. https://doi.org/10.1242/jcs.102913

Tiwari, A., J.J. Jung, S.M. Inamdar, C.O. Brown, A. Goel, and A. Choudhury. 2011. Endothelial cell migration on fibronectin is regulated by syntaxin 6-mediated alpha5beta1 integrin recycling. *J. Biol. Chem.* 286:36749–36761. https://doi.org/10.1074/jbc.M111.260828

Totta, P., V. Pesiri, M. Marino, and F. Acconcia. 2014. Lysosomal function is involved in 17β-estradiol-induced estrogen receptor α degradation and cell proliferation. *PLoS One.* 9:e94880. https://doi.org/10.1371/journal.pone.0094880

Totta, P., V. Pesiri, M. Enari, M. Marino, and F. Acconcia. 2015. Clathrin heavy chain interacts with estrogen receptor α and modulates 17β-estradiol signaling. *Mol. Endocrinol.* 29:739–755. https://doi.org/10.1210/me.2014-1385

Upla, P., V. Marjomäki, P. Kankaanpää, J. Ivaska, T. Hyypiä, F.G. Van Der Goot, and J. Heino. 2004. Clustering induces a lateral redistribution of alpha 2 beta 1 integrin from membrane rafts to caveolae and subsequent protein kinase C-dependent internalization. *Mol. Biol. Cell.* 15:625–636. https://doi.org/10.1091/mbc.e03-08-0588

van de Linde, S., A. Löschberger, T. Klein, M. Heidbreder, S. Wolter, M. Heilemann, and M. Sauer. 2011. Direct stochastic optical reconstruction microscopy with standard fluorescent probes. *Nat. Protoc.* 6:991–1009. https://doi.org/10.1038/nprot.2011.336

Vanlandingham, P.A., and B.P. Ceresa. 2009. Rab7 regulates late endocytic trafficking downstream of multivesicular body biogenesis and cargo sequestration. *J. Biol. Chem.* 284:12110–12124. https://doi.org/10.1074/jbc.M809277200

Wang, X., and J. Robbins. 2014. Proteasomal and lysosomal protein degradation and heart disease. *J. Mol. Cell. Cardiol.* 71:16–24. https://doi.org/10.1016/j.yjmcc.2013.11.006

Waxmonsky, N.C., and S.D. Conner. 2013. Avβ3-integrin-mediated adhesion is regulated through an AAK1L- and EHD3-dependent rapid-recycling pathway. *J. Cell Sci.* 126:3593–3601. https://doi.org/10.1242/jcs.122465

Yao, E.S., H. Zhang, Y.Y. Chen, B. Lee, K. Chew, D. Moore, and C. Park. 2007. Increased beta1 integrin is associated with decreased survival in invasive breast cancer. *Cancer Res.* 67:659–664. https://doi.org/10.1158/0008-5472.CAN-06-2768

Supplemental material

Sampayo et al., https://doi.org/10.1083/jcb.201703037

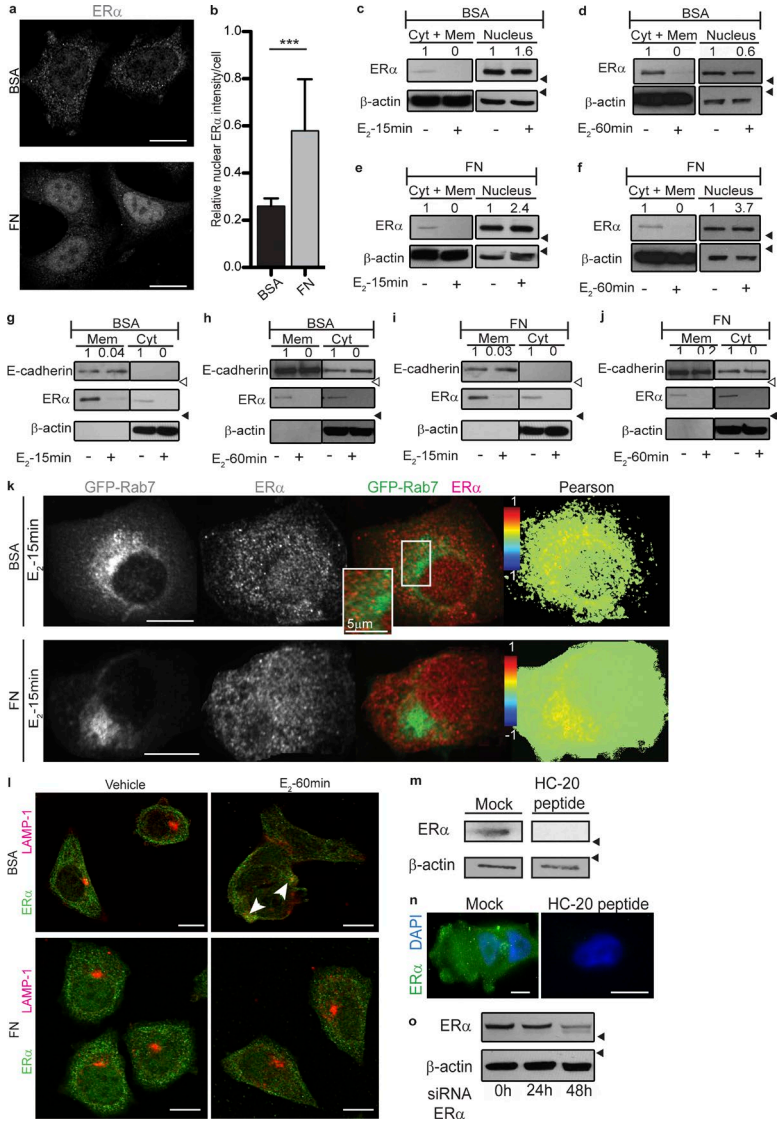

Figure S1. **FN stabilizes ERα. (a)** Confocal images of MCF7 cells seeded on BSA or FN treated with E_2 for 15 min and stained for ERα. **(b)** Quantification of a. For each experimental condition, shown is nuclear ERα intensity (mean gray value) per cell calculated using Fiji relative to the highest intensity recorded. Differences between groups were analyzed by one-tailed Student's *t* test (per replicate: BSA: n_{BSA} = 8 cells; n_{FN} = 15 cells). **(c and d)** Western blots of a subcellular fractionation of T47D cells seeded on BSA and treated for 15 (c) or 60 min (d) as indicated. Blotting antibodies are shown on the left. For each subcellular fraction, shown is the ERα/β-actin density ratio normalized to the control group. **(e and f)** Western blots of a subcellular fractionation of T47D cells seeded on FN and treated for 15 (e) or 60 min (f) as indicated. Blotting antibodies are shown on the left. For each subcellular fraction, shown is the ERα/β-actin density ratio normalized to the control group. **(g and h)** Western blots of a subcellular fractionation of MCF7 cells seeded on BSA and treated for 15 (g) or 60 min (h) as indicated. Blotting antibodies are shown on the left. For the membrane fraction, the ERα/E-cadherin density ratio is shown normalized to the control group. For the cytoplasmic fraction, shown is the ERα/β-actin density ratio normalized to the control group. **(i and j)** Western blots of a subcellular fractionation of MCF7 cells seeded on FN and treated for 15 (i) or 60 min (j) as indicated. Blotting antibodies are shown on the left. For the membrane fraction, the ERα/E-cadherin density ratio is shown normalized to the control group. For the cytoplasmic fraction, shown is the ERα/β-actin density ratio normalized to the control group. **(k)** Confocal images of T47D cells expressing GFP-Rab7 seeded on BSA (top) or FN (bottom), treated for 15 min as indicated, and stained for ERα. Pearson's correlation maps are shown on the right. **(l)** Confocal images of MCF7 cells, seeded on BSA or FN, treated for 60 min as indicated, and stained for LAMP-1 or ERα. Arrows indicate regions of colocalization between the two markers. **(m)** Western blots of MCF7 cells blotted with ERα antibody (clone HC-20) preincubated for 90 min at 4°C with HC-20 peptide or its control before using it in the blotting membranes following the standard protocol for Western blot. **(n)** Widefield images of T47D cells stained with ERα antibody preincubated with HC-20 peptide or its control. Counterstaining, DAPI. **(o)** Western blots of ERα knockdown by siRNA in MCF7 cells. Blotting antibodies are shown on the left. Data are represented as mean ± SD. ***, $P < 0.001$. Shown data are representative of at least three independent experiments. Black arrowheads indicate positions of 50-kD markers. White arrowheads indicate positions of 100-kD markers. Treatments: ethanol (vehicle) or 10^{-8} M E_2. Bars, 10 µm (unless otherwise indicated).

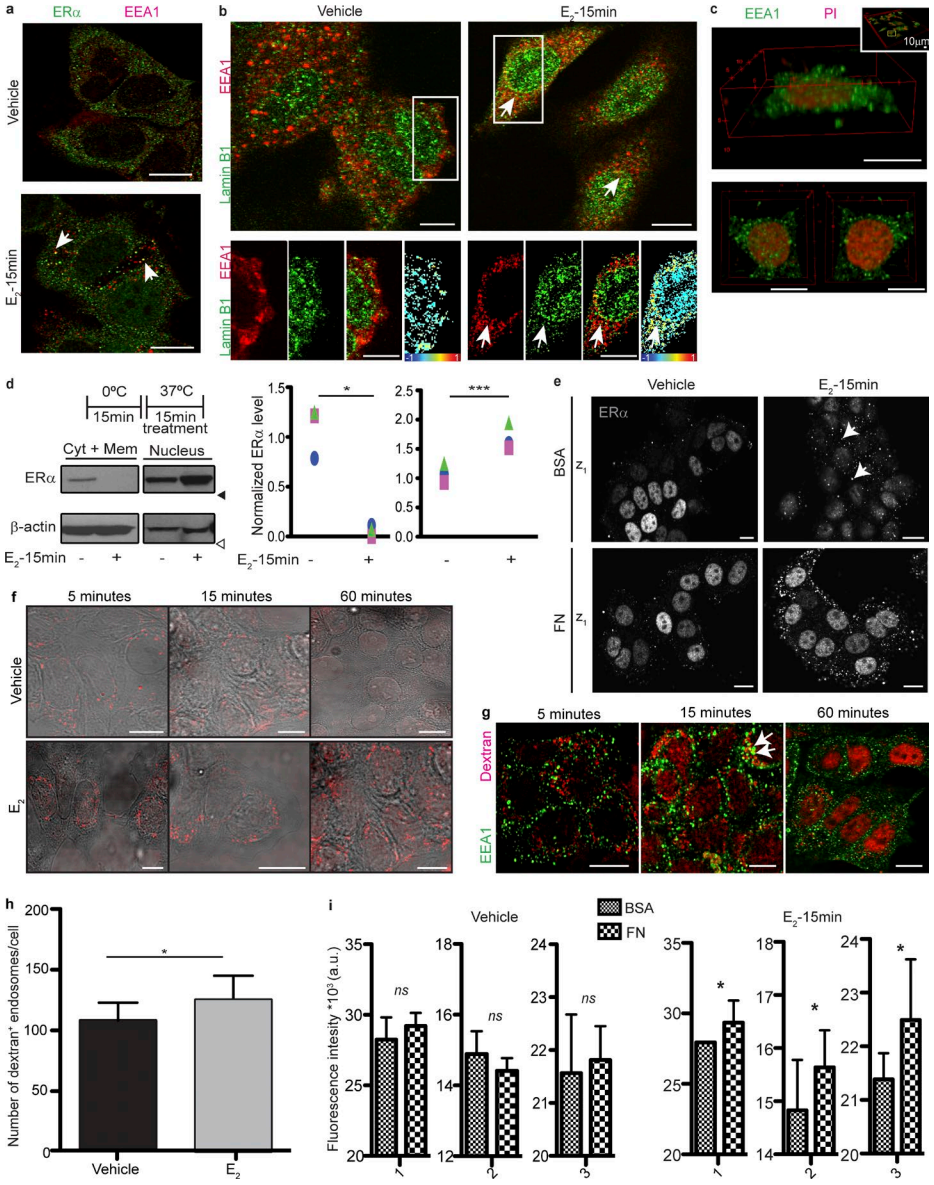

Figure S2. **ERα is endocytosed in the presence of E_2. (a)** Confocal images of MCF7 cells treated for 15 min as indicated and stained for EEA1 or ERα. Arrows indicate regions of colocalization between the two markers. **(b)** Confocal images of MCF7 cells treated for 15 min as indicated and stained for Lamin B1 or EEA1. Arrow indicates regions of colocalization between the two markers. White rectangles outline the areas whose magnifications are presented in the bottom panels, showing each channel separately and their corresponding merge. Pearson's correlation maps are shown on the bottom right. Arrows indicate regions of colocalization between the two markers. **(c)** 3D reconstruction from confocal z stacks of MCF7 cells treated for 15 min with E_2 and stained for EEA1 or propidium iodide (PI). Top: Rendered image of a side view of the cell outlined with a yellow rectangle in the inset. Bottom left: Rendered image of the top view of the outlined cell. Bottom right: Rendered image of the bottom view of the outlined cell. Renderizations were done using the plugin 3D viewer of Fiji. The inset shows the full reconstructed field. **(d)** Left: Outline of the protocol followed and Western blot of a subcellular fractionation of MCF7 cells treated as indicated. Blotting antibodies are shown on the left. Right: Densitometry. For each subcellular fraction, the ERα/β-actin density ratio is shown, normalized to the mean control group. Each symbol represents a different experiment. Differences between groups were analyzed by one-tailed paired Student's *t* test ($n = 3$). **(e)** Images of confocal microscopy of the nuclear/cytoplasmic (apical) focal plane (z1) of MCF7 cells seeded on BSA or FN treated for 15 min as indicated and stained for ERα. White arrows indicate ERα⁺ vesicles, determined as punctae of 10–15 pixels in diameter (~200 nm). **(f)** MCF7 cells were treated with E_2 for the indicated times, in the presence of dextran-CF543. Differential interference contrast (DIC) images merged with the red channel (dextran) are shown. **(g)** Images of confocal microscopy of MCF7 cells treated with E_2 for the indicated times in the presence of dextran-CF543 and stained for EEA1. Arrows indicate regions of colocalization between the two fluorophores. **(h)** Quantification of g. For each experimental condition, the number of dextran⁺ endosomes per cell is shown after a 15-min treatment. Differences between groups were analyzed by one-tailed Student's *t* test (per replicate: $n = 9$ fields). **(i)** Dextran recycling assay. MCF7 cells seeded on BSA or FN were pretreated for 15 min with E_2 or its vehicle, followed by a 10-min incubation with dextran-CF543, and then were chased for 15 min to measure the amount of dextran-CF543 in the conditioned medium. For each experimental condition, shown is the fluorescence intensity measured for three independent experiments. Data are represented as mean ± SD. Differences between groups were analyzed by one-tailed paired Student's *t* test ($n = 3$ replicates). *, $P < 0.05$; ***, $P < 0.001$. Shown data are representative of at least three independent experiments. Black arrowheads indicate positions of 50-kD markers. White arrowheads indicate positions of 37-kD markers. Treatments: ethanol (vehicle) or 10^{-8} M E_2, 10 µg/ml dextran-CF543. Bars, 10 µm.

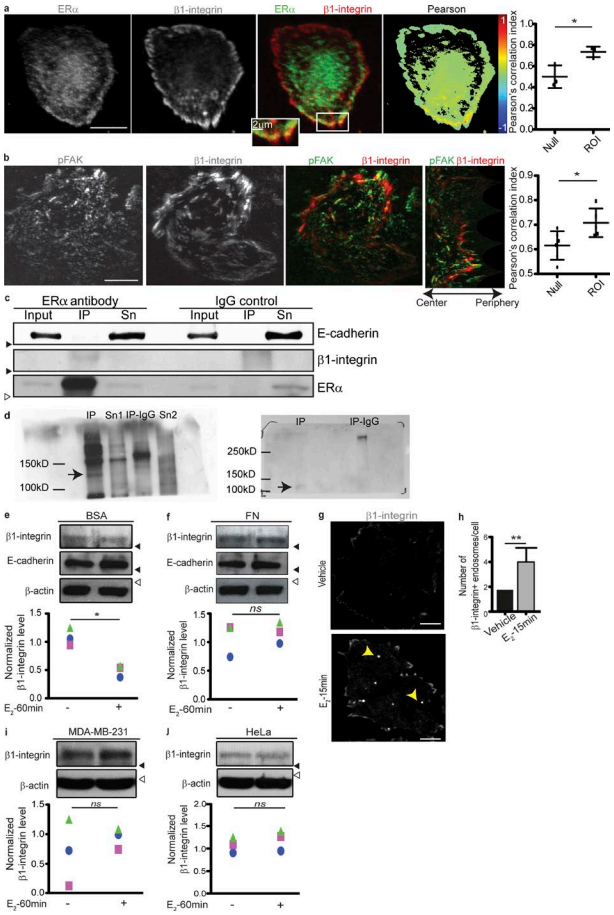

Figure S3. **ERα and β1-integrin colocalize at the plasma membrane and are internalized after treatment with E_2. (a)** Confocal images of T47D cells stained for ERα and β1-integrin. Pearson's correlation map is shown on the right. Right: Quantification. For each experimental condition, Pearson's correlation index was calculated within the areas of colocalization (ROI) and compared with random areas without colocalization (Null), using Fiji. Differences between groups were analyzed by one-tailed Student's *t* test (per replicate: n_{null} = 3 fields, n_{ROI} = 3 fields). **(b)** TIRFM images of MCF7 cells stained for pFAK and β1-integrin. Polar transformation performed with Fiji is shown on the right. Right: Quantification. For each experimental condition, Pearson's correlation index was calculated within the areas of colocalization (ROI) and compared with random areas without colocalization (Null), using Fiji. Datasets are plotted, and mean ± SD are shown on the graph. Differences between groups were analyzed by one-tailed Student's *t* test (per replicate: n_{null} = 4 fields, n_{ROI} = 4 fields). **(c)** Western blot of a coimmunoprecipitation assay on MCF7 cells. IP antibodies are shown on the top. Blotting antibodies are shown on the right. Input, whole lysate; IP, immunoprecipitated fraction; Sn, supernatant fraction from the IP. **(d)** Left: IP experiment following the protocol described by Bonifacino et al. (2001) with slight modifications. Immunoblot: β1-integrin (1981-LM534). The specific band corresponding with β1-integrin upon IP with ERα (F10) antibody, and blotted with β1-integrin LM534 antibody can be seen. As expected, IP with control IgG does not show the specific β1-integrin band. Lanes: IP, ERα antibody; Sn1, supernatant from IP with ERα antibody; IP-IgG, control IgG; Sn2, supernatant from IP with control IgG. Right: Improved IP protocol adding more stringent washing conditions to remove the remaining IP primary antibodies, leading to cleaner IPs. Immunoblot: β1-integrin. This blot is one of the replicates of the original Western blot shown in c. The specific, albeit faint, β1-integrin band can be seen in the IP lane, whereas this band is absent in the lane from control IgG. Lanes: IP, ERα antibody; IP-IgG, control IgG. Arrows indicate the band corresponding with β1-integrin. **(e)** Top: Western blot of total lysates of T47D cells seeded on BSA and treated for 60 min as indicated. Blotting antibodies are shown on the left. Bottom: Densitometry. For each experimental condition, shown is the β1-integrin/β-actin density ratio normalized to the mean control group. Each symbol represents a different experiment. Differences between groups were analyzed by one-tailed paired Student's *t* test (*n* = 3 replicates). **(f)** Top: Western blot of total lysates of T47D cells seeded on FN and treated for 60 min as indicated. Blotting antibodies are shown on the left. Bottom: Densitometry. For each experimental condition, shown is the β1-integrin/β-actin density ratio normalized to the mean control group. Each symbol represents a different experiment. Differences between groups were analyzed by one-tailed paired Student's *t* test (*n* = 3 replicates). **(g)** Widefield images of MCF7 cells live-stained for β1-integrin and then treated for 15 min as indicated to chase β1-integrin internalization dynamics. Arrows indicate β1-integrin$^+$ vesicles determined as punctae of ∼200-nm diameter (10–15 pixels). **(h)** Quantification of g. For each experimental condition, shown is the number of β1-integrin$^+$ vesicles per cell, among cells with these endosomes. Shown data are mean ± SD. Differences between groups were analyzed by one-tailed Student's *t* test (per replicate: *n* = 5 fields). **(i)** Top: Western blot of total lysates of MDA-MB-231 cells (human mammary adenocarcinoma) seeded on BSA and treated for 60 min as indicated. Blotting antibodies are shown on the left. Bottom: Densitometry. For each experimental condition, shown is the β1-integrin/β-actin density ratio normalized to the mean control group. Each symbol represents a different experiment. Differences between groups were analyzed by one-tailed paired Student's *t* test (*n* = 3 replicates). **(j)** Top: Western blot of total lysates of HeLa cells (human cervical cancer) seeded on BSA and treated for 60 min as indicated. Blotting antibodies are shown on the left. Bottom: Densitometry. For each experimental condition, shown is the β1-integrin/β-actin density ratio normalized to the mean control group. Each symbol represents a different experiment. Differences between groups were analyzed by one-tailed paired Student's *t* test (*n* = 3 replicates). *, $P < 0.05$. Shown data are representative of at least three independent experiments. Black arrowheads indicate positions of 100-kD markers. White arrowheads indicate positions of 50-kD markers. Treatments: ethanol (vehicle) or 10^{-8} M E_2. Bars, 10 µm (unless otherwise indicated).

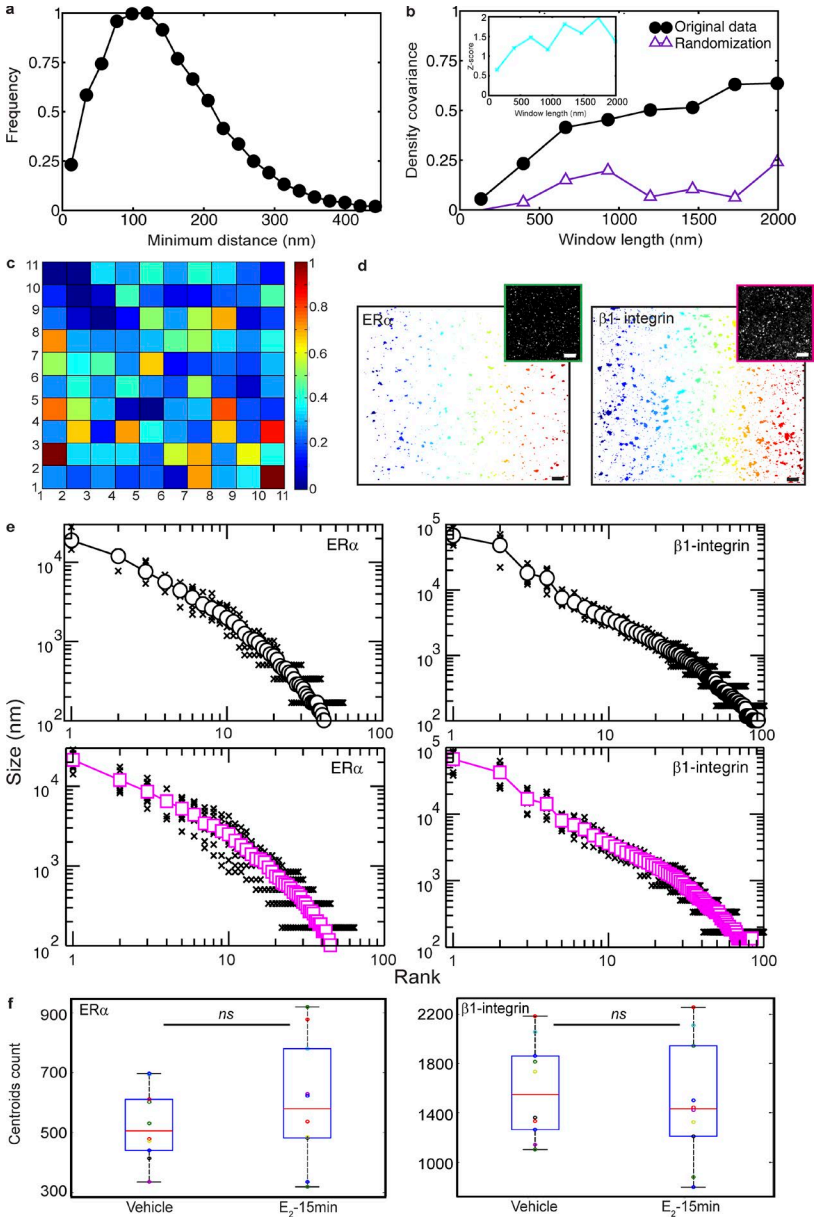

Figure S4. **Conditional distribution of ERα versus β1-integrin and its statistical properties. (a)** Shown is the histogram for normalized frequencies for the MDs between β1-integrin and ERα in filopodia of MCF7 cells among all the analyzed fields from STORM images. For each domain detected, centroids were identified, and MDs were calculated from each β1-integrin to its nearest ERα domain throughout each 500 × 500-pixel frame. Frequency of each distance bin was normalized to the highest frequency detected. The graph shows that the mean MD between ERα and β1-integrin is ∼100 nm. **(b)** Shown is the mean density covariance between ERα and β1-integrin domains. Each frame was divided into square ROIs of different sizes as depicted in c. Within each window, the density of ERα or β1-integrin was computed, and the correlation coefficient (C) between these densities was calculated for each frame analyzed. The mean of C among all the analyzed cells (black full circles) or randomized data generated by mixing β1-integrin images with random ERα images (violet empty triangles) was plotted as a function of the window side length. The inset shows the z score. It was calculated as the difference between the mean of the original dataset for each window minus the mean of the randomized group divided by the square root of the sum of the SD of each group normalized by *n*. This result shows a significant difference in density covariance between both groups, indicating that ERα and β1-integrin have a positive spatial association and that this organization is not a consequence of a random process. **(c)** Each 500 × 500–pixel field was divided into squares or windows of different sizes (from 130 nm [10 pixels] to 2,000 nm [150 pixels] in side length) to evaluate ERα and β1 intensities in each window. The figure shows one field divided into 50 × 50–pixel windows and colored as a function of the ratio between ERα and β1-integrin densities, going from 0 to 1 as shown in the color bar on the right. **(d)** Each color represents a different ERα or β1-integrin domain from the STORM fields of filopodia of MCF7 cells shown on the top right corners. **(e)** Rank size distribution plot of the domains depicted in d. From the largest sizes on the left and decreasing to the right of the plot, the empty symbols represent averages over 10 frames denoted by crosses. A simple visual inspection already reveals no significant differences between the datasets obtained under vehicle (upper) or treated (bottom) conditions. **(f)** Box plots representing the total number of domains identified among all the analyzed fields for ERα or β1-integrin in control or E_2-treated cells. Central red marks represent the median, and the bottom and top edges of each box indicate the 25th and 75th percentiles, respectively. The whiskers extend to the most extreme data points. This plot shows no significant differences in the number of domains between control and treated cells. Student's *t* test (*n* = 3 replicates). Shown data are representative of at least three independent experiments. Treatments: ethanol (vehicle) or 10^{-8} M E_2. Bars, 2 µm.

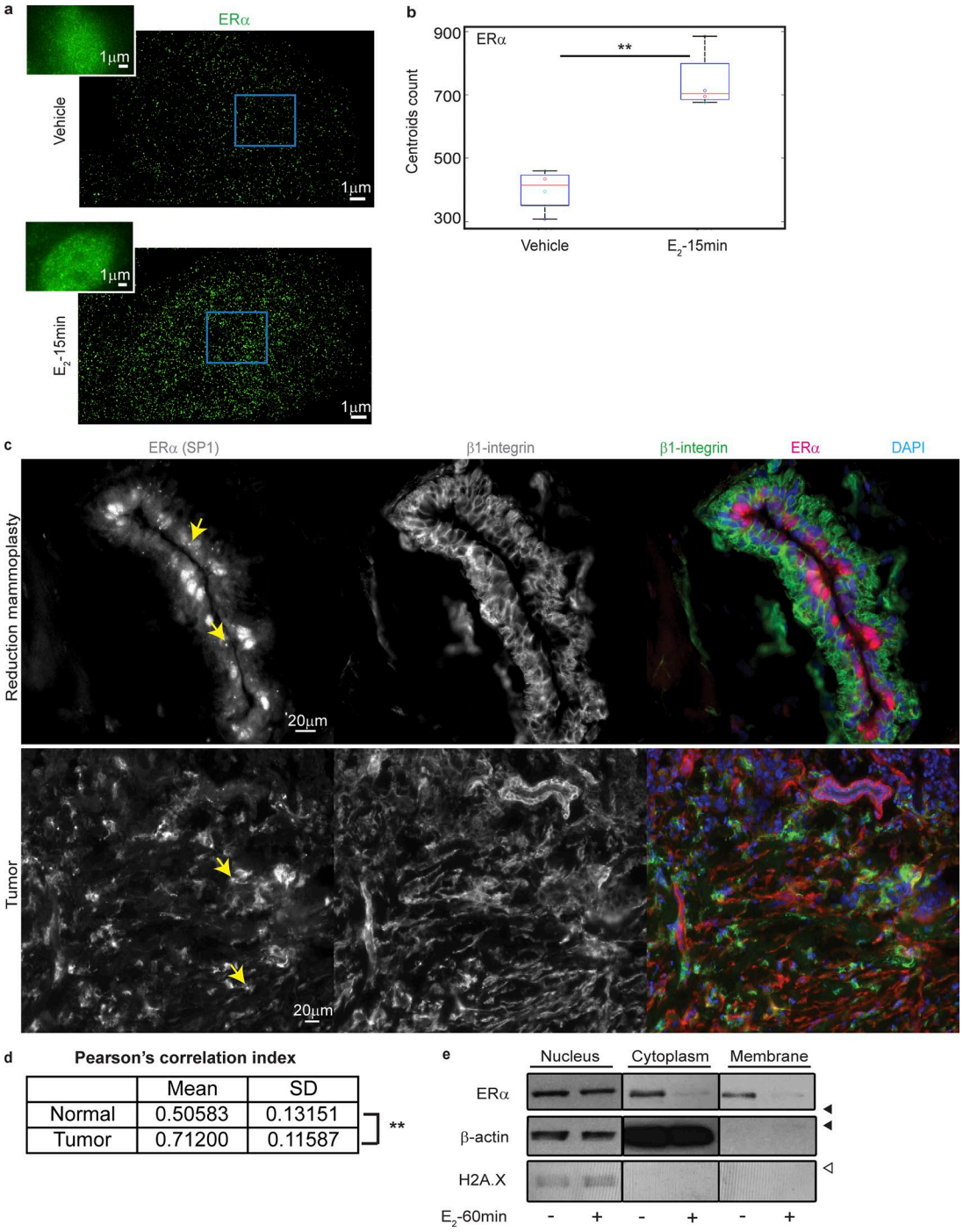

Figure S5. **Nuclear distribution of ERα and colocalization with β1-integrin in human breast samples. (a)** Images from STORM of the nuclear region of MCF7 cells treated as indicated for 15 min and stained for ERα or β1-integrin. Insets in the top left corners show the same images taken with widefield microscopy. Blue squares outline representative areas of 500 × 500 pixels used for subsequent analysis. **(b)** Box plot representing the total number of centroids (domains) identified among all the analyzed nuclear fields for ERα in control or E_2-treated cells. Central red mark represents the median, and the bottom and top edges of the box indicate the 25th and 75th percentiles, respectively. The whiskers extend to the most extreme data points. This plot shows that E_2 treatment significantly increases the number of ERα nuclear domains compared with control. Student's *t* test (n = 3 replicates). **(c)** Top: Confocal images of a normal human breast tissue (reduction mammoplasty; sample N211) stained for ERα (SP1 clone), β1-integrin, and DAPI. Arrows indicate the presence of ERα$^+$ endosomes. Similar results were obtained in the four different specimens analyzed. Bottom: Confocal images of a human breast tumor (Luminal A subtype adenocarcinoma; sample T171) stained for ERα (SP1 clone), β1-integrin, and DAPI. Arrows indicate the presence of ERα$^+$ endosomes. Similar results were obtained in the three different specimens analyzed. **(d)** Table showing mean and SD of Pearson's correlation index calculated for the overall colocalization between ERα and β1-integrin. Differences between groups were analyzed by two-tailed Student's *t* test (per replicate: n_{normal} = 6 fields; n_{tumor} = 6 fields). **(e)** Western blot of a subcellular fractionation of MCF7 cells, seeded on BSA and treated for 60 min as indicated. Blotting antibodies are shown on the left. **, P < 0.01. Shown data are representative of at least three independent experiments. Black arrowheads indicate positions of 50-kD markers. White arrowheads indicate positions of 20-kD marker. Treatments: ethanol (vehicle) or 10^{-8} M E_2.

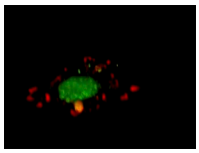

Video 1. **ERα and β1-integrin colocalize in membrane structures.** Fiji 3D-reconstruction of confocal images of a cell (MCF7) stained for ERα and β1-integrin. Frame rate: seven frames per second.